JNC TY8400 2000-007

# JNC-DOE Collaborative Program on Mass Transport: Characterization and Predictive Technologies

## 1999-2000 Annual Report

July 2000

**Ernest Orlando Lawrence Berkeley National Laboratory**

〒319-1184　茨城県那珂郡東海村村松4番地49
核燃料サイクル開発機構
技術展開部　技術協力課
Inquiries about copyright and reproduction should be addressed to :
Technical Cooperation Section,
Technology Management Division,
Japan Nuclear Cycle Development Institute
4-49 Muramatsu, Tokai-mura, Naka-gun, Ibaraki, 319-1184
Japan



Ⓢ

JNC TY8400 2000－007
２０００年７月

# JNC-DOE Collaborative Program on Mass Transport : Characterization and Predictive Technologies

## 1999 – 2000 Annual Report
（研究報告）

Principal Investigator : Chin –Fu Tsang[1] and Kenzi Karasaki[1]

## 要　旨

JNC/DOE 間の共同研究計画は、地層中への放射性廃棄物の処分において重要な役割を担っているプロセスを支配する基本的な物理及び化学特性についての理解を深めるとともに、不均質な地層中での核種移行や地層からの核種放出についての調査手法や予測手法を開発することを目的として策定されている。

共同研究計画にしたがって、本年度は以下の６つのタスクを実施した。

1. 階層構造的な亀裂性岩盤中の流れと物質移行についての検討
本タスクでは、階層構造を有する亀裂性岩盤のサイト特性調査を行なうにあたり、最小の本数の井戸のみしか利用できない場合を想定し、自然勾配トレーサ試験及び単一孔揚水試験をシミュレートし、階層構造を有する亀裂性岩盤のフラクタル次元がこれらの試験に与える影響について調べた。

2. ロバストで高速に解を求めることができる逆解析手法の開発
詳細なサイト特性調査を行なう場合、多数の圧力試験を実施し、データを実測する必要がある。本タスクでは、このような状況において、数百、数千ものパラメータを同時に推定することができる逆解析アルゴリズムの開発を行ない、原位置試験サイトで実施された圧力干渉試験に適用することにより亀裂の存在及びその特性を予測した。また、別途実施したボアホール試験と物理探査データから予測結果を検証した。

3. 複雑な不均質性媒体中の流れのモデル化
亀裂性媒体中の流れのモデル化を行なう場合の最も一般的な仮定は、亀裂

[1] Earth Science Division, Ernest Orlando Lawrence Berkeley National Laboratory, University of California, Berkeley, California 94720, USA.

部とマトリクス部をそれぞれ連続体として取り扱うことである。また、亀裂部とマトリクス部との間の流れは平均的な圧力差により生じると仮定される。本タスクでは、このような仮定を、ランダムに発生させた不均質媒体中の流れの方程式を厳密に解くことにより検討した。

4. 簡単な亀裂システムにおける物質移行についての検討
本タスクでは、３つの亀裂からなるシステム中の流れと物質移動について、パイプモデルを使用した解析結果と亀裂を不均質性媒体として取り扱った場合の解析結果との比較を行なうことにより、モデルの単純化の妥当性に関する検討を行なった。また、亀裂中に存在する澱み領域が物質移動に与える影響について調べた。

5. TILA-99 のレビュー
本タスクでは、フィンランドの実施主体 POSIVA OY により取りまとめられた安全評価レポート TILA-99 についてのレビューを実施した。レビューでは特に性能評価における地層中の地下水流れと物質移動についてのモデル化手法及び方法論を中心にまとめた。

6. 地層中の流れと物質移行に関する主要な問題と今後の課題についてのまとめ
本タスクでは、不均質媒体中の地下水流れと物質移動のモデル化における重要な問題と今後の課題についての議論をまとめた。まとめでは、流れのチャンネリング、トレーサの破過曲線、亀裂性岩盤中の流れのスケール依存性、異なるスケールでの計測、モデル化、予測、不均質性、サイト特性調査等について記述した。

# List of Contents

JNC TY8400 2000−007
J u l y , 2 0 0 0

# 1999-2000 Annual Report

# JNC-DOE Collaborative Program on Mass Transport: Characterization and Predictive Technologies

Principal Investigator

Chin-Fu Tsang and Kenzi Karasaki

Earth Sciences Division
Ernest Orlando Lawrence Berkeley National Laboratory
One Cyclotron Road
Berkeley, CA 94720, USA
Email: cftsang@lbl.gov; Fax: 1 510 486 5686

## Background

This is the seventh year of a continuing collaborative program which started in April, 1993 under an Annex pursuant to the Agreement of November 20, 1986 between the Nuclear Power and Fuel Development Corporation (PNC), Japan and United States Department of Energy (DOE) on Cooperation in the Area of Radioactive Waste Management. The Annex was originally signed on March 26, 1993 to be effective for four years, and was subsequently renewed on September 15, 1997 for three additional years based on the renewed PNC-DOE Binational Agreement. The subject of research covered under this Annex is Mass Transport: Characterization and Predictive Technologies. In 1998, PNC was renamed Japan Nuclear Cycle Development Institute (JNC). The DOE Office overseeing this annex agreement is the Office of Environmental Management, Office of Science and Technology (EM-50). The work is performed at the Earth Sciences Division of the Ernest Orlando Lawrence Berkeley National Laboratory with funding support from JNC.

## Objectives

The primary objective of this Collaborative Program is to (a) improve the understanding of the fundamental physics and chemistry that govern the processes which play a significant role in radio-active waste isolation/disposal in geologic systems and (b) develop characterization and predictive technologies of release and transport of radio-nuclides in heterogeneous geologic media. The Collaborative Program focuses on the definition and investigation of the processes of primary importance to the release and transport of radionuclides, and the development and application of theories and models to predict the phenomena accurately. Available laboratory and field experiments within and outside of the Collaborative Program provide the basic phenomenological data to test the validity of the theories and the modeling approach itself.

## 1999-2000 Activities

This year's activities cover six tasks, at different stages of progress.

The first study examines flow and transport in hierarchically fractured rocks. In the study of hierarchically fractured rocks, we are primarily concerned with the situation that arises when a hierarchically fractured site is encountered in which a minimum number of wells are available for subsurface characterization. This is most likely the case when selecting a suitable site for high-level nuclear waste storage. In the early stages of site characterization, when only one or a few wells are available, single-well pumping tests are likely to be the primary characterization tool. We simulate natural-gradient tracer tests as well as single-well pumping tests in hierarchically structured fracture networks. We examine how fractal dimension affects the performance measures of the natural-gradient tracer tests, including flow through the model, tracer travel time, front width, and maximum concentration. Our primary goal is to illustrate the types of flow and transport behavior that are representative of hierarchically fractured rock, and thereby aid the design of field tests and the interpretation of field data. The present approach is more practically oriented, with the goal of providing insights and information for designing and interpreting field experiments.

The second study focuses on the development of a robust and fast inversion algorithm. In hydraulic well tests, pressure changes are monitored in response to a

fluid being pumped into or out of an aquifer. The response is a function of the geometry and the flow parameters of the reservoir. Therefore, by analyzing the pressure changes one can estimate such reservoir parameters. In this regard, well test analysis is an inverse problem. The simplest type of inversion is the traditional analytical approach, where the pressure data are compared to those of known analytical models. However, analytical models are only available for a handful of idealized situations. When a more detailed characterization is needed, multiple pressure tests with many observation points must be conducted. In such cases a numerical inversion is usually employed. It is not uncommon that in such inversions, hundreds of thousands of unknown parameters have to be estimated. In the second study, the focus is to develop an inversion algorithm that can be used in such situations.

The third study investigates the multi-continua description of flow in composite heterogeneous media. One of the most common assumptions that are made in modeling flow in fractured rock is to assume that the fracture system forms one continuum and the rock matrix another. It is further assumed that the cross-flow between them is proportional to the mean pressure difference. We examine this assumption by formulating and exactly solving the equations for flow in random composite media. After a lengthy mathematical development, we find the assumption generally unsatisfactory considering its region of applicability.

The fourth task includes two topical studies of solute transport in simple fracture systems. The first is an evaluation of the simulation of particle transport in a three-fracture system using a simple pipe model as compared with a fully heterogeneous model. The former is often used in complex fracture network modeling which demands a simple representation at the one, two or three-fracture level. By taking into account permeability heterogeneity and flow channeling effect, we calculate the effective flow wetted surface fraction for the flowing particles. This is the surface area of the fractures through which the particles can diffuse into the matrix and chemically react with the matrix materials. This year, the flow wetted surface area as a function of the degree of heterogeneity is evaluated. The second subtopic is a study of the diffusion process at an intersection between two fractures. If the diffusion is very small, particles will follow the streamlines and enter into a neighboring fracture. But if the diffusion is large, they will be distributed into outflow fractures according to their respective flow rates. Such a phenomenon has important implications to solute dispersion in fractured rocks and many authors used an arbitrary assumption. The

study investigates the effects on tracer breakthrough curves due to diffusion at the intersections as a function of flow velocities and fracture dimensions.

The fifth task is a summary, review, and comment of the TILA-99 report. The TILA-99 project is a postclosure safety assessment for a potential nuclear waste repository by the responsible Finnish organization POSIVA OY. Its focus is on the normal evolution of the repository at candidate sites in Finland and on the potential release and transport of radionuclides from the repository into the geosphere and biosphere. The summary 's focus is on the approach and methodology for geosphere flow and transport predictions in performance assessment, as discussed in the report, and on lessons learned. TILA-99 is an interesting report. As noted above, it attempts to do performance assessment of a potential nuclear waste repository using simplified, conservative conditions It is also interesting that TILA-99 does not perform multiple-case analysis, in which each case is deterministic and specifically defined. Then ranges of predictions are built from many such case calculations. Rather in TILA-99, ranges of parameters and conditions are used from data and submodel calculations, which are then combined to give ranges of predictions. One strength of the TILA-99 report is its careful analysis and clear presentation of sensitivity and "what if" analysis, which is a good pattern for other performance assessment efforts.

The final Task is a discussion on the key issues and challenges related to geosphere flow and transport. This discussion forms the invited Keynote Paper for the International Association of Hydrogeologists XXX Congress to be held in Cape Town in November 2000. The need for predictions of groundwater flow and contaminant transport in the subsurface—over large distances and long time periods—has imposed extraordinary demands on the field of hydrogeology. Such a need arises in assessing the safety of a geologic nuclear waste repository and in evaluating groundwater contamination and remediation designs. One of the main difficulties in modeling groundwater flow and mass transport is the heterogeneity of the flow system, both in terms of its characterization through *in situ* measurements and its conceptualization and simulation. This paper reviews some important issues and challenges in modeling flow and transport in heterogeneous media, and discusses approaches to address certain aspects of the problem. Topics discussed include dynamic flow channeling, tracer breakthrough curves, multiple scales for flow in fractured rocks, different scales in measurement, modeling, prediction and heterogeneity, and system characterization and analysis for predictive modeling.

## 1999-2000 Reports

Flow and Transport in Hierarchically Fractured Rock
Christine Doughty and Kenzi Karasaki

Estimation of Reservoir Properties Using Transient Pressure Data: An Asymptotic Approach
D.W. Vasco, H. Keers, and K. Karasaki

Multi-Continua Description of Flow in Composite Heterogeneous Media
Mark Shvidler and Kenzi Karasaki

Progress Report: Calculation of Flow Wetted Surface Area in Single Fractured System
Guomin Li and Chin-Fu Tsang:

Progress Report: Tracer Mixing at Fracture Intersections
Guomin Li and Chin-Fu Tsang

A Summary and Review of the TILA-99: Approach to Performance Assessment
Chin-Fu Tsang

Modeling Groundwater Flow and Mass Transport in Heterogeneous Media–Issues and Challenges
Chin-Fu Tsang

# Flow and Transport in Hierarchically Fractured Rock

Christine Doughty and Kenzi Karasaki
Earth Sciences Division
E.O. Lawrence Berkeley National Laboratory

July 2000

## Abstract

We construct multiple realizations of hierarchical fracture networks with fractal dimensions between one and two, and then simulate single-well pumping tests and natural-gradient tracer tests on them. We calculate averages and standard deviations of test results over the multiple realizations, and show individual results for selected cases to illustrate key features of flow and transport through hierarchically fractured rock. We examine the relationship between the fractal dimension of the fracture network itself and the fractal dimension of the flow field arising during a well test. We then investigate the effect of these dimensions on the performance measures of the natural-gradient tracer tests, including flow through the model, tracer travel time, front width, and maximum concentration. These studies illustrate the range of possible behavior that might be obtained during field tracer tests conducted in hierarchically fractured rock, and provide insights into how to interpret field responses. It is found that there is large variability among the transport simulation results even in networks whose dimension is close to two. This finding is consistent with the large variability in the experimental results observed at fractured rock field sites.

## 1. Introduction

Hydrogeological problems involving fractured rock are challenging to solve because contrasts in permeability of the fractures and surrounding rock matrix are extreme and localized, making flow strongly dependent on the interconnections between conductive fractures (i.e., the connectivity of the fracture network). Site characterization is difficult because the key features controlling flow are likely to be impossible to identify a priori,

and they often respond to field tests in ways that are not amenable to simple interpretations [e.g., *Karasaki*, 1987a; *National Research Council*, 1996, Ch. 5]. With the introduction of the concepts of fractal geometry to geological systems [*Mandlebrot*, 1982; *Turcotte*, 1992], the notion that fracture networks often have a hierarchical (i.e., fractal) structure has gained support [e.g., *Sahimi*, 1993 and references therein; *National Research Council*, 1996, Ch. 2 and references therein]. In hierarchically fractured rock, both the extent and spacing of fractures varies over a wide range of length scales, which can exacerbate the difficulties associated with understanding flow and transport.

In the present study, we are primarily concerned with the situation that arises when a hierarchically fractured site is encountered in which a minimum number of wells are available for subsurface characterization. This may occur when multiple sites are under consideration for a particular activity (constructing a geologic nuclear waste repository, for example). It would not be cost effective to drill many wells at many candidate sites, but enough information must be gleaned from each site for a reasonable choice of the ultimate site to be made. For a nuclear waste repository site it is critical to develop an understanding of how water flow and radionuclide transport will occur through and away from the repository. Important characterization tools in this regard are pumping tests and tracer tests. In the early stages of site characterization, when only one or a few wells are available, single-well pumping tests are likely to be the primary characterization tool. On the other hand, a natural-gradient tracer test more closely mimics the conditions under which radionuclide escape from a repository is likely to occur, and hence provides more reliable characterization information. Such tracer tests require careful design if the results are to be interpretable, making it is worthwhile to study the relationships between the responses from single-well pump tests and natural-gradient tracer tests that arise in hierarchically fractured rock.

In a seminal paper, *Barker* [1988] described how a well test can be used to determine not only the effective transmissivity of a fracture network, but also the dimension of the flow field, which he denotes the generalized radial flow dimension, n. Values of n range from 1 to 3, where the integral values of 1, 2, and 3 correspond to linear, radial, and spherical flow, respectively, and intermediate non-integral values describe flow fields with fractal dimension. *Polek* [1990] simulated well tests in hierarchical fracture

networks with a range of fractal dimensions, and found that Barker's generalized radial flow dimension was smaller than the fractal dimension of the fracture network itself. He interpreted this as indicating that flow occurs primarily on a subset of the fracture network, denoted the backbone. In the present paper, we follow a procedure similar to that of Polek, but broaden the focus to include transport as well as flow, by simulating natural-gradient tracer tests as well as single-well pumping tests. We examine how fractal dimension affects the performance measures of the natural-gradient tracer tests, including flow through the model, tracer travel time, front width, and maximum concentration. Our primary goal is to illustrate the types of flow and transport behavior that are representative of hierarchically fractured rock, and thereby aid the design of field tests and the interpretation of field data.

A number of researchers have used numerical simulations to investigate flow and transport in heterogeneous porous or fractured media [e.g., *Moreno and Tsang*, 1994; *Birkhölzer and Tsang*, 1997; *Berkowitz and Scher*, 1997], including several who have explicitly invoked hierarchical concepts [*Grindrod and Impey*, 1993; *Clemo and Smith*, 1997]. However, none of these authors have systematically investigated how transport processes vary with the fractal dimensions for flow and the fracture network itself, as is done here. Others have investigated the significance of fractal geometry on transport, particularly dispersion, theoretically [e.g., *Ross*, 1986; *Cushman*, 1991; *Tyler and Wheatcraft*, 1992 and references therein; *Sahimi*, 1993 and references therein], and have provided insightful conceptualizations and elegant mathematical formalisms. The present approach is more practically oriented, with the goal of providing insights and information for designing and interpreting field experiments.

## 2. Methods

We construct hierarchical fracture networks with fractal dimensions between one and two, and then simulate a single-well pumping test and two natural-gradient tracer tests (with opposite gradients) on them. For each fractal dimension considered, eight realizations of the fracture network are constructed. We examine averages and standard deviations of test results over the multiple realizations, and show individual results for

selected cases to illustrate key features of flow and transport through hierarchically fractured rock.

*2.1 Generation of Hierarchical Fracture Networks*

Two-dimensional hierarchical fracture networks are generated as random Sierpinski lattices. We begin with a square template consisting of four fractures in two orthogonal sets as shown in Figure 1a. This template divides the original square with sides of length L into nine smaller squares, each with sides of length L/3. We then shrink the template by a factor of three, replicate it $N_{sq}$ times (where $1 \leq N_{sq} \leq 9$), and superimpose the replicates on the original template in $N_{sq}$ of the nine smaller squares chosen at random, as shown in Figure 1b for $N_{sq} = 5$. This procedure is then repeated for each of the L/3-length templates (Figure 1c), then for each of the resulting L/9-length and L/27-length templates (Figures 1d and 1e, respectively). For $1 \leq N_{sq} \leq 8$, the final fracture network contains fractures of length L, L/3, L/9, L/27, and L/81, and blocks of intact rock of length L/3, L/9, L/27, L/81, and L/243. For $N_{sq} = 0$ and $N_{sq} = 9$, the fracture network is a regular lattice in which all blocks of intact rock have length L/3 and L/243, respectively.

We denote fracture networks constructed in this manner as five-generation lattices, as they comprise five sizes of templates. Current computational limitations preclude using higher-generation lattices for the present study, but in principle, one could continue the process, using ever smaller templates to represent ever smaller fractures, until reaching the fractal cutoff length, below which fractal geometry is not expected to be the best representation of fracture flow. Sensitivity studies using four- and five-generation lattices yield similar results for the present well-test and tracer-test analyses, indicating that five generations is sufficient to illustrate hierarchical effects.

Figure 2 shows a selection of the eight random fracture networks created for each value of $N_{sq}$ between one and eight. In Figures 1 and 2a, at each level of the construction a different random set of $N_{sq}$ squares is filled with smaller fractures. If the same $N_{sq}$ squares are filled at each level, a much more regular fracture network is formed, as shown in Figure 2b. For $N_{sq} > 1$, we only consider networks containing fractures that pass close to the center of the model (these are picked out randomly from a larger suite of realizations), in order that we can compare well tests and tracer tests with a common

origin. As $N_{sq}$ decreases, the probability of a fracture passing close to the model center becomes smaller and smaller (Figure 3), until for $N_{sq} = 1$, there are only a few realizations that do so, all similar to the regular lattice shown in Figure 2b.

The fractal dimension of a fracture network can be determined using the box counting method [*Ott*, 1993] as shown in Figure 4, which is a log-log plot of the number of fractures N(r) encountered as a function of distance r from some point in the lattice. The slope of the best-fit line through these points is the fractal dimension, D. The good fit shown in the examples presented in Figure 4 is typical of all the lattices generated, and is evidence that fracture networks constructed in this manner do possess fractal geometry over a range of length scales. Figure 5 shows that D increases monotonically from one to two as $N_{sq}$ increases from one to nine. Also shown is an analytical expression for the fractal dimension of a traditional Sierpinski gasket, which is given by $D_{an} = \ln(N_{sq})/\ln(3)$. Note that $D_{an} < D$ for small values of $N_{sq}$. This is because the present algorithm for fracture network generation retains fractures of all lengths, whereas the traditional Sierpinski gasket retains only the smallest ones, i.e., those resulting from the final shrinkage, replication, and superposition of the template. When $N_{sq}$ is small, the number of shorter fractures grows slowly as the lattice is generated, and the original long fractures contribute significantly to the fractal dimension. In contrast, when $N_{sq}$ is large, the reverse is true, and consequently $D_{an} \approx D$.

Although they are highly idealized, we believe that the hierarchical fracture networks generated as random Sierpinski lattices are useful for representing real fractured rock for the following reasons. Most importantly, fractures of all lengths are present and blocks of intact rock matrix of all lengths are present. Additionally, there is a huge variability among realizations, as is seen in nature. Finally, the fractures form two orthogonal sets, another feature commonly seen in natural rocks. A possible drawback is that we are guaranteed to have long continuous fractures with a regular geometry (the tick-tack-toe pattern of the basic template). For low values of $N_{sq}$, this may dominate behavior.

Two cases are considered for the assignment of fracture transmissivity T: one in which all fractures have the same transmissivity ($T = 10^{-7}$ $m^2/s$), and one in which transmissivity is correlated with fracture length $L_j$. The constant T case provides a

simplification that allows us to focus on the fracture network geometry. It is not expected to be strictly realistic, but it should be adequate when variability in fracture transmissivity is relatively small or is not correlated to fracture length. The motivation for the correlated T case comes from pressure testing in an underground mine where a large range of fracture lengths is observed. Using steady-state pressure and flow measurements in packed-off borehole intervals, a large range of T values is obtained [*Oyamada and Takase*, 1999]. For tests conducted in this manner to yield high T values, the zones associated with the high T measurements must be spatially extensive. Consequently, the lower T values are associated with smaller fractures. We quantify this relationship by taking $T_j = R^j T_{min}$, $L_j = 3^j L_{min}$, where R is defined as the correlation ratio ($R \geq 1$), $T_{min}$ is the transmissivity of the shortest fractures whose length is $L_{min}$, and j is an index describing the hierarchical level of the fracture ($0 \leq j \leq 4$).

For the well tests, fracture aperture w and transmissivity T are related according to the cubic law (i.e., w is a hydraulic aperture). For the tracer tests, a tracer aperture with a value 10 times the hydraulic aperture is used. Thus, for the correlated transmissivity cases, as $T_j$ increases with $L_j$, so does w.

### *2.2 Flow and transport simulator*

The finite element model TRIPOLY [*Karasaki*, 1987b; *Segan and Karasaki*, 1993; *Birkhölzer and Karasaki*, 1996] is used to simulate water flow and tracer transport through the hierarchical fracture networks. Fractures are represented as one-dimensional linear elements and fracture intersections are represented as nodes. A special-purpose grid generator is used to create the hierarchical lattices described in Section 2.1. TRIPOLY models transient or steady flow according to Darcy's law, and models transport using the advection-diffusion equation (ADE). Transport calculations use a mixed Lagrangian-Eulerian scheme combined with an adaptive gridding algorithm that places additional nodes in locations of large concentration changes, in order to minimize numerical dispersion. Complete mixing is assumed at fracture intersections. For the present transport calculations, we neglect diffusion because sensitivity studies have shown that it has only a small effect compared to the mixing and dispersion that arise

from the highly irregular flow field that develops in the complicated hierarchical fracture networks. TRIPOLY can also model the effects of the porous matrix in which the fracture network is embedded. This capability is not employed for the present studies, but it will be in future work, as the sorption capacity of the rock matrix can have significant effects in retarding the movement of contaminants through fractured rocks.

### *2.3 Single-well pumping test analysis*

*Barker* [1988] generalized the diffusion equation for radial liquid flow to non-integral flow dimensions, in order to analyze data from well tests conducted in fractured rock. He obtained an analytical expression for drawdown during a constant-rate pumping test in terms of the (complementary) incomplete gamma function [*Barker*, 1988; *Press et al.*, 1986], which includes a parameter $\nu$ that is simply related to the generalized radial flow dimension n (Figure 6). For $n = 2$, the incomplete gamma function simplifies to the familiar exponential integral of the *Theis* [1935] equation. For $n < 2$, the slope of the log drawdown-log time plot becomes linear at long times, with a slope given by $\nu = 1 - n/2$. We numerically simulate single-well, constant-rate pumping tests by applying a mass sink to nodes near the center of the lattice while holding nodes along the outer boundary of the lattice at constant hydraulic head. Comparing the resulting transient drawdown to the analytical solution provides an estimation of n. For small values of n, the linear late-time slope provides a simple way to estimate n, but for larger values of n, the constant-head outer boundary of the lattice is felt before the drawdown curve becomes linear, requiring that the complete curve be matched.

### *2.4 The H-12 flow and transport problem*

The Japan Nuclear Cycle Development Institute (JNC) recently conducted a multi-national project to investigate the uncertainties involved in the prediction of the flow and transport behavior of a fractured rock mass [*Oyamada and Ikeda*, 1999; *Sawada et al.*, 1999; *Doughty and Karasaki*, 1999]. In that project, the H-12 flow comparison, several research organizations conducted numerical simulations of radionuclide transport away from a repository, using the same information regarding problem geometry and fractured

rock properties. For the present studies, we consider the same geometry as the H-12 problem and evaluate similar performance measures, but consider flow and transport through hierarchical fracture networks.

The H-12 problem involves a 200-m by 200-m by 200-m cube of granitic rock containing a 200-m long cylindrical gallery of 2.2 m diameter, located in the middle of the volume (Figure 7a). The gallery is surrounded by an excavation-damaged zone (EDZ) with a uniform thickness of 0.5 m. Flow is generally perpendicular to the gallery (along the *y*-axis) and, thus, a no-flow boundary condition is assumed for all the *x*-*y* and *y*-*z* boundary planes. Heads are assumed uniform on both *x*-*z* boundary planes and the head difference between the two planes is 1.6 m. The surface of the cylindrical gallery is a no-flow boundary condition. For the present studies, we consider a two-dimensional (2-D) slice through the middle of the granite cube in the *y*-*z* plane (Figure 7b). For simplicity, the EDZ is modeled as a 2.5 m by 2.5 m square region in which all elements have a low transmissivity ($T = 5 \cdot 10^{-10}$ m$^2$/s). The EDZ size equals the smallest size to which the original four-fracture template (Figure 1a) is reduced ($200/3^4$ m on a side). The corner nodes of the EDZ are maintained at a constant tracer concentration C = 1, to represent the potential escape of radionuclides from the EDZ.

The H-12 performance measures are

- Q, the steady-state flow rate through the model, which can be converted to the effective transmissivity of the fracture network,
- $Q_{EDZ}$, the steady-state flow rate through the EDZ, which influences the quantity of radionuclides released, and ultimately the integrity of the gallery itself,
- $t_{bt}$, the fastest tracer travel time from the EDZ to the downgradient boundary of the model,
- $t_w$, a weighted travel time, which is calculated using a weighted tracer velocity $v_w$ that approximately accounts for sorption and matrix imbibition effects.

The weighted tracer velocity in a fracture of aperture w is defined as $v_w = v\ w/2$, where v is the usual tracer velocity and 2/w approximates the surface-to-volume ratio of the fluid flow path, which has been proposed as a useful measure of retardation arising

from fracture/matrix interactions [*Elert*, 1997]. When T is not correlated to fracture length, all the apertures in the lattice are identical, so using weighted velocity merely multiplies travel time by a constant factor ($t_w = t_{bt}2/w$). On the other hand, for the correlated case we have $T \sim R^j$ and $w \sim R^{j/3}$, and consequently $v \sim T/w \sim R^{2j/3}$ and $v_w \sim T/w \times w \sim R^j$. Hence, using weighted velocity has the effect of making the medium more strongly correlated.

In addition, we monitor $C_{max}$, the maximum concentration at the downgradient boundary of the model, and $\Delta t$, the width of the concentration front at the location where $C_{max}$ occurs. Furthermore, we can convert $\Delta t$, the front width in time, to $\Delta y$, the front width in space, by multiplying $\Delta t$ by the average velocity of the front, $L/(2t_{bt})$, where, $L/2$ is the distance from the EDZ to the downgradient boundary of the model, 100 m. Then $\Delta y$ may be used as a measure of the effective dispersion occurring in the lattice.

## 3. Results

### *3.1 Uncorrelated fracture transmissivity*

Flow

Figure 8 shows several examples of the numerically simulated drawdown response for single-well, constant-rate pumping tests in hierarchical fracture networks. In Figure 8a, the generalized radial flow dimension n is determined from the late-time slope v of the log drawdown-log time plot for two realizations with $N_{sq} = 3$ ($v = 1 - n/2$). Some lattices produce late-time drawdowns that show distinctive breaks in slope, indicating sub-regions with different flow dimensions. Figure 8b compares the entire drawdown curve for the regular lattice with $N_{sq} = 7$ and Barker's analytical solution, and indicates that the flow dimension for this lattice is about $n = 1.65$. We estimate flow dimensions for all the hierarchical lattices for each $N_{sq}$ value using one of these two methods, and calculate the arithmetic average and standard deviation, which are plotted in Figure 9a. Combining this information with the plot of fractal dimension D versus $N_{sq}$ (Figure 5) enables us to plot flow dimension n versus fractal dimension D (Figure 9b). For all $N_{sq}$, we see that $n < D$. Following *Polek* [1990], we interpret this as indicating that flow occurs primarily on a "backbone" portion of the fracture network. It is important to

realize that no dead-end fractures exist in the hierarchical fracture networks, by virtue of their construction as random Sierpinski lattices. Hence, our usage of the term backbone is distinct from the common network or percolation theory usage in which the backbone contains all conductive (i.e., non dead-end) fractures.

The finding that there are distinct fractal dimensions for geometry (D) and flow (n), and in particular that $n < D$, is reminiscent of the case in nonlinear dynamics where chaotic attractors, known as multifractals, are associated with a spectrum of fractal dimensions. The first dimension, denoted $D_0$, describes the geometry of the attractor and can be obtained by the box counting method. Higher order dimensions, $D_1$, $D_2$, ..., describe dynamical processes occurring on the attractor, and in general, $D_{j+1} < D_j$. $D_1$ is of particular importance and is known as the information dimension [*Ott*, 1993]. Similarly, in hydrological applications, an understanding of flow geometry, embodied in n, adds a great deal to the picture presented by the fracture geometry.

Figure 10a shows the steady linear flow rate Q through the model during the simulation of the H-12 tracer test. For each value of $N_{sq}$ from two to eight, the values of Q represent an average over eight lattices. The relationship between Q and $N_{sq}$ can be reasonably well fit with the expression

$$Q = Q_0 \exp [(N_{sq}/4)^2],$$

where $Q_0$ is the flow through the basic tick-tack-toe pattern that corresponds to $N_{sq} = 0$. With the H-12 boundary conditions specifying a fixed head gradient $\nabla h$, Q is easily converted into the effective transmissivity of the fracture network $T_{eff}$:

$$Q = - T_{eff} \nabla h,$$

$Q_0 = - T_0 \nabla h$, where $T_0 = 2 \cdot 10^{-7}$ $m^2/s$ is the network transmissivity for $N_{sq} = 0$.

Thus,

$$T_{eff}/T_0 = Q_{eff}/Q_0 = \exp [(N_{sq}/4)^2],$$

$$\ln (T_{eff}/T_0) = (N_{sq}/4)^2.$$

Given the smooth relationships between $N_{sq}$, D, and n (Figure 9), we could fit curves to $D(N_{sq})$ and $n(N_{sq})$, and hence express $T_{eff}/T_0$ as a function of D or n as well. Note that

during the well tests, as $N_{sq}$ increases from 1 to 9, the generalized radial flow dimension n increases from 1 to 2, but $T_{eff}$ remains constant. In contrast, during the tracer tests, the overall flow field remains linear (controlled by the constant head boundary conditions) and $T_{eff}$ increases with $N_{sq}$ as shown above.

Figure 10b shows the standard deviation of Q divided by the average Q. It features a maximum for intermediate values of $N_{sq}$, indicating that a greater variety of flow fields occur for intermediate values of $N_{sq}$. This is simply a consequence of the greater variety of fracture networks that can be constructed under these conditions.

Figure 11a shows the average and standard deviation over eight realizations of $Q_{EDZ}$, the flow rate passing through the EDZ during the tracer test. $Q_{EDZ}$ generally increases with $N_{sq}$, but the standard deviation is huge, indicating large variability between realizations. The fact that the standard deviation for $Q_{EDZ}$ is much larger than that for Q and n is reasonable, as Q and n embody integration over all the flow paths through the fracture network, whereas $Q_{EDZ}$ depends strongly on the particular flow paths intersecting the EDZ. Another way to look at EDZ flow is to plot $Q_{EDZ}/Q$ versus $N_{sq}$, as shown in Figure 11b. We see an overall decrease with $N_{sq}$, indicating that as more alternative flow paths become available, more flow bypasses the EDZ. Note that dividing by Q is equivalent to considering fracture networks that have the same $T_{eff}$, regardless of $N_{sq}$. From a well testing point of view, this may be the most common situation to find in practice. Recall that the eight lattice realizations used for each $N_{sq}$ were chosen specifically so that the fracture network would intersect the EDZ. We can combine the probability that the fracture network intersects the EDZ ($P_{EDZ}$, Figure 3) and EDZ flow by plotting $P_{EDZ}Q_{EDZ}/Q$ versus $N_{sq}$ (Figure 11c), which shows an increase for low $N_{sq}$, followed by a plateau for higher values. At small $N_{sq}$ values, the small probability of the fracture network intersecting the EDZ dominates, but at large $N_{sq}$, the probability flattens out and more nearly balances the decrease that occurs as more alternative flow paths are added.

Transport

To compare transport through the hierarchical fracture networks, we identify the location along the downgradient boundary of the model where the maximum concentration $C_{max}$ occurs for each simulation. For this location, we define the breakthrough time $t_{bt}$ as the time when the concentration reaches $C_{max}/2$, and the width of front $\Delta t$ as the time over which the concentration increases from zero to $C_{max}$. These quantities are averaged over 16 simulations (eight fracture network realizations each with tracer tests in two directions) and plotted as a function of $N_{sq}$ (Figures 12a, 13a, and 14). Another way to compare breakthrough times for different $N_{sq}$ values is to normalize $t_{bt}$ by the effective transmissivity and total void space of the lattice. Normalizing $t_{bt}$ is equivalent to assuming that for each value of $N_{sq}$, the transmissivity and aperture of the fractures are chosen such that the effective transmissivity and total void space of the model remains constant. In a sense, this normalization isolates fractal geometry effects from other influences. Figure 12b shows $t_{bt}^*$ as a function of $N_{sq}$, where $t_{bt}^*$ is defined as

$$t_{bt}^* = t_{bt}\, Q(N_{sq})/Q(5)\, N_{el}(5)/N_{el}(N_{sq}),$$

and $N_{el}$ is the number of fracture elements in the lattice (although fracture length varies, all fracture elements are the same length – the length of the shortest fractures). There is a general decline in $t_{bt}^*$ as $N_{sq}$ increases, suggesting that the additional flow paths introduced for higher fractal geometry provide more direct routes for tracer travel through the model.

Just as converting $t_{bt}$ to $t_{bt}^*$ serves to isolate the effects of fractal geometry, so does converting front width in space $\Delta t$ to front width in time $\Delta y$. Figure 13b shows $\Delta y$ as a function of $N_{sq}$. For small values of $N_{sq}$, few alternative flow paths are available, so $\Delta y$ is small, and for $N_{sq} = 9$, only the most direct flow path need be taken, again yielding small $\Delta y$. For $3 \leq N_{sq} \leq 8$, $\Delta y$ is roughly constant and approximately equal to the distance traveled, L/2. For some of the tracer test simulations, C(t) curves are available at a series of distances y from the EDZ along the path of peak concentration. At each distance, $\Delta t$ can be converted to $\Delta y$, which is then plotted versus y. There is a good deal of scatter between realizations (as in Figure 13b), but on average, the trend of $\Delta y \approx y$ is maintained for all values of $N_{sq}$ between 3 and 8. The lack of dependence on $N_{sq}$ (or equivalently, on

D or n) appears to be a fundamental result for these hierarchical lattices, and is further discussed in Section 4.

The maximum concentration arriving at the downgradient boundary of the model (Figure 14) is quite low compared to the constant concentration (C = 1) maintained at the EDZ. This is because the EDZ is located away from the long through-going fractures of the full-size template, and there is rarely a direct path across the model that intersects the EDZ but misses these long fractures, which contribute clean water from the upgradient boundary of the model. Most of the variability of $C_{max}$ with $N_{sq}$ is small, showing only a gradual increase for $N_{sq} < 9$. Apparently even for the large $N_{sq}$ values of 7 and 8, where one might expect a direct path from the EDZ to the downgradient model boundary would result in a large $C_{max}$, the occasional presence of large gaps in the fracture network is sufficient to disorganize the flow pattern, enabling mixing to reduce $C_{max}$.

The standard deviations tend to be very large for parameters that reflect preferential flow through one or only a few flow paths: $Q_{EDZ}$, $t_{bt}$, $\Delta t$, and $C_{max}$ (Figures 11, 12, 13, and 14). This illustrates the basic difficulty of attempting to obtain meaningful results by averaging over multiple realizations for any quantity which itself is not representative of average behavior within a given realization. It makes more sense to consider the range of results possible for different realizations than to focus on the averages themselves.

It is apparent from Figures 12, 13, and 14 that the standard deviations of $t_{bt}$, $\Delta t$, and $C_{max}$ all show peaks at intermediate values of $N_{sq}$, as seen for Q (Figure 10b). This decrease in predictability arises because intermediate values of $N_{sq}$ (or equivalently, fractal dimensions midway between one and two) have the widest range of possibilities for connectivity of the fracture network. For n or D close to one, there is rarely more than one flow path between any two points, and for n or D close to two, there are generally many paths. In contrast, for intermediate values of n or D, there could be any number of flow paths, and hence a wide range of flow and transport behavior must be expected.

Figures 15 - 25 show steady-state concentration distribution, C(y,z), and transient breakthrough curves, C(t), for various values of $N_{sq}$, in order to illustrate some of the key the features of flow and transport in hierarchically fractured rock. For small values of

$N_{sq}$, the situation shown in Figure 2 for $N_{sq} = 2$ and $N_{sq} = 3$ is typical in that at least one of the constant head boundaries is intersected by only two long fractures. If this is the upgradient boundary of the model, then flow through the EDZ tends to have a diverging character, as shown in Figure 15a for $N_{sq} = 2$. Conversely, if the downgradient boundary of the model intersects only two long fractures, then all flow through the EDZ must ultimately converge into these two fractures (Figure 15b). These different flow distributions produce sharply different breakthrough curves. The diverging flow fields tend to produce lots of mixing and spreading of tracer, resulting in classical S-shaped breakthrough curves with late breakthrough times (exemplified by the break through curves for $z < 0$ in Figure 15a). Converging flow occurs along fewer flow paths, leading to earlier, sharper breakthrough curves in which concentration is more likely to show oscillations, due to instabilities in the mixing of clean and traced water at a few fracture intersections (in particular, the break through curve at $z = 33$ m in Figure 15b). Within an overall diverging flow field, there are often "pinch points," where flow through a network of fractures must converge to a single fracture intersection (e.g., at $y = 33$ m, $z = -33$ m in Figure 15a), resulting in converging flow at one scale, and diverging flow at another. Furthermore, this converging-within-diverging pattern can occur at different scales (e.g., the pinch point at $y = -11$ m, $z = -11$ m in Figure 15b), ultimately leading to a great deal of variety in spatial concentration distributions and breakthrough curves.

Figure 16 shows an example for $N_{sq} = 3$. Figure 16a shows diverging flow, and a classical S-shaped breakthrough curve. However, there is a direct flow path from the EDZ to the downgradient boundary of the model that does not intersect the two long fractures that bring in clean water from the upgradient boundary, hence $C_{max}$ is bigger than usual. The converging flow in Figure 16b shows the usual features of early $t_{bt}$, small $\Delta t$, and oscillating $C_{max}$. It also illustrates the phenomenon of crossing breakthrough curves, in which the location with the earliest arrival of tracer does not end up being the location with the maximum tracer concentration. This occurs frequently in the hierarchical fracture networks.

For larger values of $N_{sq}$, the convergence of the flow field down to only two fractures becomes less common, but converging/diverging features of the fracture network at

different scales still have a strong impact on the tracer flow paths leaving the EDZ. As $N_{sq}$ increases from four to five, the fracture network undergoes a transition from having more gaps than fractures to having more fractures than gaps. It is during this transition region that the most variability in fracture network connectivity is possible. Figures 17 and 18 show examples for $N_{sq} = 4$. In Figure 17a, many fracture intersections between the EDZ and the downgradient boundary result in S-shaped breakthrough curves, but the crossing pattern indicates that flow is not occurring uniformly through the network. In Figure 17b, there are fewer fracture intersections, and consequently more irregular breakthrough curves. In Figure 18a, a diverging flow pattern following pinch points results in uniformly low concentrations. In Figure 18b, there is less divergence, and a relatively sharp concentration gradient is apparent across the fracture zone downgradient of the EDZ. Note that several fractures to the left of the EDZ show no concentration increase, as the flow field bypasses them entirely.

Figure 19 shows an example for $N_{sq} = 5$. In Figure 19a, much of the flow through the model is funneled through the EDZ, and a relatively direct, narrow flow path from the EDZ to the downgradient boundary results in a large value of $C_{max}$. In Figure 19b, there is a narrow plume for a while, but then diverging flow following a pinch point causes widening and a decreased $C_{max}$. The oscillations in the breakthrough curve for $z = 33$ m probably reflect instabilities in the mixing of clean water from the upgradient boundary and traced water from the EDZ at the pinch point. Although this is purely a numerical effect, it may have natural analogs in the less ideal world, where changes in stress or other non-linearities could subtly alter fracture transmissivities or hydraulic boundary conditions.

Figure 20 shows examples for $N_{sq} = 6$ with breakthrough curves that illustrate a small, early increase in concentration followed some time later by the main concentration front. This low-concentration "tail" is typical of fracture networks with a relatively direct flow path from the EDZ to the downgradient boundary that is surrounded by many longer flow paths that lead to the same downgradient point. It is a common feature of hierarchical fracture networks. In Figure 20a, an overall diverging flow field leads to a wide tracer plume and a gradual breakthrough curve, whereas in Figure 20b, L/9 size gaps keep the main part of the plume rather narrow, leading to a sharper breakthrough

curve. Figure 21 shows two more examples for $N_{sq} = 6$. In Figure 21a, the flow field follows an S-shape around the largest gaps that is reflected in the tracer plume. In Figure 21b, much of the flow through the model occurs in the fractured zone at $33 < z < 100$ m, bypassing the EDZ, and resulting in a very low value of $C_{max}$. A pinch point at $z = -33$ m and the subsequent divergent flow creates a remarkably uniform concentration in the $y < -33$ m, $z < -33$ m region.

For large values of $N_{sq}$, there are often relatively direct paths from the EDZ to the downgradient boundary, but there is still a wide variety among concentration distributions. Figures 22 and 23 show some examples for $N_{sq} = 7$. In Figure 22a, the overall converging character of the flow field causes the plume to remain narrow as it skirts around large gaps in the fracture network, and it shows an early $t_{bt}$. In contrast, in Figure 22b, the diverging flow field causes the plume to grow broad as it moves around L/9 size gaps, and it shows a much later $t_{bt}$. The higher value of $C_{max}$ for Figure 22b is indicative of the greater fraction of flow from the upgradient boundary passing through the EDZ for that case. In Figure 23, the flow field shows neither a global converging nor diverging character. The deflection around an L/9 size gap in Figure 23a is obvious, but the shepherding caused by L/27 size gaps is subtler, leading to a nearly straight-line path in Figure 23b.

Figures 24 and 25 show examples for $N_{sq} = 8$. Despite the nearly completely filled fracture networks, gaps of all sizes exist, so there is a significant variability among realizations. In Figure 24a, the flow field shows a gradual convergence to the right of the large gap, which keeps the concentration plume narrow. When the flow direction is reversed (Figure 24b), the plume bifurcates around the gap and the breakthrough curves feature the low-concentration tails and crossing pattern seen for previous examples. In Figures 25a and 25b, the largest gaps control the overall flow pattern by creating slightly diverging, diagonal flow fields. The diagonal flow is strongly reflected in the concentration plumes, despite the fact that the plumes never get close to the gaps. If this global character of the flow field were not appreciated during the experimental design, and tracer monitoring only occurred at $z = 0$ (presumably downstream of the EDZ), nearly the entire plume would be missed.

### *3.2 Fracture transmissivity correlated to fracture length*

Flow

During a pumping test, when fracture transmissivity is correlated to fracture length according to $T_j = T_{min}R^j$, $L_j = 3^jL_{min}$, any value of $N_{sq}$ can produce a drawdown curve consistent with a generalized radial flow dimension of n = 2 by a suitable choice of R (Figure 28a). Conversely, for a given $N_{sq}$ ($N_{sq}$ = 5) we can produce any value of n by a suitable choice of R (Figure 26b). Formally, it is not readily apparent that using $T \sim R^j$ in the n-dimensional flow equation is equivalent to using a constant T in the two-dimensional flow equation, but matching numerical simulations employing correlated transmissivity to Barker's analytical solution does seem to work.

Figure 27 shows the steady linear flow rate Q through the model during the simulation of the H-12 tracer test, as in Figure 10a, but now instead of plotting Q as a function of $N_{sq}$, it is plotted against flow dimension n ($N_{sq}$ is converted to n using Figure 9a). Also shown in Figure 27 are the Q values obtained for the $N_{sq}$ = 5 lattice using correlated transmissivity with a range of values for R, which is converted to n using Figure 26b. Flow rates obtained with the correlated transmissivity case agree well with the uncorrelated cases, indicating that a correlated transmissivity distribution has the same effect on transient flow to a well (generalized radial flow) and steady linear flow.

Figure 28 shows flow through the EDZ including two correlated transmissivity cases, one with a regular lattice, and one with a random lattice. Note that the EDZ is located well away from the longest, highest-T fractures. Thus, as n increases, $Q_{EDZ}$ increases more slowly for the correlated transmissivity cases.

Transport

Figures 29 - 31 show $t_{bt}$, $\Delta t$, and $C_{max}$ as a function of n, including uncorrelated transmissivity cases where n depends on $N_{sq}$, and correlated transmissivity cases for $N_{sq}$ = 5 where n depends on R. Values of $t_{bt}$ and $\Delta t$ for the correlated cases show the same trend but are generally smaller than for the uncorrelated cases. However, the spread among the uncorrelated realizations is so large that is difficult to say how significant the

effect of correlated transmissivity is. In contrast, $C_{max}$ for the correlated and uncorrelated cases show diverging trends as n gets large (Figure 31). This is because for the uncorrelated case, as $N_{sq}$ increases there are more direct flow paths from the tracer source to the downgradient boundary, so $C_{max}$ increases, whereas for the correlated case, as R increases more flow goes through the long high-T fractures, which are far away from the tracer source, causing a decrease in $C_{max}$.

When R = 1, using a weighted tracer velocity as defined in Section 2.4 just multiplies $t_{bt}$ and $\Delta t$ by a constant factor ($2/w = 4.1 \cdot 10^4$ for $T = 10^{-7}$ $m^2/s$). But when R > 1, the existence of fractures having a range of apertures means that the local weighted velocity differs from the usual tracer velocity, so calculating weighted travel time requires an integration along the weighted flow path. The resulting values of weighted $t_{bt}$ and $\Delta t$ are shown in Figures 29 and 30 (multiplied by w/2 to enable plotting on the same scale as the unweighted times). In all cases, the correlation effect of using a weighted velocity is small. That is, once the weighted $t_{bt}$ and $\Delta t$ values are multiplied by w/2, they not differ significantly from the unweighted ones.

Figure 32 shows the steady-state concentration distribution for the random $N_{sq} = 5$ lattice for several values of R, and illustrates a narrowing concentration plume as the correlation between transmissivity and fracture length grows.

## 4. Discussion and Comparison to Other Studies

A common feature of most of the hierarchical fracture networks studied is that they produce quasi-channelized flow, with localized, rapid transport from the EDZ to the downgradient model boundary. Many of the breakthrough curves also show evidence of multiple flow paths, indicating interaction between channels. In general, subtle features of the flow field can produce strong responses in transport phenomena.

We initiate transport by imposing a localized step change in concentration at the EDZ, follow the resulting tracer plume through the model, and examine its arrival at the downgradient model boundary. This procedure reproduces the processes associated with radionuclide release from a nuclear waste repository, and the associated natural-gradient tracer test designed to mimic that release. Another approach is to introduce tracer all

along the upgradient boundary of the model and construct a breakthrough curve by averaging over the entire downgradient boundary of the model. [*Birkhölzer and Tsang*, 1997]. This method has the advantage of incorporating the effect of flow paths throughout the medium, but it does not illustrate what is likely to happen during a given tracer test with a localized tracer release point and a limited number of observation points. Others have used localized releases of tracer, but primarily focus on spatially averaged breakthrough curves [*Grindrod and Impey*, 1993; *Berkowitz and Scher*, 1997; *Clemo and Smith*, 1997]. These investigations also predict channelized flow, which leads to irregular, difficult-to-predict transport, making any prediction for a single point highly likely to be completely wrong. This appears to be the motivation for examining average rather than local breakthrough curves. However, we have found that looking at average rather than local behavior is generally not helpful for elucidating the physical processes occurring in the fracture network. Moreover, it is often misleading as to the range of responses expected in an actual field experiment with only a few observation points, precisely because the critical fast flow paths that produce the earliest tracer arrivals are not representative of the average behavior of the medium. Although local predictions for tracer breakthrough are likely to be in the wrong location, they are more useful than average predictions, which say nothing about breakthrough location and are less likely to show the right physics. A preferable situation is to be able to monitor over a spatially extensive region, such as an underground drift or a surface exposure such as a cliff face. Then both local and average predictions can be made, and compared to local and average observations, respectively.

The finding that $\Delta y \approx y$ for a large range of fractal dimensions (Figure 13b) may seem surprising in view of numerous authors suggestions that the commonly observed scale-dependence of dispersivity [*Gelhar et al.*, 1985] can be explained as a consequence of the fractal dimension of the tracer flow path [*Tyler and Wheatcraft*, 1992 and references therein]. In the conventional ADE (Advection Dispersion Equation) with constant values of groundwater velocity and dispersivity $\alpha_L$, one finds $\Delta y \sim (\alpha_L t)^{1/2}$, or equivalently $\Delta y \sim (\alpha_L y)^{1/2}$. In contrast, for scale-dependent or anomalous dispersion, one observes $\Delta y \sim t^r$ or $\Delta y \sim y^r$ where $r > 1/2$. To preserve the connection with the conventional ADE, a variable dispersivity $\alpha_m$ is introduced so that $\Delta y \sim (\alpha_m t)^{1/2}$ with $\alpha_m \sim t^{2r-1}$ or $\Delta y \sim (\alpha_m y)^{1/2}$

with $\alpha_m \sim y^{2r-1}$. To explain this phenomenon with a fractal model, one then derives an expression for r as a function of D. For example, *Wheatcraft and Tyler* [1988] obtain $\alpha_m \sim y^{2D-1}$, based on a random walk over a set of fractal streamtubes.

In the present studies, we find $\Delta y \sim y$, which requires $\alpha_m \sim y$ or $r = 1$, which is the dispersivity dependence for a stratified aquifer [*Mercado*, 1967]. *Neretnieks* [1983] recognized that this relationship applies to channelized flow as well. It is natural for heterogeneous models to produce channelized flow at one scale, but *Ross* [1986] points out that fractal media have the unique capability of producing channelized flow at all scales: at any experimental scale, there are always a few fractures that are nearly as large as the experimental scale; these provide quasi-independent channels through which most of the flow occurs; as the experimental scale increases, longer fractures come into play and channeling is maintained. This explanation is consistent with the finding that $\Delta y \approx y$, independent of fractal dimension, for a range of y values between 5 and 100 m.

However, it must be noted that the expression $\Delta y \approx y$ produces only a roughly approximate fit to the numerical results, and there is a great deal of scatter around it, both for observations at $y = 100$ m (Figure 13b) and for smaller values of y. This is not surprising, since using the conventional ADE with dispersivity made a function of time or space to account for scale-dependent dispersivity is an ad hoc approach. In fact, *Berkowitz and Scher* [1995] are able to prove that using $\alpha_m(t)$ leads to quantifiably incorrect solutions for the anomalous dispersion caused by differential advection through a highly heterogeneous medium. *Cushman* [1991] treats transport in a fractal medium rigorously and obtains a non-local integrodifferential governing equation in place of the conventional ADE. In other words, transport at a given point depends on the history of concentration at that point, as well as concentrations elsewhere in space.

## 5. Summary and Conclusions

We have generated hierarchical fracture networks with well-defined fractal dimensions and simulated well test and tracer tests through them. By examining multiple realizations, we have looked for trends that describe the variation of transport with fractal

dimension, and features that are unique to particular fracture network geometries. The studies attempt to illustrate the range of possible behavior that might be obtained during field tracer tests conducted in hierarchically fractured rock, and provide insights into how to interpret field responses. Some specific findings are presented below, followed by more general concluding remarks.

1. As the number of filled squares $N_{sq}$ in the random Sierpinski lattices increases, the fractal dimension of the fracture network D increases, as does the generalized radial flow dimension n obtained during a well test. For all fracture networks, $n < D$.

2. For linear flow during a tracer test, the effective transmissivity of the fracture network is well fit by the relationship $\ln (T_{eff}/T_0) = (N_{sq}/4)^2$, where $T_0$ is the transmissivity of a fracture network with $N_{sq} = 0$. Given the smooth relationships between $N_{sq}$, D, and n, simple analytical expressions could also be written for $T_{eff}(D)$ and $T_{eff}(n)$.

3. During tracer tests, the relative amount of flow through the EDZ (the tracer source) tends to increase with fractal dimension, as smaller gaps in the fracture network make it less likely that the EDZ will be bypassed by the primary flow channels.

4. During tracer tests, channelized flow tends to produce early, localized tracer breakthroughs, but some interaction between channels is also apparent, as breakthrough curves show evidence of multiple flow paths arriving at a given point.

5. Normalized breakthrough time $t_{bt}^*$ decreases as fractal dimension increases, due to the addition of more and more direct flow paths through the model.

6. Front width $\Delta y$ is independent of fractal dimension over the range $3 \leq N_{sq} \leq 8$, and is approximately equal to the distance traveled by the front. This linear dependence is consistent with channeling that occurs over a range of length scales, which is quite plausible for a hierarchical fracture network.

7. Maximum concentration at the downgradient boundary $C_{max}$ is quite low compared to the unit concentration maintained at the EDZ, and $C_{max}$ shows only a slight increase with fractal dimension for $N_{sq} \leq 8$. This suggests that even for dense fracture networks the occasional gaps disrupt and disorganize the flow pattern, leading to low values of $C_{max}$.

8. For flow properties, assuming that transmissivity is directly correlated with fracture length makes the fracture network act as though it had a higher value of n and no transmissivity correlation. However, for transport properties, the relationship is not so simple, as some transport properties follow the trends of uncorrelated networks and others do not.

Geometry and flow-related properties D, n, and $T_{eff}$ represent average behavior over the whole fracture network and thus show little variability between realizations for a given $N_{sq}$. Consequently, the averaged relationships for D, n, and $T_{eff}$ as a function of $N_{sq}$ apply quite well to all realizations. In contrast, transport-related properties $Q_{EDZ}$, $t_{bt}$, $\Delta t$, and $C_{max}$ are controlled by a relatively few fractures and consequently are very sensitive to subtle variations in the fracture network and the flow field. By virtue of the hierarchical fracture network structure, flow field variations occur at all scales. In particular, the existence of gaps of all sizes means that the converging-diverging pattern associated with pinch points occurs at all scales. Large-scale flow-field features control the overall direction of the tracer plume, and whether it broadens or remains narrow. At smaller scales, flow can be focused toward the EDZ or largely bypass it, strongly affecting the resulting tracer plume. Consequently, there is a great deal of variability in transport properties among realizations, which must be appreciated when looking for trends associated with fractal dimension.

At a fractal dimension of D = 1.5, there is a transition from networks with more gaps than fractures ($N_{sq} \leq 4$) to networks with more fractures than gaps ($N_{sq} \geq 5$). This is where the greatest variability in fracture network geometry occurs, leading to the biggest uncertainty in flow and transport properties. However, even for fractal dimensions near D = 2 there is still a very large variability among transport simulation results for different realizations. Moreover, within a given realization, there is also a great deal of variability, as evidenced by the large values of $\Delta y$ and small values of $C_{max}$. These finding are consistent with and may partially explain the large variability in the experimental results observed at fractured rock field sites.

## 6. Future Directions

The present study has continued and expanded on earlier works by *Barker* [1988] and *Polek* [1990] to investigate flow and transport in hierarchically fractured rock, but it has by no means exhausted the subject. Much more can be done using the approach of generating hierarchical fracture networks as random Sierpinski lattices. The resulting hierarchical fracture networks are simple to generate, straightforward to use in simulations, capture the variability of the real world, and thereby allow a systematic study of the relationships between flow and transport behavior and fractal geometry. Specific topics for further work include:

- Develop three-dimensional hierarchical fracture networks, in which individual fractures are represented as planar disks or squares and fracture intersections become line segments.
- Examine transmissivity distributions more carefully by considering more realistic correlation structures.
- Include the rock matrix in which the fracture network is embedded. In particular, model matrix diffusion and sorption explicitly, rather than through the weighted velocity approximation presently used.
- Extend the notion of site characterization with a minimal number of wells to include tracer tests. *Novakowski et al.* [1998] describe a tracer test procedure using only one well, consisting of radial injection followed by linear drift along with the regional flow. It would be very interesting to simulate this type of test for hierarchically fractured rock and compare the results to single-well hydraulic tests and the more conventional tracer tests discussed in the present paper.

*Acknowledgements*

We thank Don Vasco and Chin-Fu Tsang for reviewing this paper. This work has been supported by Japan Nuclear Cycle Development Institute (JNC) through the U.S. Department of Energy Contract No. DE-AC03-76SF00098.

## 7. References

Barker, J.A., A generalized radial flow model for hydraulic tests in fractured rock, *Water Resources Res.*, *24*(10), 1796-1804, 1988.

Berkowitz, B. and H. Scher, On characterization of anomalous dispersion in porous and fractured media, *Water Resources Res.*, 31, 6, 1461-1466, 1995.

Berkowitz, B. and H. Scher, Anomalous transport in random fracture networks, *Physical Review Letters*, 79, 20, 4038-4041, 1997.

Birkhölzer, J. and K. Karasaki, FMGN, RENUMN, POLY, TRIPOLY: Suite of programs for calculating and analyzing flow and transport in fracture networks embedded in porous matrix blocks, *Rep. LBNL-39387*, Lawrence Berkeley National Laboratory, Berkeley, Calif., 1996.

Birkhölzer, J. and C.-F. Tsang, Solute channeling in unsaturated heterogeneous porous media, *Water Resources Res.*, 33, 10, 2221-2238, 1997.

Clemo, T. and L. Smith, A hierarchical model for solute transport in fractured media, *Water Resources Res.*, 33, 8, 173-1783, 1997.

Cushman, J.H., On diffusion in fractal porous media, *Water Resources Res.*, 27, 4, 643-644, 1991.

Doughty, C. and K. Karasaki, Using an effective continuum model for flow and transport in fractured rock: The H-12 flow comparison, *Rep. LBNL-44966*, Lawrence Berkeley National Laboratory, Berkeley, Calif., 1999.

Elert, M., Retention mechanisms and the flow wetted surface – implications for safety analysis, *Tech. Rep. 97-01*, SKB, Sweden, 1997.

Gelhar, L.W. A. Mantoglou, C. Welty, and K.R. Rehfeldt, A review of field scale physical solute transport processes in saturated and unsaturated porous media, *Rep. EA-4190*, Electric Power Res. Inst., Palo Alto, Calif., 1985.

Grindrod, P. and M.D. Impey, Channeling and fickian dispersion in fractal simulated porous media, *Water Resources Res.*, 29, 12, 4077-4089, 1993.

Karasaki, K., Well test analysis in fractured media, Ph.D. thesis, Department of Material Science and Mineral Engineering, University of Calif., Berkeley, *Rep. LBL-21442*, Lawrence Berkeley Laboratory, Berkeley, Calif., 1987a.

Karasaki, K., A new advection-dispersion code for calculating transport in fracture networks, in Earth Sciences Division 1986 annual report, pp. 55-58, *Rep. LBL-22090*, Lawrence Berkeley Laboratory, Berkeley, Calif., 1987b.

Mandlebrot, B.B., *The fractal geometry of nature*, Freeman, San Francisco, 1982.

Mercado, A., The spreading pattern of injected water in a permeability-stratified aquifer, *IAHS AISH Publ.*, 72, 23-36, Gentbrugge, Belgium, 1967.

Moreno, L. and C.-F. Tsang, Flow channeling in strongly heterogeneous porous media: A numerical study, *Water Resources Res.*, 30, 5, 1421-1430, 1994.

National Research Council (Committee on Fracture Characterization and Fluid Flow), *Rock fractures and fluid flow: Contemporary understanding and applications*, National Academy Press, Washington, D.C., 1996.

Neretnieks, I., A note on fracture flow dispersion mechanisms in the ground, *Water Resources Res.*, 19, 2, 364-370, 1983.

Novakowski, K.S., P.A. Lapcevic, J.W. Voralek, and E.A. Sudicky, A note on a method for measuring the transport properties of a formation using a single well, *Water Resources Res.*, 34, 5, 1351-1356, 1998.

Ott, E., *Chaos in dynamical systems*, Ch. 3 and 9, Cambridge University Press, New York, 1993.

Oyamada, K. and T. Ikeda, Uncertainty analysis on hydrologic modeling in heterogeneous media (CORE Collaborative Study), Japan Nuclear Fuel Cycle Development Institute, TJ1400 99-023, 1999.

Oyamada, K. and H. Takase, Specification for the second stage H-12 flow comparison, Appendix B, in Uncertainty analysis on hydrologic modeling in heterogeneous media (CORE Collaborative Study), K. Oyamada and T. Ikeda, Japan Nuclear Fuel Cycle Development Institute, TJ1400 99-023, 1999.

Polek, J.M., Studies of the hydraulic behavior of hierarchically fractured rock geometries, M.S. thesis, Department of Material Science and Mineral Engineering, University of Calif., Berkeley, *Rep. LBL-28612*, Lawrence Berkeley Laboratory, Berkeley, Calif., 1990.

Press, W.H., B.P. Flannery, S.A. Teukolsky, and W.T. Vetterling, *Numerical recipes: The art of scientific computing*, Cambridge University Press, New York, 1986.

Ross, B., Dispersion in fractal fracture networks, *Water Resources Res.*, 22, 5, 823-827, 1986.

Sahimi, M., Flow phenomena in rocks: From continuum models to fractals, percolation, cellular automata and simulated annealing, *Reviews of Modern Physics*, 65, 4, 1393-1534, 1993.

Sawada, A., M. Shiotsuki, K. Oyamada, and H. Takase, Study of flow model comparison in fractured rock, in Proceedings of the 30th symposium of rock mechanics, Japan Society of Civil Engineering, Tokyo, Jan 26-27, 1999.

Segan, S. and K. Karasaki, TRINET: A flow and transport code for fracture networks – user's manual and tutorial, *Rep. LBL-34839*, Lawrence Berkeley Laboratory, Berkeley, Calif., 1993.

Theis, C.V., The relation between the lowering of the piezometric surface and the rate and duration of discharge of a well using ground-water storage, *Trans., Amer. Geophys. Union, 16*, 519-524, 1935.

Turcotte, D.L., *Fractals and chaos in geology and geophysics*, Cambridge University Press, New York, 1992.

Tyler, S.W. and S.W. Wheatcraft, Reply, *Water Resources Res.*, 28, 5, 1487-1490, 1992.

Wheatcraft, S.W. and S.W. Tyler, An explanation of scale-dependent dispersivity in heterogeneous aquifers using concepts of fractal geometry, *Water Resources Res.*, 24, 4, 566-578, 1988.

## 8. Figure Captions

Figure 1. Construction of a random Sierpinski lattice for $N_{sq} = 5$: (a) the basic template with four fractures of length L, (b) addition of fractures of length L/3, (c) addition of fractures of length L/9, (d) addition of fractures of length L/27, and (e) addition of fractures of length L/81.

Figure 2. Some of the fracture networks constructed as (a) random, and (b) regular Sierpinski lattices.

Figure 3. Probability of the fracture network intersecting the EDZ as a function of $N_{sq}$.

Figure 4. Example of the box counting method. The plot shows the number of fractures encountered within a radius r of a central point; the slope of the lines is the fractal dimension D.

Figure 5. Fractal dimension D of the lattice as a function of $N_{sq}$, with D averaged over eight random lattices for each value of $N_{sq}$ from two to eight. $D_{an}$ is the fractal dimension for a traditional Sierpinski gasket in which only the shortest fractures are retained.

Figure 6. The incomplete gamma function (dimensionless drawdown) versus dimensionless time [*Barker*, 1988].

Figure 7. Schematic of the H-12 problem: (a) full 3-D problem, and (b) 2-D slice through the center of the block modeled in the present studies. The EDZ is shown as a solid black square in the center.

Figure 8. Comparison of numerically simulated drawdown and Barker solution for single-well, constant-rate pumping tests for lattices with (a) $N_{sq} = 3$, and (b) $N_{sq} = 7$.

Figure 9. Generalized radial flow dimension n as a function of (a) $N_{sq}$ and (b) D.

Figure 10. Flow through the model during a tracer test: (a) average Q as a function of $N_{sq}^2$, and (b) standard deviation of Q divided by average Q as a function of $N_{sq}$.

Figure 11. Different ways of evaluating flow through the EDZ during a tracer test: (a) $Q_{EDZ}$ versus $N_{sq}$, (b) $Q_{EDZ}/Q$ versus $N_{sq}$, (c) $P_{EDZ}Q_{EDZ}/Q$ versus $N_{sq}$.

Figure 12. Breakthrough time at the downgradient boundary of the model as a function of $N_{sq}$: (a) actual breakthrough time $t_{bt}$, and (b) normalized breakthrough time $t_{bt}$*, with the influence of effective lattice transmissivity and total void space removed.

Figure 13 Concentration front width at the downgradient boundary of the model as a function of $N_{sq}$: (a) front width in time $\Delta t$, and (b) front width in space $\Delta y$.

Figure 14. Maximum concentration at the downgradient boundary of the model as a function of $N_{sq}$.

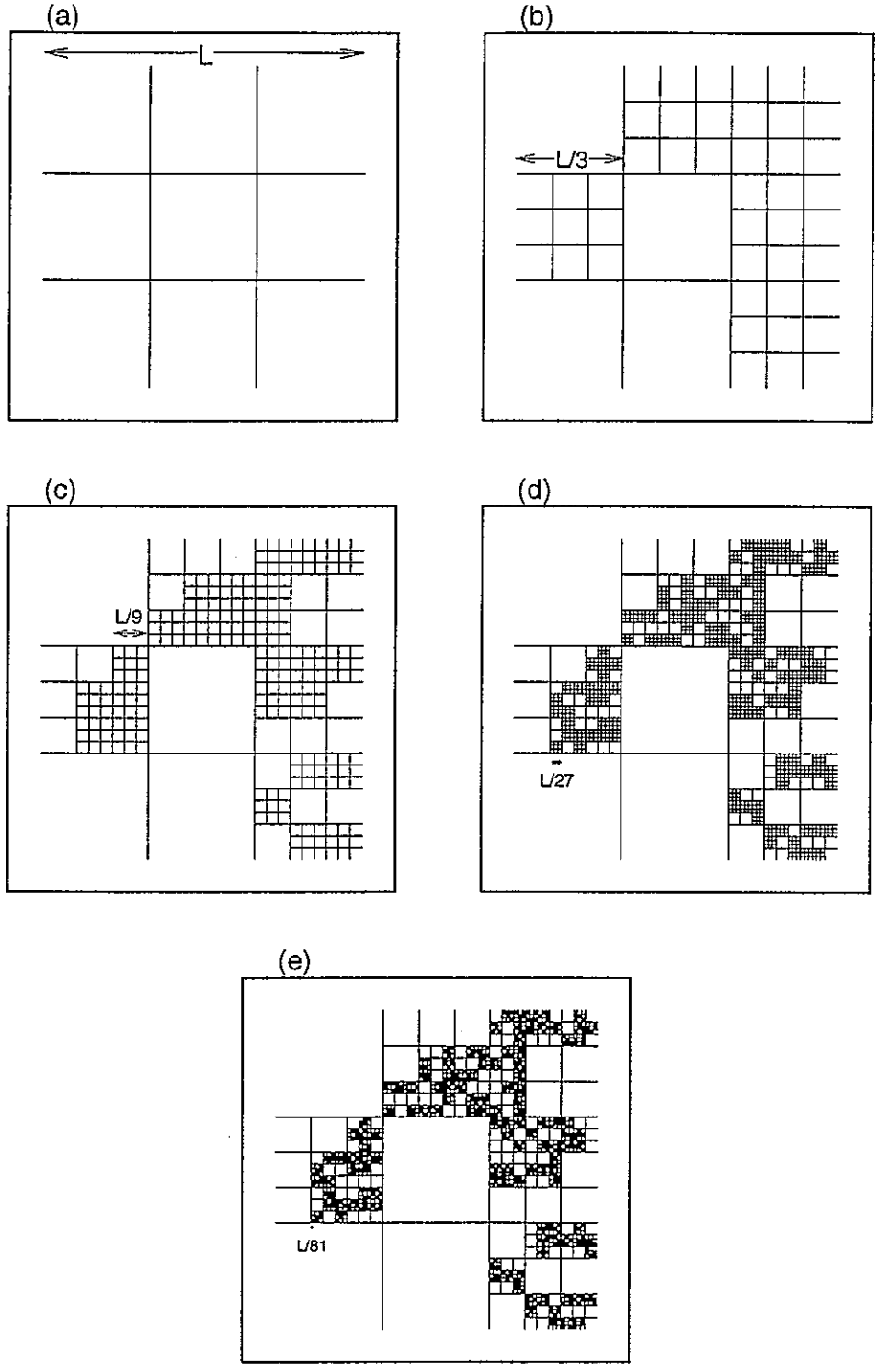


Figure 1. Construction of a random Sierpinski lattice for $N_{sq} = 5$: (a) the basic template with four fractures of length L, (b) addition of fractures of length L/3, (c) addition of fractures of length L/9, (d) addition of fractures of length L/27, and (e) addition of fractures of length L/81.

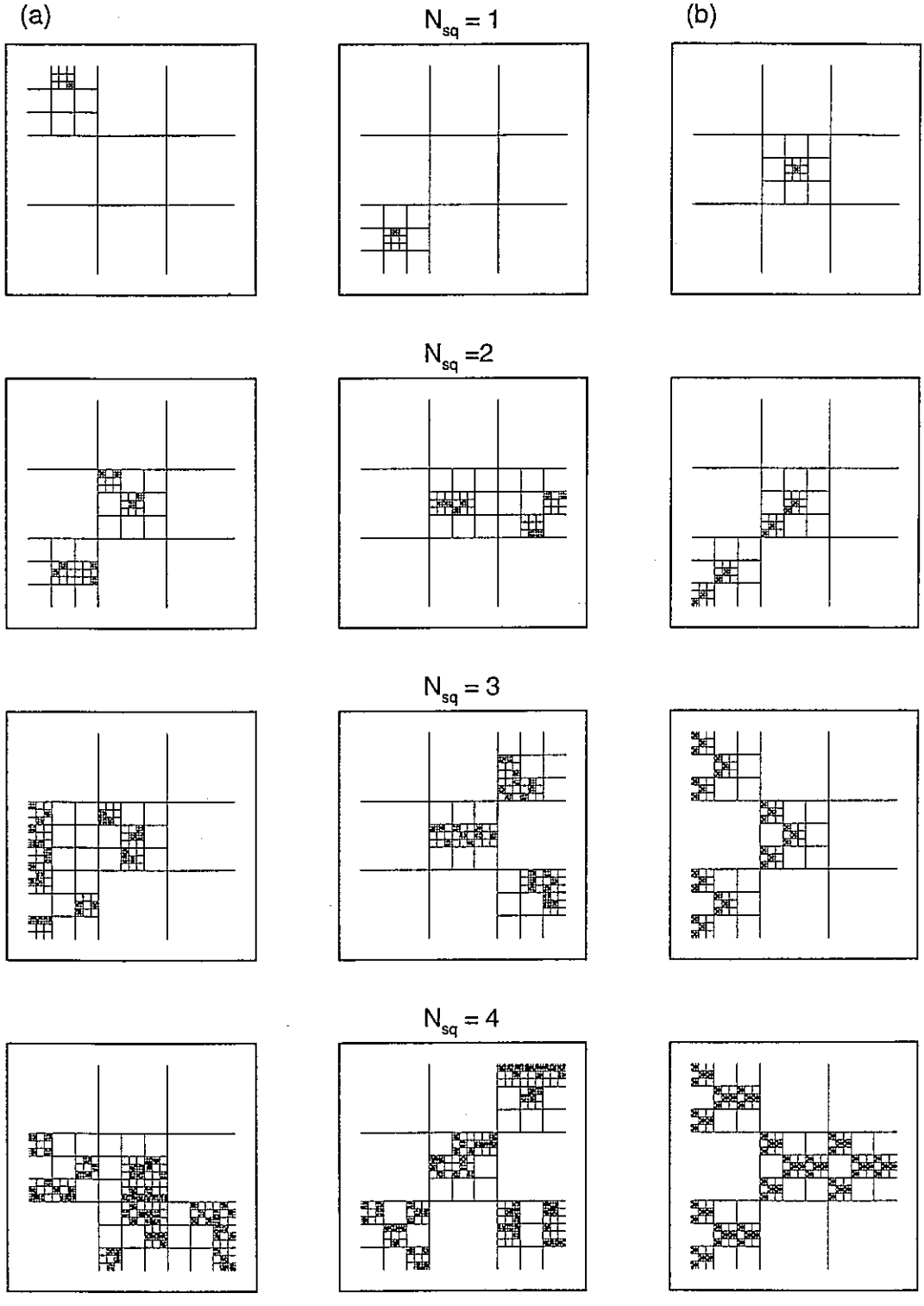


Figure 2. Some of the fracture networks constructed as (a) random, and (b) regular Sierpinski lattices.

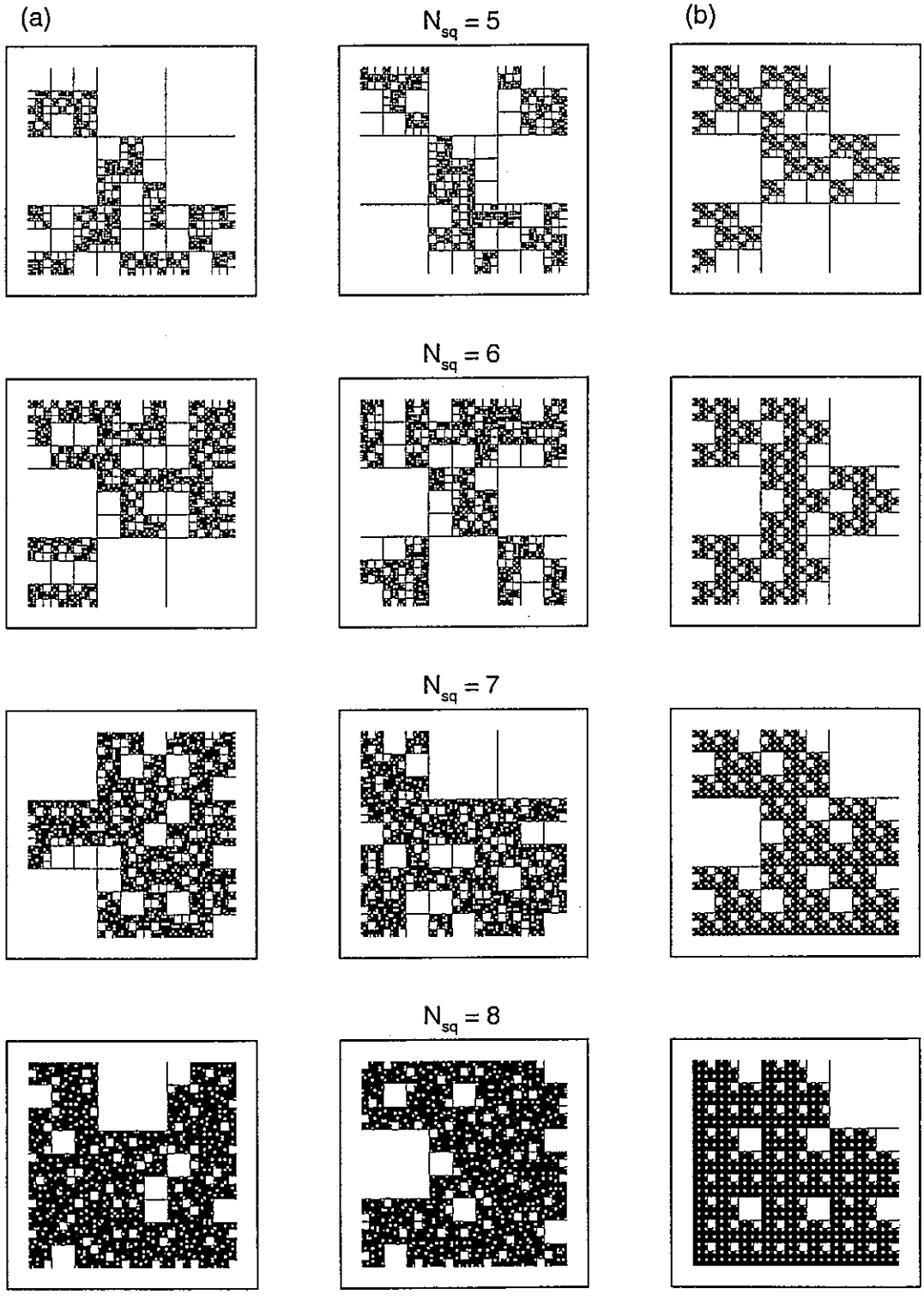


Figure 2 continued.

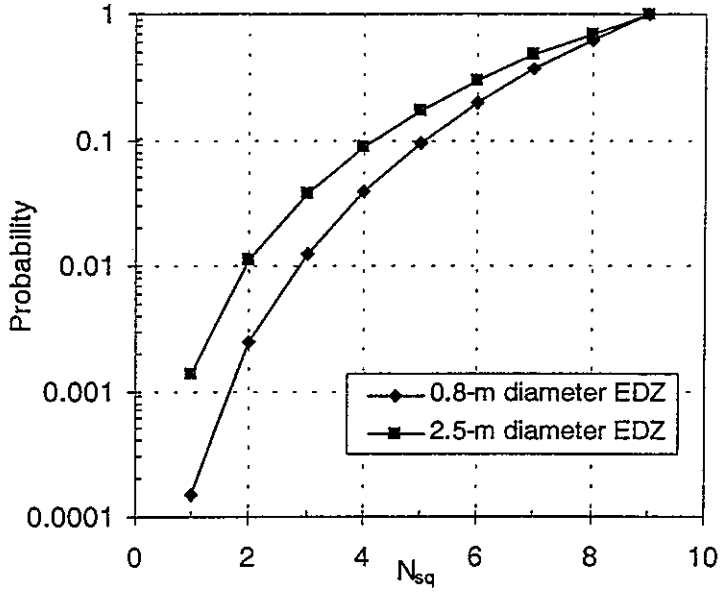


Figure 3. Probability of the fracture network intersecting the EDZ as a function of $N_{sq}$.

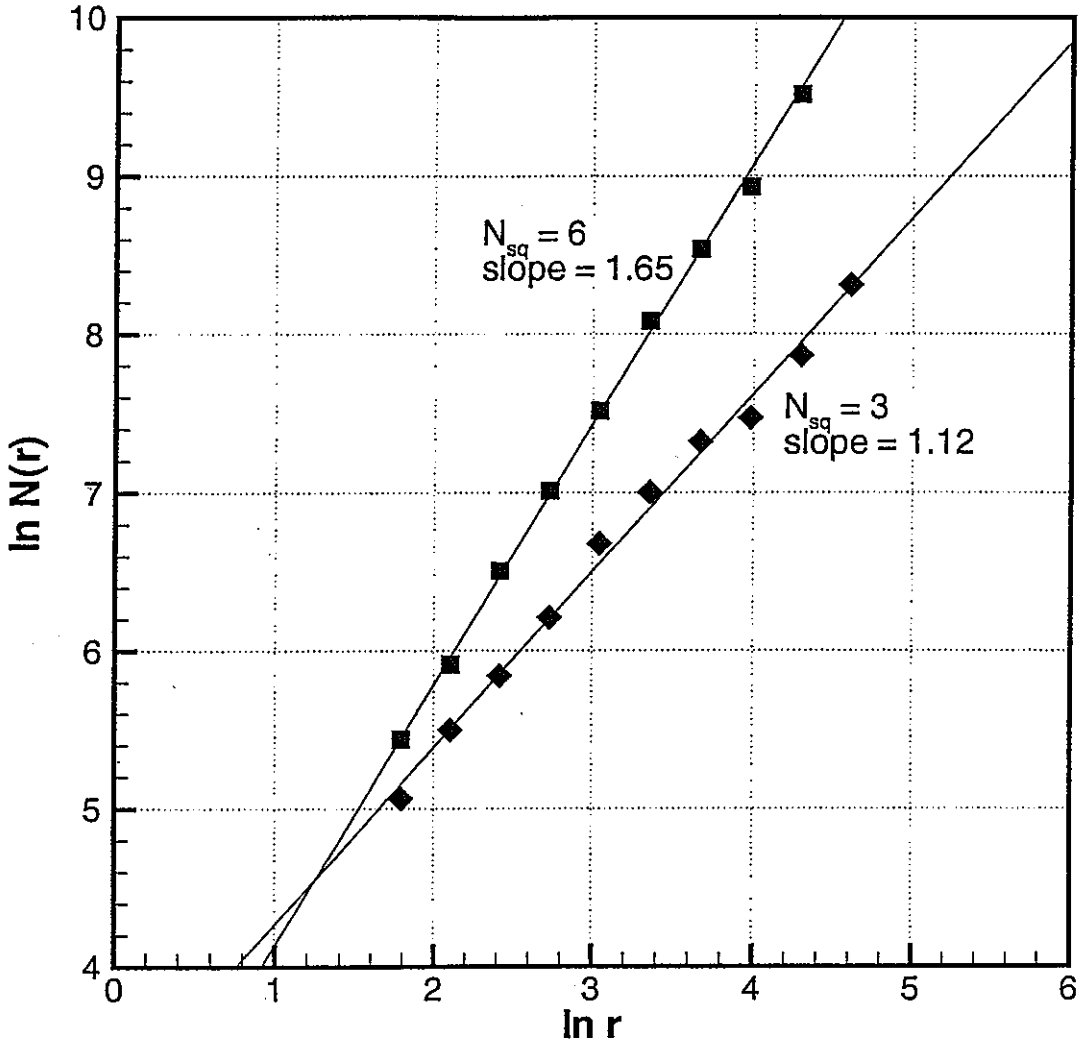


Figure 4. Example of the box counting method. The plot shows the number of fractures encountered within a radius r of a central point; the slope of the lines is the fractal dimension D.

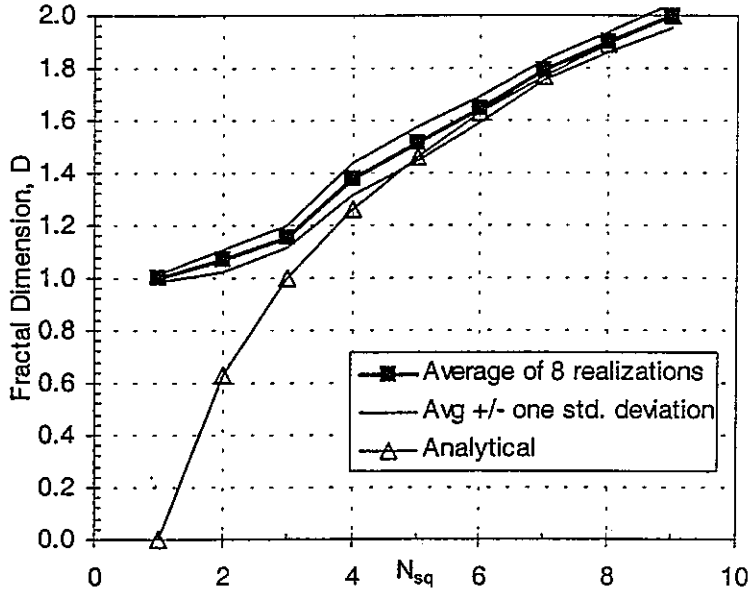


Figure 5. Fractal dimension D of the lattice as a function of $N_{sq}$, with D averaged over eight random lattices for each value of $N_{sq}$ from two to eight. $D_{an}$ is the fractal dimension for a traditional Sierpinski gasket in which only the shortest fractures are retained.

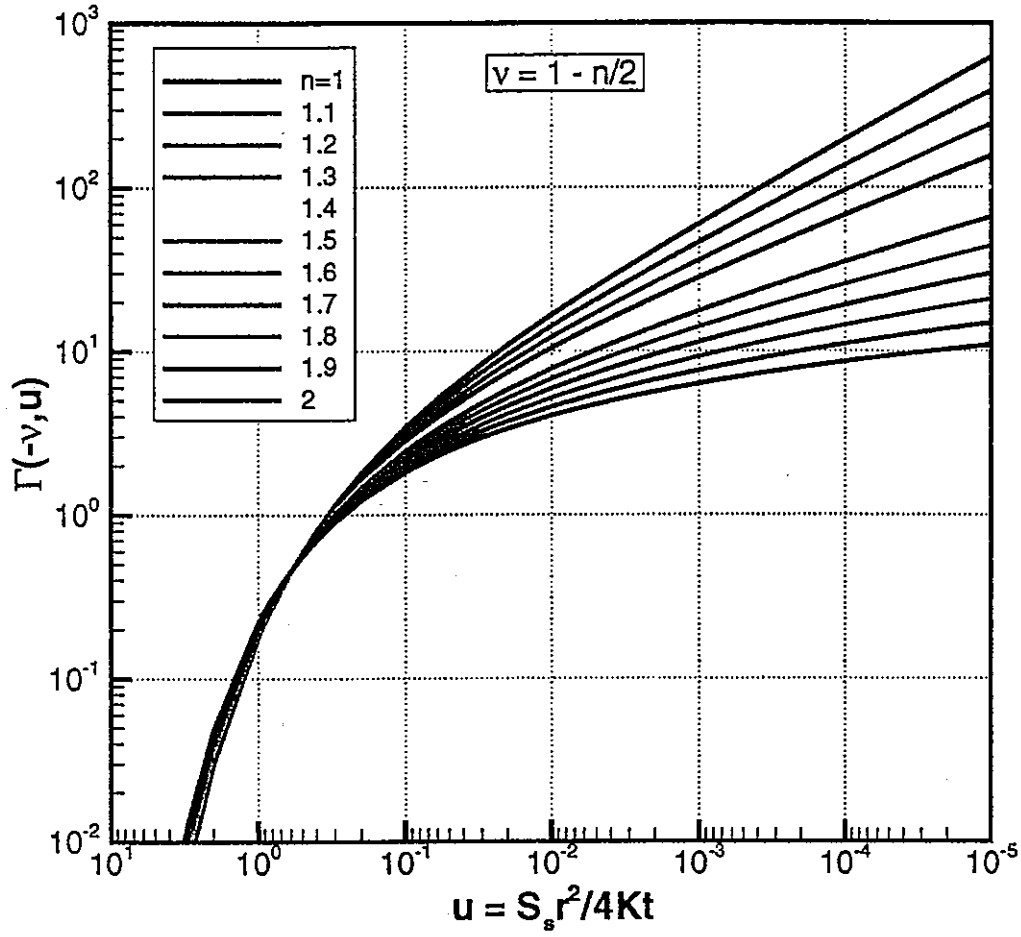


Figure 6. The incomplete gamma function (dimensionless drawdown) versus dimensionless time [*Barker*, 1988].

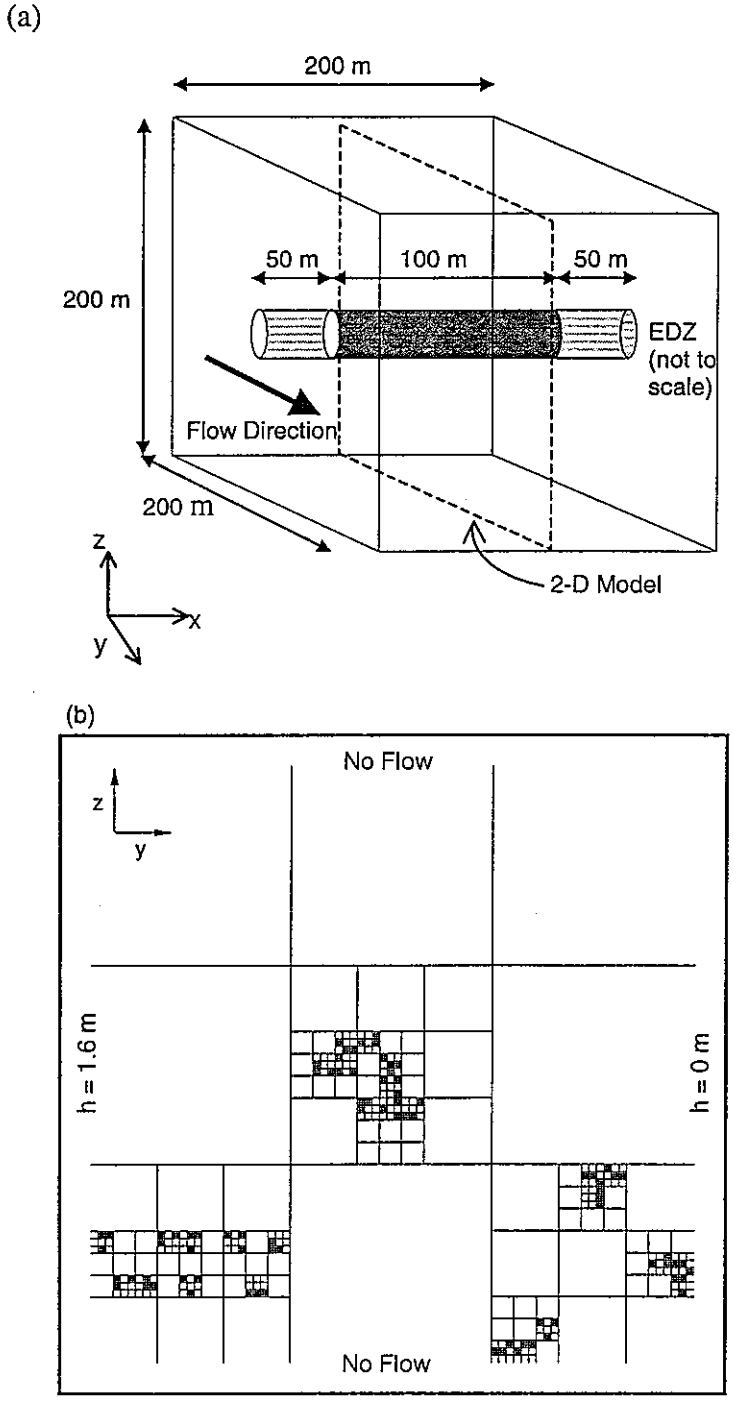


Figure 7. Schematic of the H-12 problem: (a) full 3-D problem, and (b) 2-D slice through the center of the block modeled in the present studies. The EDZ is shown as a solid black square at the center.

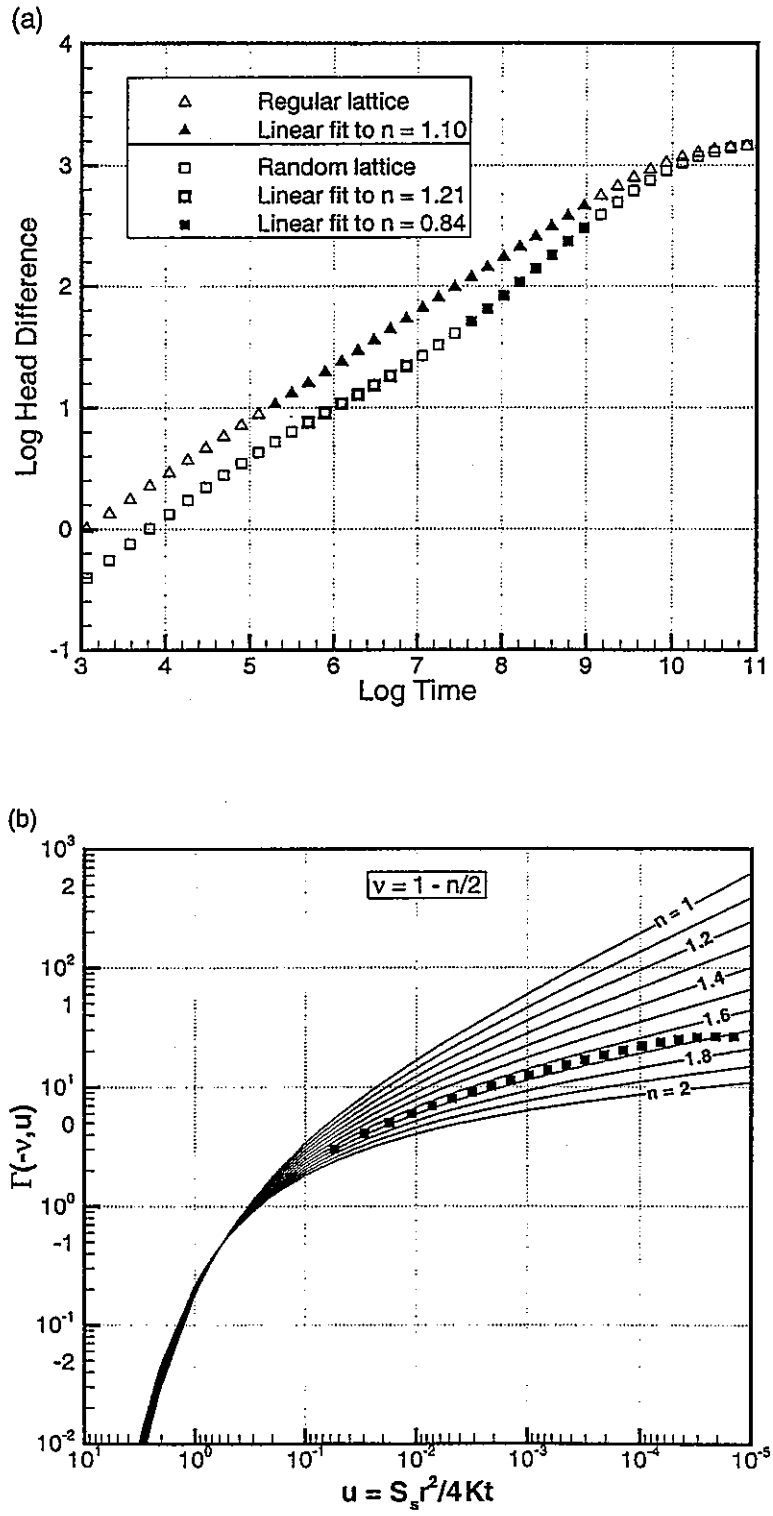


Figure 8. Comparison of numerically simulated drawdown and Barker solution for single-well, constant-rate pumping tests for lattices with (a) $N_{sq} = 3$, and (b) $N_{sq} = 7$.

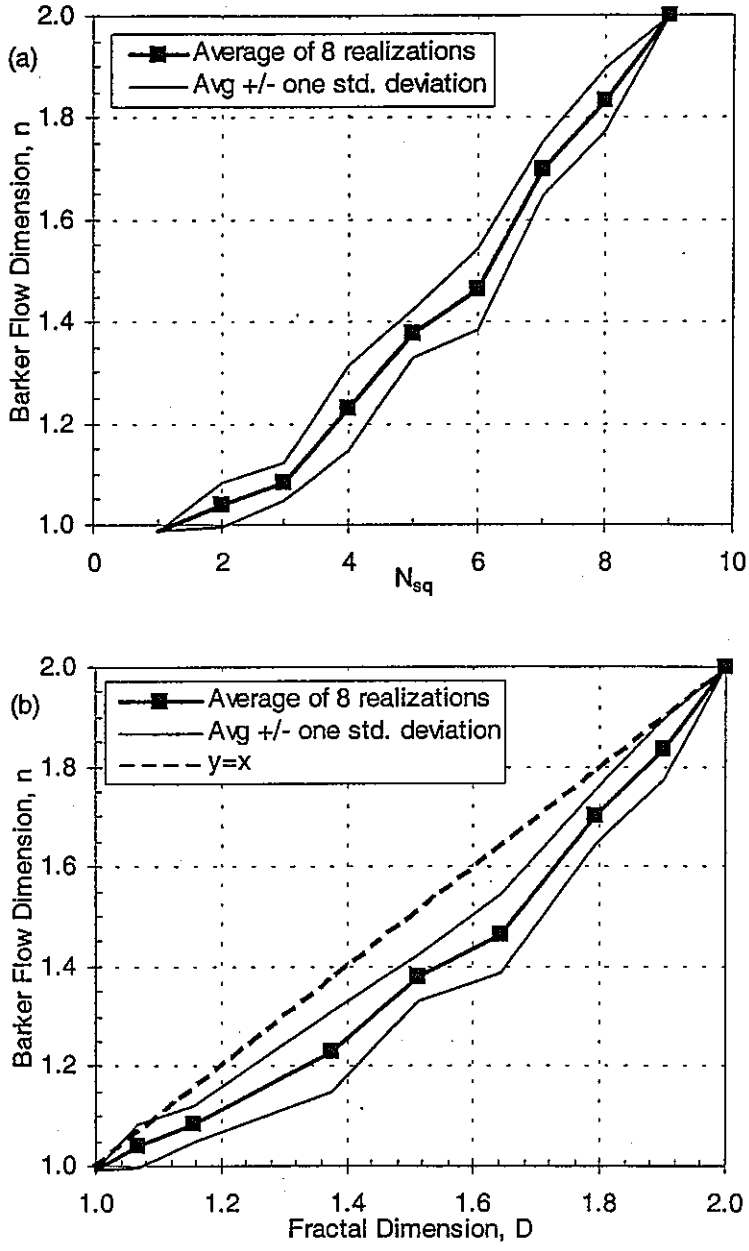


Figure 9. Flow dimension n as a function of (a) $N_{sq}$ and (b) D.

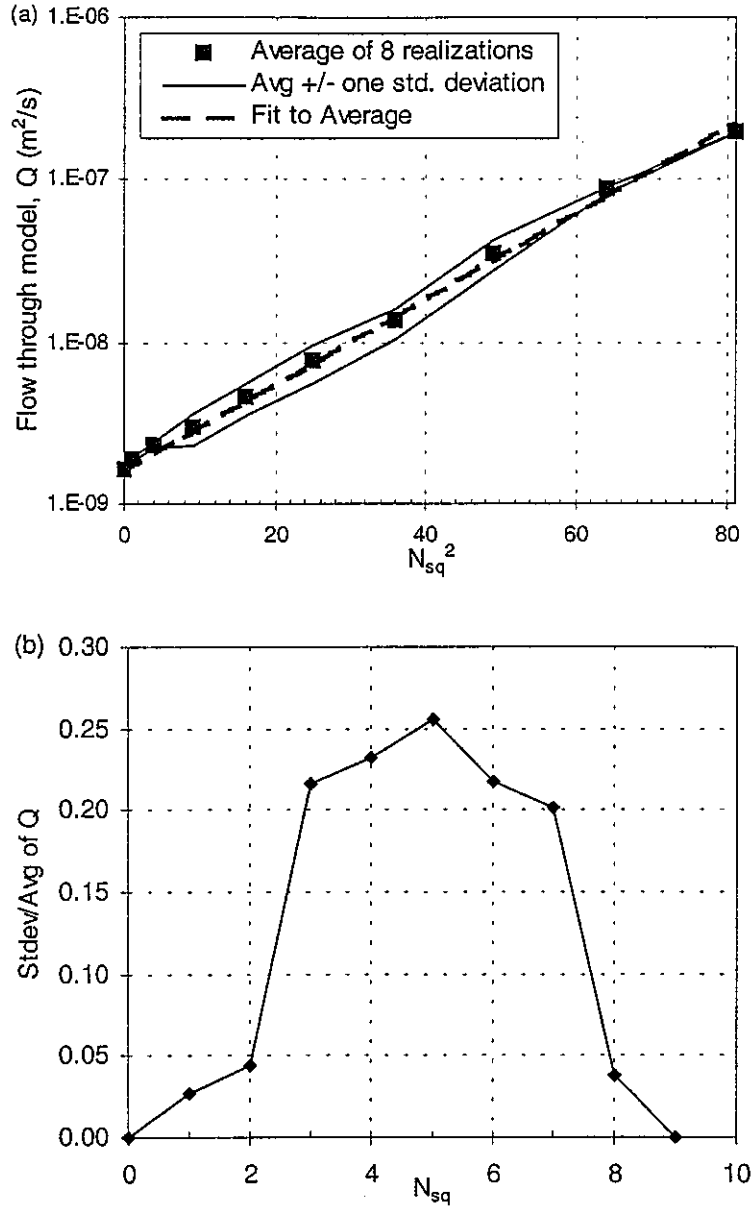


Figure 10. Flow through the model during a tracer test: (a) average Q as a function of $N_{sq}^2$, and (b) standard deviation of Q divided by average Q as a function of $N_{sq}$.

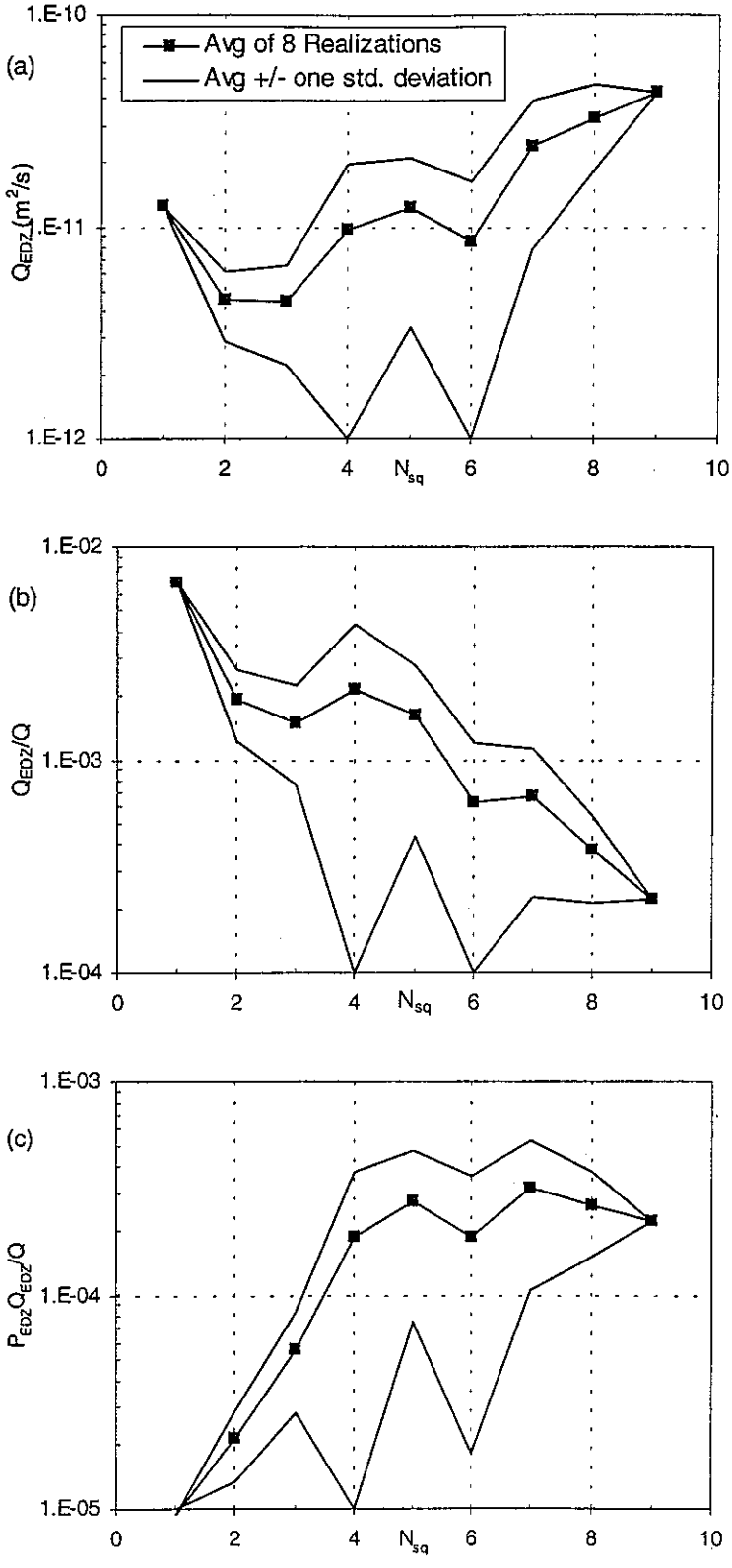


Figure 11. Different ways of evaluating flow through the EDZ during a tracer test: (a) $Q_{EDZ}$ versus $N_{sq}$, (b) $Q_{EDZ}/Q$ versus $N_{sq}$, (c) $P_{EDZ}Q_{EDZ}/Q$ versus $N_{sq}$.

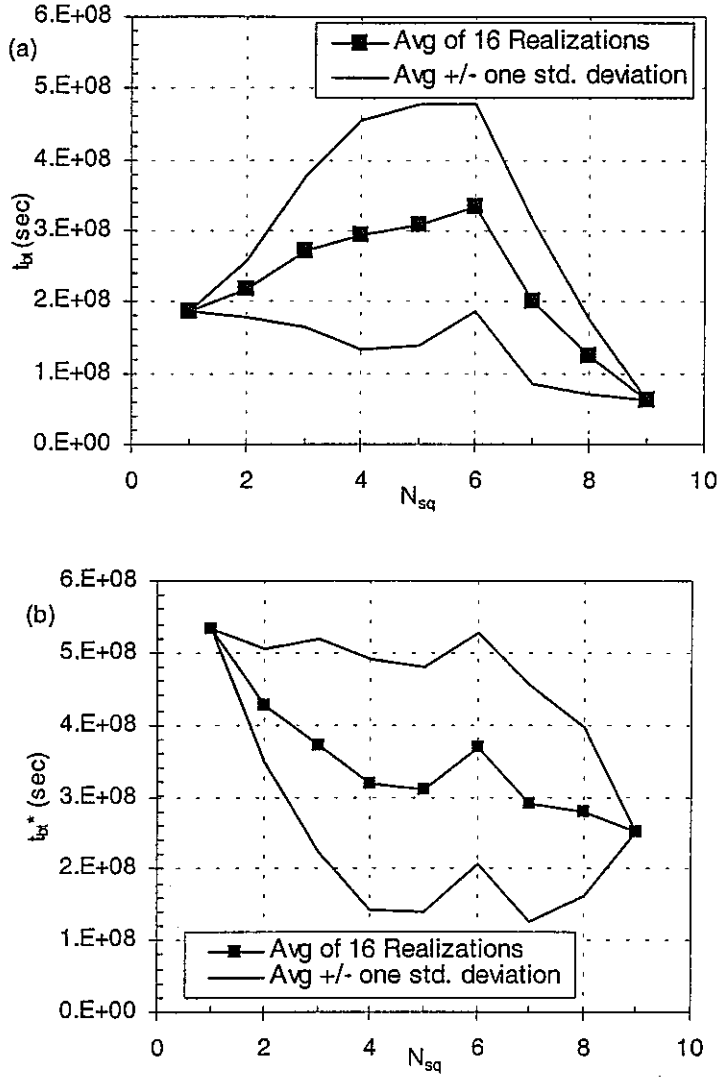


Figure 12. Breakthrough time at the downgradient boundary of the model as a function of $N_{sq}$: (a) actual breakthrough time $t_{bt}$, and (b) normalized breakthrough time $t_{bt}$*, with the influence of effective lattice transmissivity and total void space removed.

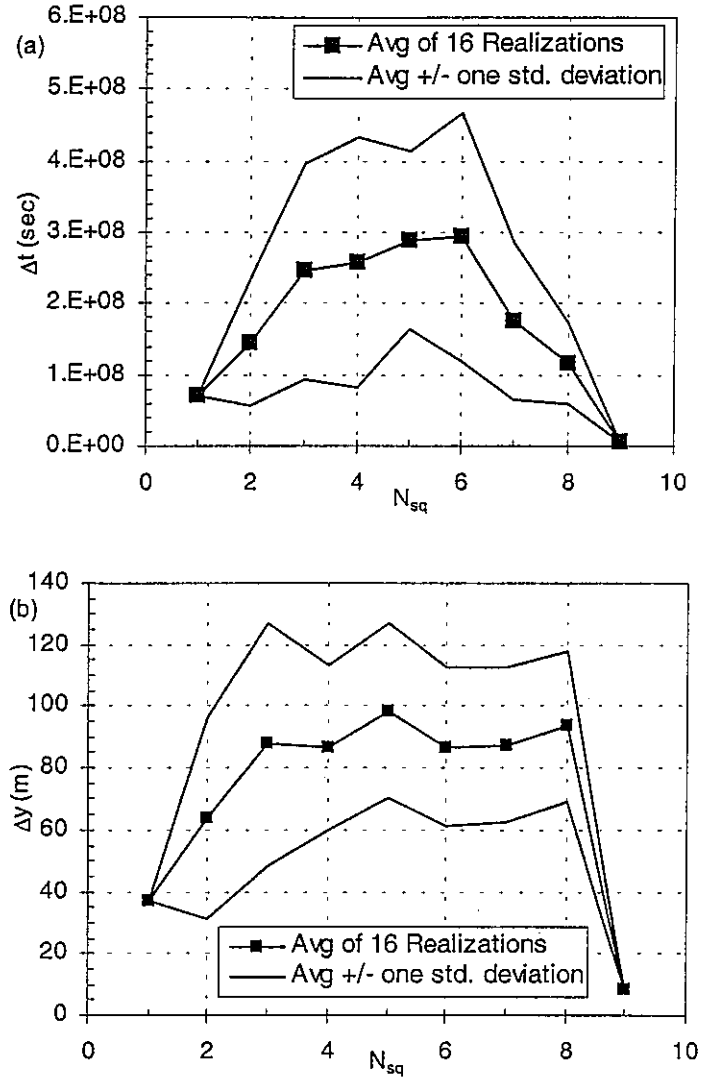


Figure 13 Concentration front width at the downgradient boundary of the model as a function of $N_{sq}$: (a) front width in time Δt, and (b) front width in space Δy.

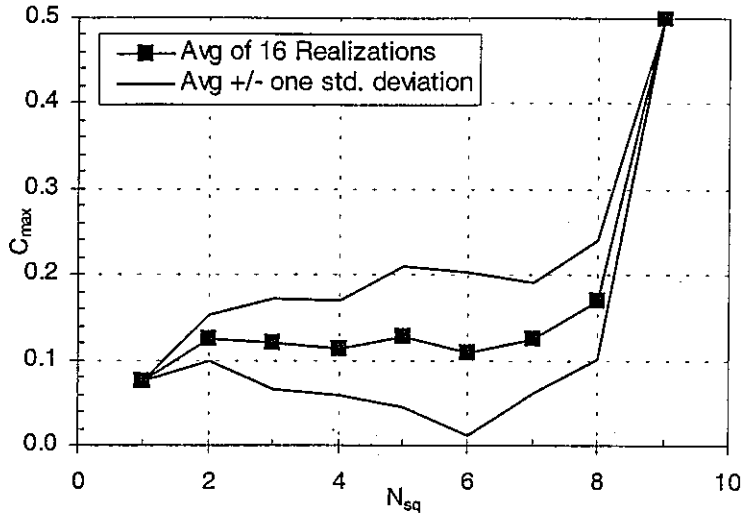


Figure 14. Maximum concentration at the downgradient boundary of the model as a function of $N_{sq}$.

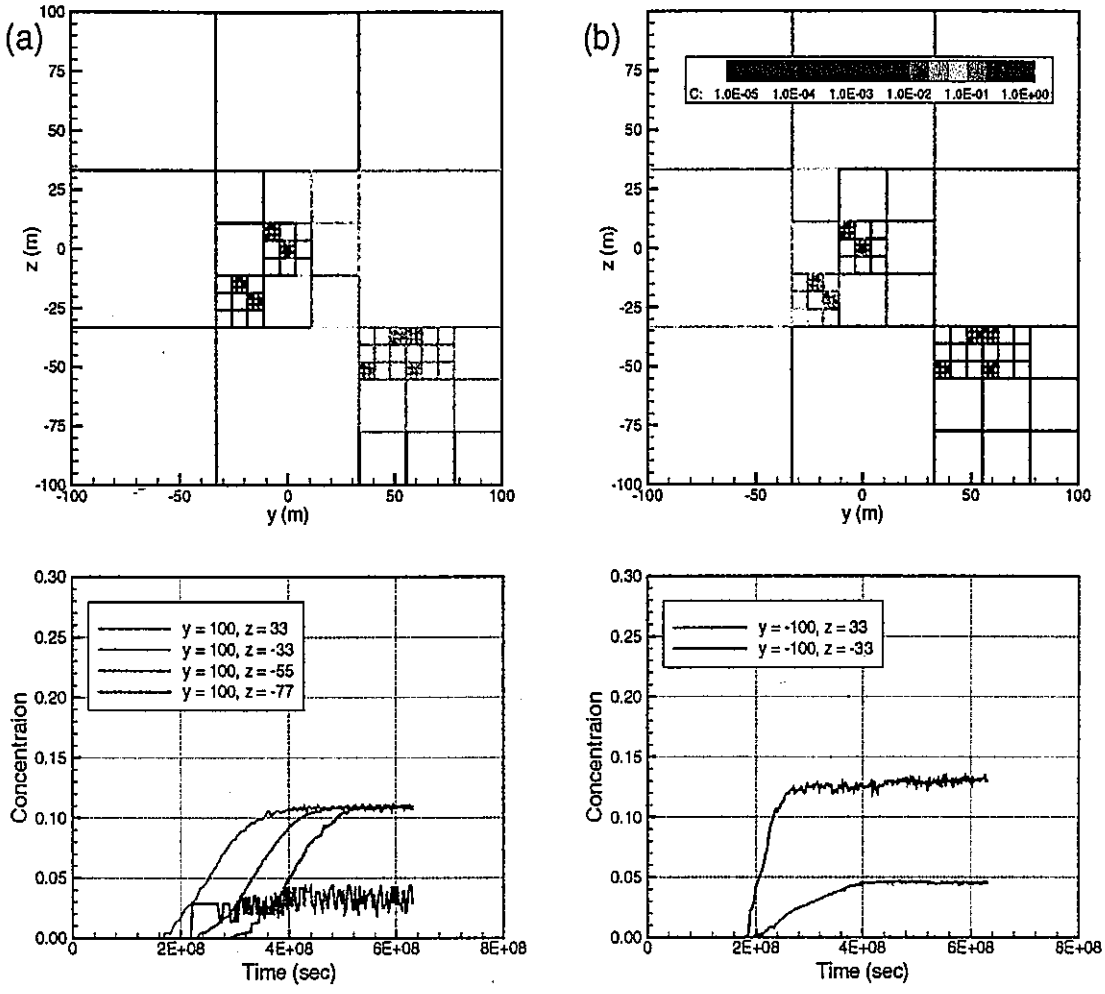


Figure 15. Steady-state concentration distribution and breakthrough curves at selected points on the downgradient boundary for an $N_{sq} = 2$ lattice in which flow is from (a) left to right and (b) right to left.

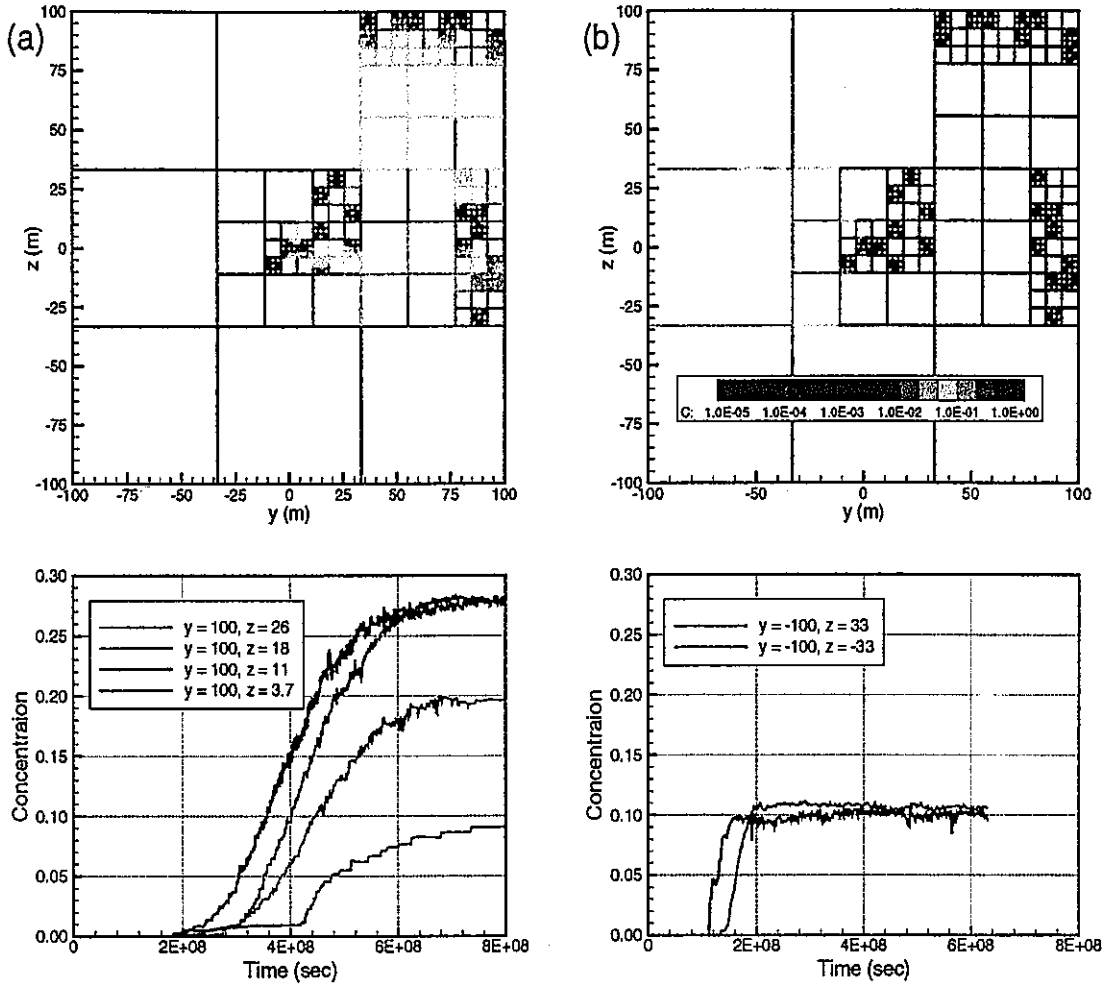


Figure 16. Steady-state concentration distribution and breakthrough curves at selected points on the downgradient boundary for an $N_{sq}$ = 3 lattice in which flow is from (a) left to right and (b) right to left.

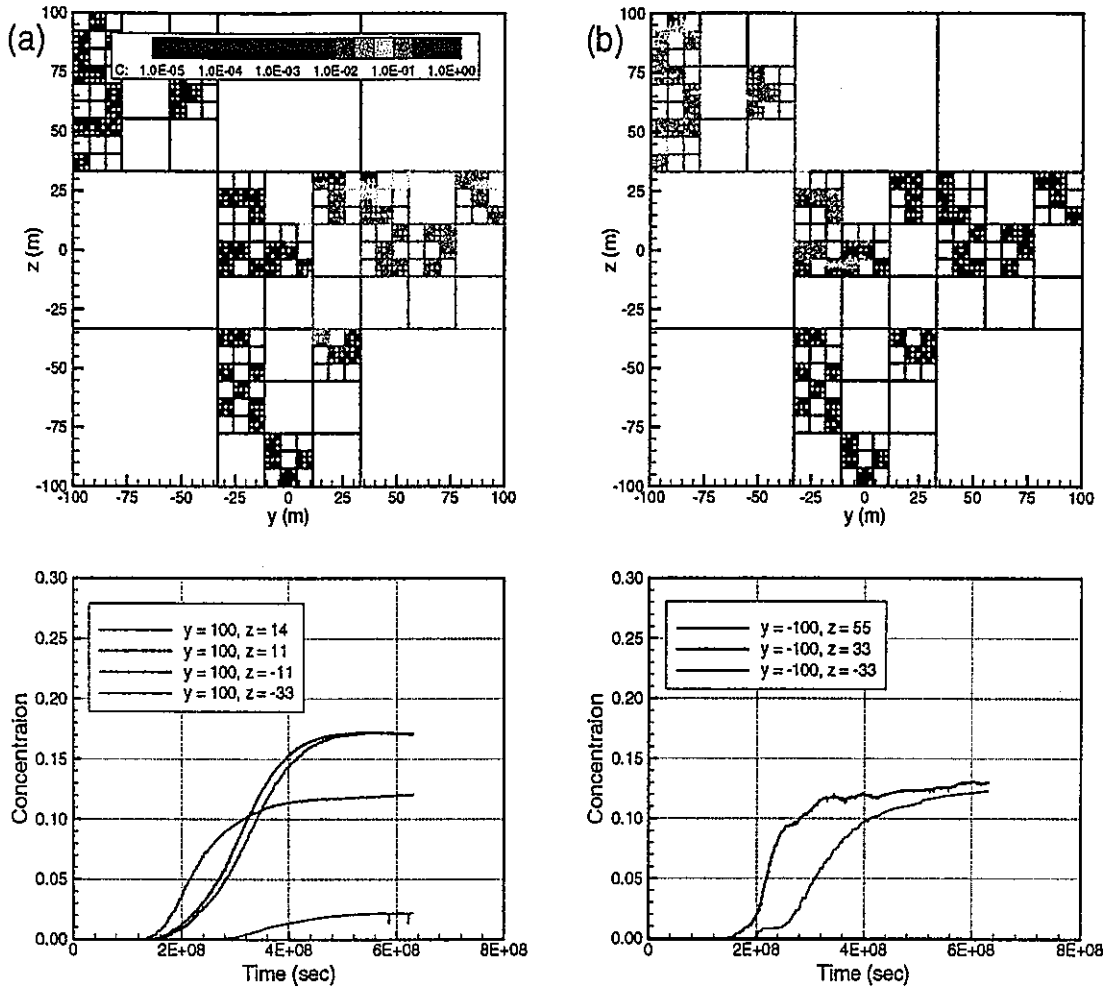


Figure 17. Steady-state concentration distribution and breakthrough curves at selected points on the downgradient boundary for an $N_{sq} = 4$ lattice in which flow is from (a) left to right and (b) right to left.

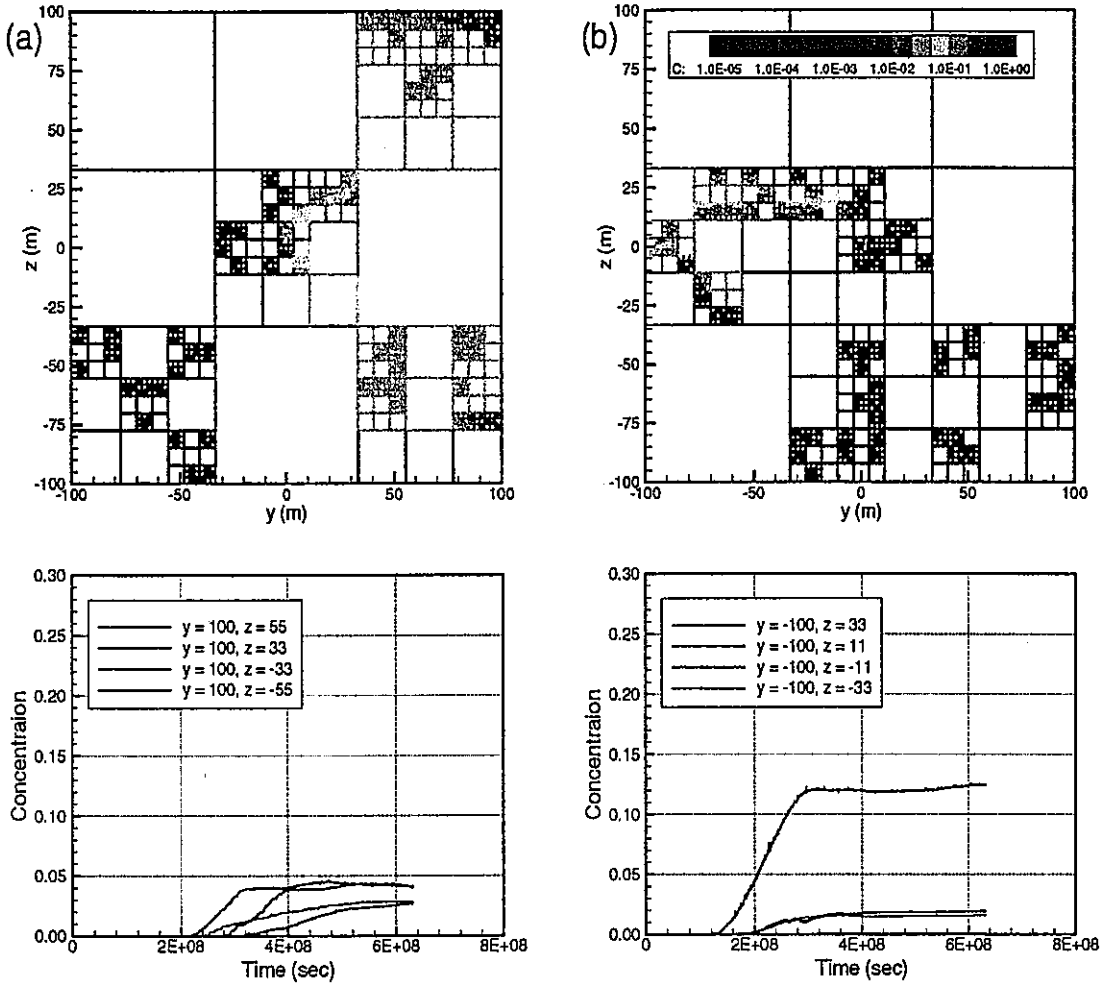


Figure 18. Steady-state concentration distribution and breakthrough curves at selected points on the downgradient boundary for $N_{sq} = 4$ lattices in which flow is from (a) left to right and (b) right to left.

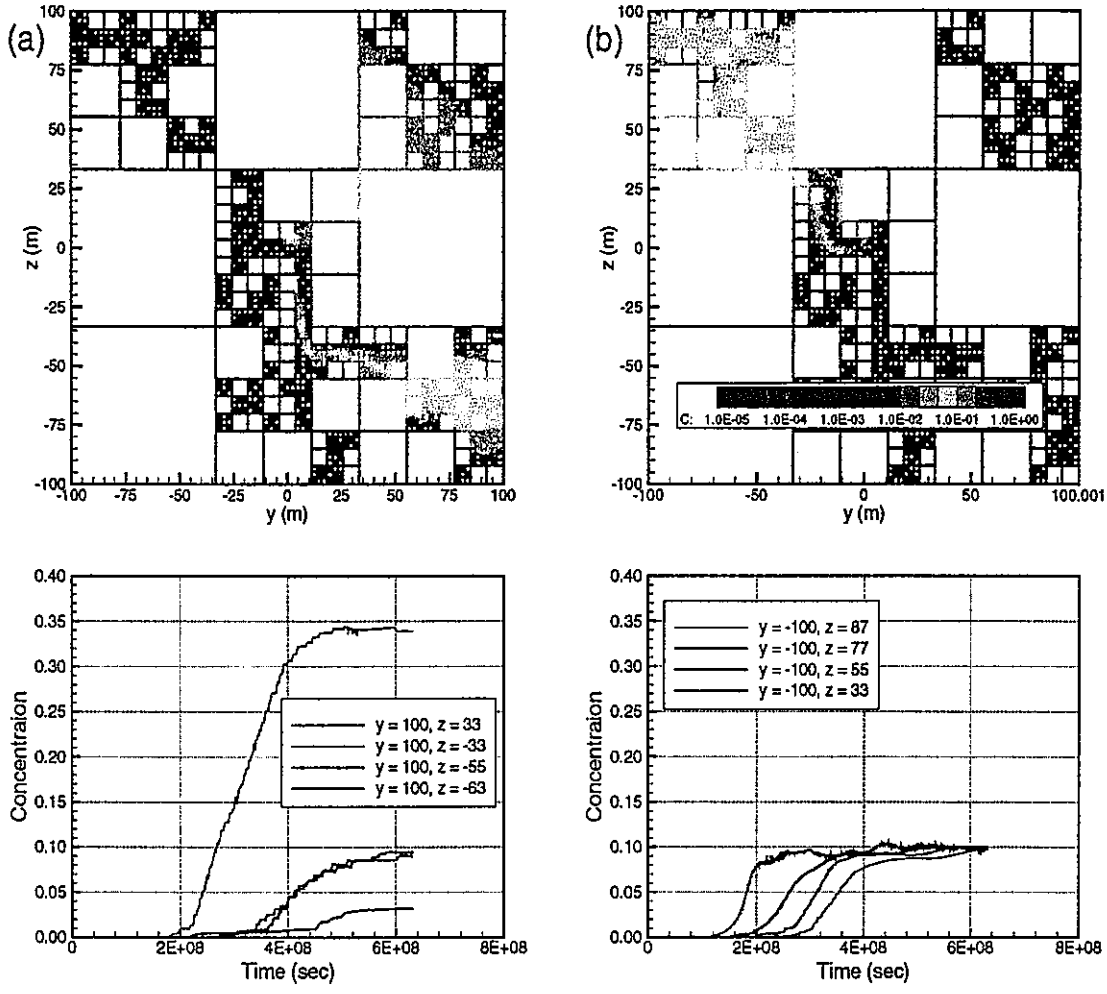


Figure 19. Steady-state concentration distribution and breakthrough curves at selected points on the downgradient boundary for an $N_{sq} = 5$ lattice in which flow is from (a) left to right and (b) right to left.

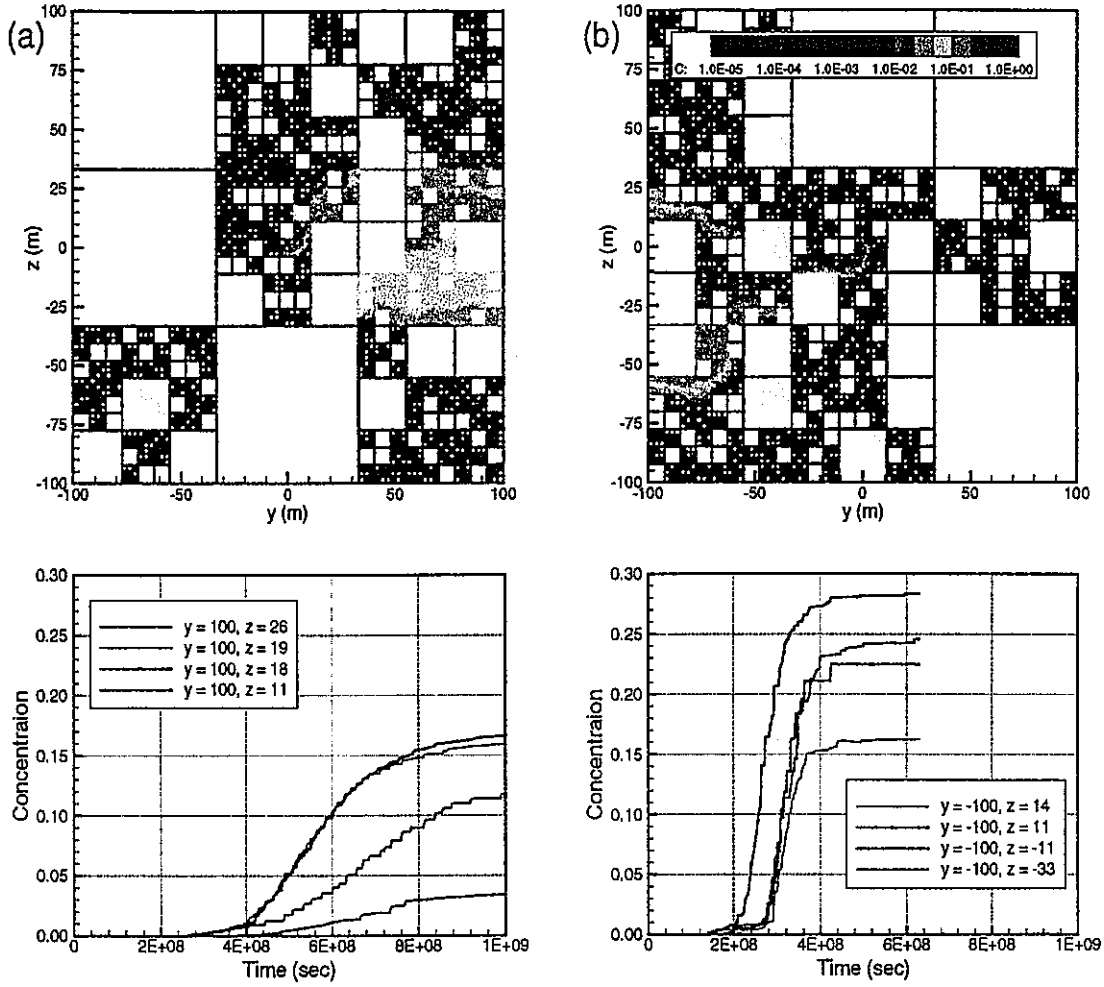


Figure 20. Steady-state concentration distribution and breakthrough curves at selected points on the downgradient boundary for $N_{sq} = 6$ lattices in which flow is from (a) left to right and (b) right to left.

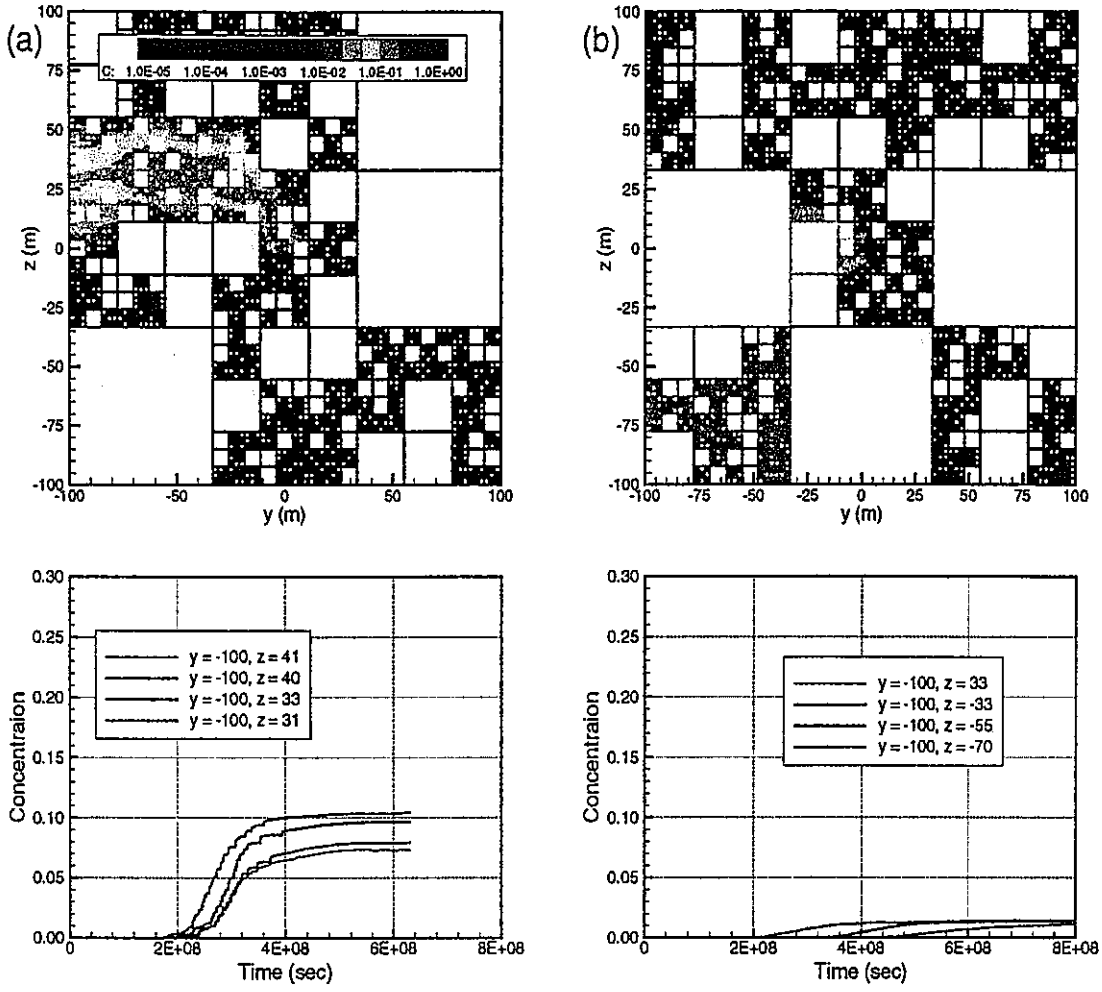


Figure 21. Steady-state concentration distribution and breakthrough curves at selected points on the downgradient boundary for $N_{sq} = 6$ lattices in which flow is from right to left.

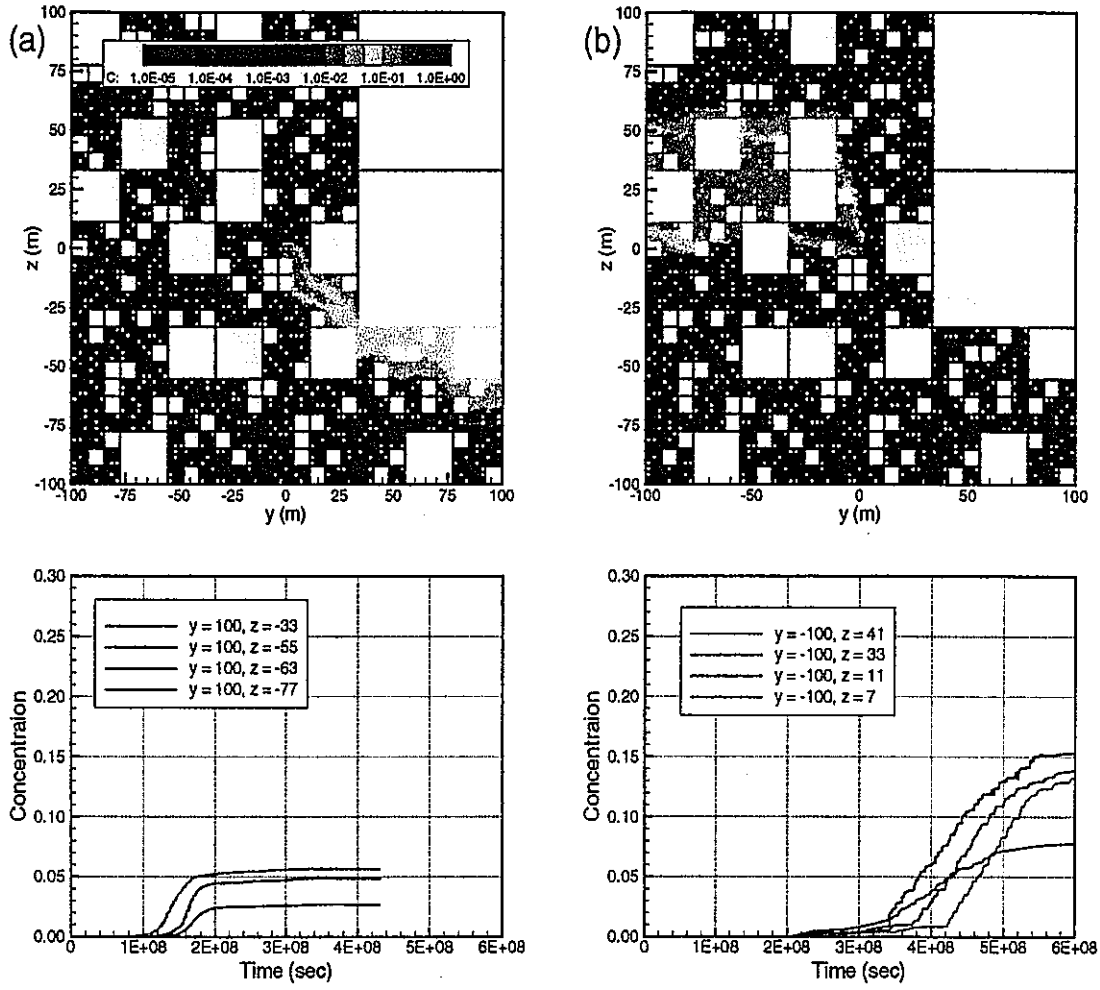


Figure 22. Steady-state concentration distribution and breakthrough curves at selected points on the downgradient boundary for an $N_{sq} = 7$ lattice in which flow is from (a) left to right and (b) right to left.

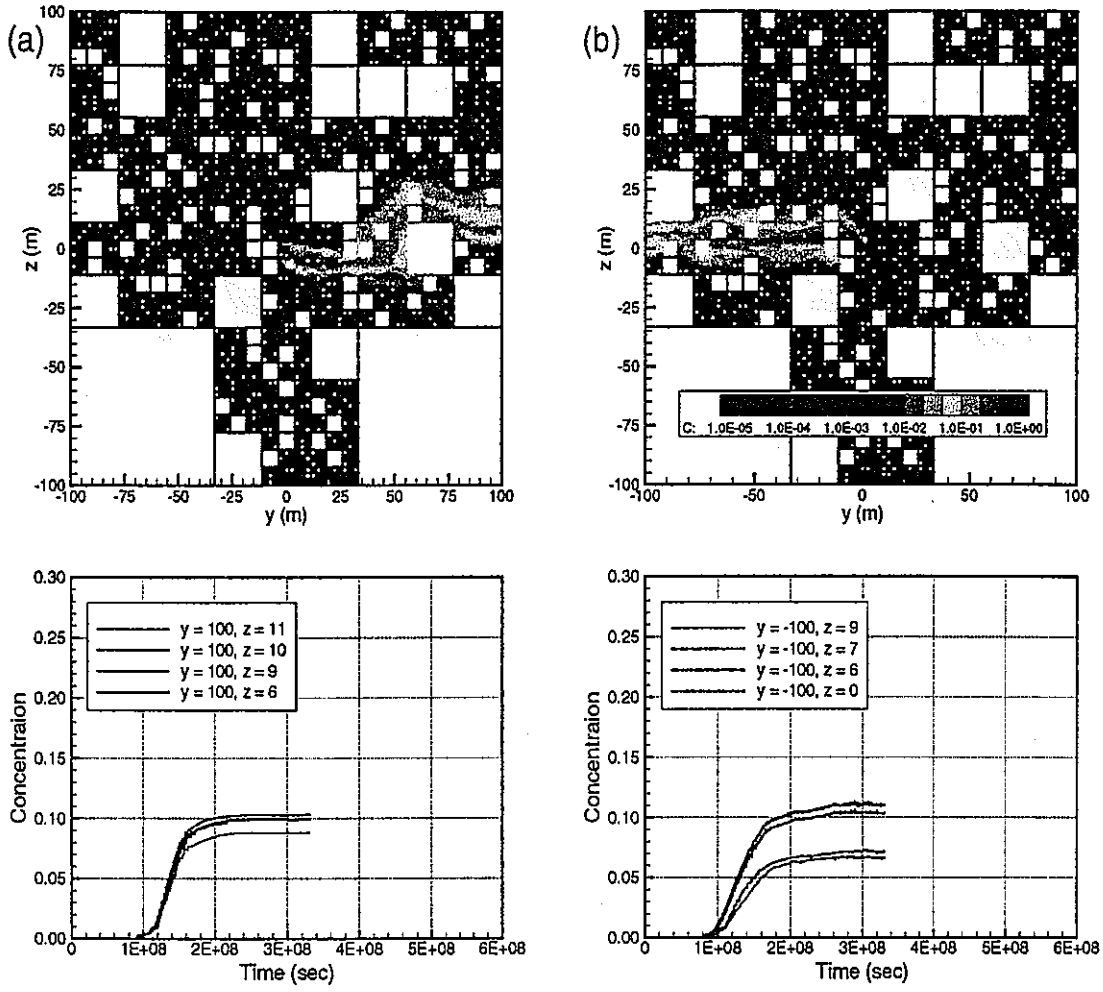


Figure 23. Steady-state concentration distribution and breakthrough curves at selected points on the downgradient boundary for an $N_{sq} = 7$ lattice in which flow is from (a) left to right and (b) right to left.

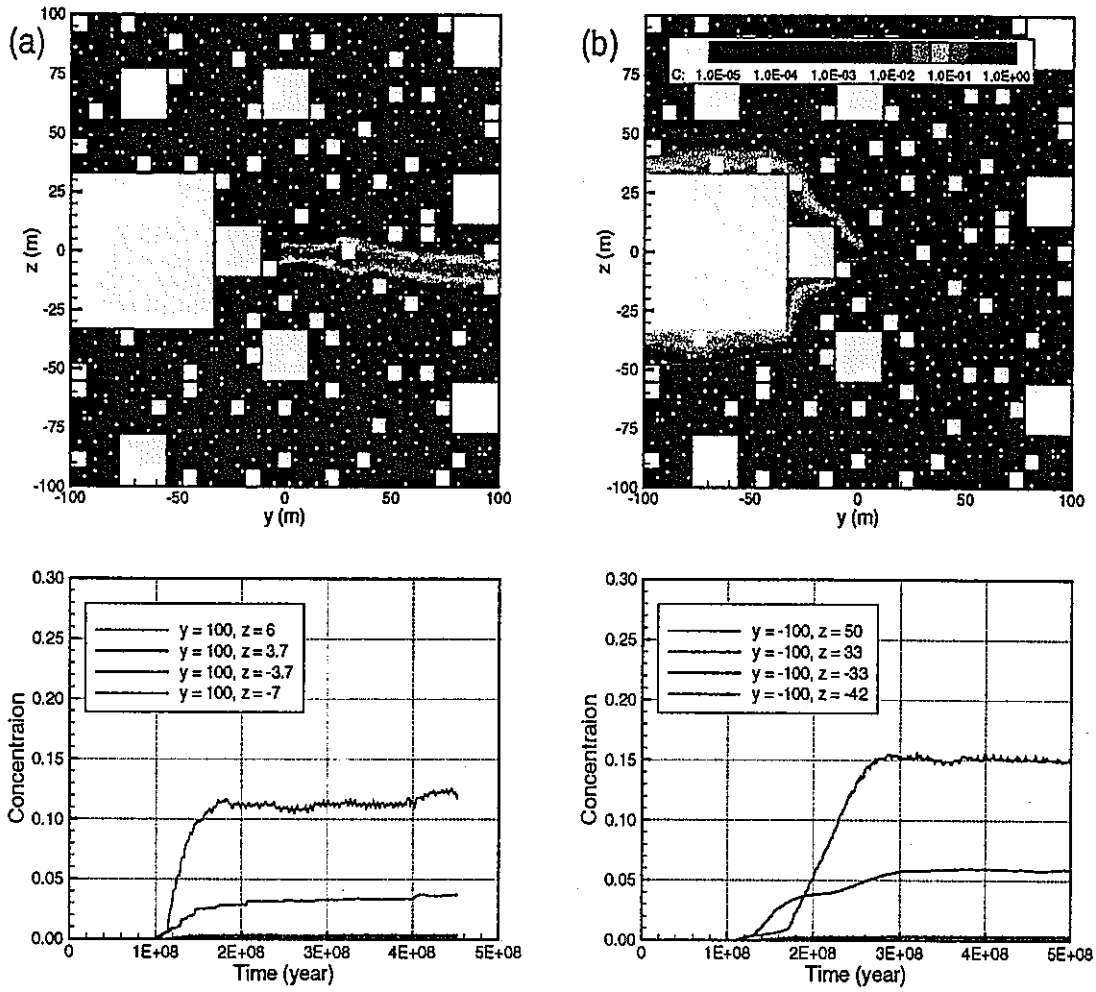


Figure 24. Steady-state concentration distribution and breakthrough curves at selected points on the downgradient boundary for an $N_{sq} = 8$ lattice in which flow is from (a) left to right and (b) right to left.

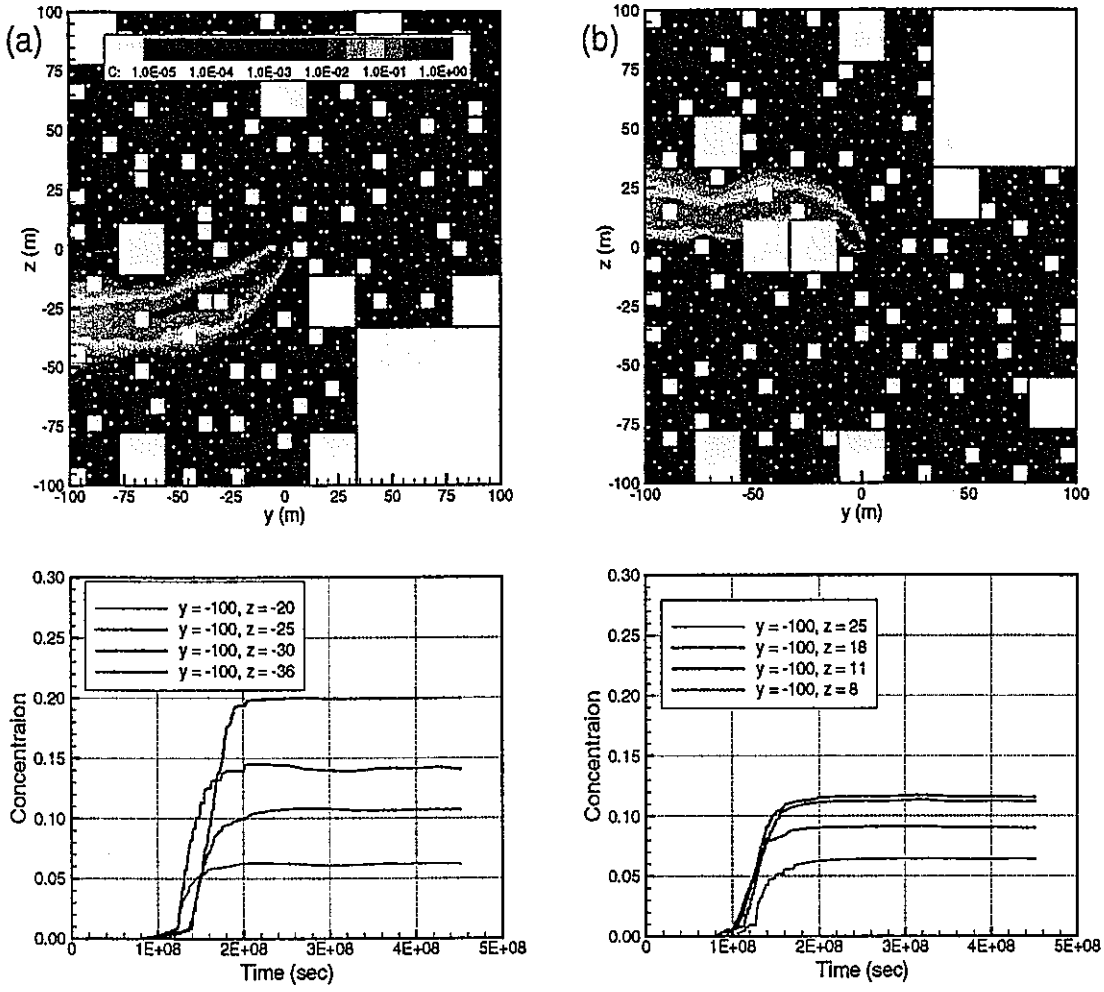


Figure 25. Steady-state concentration distribution and breakthrough curves at selected points on the downgradient boundary for $N_{sq} = 8$ lattices in which flow is from right to left.

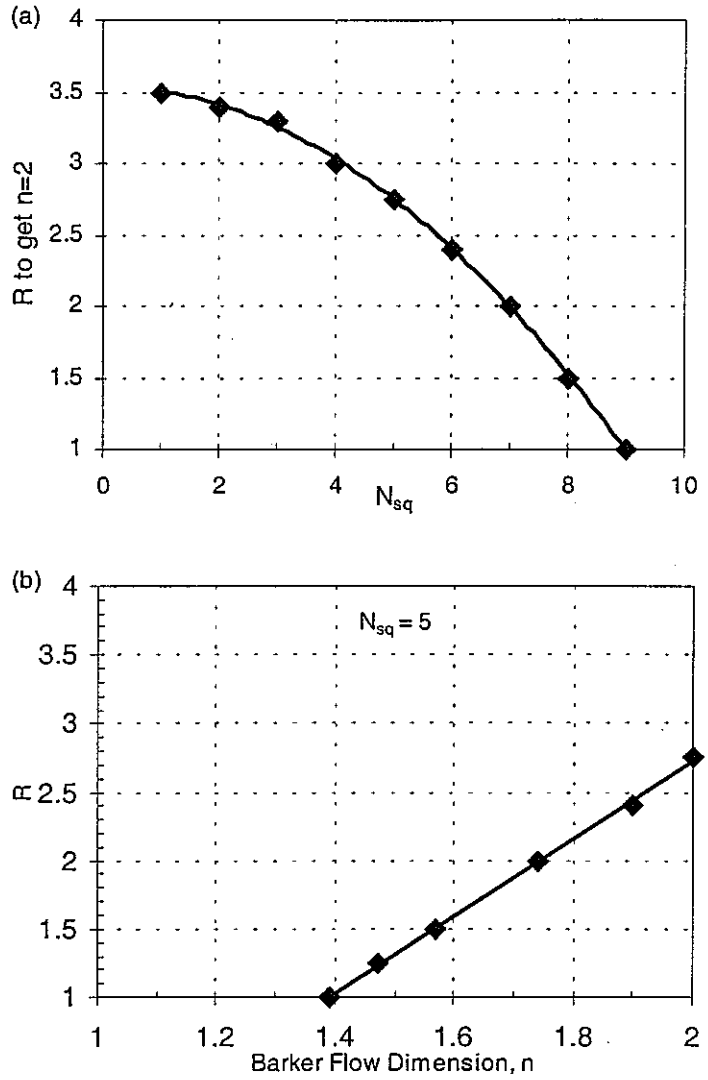


Figure 26. Well-test results for correlated transmissivity: (a) the value of R required to produce a drawdown curve consistent with n = 2, for various values of $N_{sq}$, and (b) the relationship between R and n for $N_{sq}$ = 5.

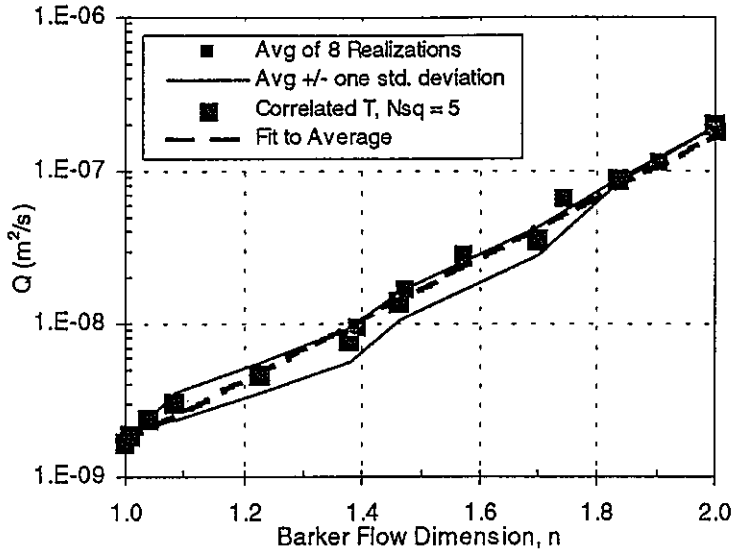


Figure 27. Flow through the model Q as a function of n, including the correlated transmissivity case with $N_{sq} = 5$.

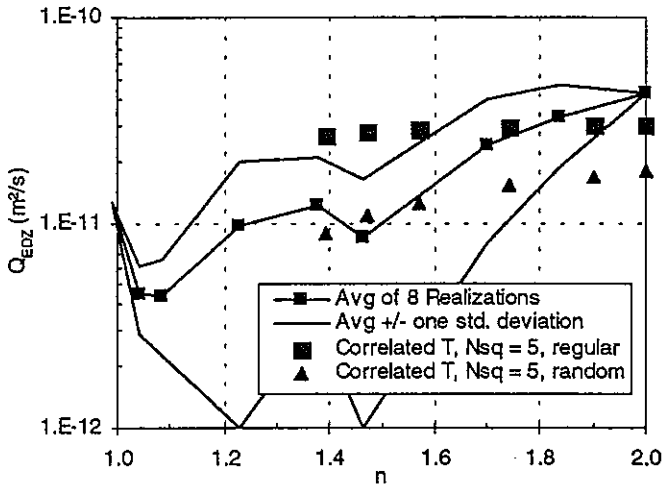


Figure 28. Flow through the EDZ as a function of n, including correlated transmissivity cases with $N_{sq} = 5$.

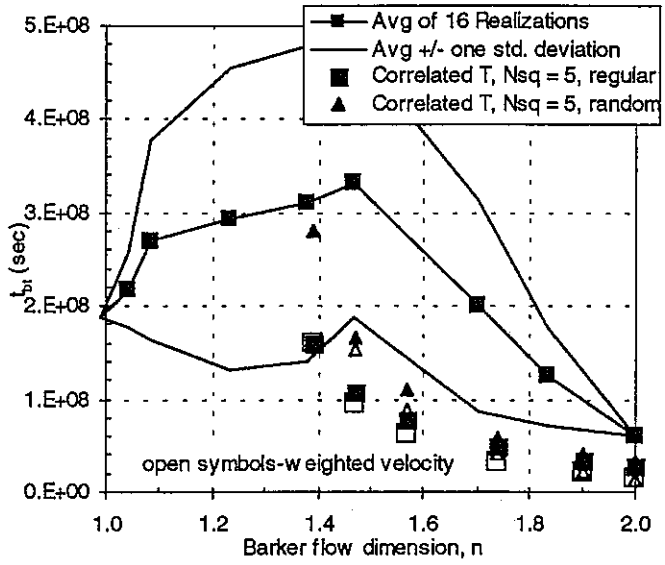


Figure 29. Breakthrough time $t_{bt}$ at the downgradient boundary of the model as a function of n, including correlated transmissivity cases.

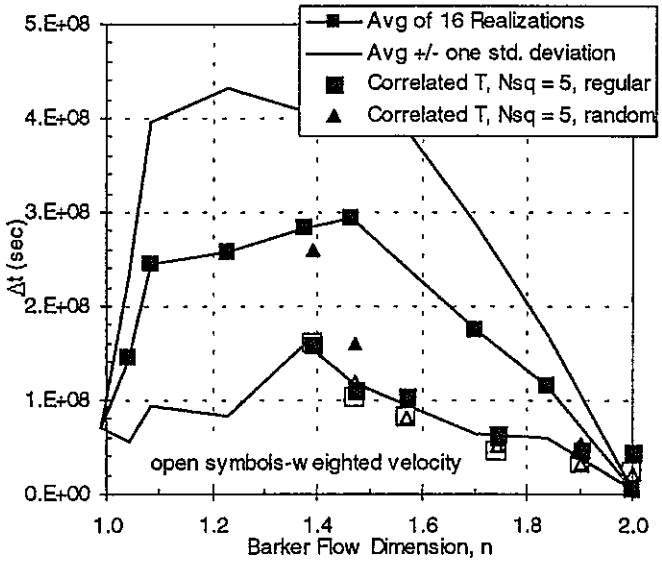


Figure 30. Concentration front width Δt at the downgradient boundary of the model as a function of n, including correlated transmissivity cases.

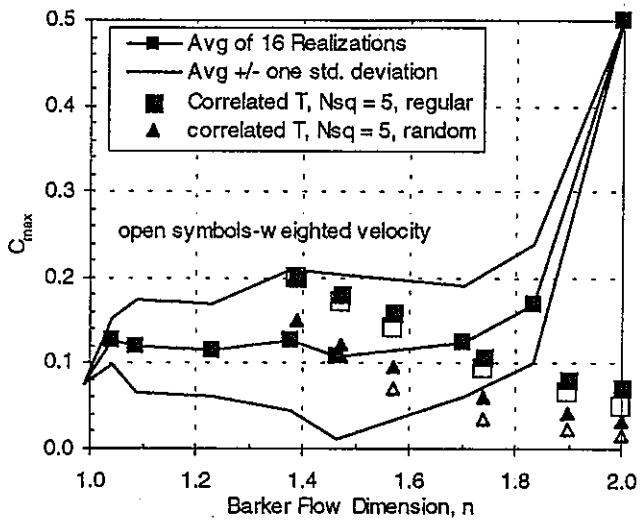


Figure 31. Maximum concentration at the downgradient boundary of the model as a function of n, including correlated transmissivity cases.

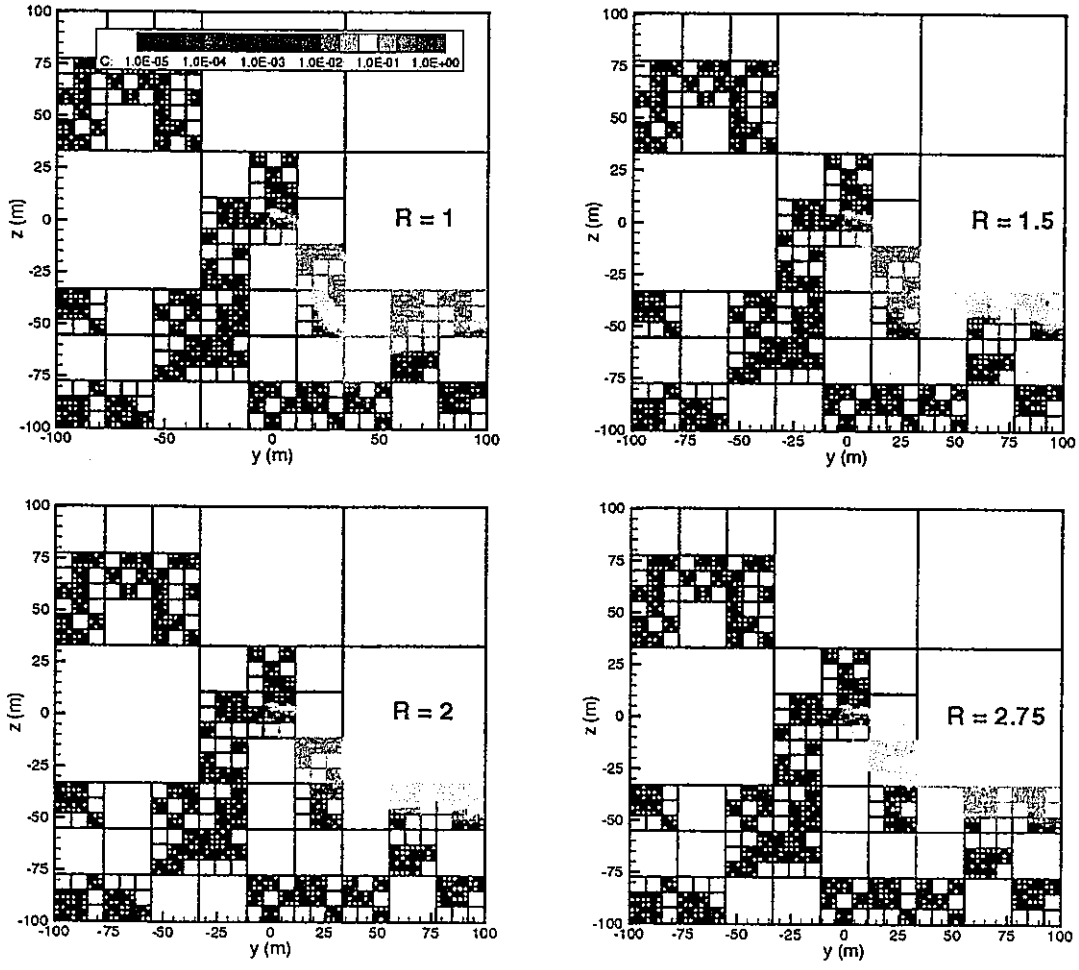


Figure 32. Steady-state concentration distributions for correlated transmissivity cases.

# Estimation of reservoir properties using transient pressure data: An asymptotic approach

D. W. Vasco, Henk Keers, and Kenzi Karasaki
Berkeley Laboratory, University of California, Berkeley, California

Short title: ASYMPTOTIC INVERSION OF PRESSURE DATA

**Abstract.** An asymptotic formulation of the inverse problem for flow reveals that the inversion may be partitioned into two complementary sub-problems. In the first problem, the arrival time associated with the peak slope of the transient curve is directly related to reservoir properties. The second inverse problem is similar to current methods for interpreting flow data, the transient head amplitudes are related to reservoir storage and conductivity. The first sub-problem, the arrival time inversion, involves much less computation than does amplitude matching. Furthermore, it appears to be more robust with respect to the starting model. Therefore, the solution to the arrival time inversion provides a starting model for amplitude matching. The methodology is particularly suited to the analysis of observations from well tests. We apply the approach to observations from two interference tests conducted at the Borehole Test Facility in Oklahoma. Using the transient pressure measurements, we image a shallow conductive fracture. The existence and location of the fracture has been verified by both geophysical and borehole data. In particular, core from a slant well contains an open, vertical fracture which coincides with our conductive feature.

## Introduction

There are advantages in utilizing head or pressure data to characterize aquifer structure. For example, pump tests are generally easier to conduct than are tracer tests. Pressure observations are rather directly related to reservoir conductivity and storage. By contrast, the interpretation of quantities such as tracer concentrations and multi-phase flow data are dependent on variations in reservoir pressure, reservoir conductivity and storage, as well as on additional quantities such as tracer dispersion and fractional flow properties.

In hydraulic well tests, pressure changes are monitored in response to a fluid being pumped into or out of a reservoir. The response is a function of the geometry and the flow parameters of the reservoir. Therefore, by analyzing the pressure changes one can estimate such reservoir parameters. In this regard, well test analysis is an inverse problem. The simplest type of inversion is the traditional analytical approach, where the pressure data are compared to those of known analytical models. However, analytical models are only available for a handful of idealized situations. Although care must be used, the analytical approach is nonetheless a powerful tool for estimating bulk reservoir parameters.

When a more detailed reservoir description is called for, multiple pressure tests with many observation points must be conducted. In such cases a numerical inversion is usually employed to analyze the data. There are by now a wealth of computational techniques for interpreting and inverting pressure or head variations. Due to their great diversity, it is difficult to categorize the various approaches. Some are primarily geostatistical while others are more deterministic in nature, though it is possible to treat the problem in a somewhat unified manner [McLaughlin and Towney, 1996]. Some methods attempt to estimate parameters using stochastic optimization methods such as simulated annealing [Mauldon et al., 1993] or hybrid schemes such as simplex annealing [Pan and Wu, 1998]. More commonly, a linearized inversion technique is used iteratively

to estimate parameter values. Linearized approaches require the computation of the sensitivity coefficients relating perturbations in reservoir properties to perturbations in flow. Since the early work of Jacquard and Jain [1965] several classes of methods have been developed for computing such sensitivities. For more details interested readers should consult the reviews by Yeh [1986], Kuiper [1986], Carrera [1987], Ginn and Cushman [1990], Sun [1994], and Mclaughlin and Towney [1996].

Some difficulties in interpreting pressure observations are due to the computation required to solve the inverse problem and due to the localized nature of pressure sensitivities. Inverting transient pressure data involves extensive computation, particularly for three-dimensional problems. Most solutions of the forward problem, calculating pressure given a reservoir model, rely on purely numerical solutions, which can be expensive. The solution of the inverse problem entails repeated solution of the forward problem, either to compute sensitivities for a linearized inversion or to construct a solution using a stochastic technique. The spatial variations in pressure sensitivity also introduce difficulties into the inversion process. In particular, well pressure variations are far more sensitive to flow properties near the pumping and observing boreholes than to conductivity and storage at a distance. Furthermore, the pressure sensitivities to variations in conductivity and storage are fairly similar over time. Thus, the pressure history at a well is in many ways redundant. That is, a large number of pressure observations do not necessarily produce a corresponding number of independent constraints on the spatial variation of reservoir properties.

In this paper we describe an approach to transient pressure inversion which is based upon an asymptotic solution to the flow equation. The approach has some useful properties, particularly when treating the inverse problem. First, the solutions are defined along trajectories or paths in the model, between the source well and the observation point. Thus, the three-dimensional problem of calculating pressure is reduced to a sequence of one-dimensional problems. This is particularly important for

the inverse problem because sensitivities may be computed by integrating analytical expressions along the trajectories. Secondly, the inverse problem divides into two complementary estimation problems. Initially, we use the arrival time of the maximum slope in pressure curve to infer conductivity and storage. Subsequently, the pressure variations themselves are inverted for flow properties. The advantage of this two-step procedure is that, as we shall show, the travel time is equally sensitive to structure between the pumping and observing wells, it is not more strongly influenced by variations in the vicinity of the boreholes. Furthermore, the arrival time inverse problem is more robust with respect to the starting model. Thus, the arrival times may be used to find a initial three-dimensional reservoir model which may be used as the starting model for the inversion of the pressure values themselves.

Our asymptotic approach follows that of Vasco et al. [1999], Vasco and Datta-Gupta [1999], and Virieux et al. [1994]. A number of studies have extended asymptotic methods to propagation problems with a diffusive component, amoung them are Chapman et al. [1999], Smith [1981], Kravtsov [1968], and Cohen and Lewis [1967]. There is a related body of work in which the diffusion equation is explicitly transformed into a wave equation [Wilson, 1983; Pierce, 1986; Philip, 1989; Oliver, 1994]. In these approaches similar ideas, such as arrival time matching [Oliver, 1994], do arise. However, such transform methods have been hampered by the instability of the transformation between the wave-like and diffusive domains [Oliver, 1994].

## Methodology

In this section we derive the asymptotic series solution for flow. By considering terms of various orders in $1/\sqrt{\omega}$ (where $\omega$ is the frequency) we arrive at the eikonal equation governing the phase or arrival time and the transport equation describing the evolution of pressure amplitude in space and time. Using the eikonal and transport equations we then derive the sensitivities of head to variations in aquifer storage and

conductivity.

### The equation governing drawdown

In an inhomogeneous medium the equation describing the space $\mathbf{x}$ and time $t$ evolution of head $h(\mathbf{x},t)$ is

$$K(\mathbf{x})\nabla^2 h(\mathbf{x},t) + \nabla K(\mathbf{x})\cdot\nabla h(\mathbf{x},t) = S(\mathbf{x})\frac{\partial h(\mathbf{x},t)}{\partial t} \tag{1}$$

where $K(\mathbf{x})$ denotes the hydraulic conductivity and $S(\mathbf{x})$ denotes the storage coefficient [Bear, 1972; de Marsily, 1986]. We consider the equation in the frequency domain, applying the Fourier transform

$$H(\mathbf{x},\omega) = \frac{1}{2\pi}\int_{-\infty}^{\infty} h(\mathbf{x},t)e^{i\omega t}d\omega. \tag{2}$$

In the frequency domain equation (1) becomes

$$K(\mathbf{x})\nabla^2 H(\mathbf{x},\omega) + \nabla K(\mathbf{x})\cdot\nabla H(\mathbf{x},\omega) = i\omega S(\mathbf{x})H(\mathbf{x},\omega). \tag{3}$$

Defining

$$\Lambda(\mathbf{x}) = \frac{\nabla K(\mathbf{x})}{K(\mathbf{x})} \tag{4}$$

and

$$\Delta(\mathbf{x}) = \frac{S(\mathbf{x})}{K(\mathbf{x})} \tag{5}$$

produces the more compact form

$$\nabla^2 H(\mathbf{x},\omega) + \Lambda(\mathbf{x})\cdot\nabla H(\mathbf{x},\omega) - i\omega\Delta(\mathbf{x})H(\mathbf{x},\omega) = 0. \tag{6}$$

In the frequency domain it is clear that for large $\omega$, at high frequencies, the head is sensitive to $\Delta(\mathbf{x})$, the ratio of storage to conductivity. Conversely, low frequency variations in head, such as the static change in pressure, are primarily sensitive to $\Lambda(\mathbf{x})$ which may be written as

$$\Lambda(\mathbf{x}) = \nabla \ln K(\mathbf{x}).$$

In order to motivate our particular form of the solution, in powers of $1/\sqrt{\omega}$, note that in a homogeneous medium $\mathbf{\Lambda}(\mathrm{x})$ vanishes, resulting in the diffusion equation

$$\nabla^2 H(\mathrm{x},\omega) - i\omega\Delta(\mathrm{x})H(\mathrm{x},\omega) = 0 \tag{7}$$

where $\Delta(\mathrm{x})$ is now constant. For an impulsive source $-4\pi\delta(t)$ the diffusion equation has the time-domain solution

$$h(\mathrm{x},t) = \frac{1}{t}e^{-\Delta(\mathrm{x})r^2/4t}\Sigma(t) \tag{8}$$

where $r$ is the distance from the source and $\Sigma(t)$ is a step function. If we consider the solution in the frequency domain we find that

$$H(\mathrm{x},\omega) = 2K_0(\sqrt{-i\omega}\sqrt{\Delta(\mathrm{x})r}) \tag{9}$$

where $K_0$ is a modified Bessel function of zero-th order [Virieux et al., 1994]. For large $\omega$, $K_0$ may be approximated by

$$H(\mathrm{x},\omega) = \frac{\sqrt{2\pi}}{\sqrt{\sqrt{-i\omega}\sqrt{\Delta(\mathrm{x})}}}\frac{1}{\sqrt{r}}e^{-\sqrt{-i\omega}\sqrt{\Delta(\mathrm{x})r}} \tag{10}$$

[Virieux et al., 1994]. Note in particular that the frequency enters the solution in the form $\sqrt{-i\omega}$.

### Asymptotic solutions for flow

An asymptotic solution for flow follows if we take a solution of the form

$$H(\mathrm{x},\omega) = e^{-\sqrt{-i\omega}\sigma(\mathrm{x})}\sum_{n=0}^{\infty}\frac{A_n(\mathrm{x})}{(\sqrt{-i\omega})^n} \tag{11}$$

[Fatemi et al., 1995]. The motivation for using an expansion in inverse powers of $\omega$ is that the initial terms of the series represent rapidly varying (high-frequency, large $\omega$) components of the solution and successive terms are associated with lower frequency behavior [Vasco and Datta-Gupta, 1999]. The reason for using $\sqrt{-i\omega}$, rather than simply $\omega$, is that we would like our solution to reduce to the solution given by

equation (10) in a homogeneous medium. One could also argue for a solution of the form (11) on physical grounds, based upon dimensional or similarity analysis of the equation for drawdown. This is somewhat analogous to the derivation of the Boltzmann transformation discussed by Bear [1972]. Other asymptotic expressions are also possible. For example, Chapman et al. [1999] consider an expansion of the form

$$H(\mathrm{x},\omega) = \omega^{-\epsilon} e^{i\omega\sigma(\mathrm{x})} \sum_{n=0}^{\infty} \frac{A_n(\mathrm{x})}{\omega^n}$$

where the constant $\epsilon$ is chosen such that the leading-order equation is nontrivial.

The asymptotic solution (11) is the sum of an infinite number of functions $A_n(\mathrm{x})$. However, we will generally be interested in only the first few terms in the series which we can relate to important physical quantities. In order to obtain expressions for these quantities, the sum (11) is substituted into equation (6). The operators in equation (6) may be applied term by term to the series. For example,

$$\nabla H(\mathrm{x},\omega) = e^{-\sqrt{-i\omega}\sigma(\mathrm{x})} \sum_{n=0}^{\infty} \frac{\nabla A_n(\mathrm{x})}{(\sqrt{-i\omega})^n} \tag{12}$$

$$-\sqrt{-i\omega}\nabla\sigma(\mathrm{x}) e^{-\sqrt{-i\omega}\sigma(\mathrm{x})} \sum_{n=0}^{\infty} \frac{A_n(\mathrm{x})}{(\sqrt{-i\omega})^n}$$

and similarly for $\nabla^2 = \nabla \cdot \nabla$. Thus, substituting expansion (11) into equation (6) produces an expression with an infinite number of terms. Each term will contain $\sqrt{-i\omega}$ to some order and we may consider the sets of terms for any given order. In the next two subsections we consider the two terms of order $(\sqrt{-i\omega})^2$ and $\sqrt{-i\omega}$ respectively.

### The eikonal equation and the arrival time of the maximum drawdown

For terms of highest order in $\sqrt{-i\omega}$, those of order $(\sqrt{-i\omega})^2$, we have the equation

$$i\omega\nabla\sigma(\mathrm{x}) \cdot \nabla\sigma(\mathrm{x}) A_0(\mathrm{x}) - i\omega\Delta(\mathrm{x}) A_0(\mathrm{x}) = 0. \tag{13}$$

Assuming that $A_0(\mathrm{x})$ and $\omega$ are non-vanishing, we find

$$\nabla\sigma(\mathrm{x}) \cdot \nabla\sigma(\mathrm{x}) - \Delta(\mathrm{x}) = 0. \tag{14}$$

Equation (14), known as the eikonal equation, governs many types of propagation processes [Kline and Kay, 1965; Kravtsov and Orlov, 1990] and there are efficient numerical methods for its solutions [Sethian, 1996]. The eikonal equation relates the function $\sigma(\mathrm{x})$ to the flow properties, as contained in $\Delta(\mathrm{x})$.

A physical interpretation of $\sigma(\mathrm{x})$ is obtained if we consider the zero-th order term in expansion (11)

$$H(\mathrm{x},\omega) = A_0(\mathrm{x})e^{\sqrt{-i\omega}\sigma(\mathrm{x})}. \tag{15}$$

Taking the inverse Fourier transform with respect to $\omega$ produces the time domain expression

$$h(\mathrm{x},t) = A_0(\mathrm{x})\frac{\sigma(\mathrm{x})}{2\sqrt{\pi t^3}}e^{-\sigma^2(\mathrm{x})/4t} \tag{16}$$

[Virieux et al., 1994]. At a fixed position, x, the drawdown is a maximum when

$$\frac{\partial h(\mathrm{x},t)}{\partial t} = e^{-\sigma^2(\mathrm{x})/4t}\left(-\frac{3}{2\sqrt{t^5}} + \frac{\sigma^2(\mathrm{x})}{4\sqrt{t^7}}\right) \tag{17}$$

vanishes, when $6t = \sigma^2(\mathrm{x})$. Hence, for an impulsive source the peak drawdown occurs at time $\sigma^2(\mathrm{x})/6$. For this reason $\sigma(\mathrm{x})$ is referred to as the pseudo-phase, a type of travel time. Equation (14) is a statement that the travel time is a function of $\Delta(\mathrm{x})$, the inverse of the medium diffusivity. This relationship between the arrival time of a pressure pulse and $\Delta(\mathrm{x})$ has also been noted by Oliver [1994] in the context of pressure inversion. We should emphasize that $\sigma(\mathrm{x})$ is associated with the propagating front of peak drawdown and does not necessarily represent a surface of equal drawdown. The spatially varying quantity $A_0(\mathrm{x})$ will generally ensure that the amplitude of the peak drawdown observed at various positions will differ. For some situations, such as a homogeneous medium, the surfaces of equal drawdown and peak drawdown at a given time may coincide.

Surfaces defined by constant $\sigma(\mathrm{x})$ designate positions in space at which the peak drawdown occurs at time $\sigma^2(\mathrm{x})/6$. For the moment, we shall work with $\tau = \sqrt{t}$ as our primary temporal measure. Consider the surface defined by $\tau = \sigma(\mathrm{x})/\sqrt{6}$. The normals to this iso-surface are given by $\nabla\sigma(\mathrm{x})$ and we may define the normal vector $\mathrm{p} = \nabla\sigma(\mathrm{x})$.

Note, from equation (14) we see that the magnitude of p is given by

$$|\mathrm{p}| = \sqrt{\Delta(\mathrm{x})}. \tag{18}$$

A point $\mathrm{s} = (s_1, s_2, s_3)$ on the iso-surface traces out a curve as $\tau = \sqrt{t}$ is varied. The tangent vector to this curve is proportional to the normal to the iso-surface

$$\frac{d\mathrm{s}}{d\tau} = \epsilon \mathrm{p} \tag{19}$$

for some scaling factor $\epsilon$. The shape of the surface is not influenced by the scaling factor $\epsilon$.

As outlined in Appendix A, we compute the trajectories by solving the following system of ordinary differential equaionts

$$\frac{d\mathrm{s}}{d\tau} = \mathrm{p} \tag{20}$$

$$\frac{d\mathrm{p}}{d\tau} = \nabla\left[\Delta(\mathrm{x})\right]. \tag{21}$$

Equations (20) and (21) are also subject to a set of boundary conditions. Usually, the constraints are provided by the requirement that the pressure change start at the source point $\mathrm{x}_s$ and end at another specified point, say y. That is, we have the end-points conditions

$$\mathrm{s}(0) = \mathrm{x}_s \quad \mathrm{s}(1) = \mathrm{y} \tag{22}$$

for a path starting at $\tau = 0$ and ending at $\tau = 1$. The above equations are integrated numerically to arrive at the path $\mathrm{s}(\tau)$. Note that the trajectories are generally not straight lines. Rather, they are curves in three-dimensional space.

In our treatment of the peak arrival time and amplitude, the calculations are simpler if we adopt a coordinate system based upon the trajectories or rays. That is, assuming that the trajectories have already been defined by numerically integrating equations (20)-(22), we take one coordinate, say $s$, along the raypath. The other two components are taken to lie within the appropriate iso-surface defined by $\sigma(\mathrm{x})$. Our

coordinate system is now curvilinear rather than Cartesian, but it is better suited for numerical computation. For example, in these coordinates $\sigma(\mathbf{x})$ only varies with $s$ and $\nabla\sigma$ and $\mathbf{p}$ are tangent to the $s$ coordinate curve. Thus, the $\nabla\sigma = d\sigma/ds$ and from equation (14) we find

$$\frac{d\sigma}{ds} = \sqrt{\Delta(s)} \tag{23}$$

or, remembering that $\sqrt{t} = \sigma/\sqrt{6}$,

$$\sqrt{T(\mathbf{x}_r)} = \frac{\sigma}{\sqrt{6}} = \frac{1}{\sqrt{6}} \int_\Sigma \sqrt{\Delta(s)} ds \tag{24}$$

where $T(\mathbf{x}_s)$ is the travel time from the source to the observation point $\mathbf{x}_s$ and $\Sigma$ is the trajectory from the source to the observation point. This integral relates the square root of the arrival time of the peak drawdown directly to flow properties, $\Delta(s)$, integrated along the trajectory $\Sigma$. Equation (24) is a result of our high-frequency assumption. That is, we are assuming that the permeability and porosity vary smoothly with respect to the spatial wavelength of the propagating pulse.

### The transport equation for the amplitude variation of drawdown

Now consider terms of order $\sqrt{-i\omega}$ in the asymptotic expansion. We find, after making use of equation (14), the following relationship between $\sigma(\mathbf{x})$ and $A_0(\mathbf{x})$

$$\nabla \cdot \nabla\sigma(\mathbf{x}) A_0(\mathbf{x}) + 2\nabla\sigma(\mathbf{x}) \cdot \nabla A_0(\mathbf{x}) \tag{25}$$

$$+\Lambda(\mathbf{x}) \cdot \nabla\sigma(\mathbf{x}) A_0(\mathbf{x}) = 0.$$

For a uniform medium, $\Lambda(\mathbf{x}) = 0$, this expression reduces to the standard transport equation treated in geometrical optics, electromagnetics, and seismology [Klein and Kay, 1965; Kravtsov and Orlov, 1990; Fatemi et al., 1995]. In order to integrate equation (25) let us introduce the variable $\gamma$ such that

$$d\gamma = \frac{ds}{\sqrt{\Delta(\mathbf{x})}} \tag{26}$$

and the unit vector l which points along $\nabla\sigma$. Then, $\nabla\sigma = \sqrt{\Delta(\mathbf{x})}\mathbf{l}$ and

$$\mathbf{l}\cdot\nabla = \frac{d}{ds} \tag{27}$$

and we may write

$$\nabla\sigma\cdot\nabla A_0 = \sqrt{\Delta(\mathbf{x})}\mathbf{l}\cdot\nabla A_0 = \sqrt{\Delta(\mathbf{x})}\frac{dA_0}{ds}$$
$$= \sqrt{\Delta(\mathbf{x})}\frac{dA_0}{d\gamma}\frac{d\gamma}{ds} = \frac{dA_0}{d\gamma}.$$

Similarly,

$$\mathbf{\Lambda}\cdot\nabla\sigma A_0 = \frac{\nabla K}{K}\cdot\mathbf{l}\sqrt{\Delta(\mathbf{x})}A_0 = \sqrt{\Delta(\mathbf{x})}\frac{A_0}{K}\frac{dK}{ds}$$
$$= \sqrt{\Delta(\mathbf{x})}\frac{A_0}{K}\frac{dK}{d\gamma}\frac{d\gamma}{ds} = \frac{A_0}{K}\frac{dK}{d\gamma}.$$

Equation (25) may be rewritten as an ordinary differential equation along the trajectory $\Sigma$

$$\nabla\cdot\nabla\sigma(\mathbf{x})A_0(\mathbf{x}) + 2\frac{dA_0}{d\gamma} + \frac{A_0}{K}\frac{dK}{d\gamma} = 0 \tag{28}$$

or

$$2\frac{d\ln(A_0)}{d\gamma} + \frac{d\ln(K)}{d\gamma} + \nabla\cdot\nabla\sigma = 0. \tag{29}$$

We may integrate equation (29) along the trajectory from $\gamma_0$ to $\gamma$

$$A_0(\gamma) = A_0(\gamma_0)\sqrt{\frac{K(\gamma_0)}{K(\gamma)}}\exp\left(-\frac{1}{2}\int_{\gamma_0}^{\gamma}\nabla\cdot\nabla\sigma d\gamma\right) \tag{30}$$

where $A_0(\gamma_0)$ is the initial pressure amplitude at the source and $K(\gamma_0)$ is the conductivity at the source. Note, when the medium is homogeneous $K(\gamma_0) = K(\gamma)$ and $\sqrt{K(\gamma_0)/K(\gamma)} = 1$. Based upon geometrical considerations and Gauss's divergence theorem, the integrand in equation (30) may be reduced to

$$\nabla\cdot\nabla\sigma = \frac{d}{d\gamma}\ln[\sqrt{\Delta(\gamma)}J(\gamma)], \tag{31}$$

where $J(\gamma)$ is the Jacobian which measures the expansion of the pressure front along the trajectory. Derivations are given in many books on geometrical optics and ray

theory [Kline and Kay, 1965, p. 156; Kravtsov and Orlov, 1990, p. 22]. Substituting the expression (31) into equation (30) produces

$$A_0(\gamma) = A_0(\gamma_0)\sqrt{\frac{K(\gamma_0)}{K(\gamma)}}\frac{\sqrt{\sqrt{\Delta(\gamma_0)}J(\gamma_0)}}{\sqrt{\sqrt{\Delta(\gamma)}J(\gamma)}}. \tag{32}$$

This equation describes the evolution of the amplitude along the trajectory in terms of quantities at the source and properties along the path $\Sigma$. The Jacobian is calculated during ray tracing, based upon the divergence of a bundle of rays with distance along $\Sigma$ [Kravtsov and Orlov, 1990]. That is, a family of trajectories are constructed and the change in distance between rays as a function of raylength is used to estimate the Jacobian.

Let us collect all factors depending on source properties into a single source term

$$I(\gamma_0) = A_0(\gamma_0)\sqrt{K(\gamma_0)}\sqrt{\sqrt{\Delta(\gamma_0)}J(\gamma_0)}. \tag{33}$$

Thus, we may write the amplitude as

$$A_0(\gamma) = \frac{I(\gamma_0)}{\sqrt{K(\gamma)\sqrt{\Delta(\gamma)}J(\gamma)}}, \tag{34}$$

resulting in the frequency domain expression for pressure

$$H(\gamma,\omega) = \frac{I(\gamma_0)}{\sqrt{K(\gamma)\sqrt{\Delta(\gamma)}J(\gamma)}}e^{\sqrt{-i\omega}\sigma(\gamma)} \tag{35}$$

at position $\gamma$ along the ray. Transforming back to the time domain and expressing the quantities as functions of length $s$ along $\Sigma$, the trajectory in equation (24),

$$h(s,t) = \frac{I(s_0)}{\sqrt{K(s)\sqrt{\Delta(s)}J(s)}}\frac{\sigma(s)}{2\sqrt{\pi t^3}}e^{-\sigma^2(s)/4t} \tag{36}$$

where, $\sigma(s)$ is the integral

$$\sigma(s) = \int_{s_0}^{s}\sqrt{\Delta(s')}ds'. \tag{37}$$

**Step-function source.** The solution (36) corresponds to an impulse (delta function) source. For a general source this solution must be convolved with the source time function. A temporal convolution corresponds to multiplication in the frequency domain. For our numerical tests and field application we shall be interested in a step function (Heaviside) source, in which pumping commences at time zero and continues at a constant rate. Then the frequency domain expression corresponding to equation (35) is given by

$$H(\gamma,\omega) = \frac{I(\gamma_0)}{\sqrt{K(\gamma)\sqrt{\Delta(\gamma)}J(\gamma)}} e^{\sqrt{-i\omega}\sigma(\gamma)} \mathcal{H}(\omega) \tag{38}$$

where $\mathcal{H}(\omega)$ denotes the Fourier transform of the step function. In the application we shall work with changes in pressure over a small time increment, the temporal derivative of the pressure. In the frequency domain this corresponds to multiplication by $i\omega$ [Bracewell, 1978]

$$H'(\gamma,\omega) = i\omega \frac{I(\gamma_0)}{\sqrt{K(\gamma)\sqrt{\Delta(\gamma)}J(\gamma)}} e^{\sqrt{-i\omega}\sigma(\gamma)} \mathcal{H}(\omega) \tag{39}$$

where the prime signifies the Fourier transform of the derivative of the pressure. We can move the $i\omega$ onto the $\mathcal{H}(\omega)$ term and use the fact that the derivative of a step function is an impulse to arrive at

$$\frac{dh}{dt} = \frac{I(s_0)}{\sqrt{K(s)\sqrt{\Delta(s)}J(s)}} \frac{\sigma(s)}{2\sqrt{\pi t^3}} e^{-\sigma^2(s)/4t} \tag{40}$$

which is of the same form as equation (36).

## Arrival Time and Amplitude Sensitivities

In performing an inversion for reservoir properties we need to relate changes or perturbations in flow properties to variations in the predicted responses. For example, how do changes in reservoir storage and conductivity lead to deviations in head? For small deviations in properties we may use a perturbation approach to calculate the

resulting changes in observed quantities. That is, we consider a perturbation to some background model. The background reservoir structure is characterized by the spatial distribution of hydraulic conductivity $K^0(\mathrm{x})$ and storage $S^0(\mathrm{x})$. If we perturb these quantities

$$K(\mathrm{x}) = K^0(\mathrm{x}) + \delta K(\mathrm{x})$$

and

$$S(\mathrm{x}) = S^0(\mathrm{x}) + \delta S(\mathrm{x})$$

the distribution of $H(\mathrm{x},\omega)$ will also change

$$H(\mathrm{x},\omega) = H^0(\mathrm{x},\omega) + \delta H(\mathrm{x},\omega).$$

**Arrival Time Sensitivities.** The simplest sensitivities are those relating the arrival time of the maximum drawdown, due to an impulsive source, to reservoir storage and conductivity. The relationship between these quantities is given by equation (24). In actual field practice we will not have an impulsive pressure source. Rather, the source will likely be a step function in which the flow rate discontinuously jumps from zero to some finite value. There are several ways to derive the appropriate equation for this situation. Consider equation (1) with an additional step function source term on the right-hand-side. Because of the linearity of equation (1), we could simply differentiate equation (1) with respect to time. The form of the equation remains the same except that it is now an equation in the time derivative of head and the source term is now an impulse function. Thus, all the preceding derivations up to and including equation (24) hold, but for the time derivative of head. Alternatively, as in equations (38)-(40), we could follow through with the Fourier transform of the step function and transfer the $i\omega$ onto the step function to arrive at equation (40). Then, as in (17), we could differentiate (40) to produce the expression (24) relating the arrival time of the peak slope to the integral of $\Delta(s)$ over the trajectory.

The basic idea is that, for a step-function source there is no well defined arrival time. Because pressure behaves diffusively, the head will gradually increase with time (Figure 1a). However, as indicated in equation (17), for a step-function source we can define the arrival time of the maximum slope (Figure 1b), which is related to reservoir properties by equation (24). From equations (5) and (24) we may compute the sensitivity associated with the square root of the arrival time to changes in storage

$$\frac{\partial\sqrt{T}}{\partial S(\mathrm{x})} = \frac{\sqrt{\Delta(\mathrm{x})}}{S(\mathrm{x})} \tag{41}$$

and conductivity

$$\frac{\partial\sqrt{T}}{\partial K(\mathrm{x})} = -\frac{\sqrt{\Delta(\mathrm{x})}}{K(\mathrm{x})}. \tag{42}$$

Hence, a perturbation in arrival time is related to perturbations in $S(\mathrm{x})$ and $K(\mathrm{x})$ by

$$\delta\sqrt{T} = \int_{\Pi} \left[ \frac{\sqrt{\Delta(s)}}{S(s)}\delta S(s) - \frac{\sqrt{\Delta(s)}}{K(s)}\delta K(s) \right] ds \tag{43}$$

where $\Pi$ is the trajectory between the pumping and observing boreholes. Note, the sensitivity in a homogeneous medium is uniform between the pumping and observing well. Unlike pressure amplitudes, the arrival times are not dominated by structure in the vicinity of the boreholes. As in medical and geophysical imaging, we may adopt a tomographic approach in order to invert the arrival times. Some initial reservoir model is assumed and the trajectories are traced through the model. By backprojecting the arrival time anomalies along the trajectories, we may estimate variations in storage and conductivity between the boreholes. A more detailed account of this approach will be given in the numerical illustration below.

**Amplitude Storage Sensitivities.** Now, we shall consider the effect of a perturbation in storage on head amplitudes. As shown in the Appendix B, we may relate this to the change in head, $\delta H(\mathrm{x},\omega)$,

$$\delta H(\mathrm{x},\omega) = i\omega \int G(\mathrm{x},\mathrm{y},\omega) H^0(\mathrm{y},\omega)\delta S(\mathrm{y}) d\mathrm{y} \tag{44}$$

where $G(\mathrm{x},\mathrm{y},\omega)$ is a Green's function solution of equation (6) [Stakgold, 1979], with respect to the background medium. The sensitivity, the coefficient relating the perturbations in $S(\mathrm{y})$ to changes in $H(\mathrm{x},\omega)$, is $i\omega G(\mathrm{x},\mathrm{y},\omega)H^0(\mathrm{y},\omega)$. Implicit in the term $H^0(\mathrm{y},\omega)$ is the temporal variation of the source and as well as its location. Using the asymptotic expressions for $G(\mathrm{x},\mathrm{y},\omega)$ and $H^0(\mathrm{y},\omega)$, as in Appendix B, we find a time domain expression for (44),

$$\delta h(\mathrm{x},t) = \int \Pi_S(\mathrm{y},\mathrm{x},t)\delta S(\mathrm{y})d\mathrm{y} \tag{45}$$

where

$$\Pi_S(\mathrm{y},\mathrm{x},t) = A_0(\mathrm{x_s},\mathrm{x})\frac{\sigma(\mathrm{x}_s,\mathrm{x})}{2\sqrt{\pi t^3}}e^{-\sigma^2(\mathrm{x}_s,\mathrm{x})/4t} \tag{46}$$

and

$$A_0(\mathrm{x_s},\mathrm{x}) = A_0(\mathrm{x}_s,\mathrm{y}) \times A_0(\mathrm{y},\mathrm{x}) \tag{47}$$

$$\sigma(\mathrm{x_s},\mathrm{x}) = \sigma(\mathrm{x}_s,\mathrm{y}) + \sigma(\mathrm{y},\mathrm{x}). \tag{48}$$

The quantities $A_0(\mathrm{x_s},\mathrm{x})$ and $\sigma(\mathrm{x_s},\mathrm{x})$ represent the amplitude and phase, respectively, for the propagation of the pressure from the source ($\mathrm{x}_s$) to the point y and then from the point y to the receiver at x [see Appendix B].

**Amplitude Conductivity Sensitivities.** As shown in the Appendix B, a perturbation in hydraulic conductivity is related to a change in head via the integral

$$\delta H(\mathrm{x},\omega) = -2\int \nabla G(\mathrm{x},\mathrm{y},\omega)\cdot\nabla H^0(\mathrm{y},\omega)\delta K(\mathrm{y})d\mathrm{y}. \tag{49}$$

The time domain equivalent of equation (49) is

$$\delta h(\mathrm{x},t) = \int \Pi_K(\mathrm{y},\mathrm{x},t)\delta K(\mathrm{y})d\mathrm{y} \tag{50}$$

where

$$\Pi_K(\mathrm{y},\mathrm{x},t) = \mathcal{I}(\mathrm{x_s},\mathrm{x})A_0(\mathrm{x_s},\mathrm{x})\frac{\sigma(\mathrm{x}_s,\mathrm{x})}{2\sqrt{\pi t^3}}e^{-\sigma^2(\mathrm{x}_s,\mathrm{x})/4t} \tag{51}$$

the terms $A_0(\mathrm{x_s},\mathrm{x})$ and $\sigma(\mathrm{x}_s,\mathrm{x})$ are defined in (47) and (48), and

$$\mathcal{I}(\mathrm{x_s},\mathrm{x}) = -2\nabla\sigma(\mathrm{x}_s,\mathrm{y})\cdot\nabla\sigma(\mathrm{y},\mathrm{x}). \tag{52}$$

## Numerical Illustration

In this section the asymptotic storage and conductivity sensitivities, given by equations (45) and (50), are compared to sensitivities calculated using a purely numerical approach. In addition, the two-step approach (arrival times/amplitudes) to inverting transient head data is illustrated using a set of synthetic head values, generated by a known permeability distribution.

### Sensitivities

As a test of our asymptotic approach for estimating head amplitude sensitivities we compared our values with sensitivities produced by a numerical reservoir simulator. Sensitivities are derived from the simulator using a numerical perturbation technique in which values in successive cells are perturbed by 0.1 percent. That is, a uniform structure of 100 mD and a porosity of 0.1 serves as our background model. The numerical model is represented on a 21 by 21 grid of cells. We cycle through the grid, perturbing one cell at a time. Thus, a total of 441 forward runs are required to estimate the storage sensitivities. An additional 441 runs are needed to calculated the conductivity sensitivities. The full transient flow problem must be solved for each cell. The resulting storage and conductivity sensitivities are displayed in Figures 3 and 4, respectively. These numerical calculations are compared to sensitivities based upon our asymptotic expressions in equations (45) and (50).

In Figure 3 storage sensitivities are given for head measurements at 0.2, 0.4, and 0.9 days. Overall, there is excellent agreement between the numerical and asymptotic sensitivities, both in amplitude and pattern. The sensitivity coefficients are all negative, increasing storage decreases the observed drawdown. In general, we find peak sensitivities centered on both the pumping and the observing wells. The two wells are the focii of a roughly elliptical region in which the sensitivity is non-zero. The size of this elliptical area grows with time but the general pattern does not change significantly.

The patterns in Figure 3 are very much like those published previously by Oliver [1993].

Because the sensitivities are so similar over time, taking many measurements does not necessarily translate into a large number of independent constraints. Rather, there is considerable redundancy in a set of head observations. This does not imply that there is no value in head measurements over long periods. From equation (3), the pressure equation in the frequency domain, we see that when $\omega$ is small there is increased sensitivity to conductivity and decreased sensitivity to storage. Thus, the long wavelength component of the transient curve contains useful information. However, the similarity in sensitivities with time does imply that dense sampling over the entire observation period may not be necessary.

Numerical and asymptotic conductivity sensitivities are shown in Figure 4. Again, the patterns and amplitudes agree quite well. However, the degree of similarity is somewhat less than it was for the storage sensitivities (Figure 3). There is an additional approximation in the conductivity sensitivities associated with deriving equation (51). Terms of lower order in $\omega$ were neglected in the expression for the inner product of $\nabla G(\mathrm{x},\mathrm{y},\omega)$ and $\nabla H(\mathrm{y},\omega)$. Regardless, the similarity between the conductivity sensitivities in Figure 4, and the similarity of these sensitivities to those obtained previously [Oliver, 1993; Vasco et al., 1997], is sufficient for their use in the inversion scheme described next.

### Inversion of pressure values

As a demonstration of our two-step inversion approach we have constructed a set of synthetic head values. The values were obtained by simulating three interference tests in a single layer reservoir model. The test structure, shown in Figure 5, contains a 300% variation in permeability. On average, permeabilities are lower to the west and higher to the east. The lowest values are located in the northwestern quadrant of our model. The pumping and observing boreholes are configured in a three by three

grid pattern (Figure 5). Three interference tests were simulated in which three wells, those centered in the north-south direction, pumped at distinct times. For each episode of pumping six adjacent observation wells recorded head variations for 1.4 days. As an example, consider the first test in which fluid was injected into the westernmost borehole at X=50M, Y=225M. Head variations were simulated for all wells lying to the east of this borehole. The results of this first test are given in Figure 6. In this figure we present both the transient head values as well as the changes in head over the given time intervals, an estimate of the slope.

**Arrival time matching.** The peak slope of the head variation, the ratio of the head difference over the respective time increment, is used to estimate arrival times for the initial stage of the inversion. Specifically, we take the square root of the arrival time associated with the peak slope for each transient curve in Figure 6. Given an initial estimate of reservoir structure, in this case a uniform layer with a permeability of 70 mD, we predict the arrival time of the peak slope, Figure 7. The residual is the difference between the observed and calculated times, $\delta\sqrt{T}$, which is related to perturbations in reservoir parameters via expression (43). For the case at hand, only perturbations in conductivity are considered and equation (43) reduces to

$$\delta\sqrt{T} = -\int_{\Sigma} \frac{\sqrt{\Delta(s)}}{K(s)} \delta K(s) ds \tag{53}$$

In general, there will be a trade-off between storage and conductivity which is difficult to resolve. One possibility is to consider low frequency variations in head, variations associated with small $\omega$. Such variations are primarily sensitivity to conductivity as is evident in equation (3). Thus, by cycling between high and low frequency data it may be possible to resolve spatial variations in both conductivity and storage.

In order to use equation (53) to estimate variations in conductivity we first determine trajectories, the path of integration denoted by $\Sigma$, between the pumping and observing wells. This is accomplished by solving the ray equations (20)-(22) numerically

for the background model. Knowing the trajectory, we subdivide the reservoir into a 21 by 21 grid of cells and consider the segments of the path in each block. The integral (53) may then be approximated by a summation over the segments of the trajectory for the ($N = 441$) cells of our model. Thus, given background values for $S(s)$ and $K(s)$, equation (53) becomes a linear equation relating a perturbation in conductivity to a perturbation in the ith root arrival time

$$\delta\sqrt{T}_i = \sum_{j=1}^{N} M_{ij}\delta K_j ds \tag{54}$$

with the coefficient matrix $M_{ij}$ given by

$$M_{ij} = -\frac{\sqrt{\Delta_j}}{K_j}\delta s_{ij} \tag{55}$$

where $s_{ij}$ represents the length of trajectory $i$ in cell $j$ and $\Delta_j$ and $K_j$ are the values of $\Delta(\mathbf{x})$ and $K(\mathbf{x})$ in cell $j$. The quantity which we minimize is the sum of the squares of the residuals

$$||\delta\mathbf{d} - \mathbf{M}\delta\mathbf{K}|| = \sum_{i=1}^{M}\left(\delta\sqrt{T}_i - \sum_{j=1}^{N} M_{ij}\delta K_j\right)^2 \tag{56}$$

where $||\cdot||$ denotes the $L^2$ norm of a vector. For a set of transient head curves we will have an associated linear system of equations which we may solve for perturbations in conductivity. Because the system of equations is extremely sparse, this is efficiently accomplished using the LSQR algorithm of Paige and Saunders [1982]. Note that, due to the non-linearity of the inverse problem, we must iteratively solve the system for a series of perturbations to our initial model.

In addition to minimizing the misfit to the data we also included penalty terms to regularize (stabilize) the inversion. Inclusion of such penalty terms is standard practice for hydrological and geophysical inversions [Tarantola, 1987; Parker, 1994; Sun, 1994]. We include terms which penalize large parameters deviations and models which are not smoothly varying. The underlying motivation is that, in the absence of strong data constraints, we should like to stay close to our initial model. Also, because of the

smoothing nature of hydrologic data [Vasco et al., 1997], we do not expect to resolve rapid spatial variations in flow properties. We have described our particular approach elsewhere [Vasco et al., 1999] and will only outline the mechanics of the procedure here. The penalty terms most often take the form of quadratic functions on the set of models, for example model perturbation vector norm, the size of the perturbations, is measured by

$$||\delta \mathbf{K}|| = \sum_{j=1}^{N} (\delta K_j)^2 \tag{57}$$

and model roughness, a measure of spatial variability, is given by

$$||\mathbf{L}\delta \mathbf{K}|| = \sum_{j=1}^{N} (\nabla \delta K_j)^2 \tag{58}$$

where $\mathbf{L}$ is a spatial difference operator which computes the spatial gradient of the model by differencing adjacent block values [Parker, 1994]. Solving the regularized inverse problem entails finding those elements of $\delta \mathbf{K}$ which minimize the sum

$$||\delta \mathbf{d} - \mathbf{M}\delta \mathbf{K}|| + ||\delta \mathbf{K}|| + ||\mathbf{L}\delta \mathbf{K}||. \tag{59}$$

The necessary equations for a minimum are an augmented linear system

$$\begin{pmatrix} \mathbf{M} \\ \mathbf{I} \\ \mathbf{L} \end{pmatrix} \delta \mathbf{K} = \begin{pmatrix} \delta \mathbf{d} \\ \mathbf{0} \\ \mathbf{0} \end{pmatrix} \tag{60}$$

[Vasco et al., 1999].

In Figure 8a we show the mean squared arrival time error for ten iterations of the inversion. Each travel time iteration took approximately 0.5 CPU minutes, for a total computation time of 5 CPU minutes to complete the ten arrival time iterations. Some 21 CPU seconds were used to calculate the pressures and set up the system of equations for each iteration. The remaining time was spent in the solver, estimating the permeability deviations. The resulting permeability variations are indicated in Figure 9a. On comparison of this figure with Figure 5 we see that the large-scale spatial

variations in permeability are recovered in the arrival time inversion. In particular, the general pattern of higher conductivities to the east and lower conductivities to the west is reproduced in the inversion. Furthermore, the large low permeability area to the northwest is recovered in our arrival time model. The average amplitude of the variations are slightly smaller than those in Figure 5, but the amplitudes are generally more sensitive to details of the inversion, such as prior constraints or regularization.

**Amplitude matching.** The next stage of the inversion involves matching the amplitudes of the head variations. The arrival time matching has produced a starting model for this part of the inversion (Figure 9a). In our experience, the convergence of amplitude inversion algorithm is more sensitive to the starting model. Furthermore, amplitude matching is much more computationally intensive than is the arrival time inversion, and any reduction in the number of amplitude iterations is helpful. Therefore, it is a real advantage to have the arrival time result as a starting point. Even with the initial estimates provided by the arrival time inversion, some 20 amplitude iterations are required to match the transient head values (Figure 8b). Each amplitude inversion required almost 10 minutes of CPU time. Thus, the entire amplitude match took some 3 hours to complete. The resulting amplitude inversion, shown in Figure 9b, contains some details not seen in the arrival time inversion. In particular, there is a roughly north-south trough of low permeability in the western half of the model which is imaged. The size of the variations in permeability are closer to the amplitude of the heterogeneity seen in Figure 5. However, there are some smaller scale features in Figure 5 which are not observed in our result (Figure 9b). Because of the diffusive nature of pressure, such data are unable to resolve fine scale variations in reservoir properties [Vasco et al., 1997]. Additional information, such as tracer or multi-phase flow data may help in this regard. The final match to the transient head values is shown in Figure 10. For the most part the agreement is quite good, a significant improvement over the initial predictions (Figure 7). The pressure slope data is slightly under-estimated. This is due

to the inclusion of model norm and model roughness penalty terms in the inversion. Such terms bias the model towards a smoother solution with less overall variation. By exploring the range of penalty term weightings we can attempt to better fit the data with a somewhat rougher and higher amplitude model [Parker, 1994].

## Field Application: Interference Tests

We now apply our methodology to a pair of interference tests obtain at the Borehole Test Facility in Kay County Oklahoma. The facility, which is owned and operated by Conoco, contains five shallow (50 M) wells which are configured in a skewed five-spot pattern. The wells penetrate the Fort Riley, a fractured limestone between about 10 and 28 meters in depth. As part of a program developing geophysical and hydrological methods for detecting and characterizing natural fracture systems, Conoco and Berkeley Laboratory conducted a series of field experiments at the site. The experiments included a set of interference and tracer tests, both crosswell and single-well seismic surveys, and the drilling of a slant well to penetrate a suspected fracture. The results of this work are described by Majer et al. [1996] and D'Onfro et al. [1998].

The Fort Riley Limestone is part of the Lower Permian Chase Group which consists primarily of limestones and shales [Toomey, 1992]. The sediments in this region are, for the most part, flat lying with a regional dip of less than 1 degree. Two roughly orthogonal, near vertical, fracture sets have been mapped in the area, a dominant east-northeast set and a less pervasive north-northwest striking set [D'Onfro et al., 1998]. The Fort Riley Limestone itself has a low average permeability, ranging between 0.11 and 6.06 mD with an average of 1.23 mD. However, the presence of fractures is very likely to modify these laboratory estimates considerably.

The initial characterization effort was associated with the execution and interpretation of a series of interference tests at the Borehole Test Facility [Datta-Gupta et al., 1995]. The first test involved withdrawing groundwater from the westernmost

well (GW-5) at a constant rate of 2.3 L/min for approximately one day. The transient head variations are shown in Figure 11a. Rather surprisingly, the furthest borehole (GW-2) responded earlier and more vigorously than the others. A reciprocal test in which groundwater was withdrawn from well GW-2 at a rate of 1.8 L/min, produced a corresponding anomalous response from GW-5 (Figure 11b). This was the initial indication of significant reservoir heterogeneity at the facility. In order to estimate arrival times we construct estimates of the slope of the temporal variation in head (Figure 12) using differences. As is evident from the curves in Figure 11 the maximum slope travels faster between wells GW-2 and GW-5.

As a starting model for the two stage inversion we assume a background permeability of 1 mD, a value close to the estimated average matrix permeability. A background porosity 0.03 percent is also used and held constant in the inversion. In effect, because of the trade-off between storage and conductivity, we are solving for an equivalent permeability which may be scaled by some porosity variation. The background model roughly matches the head variations observed at wells other than GW-2 and GW-5. A two-dimensional, 21 (east-west) by 51 (north-south) grid of cells is used to represent the variations in conductivity. Starting from the background reservoir structure our inversion algorithm converged rather quickly, in just under ten iterations (Figure 13). The initial 5 iterations (0-4) are associated with matching the arrival times while the final iterations (5-9) involve amplitude matching. As is apparent in Figure 13, the arrival time iterations produce the bulk of the misfit reduction. In total, the arrival time iterations took less than three CPU minutes on a 200 MHz workstation. The ensuing amplitude match took approximately one hour and did not improve much on the pressure match or change the model significantly.

The permeability variations resulting from the inversion are indicated in Figure 14. The reservoir model is dominated by a linear, high permeability feature extending from the vicinity of well GW-2 to just above GW-5. The nature of the high permeability

structure agrees with the orientation of mapped fractures in the region. One satisfying feature of the solution in Figure 14 is the simplicity of the solution. Even though the inversion of the full data set contains sensitivities to permeabilities in all cells of the model, only a linear subset of blocks between GW-2 and GW-5 are required to have any significant variation. Previous efforts at matching these head variations did not produce such a simple structure [Datta-Gupta et al, 1995]. Rather, the reservoir model contained a complex arrangement of high and low permeabilities. The pattern of conductivities, which were derived using the stochastic simulated annealing algorithm, were sensitive to the initial permeability model [Datta-Gupta et al., 1995]. This sensitivity may be due in part to the fact that head amplitudes were matched directly, a highly non-linear procedure. We should note that a conjugate gradient algorithm produced a similar pattern of permeabilities, with the largest variations near the wells. The stochastic approach of Datta-Gupta et al. [1995] required extensive computation, upwards of 10,000 forward runs and more than 24 hours of CPU time.

We should note that seismic measurements and additional drilling both support a narrow, high conductivity structure just to the north of the central well (GW-3) of the five-spot [D'Onfro et al., 1998]. In particular, seismic crosswell experiments between wells the central well (GW-3), the northernmost well (GW-1), and the southernmost (GW-4), provide direct evidence for a fracture or fracture zone just to the north of GW-3 [Majer et al., 1996]. In these experiments air was injected into well GW-5 while a borehole pump in well GW-2 kept the water level below the Fort Riley Limestone (the unit thought to contain the fracture). There was a dramatic reduction in amplitude for seismic waves propagating to the north of GW-3 while those propagating to the south were relatively unaffected. In fact, energy reflected off a fracture to the north of GW-3 was detected. Examination of seismograms from a single-well experiment in GW-3 confirmed a reflection from a fracture near this well. The time delay of 3.5 ms associated with the reflection implies that the fracture is approximately 14 meters north of GW-3.

This location is in very good agreement with the location of our high conductivity feature (Figure 14). The final, most conclusive evidence for a narrow conductive feature to the north of GW-3 is provided by a slant well which was recently drilled into the Fort Riley Limestone [D'Onfro et al., 1998]. Commercial air drilling equipment was used to actually penetrate the fracture. Indeed, a single, narrow fracture was recovered during coring at the targeted depth (Figure 15). A near vertical fracture, containing euhedral mineral crystals (indicating an open fracture), was observed. Recent well tests in the new slant well, in which air was injected into the observed fracture, resulted in water flowing out of both GW-2 and GW-5. This indicates a conductive flow path between the fracture and these wells. On the other hand, there was only a slight change in water level in the much nearer central well (GW-3). A more recent experiment supports the increased permeability in the western half of the fracture. Injection of water into the slant well blew the cap off well GW-5, while the water level in GW-2 only underwent a moderate change [Kurt Nihei, personnel communication]. Taken together, our head inversion, the geophysical observations and the well data provide compelling evidence for a narrow conductive fracture at the Borehole Test Facility.

## Conclusions

The asymptotic approach described here should complement existing techniques for inverting head observations. Some insight is offered by the methodology. In particular, the inverse problem partitions into an inverse problems for arrival times and an inverse problem for amplitudes. The arrival time is associated with the moment the peak slope in the transient head curve is observed at a particular borehole. The inversion of the arrival times is particularly efficient. Furthermore, in applications to both synthetic head values and actual field measurements we find that the inversion of the arrival times produces the largest misfit reductions. In just a few CPU minutes we are able to deduce reservoir models which match the observations. For the synthetic interference tests the

resulting model revealed the large scale variations that are present in the model used to generate the data. In the actual field case the reservoir model agrees with independent geophysical and borehole observations. The inversion of arrival times should work best in three-dimensional situations, where there are a large number of observation points and many interference tests. Such situations are likely to tax conventional methods for directly inverting head amplitudes.

Amplitude matching, even using the asymptotic approach, is still a fairly computationally intensive endeavor. For example, our implementation of the Born inversion of amplitudes is not significantly faster than some other current techniques [Carter et al., 1982]. However, there are enhancements which could substantially speed up our approach. Most computation is associated with the calculation of trajectories from the source to all cells of the model and from all cells to the observation wells. It turns out that the sensitivities associated with many cells are quite small and may be neglected. One possibility is to roughly estimate sensitivities using straight line paths between the cells and the wells. Then, sensitivities could be computed only for cells which have estimated values above some cutoff. This would be particularly helpful in three-dimensional problems. Alternatively, the paths could be recomputed after a specified number of iterations, rather than at every cycle. We are currently working on a perturbation approach for the inversion of amplitudes. The perturbation technique should significantly speed up the pressure amplitude inversion. Finally, our experience with both synthetic tests and field data indicates that the inversion of the travel times often succeeds in providing an approximate match to the amplitude values.

In our derivation and applications we have assumed a constant flow rate. A constant rate is not really necessary for application of the technique. Using an estimate of the flow rate one can convolve the times series with the sensitivity functions in order to invert the amplitudes. Alternatively, deconvolution could be used to remove the effects of the flow rate variation, either in the time or frequency domain.

In our current tests and application the permeability varied by one to two orders of magnitude. Future work is planned on testing the approach for contrasts of four or more orders of magnitude. Based on our experience using a similar formalism for solute transport [Vasco and Datta-Gupta, 1999] and multi-phase flow [Vasco et al., 1999; Vasco and Datta-Gupta, 2000], we anticipate that the asymptotic approach will work for contrasts of three or more orders of magnitude variation in flow properties.

# APPENDIX A: Computation of the Trajectories

The trajectories, defined by the normals to the iso-surfaces, are generally obtained by a procedure much like optical raytracing [Luneburg, 1966; Kline and Kay, 1965]. That is, a system of ordinary differential equations for the components of the trajectories s are derived. A trajectory, also known as a bi-characteristic [Luneburg, 1966, p. 25], is found by solving a system of ordinary differential equations in terms of the curve itself $\mathrm{s}(\tau)$ and its tangent vector $\mathrm{p}(\tau)$. Our development starts from equation (19) [with $\epsilon = 1$] and the eikonal equation (14). From equation (19) we have our first relationship between $\mathrm{s}(\tau)$ and $\mathrm{p}(\tau)$,

$$\frac{d\mathrm{s}}{d\tau} = \mathrm{p} \tag{A1}$$

A second set of relations may be derived by considering second derivatives of $\mathrm{s}(\tau)$. First, we shall make a slight modification in our notation for the trajectory in order to facilitate an identification of the path coordinates with the spatial variables. That is, we shall denote the components of $\mathrm{s} = (s_1, s_2, s_3)$ as $(x(\tau), y(\tau), z(\tau))$. Here $x, y, z$ are the variables of global coordinate system, we are just referencing the path to these variables. Now the second derivative of s becomes, under the above identification

$$\begin{aligned}\frac{d}{d\tau}\left(\frac{d\mathrm{s}}{d\tau}\right) &= \sigma_{xx}\frac{dx}{d\tau} + \sigma_{yx}\frac{dy}{d\tau} + \sigma_{zx}\frac{dz}{d\tau} \\ &= \sigma_{xx}\frac{ds_1}{d\tau} + \sigma_{yx}\frac{ds_2}{d\tau} + \sigma_{zx}\frac{ds_3}{d\tau}.\end{aligned} \tag{A2}$$

From equation (A1) and the fact that $\mathrm{p} = \nabla\sigma(\mathrm{x})$ we may write (A2) as

$$\begin{aligned}\frac{d}{d\tau}\left(\frac{d\mathrm{s}}{d\tau}\right) &= \sigma_{xx}\sigma_x + \sigma_{yx}\sigma_y + \sigma_{zx}\sigma_z \\ &= \frac{1}{2}\frac{\partial}{\partial x}\left({\sigma_x}^2 + {\sigma_y}^2 + {\sigma_z}^2\right).\end{aligned} \tag{A3}$$

Making use of the eikonal equation (14) we arrive at

$$\frac{d}{d\tau}\left(\frac{d\mathrm{s}}{d\tau}\right) = \frac{1}{2}\nabla\left[\Delta(\mathrm{x})\right]. \tag{A4}$$

From the relationship (A1) we have our second relationship

$$\frac{d\mathbf{p}}{d\tau} = \nabla\left[\Delta(\mathbf{x})\right]. \qquad (A5)$$

Equations (A1) and (A5) constitute a system of first-order ordinary differential equations for $\mathbf{s}(\tau)$ and $\mathbf{p}(\tau)$. These equations are subject to the two-point boundary condition that the trajectory start at the source point $\mathbf{x}_s$ and end at a particular location $\mathbf{y}$. We may solve the system of differential equations using numerical techniques such as shooting or bending methods [Keller, 1968]. In our applications we use an iterative shooting method with a bisection technique to solve the two-point problem.

In general, the trajectories are curves in three-dimensional space. Using arguments from the calculus of variations one may show that the trajectories are extremals [Luneburg, 1966; Kline and Kay, 1965]. That is, the trajectory corresponds to the path which minimizes the travel time, as given by (24). Note that the trajectories are generally not identified with streamlines [Datta-Gupta and King, 1995; King and Datta-Gupta, 1998].

# APPENDIX B: Sensitivity Computations

## Storage Sensitivities

Given an initial reservoir structure, characterized by $K^0(\mathrm{x})$ and $S^0(\mathrm{x})$, consider a model in which the storage coefficient is perturbed

$$S(\mathrm{x}) = S^0(\mathrm{x}) + \delta S(\mathrm{x}) \tag{B1}$$

there will be a corresponding change in the transformed hydraulic head, $H^0(\mathrm{x},\omega)$,

$$H(\mathrm{x},\omega) = H^0(\mathrm{x},\omega) + \delta H(\mathrm{x},\omega). \tag{B2}$$

Substituting expressions (B1) and (B2) into equation (3) produces the equation

$$\begin{aligned} &K^0(\mathrm{x})\nabla^2 H^0(\mathrm{x},\omega) + \nabla K^0(\mathrm{x})\cdot\nabla H^0(\mathrm{x},\omega) \\ &+K^0(\mathrm{x})\nabla^2\delta H(\mathrm{x},\omega) + \nabla K^0(\mathrm{x})\cdot\nabla\delta H(\mathrm{x},\omega) \\ &-i\omega S^0(\mathrm{x})\delta H(\mathrm{x},\omega) \\ &= i\omega S^0(\mathrm{x})H^0(\mathrm{x},\omega) + i\omega\delta S(\mathrm{x})H^0(\mathrm{x},\omega) \end{aligned} \tag{B3}$$

where the second order quantity $\delta S(\mathrm{x})\delta H(\mathrm{x},\omega)$ has been neglected. Because $H^0(\mathrm{x},\omega)$ satisfies equation (3), equation (B3) reduces to

$$\begin{aligned} &K^0(\mathrm{x})\nabla^2\delta H(\mathrm{x},\omega) + \nabla K^0(\mathrm{x})\cdot\nabla\delta H(\mathrm{x},\omega) \\ &-i\omega S^0(\mathrm{x})\delta H(\mathrm{x},\omega) = i\omega\delta S(\mathrm{x})H^0(\mathrm{x},\omega) \end{aligned} \tag{B4}$$

a partial differential equation for $\delta H(\mathrm{x},\omega)$. Note that equation (B4) is of the same form as equation (3) with the coefficients of the background medium, $K^0(\mathrm{x})$ and $S^0(\mathrm{x})$, but containing the source term $i\omega\delta S(\mathrm{x})H^0(\mathrm{x},\omega)$ on the right-hand-side. Therefore, given a Green's function solution for the background medium, that is, a solution of the equation for an impulsive source located at position y

$$K^0(\mathrm{x})\nabla^2 G(\mathrm{x},\mathrm{y},\omega) + \nabla K^0(\mathrm{x})\cdot\nabla G(\mathrm{x},\mathrm{y},\omega) \tag{B5}$$

$$-i\omega S^0(\mathrm{x})G(\mathrm{x},\mathrm{y},\omega) = \delta(\mathrm{x}-\mathrm{y}),$$

we may construct a solution of equation (B4). In particular, we may represent the solution of equation (B4) as the integral

$$\delta H(\mathrm{x},\omega) = i\omega \int G(\mathrm{x},\mathrm{y},\omega)H^0(\mathrm{y},\omega)\delta S(\mathrm{y})d\mathrm{y}. \qquad (B6)$$

This equation is a linear relation between a perturbation in reservoir storage $\delta S(\mathrm{y})$ and the change in the residual transformed head $\delta H(\mathrm{x},\omega)$. As such, it provides the sensitivities in the frequency domain, they are just the coefficients relating these perturbations, the quantity $i\omega G(\mathrm{x},\mathrm{y},\omega)H^0(\mathrm{y},\omega)$.

Up to this point we have not discussed the time variation of the source. The source-time function is contained in the background pressure field $H^0(\mathrm{y},\omega)$. In particular, we solve equation (3) for the coefficients of the background medium and a source term $F(\omega)$ on the right-hand-side. For our work we shall consider a step-function source because this best represents the source used in our field application. Furthermore, such sources are frequently used in many pump tests. Note also that the location of the source is implicitly contained in the background field term $H^0(\mathrm{y},\omega)$.

In order to calculate the sensitivities efficiently we now turn to our asymptotic solutions (36) and (40). As noted above, we shall assume that the time variation of our source is a step at time zero. As such, our asymptotic solution for the background head distribution is given by equation (38). Our Green's function solution is associated with an impulse or delta function source. As discussed previously, moving the $i\omega$ coefficient onto $H^0(\mathrm{y},\omega)$ corresponds to differentiating the step function source in the time domain. This converts the step function source to a delta function source. Thus, the expression associated with the delta function source, equation (36), may be used to calculate the sensitivities. Our specific asymptotic expressions for the terms in equation (B6) are of the form

$$G(\mathrm{x},\mathrm{y},\omega) = A_0(\mathrm{y},\mathrm{x})e^{\sqrt{-i\omega\sigma}(\mathrm{y},\mathrm{x})} \qquad (B7)$$

and

$$H^0(\mathrm{y},\omega) = A_0(\mathrm{x}_s,\mathrm{y})e^{\sqrt{-i\omega}\sigma(\mathrm{x}_s,\mathrm{y})} \qquad (B8)$$

as given in equation (15). The amplitude term $A_0(\mathrm{y},\mathrm{x})$ represents propagation from the internal position y to the observation point x. Similarly, $A_0(\mathrm{x}_s,\mathrm{y})$ denotes amplitude changes associated with propagation from the source $\mathrm{x}_s$ to the internal position y. One may think of y as denoting the location of an imaginary source, a source producing a perturbation in head equivalent to that produced by the perturbation in storage at that point. Our notation for $\sigma(\mathrm{y},\mathrm{x})$ is similar, it represents the integral of equation (37) along the trajectory from internal point y to observation point x. According to equation (B6), the sensitivities are the result of multiplying expressions (B7) and (B8), producing

$$\Pi_S(\mathrm{y},\mathrm{x},\omega) = A_0(\mathrm{x_s},\mathrm{x})e^{\sqrt{-i\omega}\sigma(\mathrm{x}_s,\mathrm{x})} \qquad (B9)$$

where

$$A_0(\mathrm{x_s},\mathrm{x}) = A_0(\mathrm{x}_s,\mathrm{y}) \times A_0(\mathrm{y},\mathrm{x}) \qquad (B10)$$

and

$$\sigma(\mathrm{x_s},\mathrm{x}) = \sigma(\mathrm{x}_s,\mathrm{y}) + \sigma(\mathrm{y},\mathrm{x}). \qquad (B11)$$

The time domain expression for the sensitivities is the inverse Fourier transform of (B9), given by

$$\Pi_S(\mathrm{y},\mathrm{x},t) = A_0(\mathrm{x_s},\mathrm{x})\frac{\sigma(\mathrm{x}_s,\mathrm{x})}{2\sqrt{\pi t^3}}e^{-\sigma^2(\mathrm{x}_s,\mathrm{x})/4t}. \qquad (B12)$$

The time domain equivalent of equation (B6) is

$$\delta h(\mathrm{x},t) = \int \Pi_S(\mathrm{y},\mathrm{x},t)\delta S(\mathrm{y})d\mathrm{y}. \qquad (B13)$$

We can summarize what these expressions represent in words and a picture (Figure 2). In order to calculate the sensitivities due to perturbations in storage we construct a trajectory from the source to the perturbation location. The amplitude, $A_0(\mathrm{x}_s,\mathrm{y})$, and phase, $\sigma(\mathrm{x}_s,\mathrm{y})$, effects of this propagation are calculated along the trajectory. A similar

calculation is conducted from the perturbation to the observation point, $A_0(\mathrm{y},\mathrm{x})$. In Figure 2 we draw the trajectories from the pumping and observing wells to a vertical line of points in a two-dimensional model. Along these trajectories, the amplitude and phase terms are combined according to equations (48) and (49), respectively. As shown below, in many regions the sensitivities are essentially zero. One could use an approximate estimate of the propagated values to eliminate certain cells in the calculations, reducing the overall computation.

### Conductivity Sensitivities

We now consider a slight change in reservoir hydraulic conductivity

$$K(\mathrm{x}) = K^0(\mathrm{x}) + \delta K(\mathrm{x}) \tag{B14}$$

and derive an expression for the change in $H(\mathrm{x},\omega)$

$$H(\mathrm{x},\omega) = H^0(\mathrm{x},\omega) + \delta H(\mathrm{x},\omega). \tag{B15}$$

As for the storage coefficient perturbation, we substitute (B14) and (B15) into equation (3). Again, neglecting second order quantities and making use of the fact that $H^0(\mathrm{x},\omega)$ satifies equation (3) for the background medium we arrive at the differential equation for $\delta H(\mathrm{x},\omega)$

$$\begin{aligned} K^0(\mathrm{x})\nabla^2\delta H(\mathrm{x},\omega) + \nabla K^0(\mathrm{x})\cdot\nabla\delta H(\mathrm{x},\omega) \\ -i\omega S^0(\mathrm{x})\delta H(\mathrm{x},\omega) \\ = -\delta K(\mathrm{x})\nabla\cdot\nabla H^0(\mathrm{x},\omega) - \nabla[\delta K(\mathrm{x})]\cdot\nabla H^0(\mathrm{x},\omega). \end{aligned} \tag{B16}$$

This equation is of the same form as equation (B4). That is, it has the mathematical structure of equation (3) but with the background distributions of storage $S^0(\mathrm{x})$ and hydraulic conductivity $K^0(\mathrm{x})$. Note that the source terms on the right-hand-side are different from that of equation (B4). It is still possible to express $\delta H(\mathrm{x},\omega)$ in an integral

form, though the representation is somewhat more complicated than equation (B6)

$$\delta H(\mathrm{x},\omega) = -\int G(\mathrm{x},\mathrm{y},\omega)\nabla\cdot\nabla H^0(\mathrm{y},\omega)\delta K(\mathrm{y})d\mathrm{y}$$

$$-\int G(\mathrm{x},\mathrm{y},\omega)\nabla H^0(\mathrm{y},\omega)\cdot\nabla[\delta K(\mathrm{y})]d\mathrm{y}. \qquad (B17)$$

Treating the terms in the integrands as distributions we may transfer the gradients from both $\nabla H^0(\mathrm{y},\omega)$ and $\delta K(\mathrm{y})$ onto $G(\mathrm{x},\mathrm{y},\omega)$. The resulting expression is

$$\delta H(\mathrm{x},\omega) = -2\int \nabla G(\mathrm{x},\mathrm{y},\omega)\cdot\nabla H^0(\mathrm{y},\omega)\delta K(\mathrm{y})d\mathrm{y}. \qquad (B18)$$

Thus, the component terms in the integrand are gradients of the terms in the integrand of (B6). In addition, expression (B6) contains a factor of $i\omega$ representing a temporal derivative in the time domain.

As we did for porosity we may use our asymptotic expressions for the Green's function and the head field. In particular, we have the impulse source solution (35) which represents the Green's function, which we write as

$$G(\mathrm{x},\mathrm{y},\omega) = A_0(\mathrm{y},\mathrm{x})e^{\sqrt{-i\omega}\sigma(\mathrm{y},\mathrm{x})} \qquad (B19)$$

We compute the gradient of this term

$$\nabla G(\mathrm{x},\mathrm{y},\omega) = \nabla A_0(\mathrm{y},\mathrm{x})e^{\sqrt{-i\omega}\sigma(\mathrm{y},\mathrm{x})} \qquad (B20)$$

$$+\sqrt{-i\omega}A_0(\mathrm{y},\mathrm{x})\nabla\sigma(\mathrm{y},\mathrm{x})e^{\sqrt{-i\omega}\sigma(\mathrm{y},\mathrm{x})}.$$

In addition, there is the step response which expresses the head distribution,

$$H^0(\mathrm{y},\omega) = A_0(\mathrm{x}_s,\mathrm{y})e^{\sqrt{-i\omega}\sigma(\mathrm{x}_s,\mathrm{y})}\mathcal{H}(\omega) \qquad (B21)$$

where $\mathcal{H}(\omega)$ represents the Fourier transform of the step function. The spatial gradient of $H^0(\mathrm{y},\omega)$ is

$$\nabla H(\mathrm{y},\omega) = \nabla A_0(\mathrm{x}_s,\mathrm{y})e^{\sqrt{-i\omega}\sigma(\mathrm{x}_s,\mathrm{y})}\mathcal{H}(\omega) \qquad (B22)$$

$$+\sqrt{-i\omega}A_0(\mathrm{x}_s,\mathrm{y})\nabla\sigma(\mathrm{x}_s,\mathrm{y})e^{\sqrt{-i\omega}\sigma(\mathrm{x}_s,\mathrm{y})}\mathcal{H}(\omega)$$

Taking the inner product (B20) and (B21), retaining only terms of highest order in $\omega$ gives

$$\nabla G \cdot \nabla H = A_0(\mathrm{x}_s, \mathrm{x}) e^{\sqrt{-i\omega}\sigma(\mathrm{x}_s,\mathrm{x})}$$

$$\times i\omega \mathcal{H}(\omega) \nabla\sigma(\mathrm{x}_s, \mathrm{y}) \cdot \nabla\sigma(\mathrm{y}, \mathrm{x}) \qquad (B23)$$

where $A_0(\mathrm{x}_s, \mathrm{x})$ and $\sigma(\mathrm{x}_s, \mathrm{x})$ are defined in equations (B10) and (B11), respectively. As before, we may transfer the $i\omega$ term onto $\mathcal{H}(\omega)$, the equivalent to differentiating the step function with respect to time. Thus, we may take the inverse Fourier transform of the integrand (B23) to arrive at the time domain expression

$$\Pi_K(\mathrm{y}, \mathrm{x}, t) = \mathcal{I}(\mathrm{x_s}, \mathrm{x}) A_0(\mathrm{x_s}, \mathrm{x}) \frac{\sigma(\mathrm{x}_s, \mathrm{x})}{2\sqrt{\pi t^3}} e^{-\sigma^2(\mathrm{x}_s,\mathrm{x})/4t} \qquad (B24)$$

where we have defined the inner product

$$\mathcal{I}(\mathrm{x_s}, \mathrm{x}) = -2\nabla\sigma(\mathrm{x}_s, \mathrm{y}) \cdot \nabla\sigma(\mathrm{y}, \mathrm{x}). \qquad (B25)$$

The time domain equivalent of equation (B18) is

$$\delta h(\mathrm{x}, t) = \int \Pi_K(\mathrm{y}, \mathrm{x}, t) \delta K(\mathrm{y}) d\mathrm{y}. \qquad (B26)$$

We conclude this section by pointing out the similarity of the storage and hydraulic conductivity sensitivities. The primary modifications are a change in sign and the presence of the inner product factor $\nabla\sigma(\mathrm{x}_s, \mathrm{y}) \cdot \nabla\sigma(\mathrm{y}, \mathrm{x})$.

## Acknowledgments

This work was supported by funding provided by the Assistant Secretary for Fossil Energy, Office of Oil Gas and Shale Technologies, of the U. S. Department of Energy under contract DE-AC03-76SF00098. Computational resources were provided by the Center for Computational Seismology and the National Energy Research Scientific Computing (NERSC) Center of the Berkeley Laboratory. This work was also partially supported by JNC (Japan Nuclear Fuel Cycle Develpment Institute).

## References

Bear, J., 1972, *Dynamics of Fluids in Porous Media*, Dover Publications.

Bracewell, R. N., 1978, *The Fourier Transform and Its Applications*, McGraw-Hill, New York.

Carrera, J., 1987, State of the art of the inverse problem applied to the flow and solute transport problems, in *Groundwater Flow and Quality Modeling*, NATO ASI Ser. pp. 549-585.

Carter, R. D., L. F. Kemp, and A. C. Pierce, 1982, Discussion of comparison of sensitivity coefficient calculation methods in automatic history matching, *Soc. Petrol. Eng. J.*, **22**, 205-208.

Chapman, S. J., J. M. H. Lawry, and J. R. Ockendon, 1999, Ray theory for high-Peclet-number convection-diffusion, *SIAM J. Appl. Math.*, **1** 121-135.

Cohen, J. K., and R. M. Lewis, 1967, A ray method for the asymptotic solution of the diffusion equation, *J. Inst. Maths. Applics.*, **3** 266-290.

Datta-Gupta, A., and M. J. King, 1995, A semianalytic approach to tracer flow modeling in heterogeneous permeable media, *Advanc. Water Res.*, **18** 9-24.

Datta-Gupta, A., D. W. Vasco, J. C. S. Long, P. S. D'Onfro, and W. D. Rizer, 1995. Detailed characterization of a fractured limestone formation by use of stochastic inverse approaches, *SPE Form. Eval.*, **10**, 133-140.

de Marsily, G., 1986, *Quantitative Hydrogeology*, Academic Press, San Diego.

D'Onfro, P. S., W. D. Rizer, J. H. Queen, E. L. Majer, J. E. Peterson, T. M. Daley, D. W. Vasco, A. Datta-Gupta, and J. C. S. Long, 1998, An integrated approach for characterizing fractured reservoirs, in *Faulting, Fault Sealing, and Fluid Flow in Hydrocarbon Reservoirs*, Geol Soc London, Special Publ., pp. 193-208.

Fatemi, E., B. Engquist, and S. Osher, 1995, Numerical solution of the high frequency asymptotic expansion for the scalar wave equation, *J. Comp. Phys.*, **120**, 145-155.

Ginn, T. R., and J. H. Cushman, 1990, Inverse methods for subsurface flow: A critical review of stochastic techniques, *Stochastic Hydrol. Hydraul.*, **4**, 1-26.

Jacquard, P., and C. Jain, 1965, Permeability distribution from field pressure data, *Soc. Petrol. Eng.*, **5**, 281-294.

Keller, H. B., 1968, *Numerical Methods for Two-Point Boundary-Value Problems*, Blaisdell, Waltham, MA.

King, M. J. and Datta-Gupta, A., 1998, Streamline simulation: A current perspective, *In Situ*, **22** (1).

Kline, M., and I. W. Kay, 1965, *Electromagnetic Theory and Geometrical Optics*, John Wiley and Sons.

Kravtsov, Y. A., 1968, Two new asymptotic methods in the theory of wave propagation in inhomogeneous media, *Soviet Physics - Acoustics*, **14**, 1-17.

Kravtsov, Y. A., and Y. I. Orlov, 1990, *Geometrical Optics of Inhomogeneous Media*, Springer-Verlag, Berlin.

Kuiper, L., 1986, A comparison of several methods for the solution of the inverse problem in two-dimensional steady-state groundwater flow modeling, *Water Resour. Res.*, **22**, 705-714.

Luneburg, R. K., 1966, *Mathematical Theory of Optics*, University of California Press, Berkeley.

Mclaughlin, D. B. and Townley, L. R., 1996, A reassessment of the groundwater inverse problem, *Water Resour. Res.*, **32**, 1131-1161.

Majer, E. L., A. Datta-Gupta, J. E. Peterson, D. W. Vasco, L. R. Myer, T. M. Daley, B. Kaelin, J. H. Queen, P. S. D'Onfro, W. D. Rizer, D. Cox, and J. Sinton, 1996, Utilizing crosswell, single well and pressure transient tests for characterizing fractured gas reservoirs, *The Leading Edge*, **15**, 951-956.

Mauldon, A. D., K. Karasaki, S. J. Martel, J. C. S. Long, M. Landsfeld, A. Mensch, and S. Vomvoris, 1993, An inversion technique for developing models for fluid flow in

fracture systems using simulated annealing, *Water Resour. Res.*, **29**, 3775-3789.

Oliver, D. S., 1993, The influence of nonuniform transmission and storativity on drawdown, *Water Resour. Res.*, **29**, 169-178.

Oliver, D. S., 1994, Application of a wave transform to pressure transient testing in porous media, *Trans. Porous Media*, **16**, 209-236.

Paige, C. C., and Saunders, M. A., 1982, LSQR: An algorithm for sparse linear equations and sparse linear systems, *ACM Trans. Math. Software*, **8**, 195-209.

Pan, L., and L. Wu, 1998, A hybrid global optimization method for inverse estimation of hydraulic parameters: Annealing-simplex method, *Water Resour. Res.*, **34**, 2261-2269.

Parker, R. L., 1994, *Geophysical Inverse Theory*, Princeton University Press.

Philip, J. R., 1989, The scattering analog for infiltration in porous media, *Rev. of Geophys.*, **27**, 431-448.

Pierce, A., 1986, Wave methods for an inverse problem in diffusion, *Inverse Problems*, **2**, 205-217.

Sethian, J. A., 1996, *Level Set Methods*, Cambridge University Press.

Smith, R., 1981, The early stages of contaminant dispersion in shear flows, *J. Fluid Mech.*, **111**, 107-122.

Stakgold, I., 1979, *Green's Functions and Boundary Value Problems*, John Wiley and Sons, New York.

Sun, N.-Z., 1994, *Inverse Problems in Groundwater Modeling*, Kluwer Acad., Norwell Mass.

Tarantola, A., 1987, *Inverse Problem Theory: Methods for Data Fitting and Model Parameter Estimation*, Elsevier Sci.

Toomey, D. F., 1992, Microfacies correlation of the Early Permian Barneston Limestone, Conoco Test Facility to Vap's Pass, Kay County, Northern Oklahoma, *Oklahoma Geol. Surv. Bull.*, **145**, 193-219.

Vasco, D. W., and A. Datta-Gupta, 1999, Asymptotic solutions for solute transport: A formalism for tracer tomography, *Water Resour. Res.*, **35**, 1-16.

Vasco, D. W., and A. Datta-Gupta, 2000, Asymptotics, saturation fronts, and high resolution reservoir characterization, *Trans. Porous Media*, (in press).

Vasco, D. W., S. Yoon, and A. Datta-Gupta, 1999, Integrating dynamic data into high-resolution reservoir models using streamline-based analytic sensitivity coefficients, *Soc. Pet. Eng. J.*, **4**, 1-11.

Vasco, D. W., A. Datta-Gupta, and J. C. S. Long, 1997, Resolution and uncertainty in hydrologic characterization, *Water Resour. Res.*, **33**, 379-397.

Virieux, J., C. Flores-Luna, and D. Gibert, 1994, Asymptotic theory for diffusive electromagnetic imaging, *Geophys. J. Int.*, **119**, 857-868.

Wilson, W. J., 1983, An inverse scattering approach to the pressure transient analysis of petroleum reservoirs, in *Conference on Inverse Scattering: Theory and Application*, J. B. Bednar, R. Redner, E. Robinson, and A. Weglein (eds.), 170-180, SIAM, Philadelphia.

Yeh, W. W.-G., 1986, Review of parameter identification procedures in groundwater hydrology: The inverse problem, *Water Resour. Res.*, **22**, 95-108.

---

D. W. Vasco, Earth Sciences Division/Building 90, Berkeley Laboratory, 1 Cyclotron Road, Berkeley, CA 94720. (e-mail:dwvasco@lbl.gov)

Henk Keers, Earth Sciences Division/Building 90, Berkeley Laboratory, 1 Cyclotron Road, Berkeley, CA 94720. (e-mail:henk@ccs.lbl.gov)

Kenzi Karasaki, Earth Sciences Division/Building 90, Berkeley Laboratory, 1 Cyclotron Road, Berkeley, CA 94720. (e-mail:kkarasaki@lbl.gov)

Received August 1999

# Figure Captions

**Figure 1.** (A) Synthetic transient head values for sensitivity calculations. The points A (0.2 days), B (0.4 days), and C (0.9 days) denote samples for which the sensitivities have been calculated. (B) Estimates of the slope of the transient head curve, derived by differencing.

**Figure 2.** Paths used in calculating transient head amplitude sensitivities to variations in storage and conductivity. Quantities are computed along the trajectories from the source to the grid point of interest and then from the grid point to the observation point. Paths are shown for a vertical line of grid points.

**Figure 3.** Storage sensitivities for the three sample points designated in Figure 1.

**Figure 4.** Conductivity sensitivities for the three sample points denoted in Figure 1.

**Figure 5.** Stochastic realization of spatially correlated random permeability field. The injection and observation wells are indicated by stars. The correlation half-width was seven grid blocks and the random deviates were drawn from a log-normal distribution.

**Figure 6.** (A) Transient head variations for the 6 observing wells associated with interference test 1. (B) Calculated temporal derivative (slope) of the head variations.

**Figure 7.** (A) Predicted transient head values for interference test 1, based upon a uniform permeability distribution of 70 milli-darcies. (B) Calculated temporal derivative of the head variations. The head variations associated with the model in Figure 5 are indicated by the individual points. The values predicted by the initial uniform model are indicated by the corresponding lines.

**Figure 8.** The mean squared misfit to the (A) arrival time and (B) transient head data as a function of the number of linearized iterations.

**Figure 9.** (A) Permeability estimates resulting from the arrival time inversion. (B) Permeability distribution produced by the amplitude inversion.

**Figure 10.** Predicted transient head values (A) and their slopes (B), based upon the final model shown in Figure 9b. As in Figure 7, the head variations associated with the actual model (Figure 5) are indicated by the individual points. The values predicted by our final model are indicated by the corresponding lines.

**Figure 11.** Transient head observations associated with two interference tests conducted at Conoco's Borehole Test Facility.

**Figure 12.** Head slope estimates produced by differencing the values in Figure 11.

**Figure 13.** Mean squared head misfit as a function of iteration number. The initial 5 points are associated with a fit to the arrival time, the latter points are misfits resulting from a fit to the transient head observations.

**Figure 14.** Final estimate of the permeability distribution in the Fort Riley Limestone at the Borehole Test Facility. The locations of the boreholes are denoted by stars.

**Figure 15.** Core containing an open fracture, obtained while slant drilling through the location indicated by seismic reflection data. The fracture location agrees with the inversion result in Figure 14.

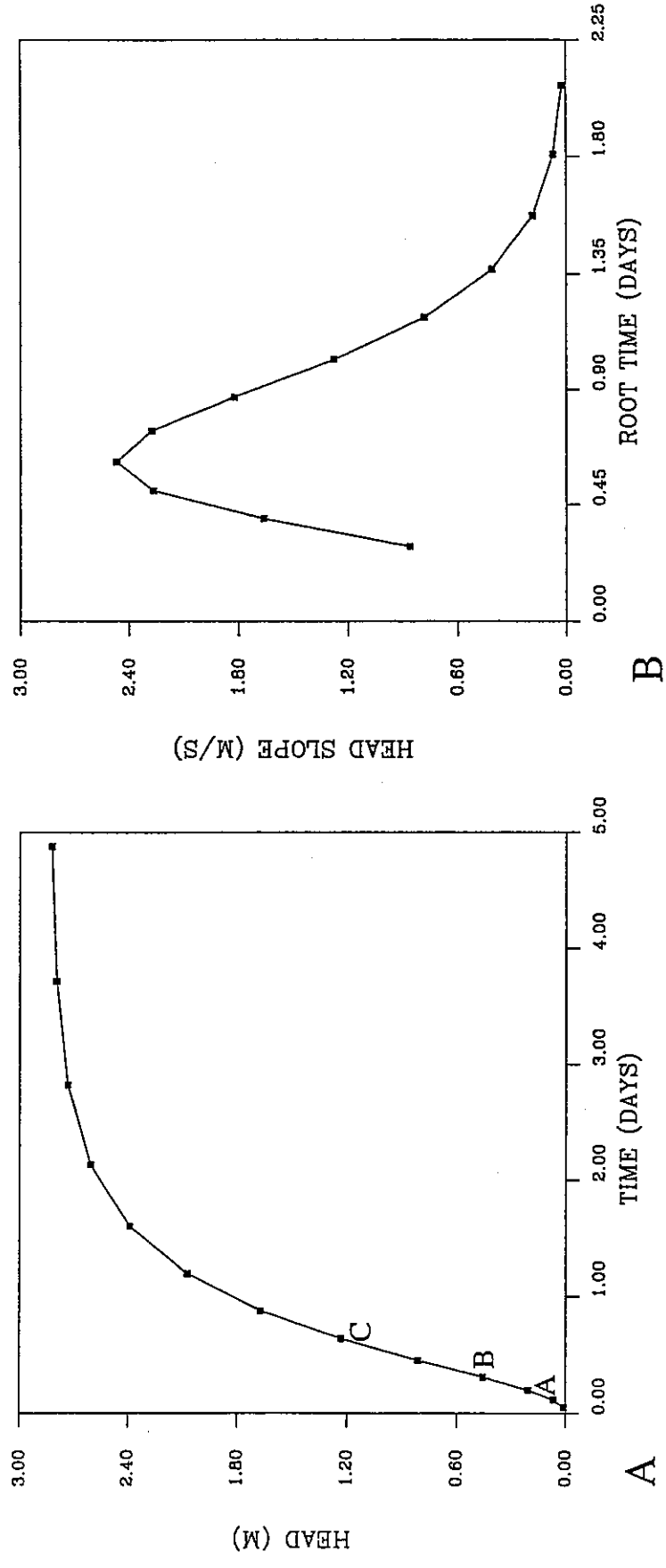
HEAD (M)
3.00
2.40
1.80
1.20
0.60
0.00
0.00
1.00
2.00
3.00
4.00
5.00
TIME (DAYS)
A
B
C
A
HEAD SLOPE (M/S)
3.00
2.40
1.80
1.20
0.60
0.00
0.00
0.45
0.90
1.35
1.80
2.25
ROOT TIME (DAYS)
B

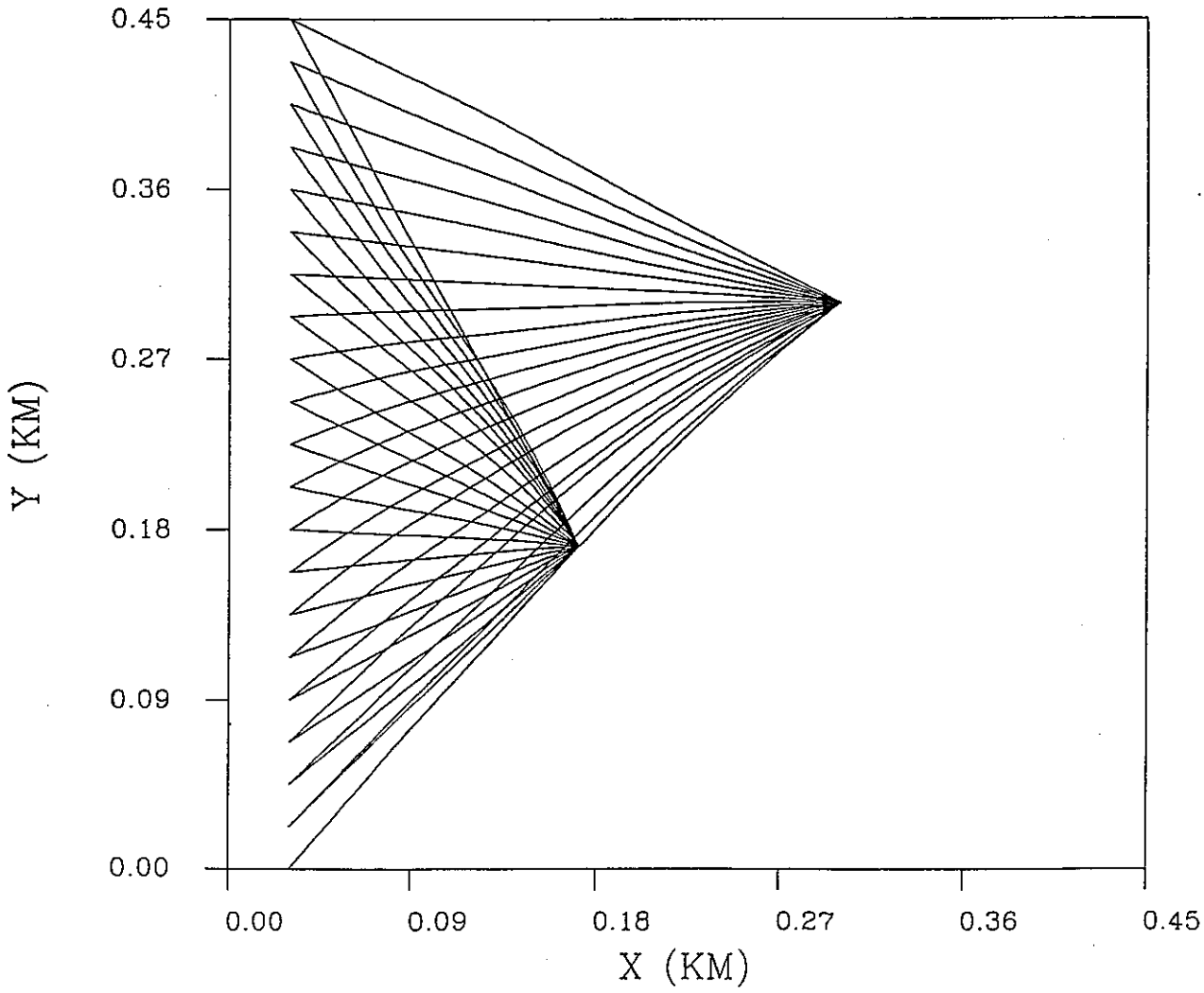
0.45
0.36
0.27
0.18
0.09
0.00
Y (KM)
0.00
0.09
0.18
0.27
0.36
0.45
X (KM)

# Storage Sensitivities

## Numerical

0.2 DAYS

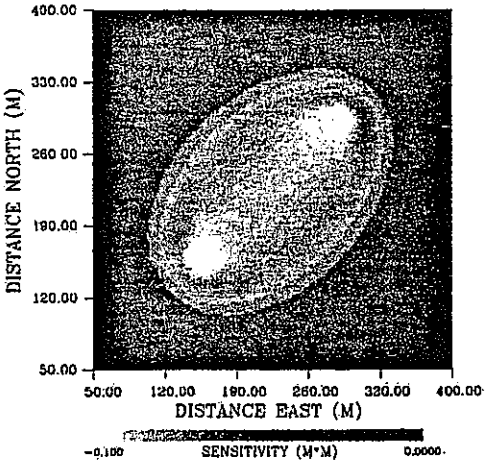


0.4 DAYS

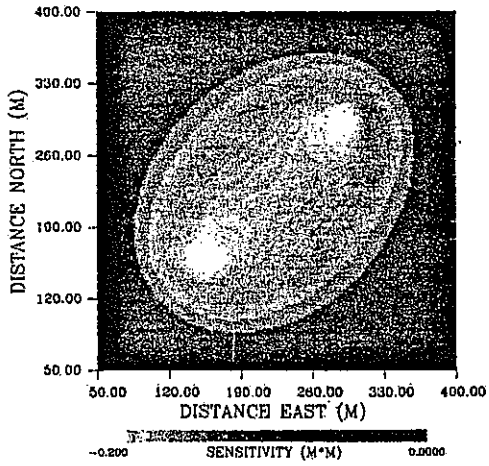


0.9 DAYS

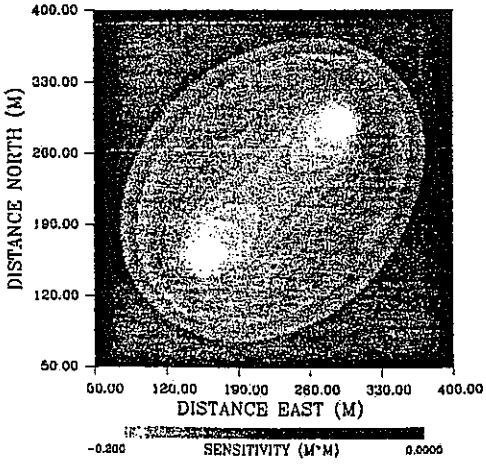


## Asymptotic

0.2 DAYS

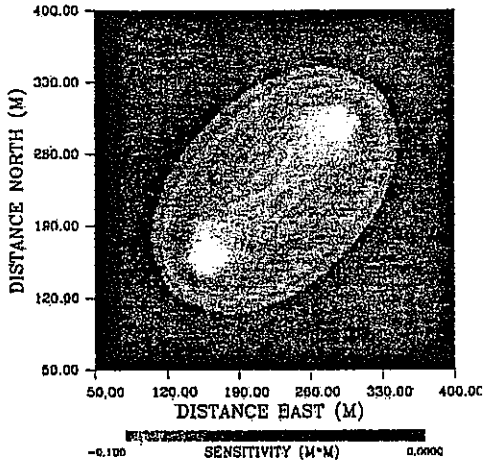


0.4 DAYS

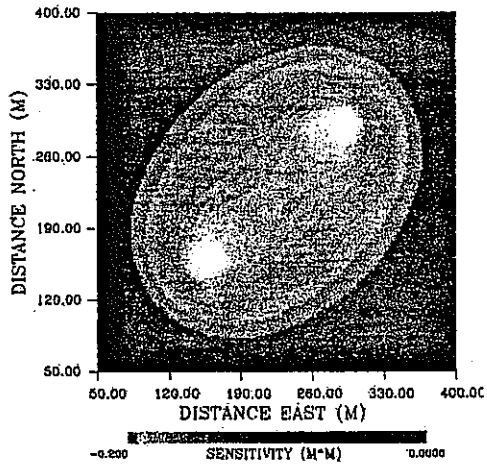


0.9 DAYS

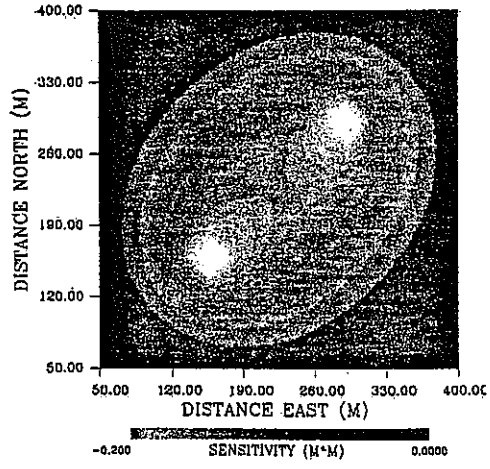

# Conductivity Sensitivities

## Numerical

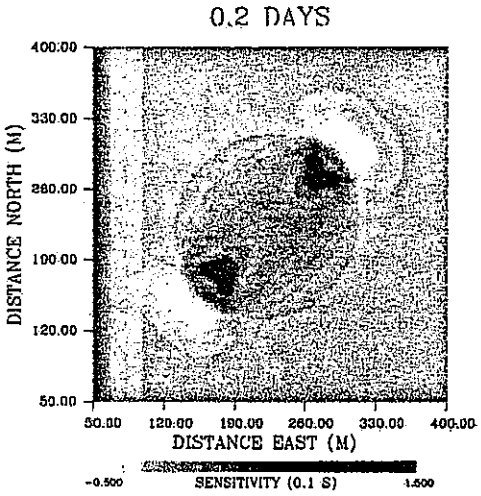


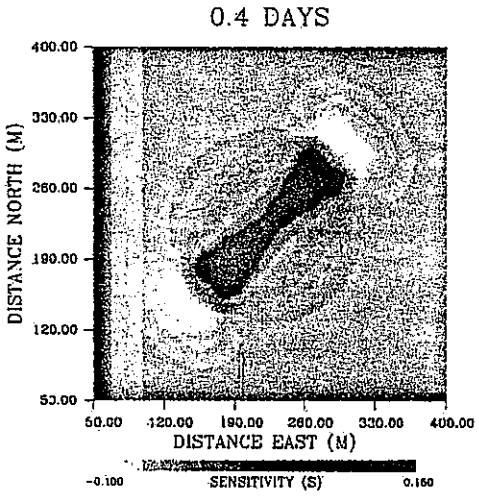


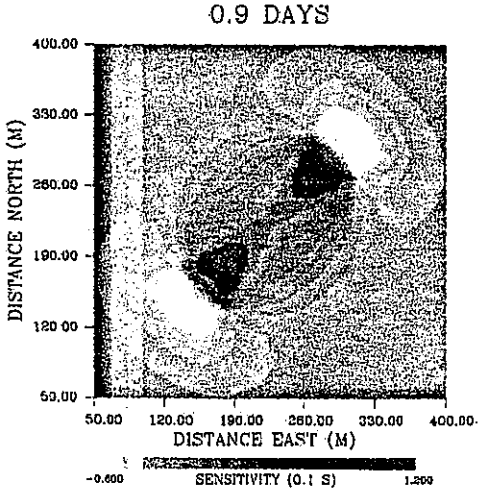


## Asymptotic

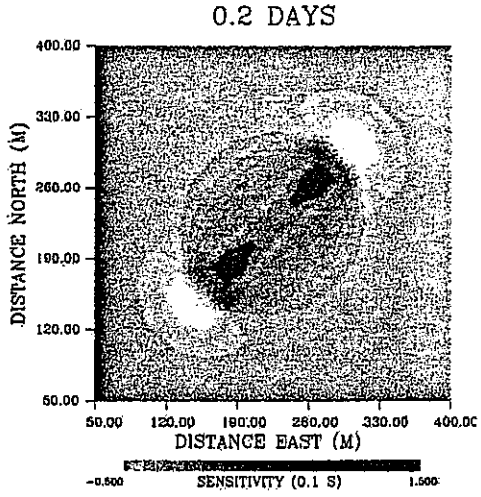


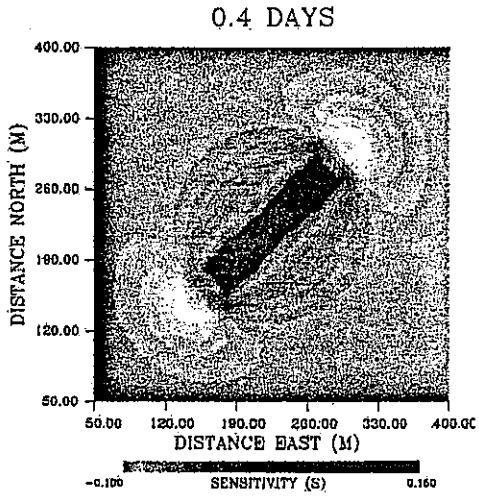


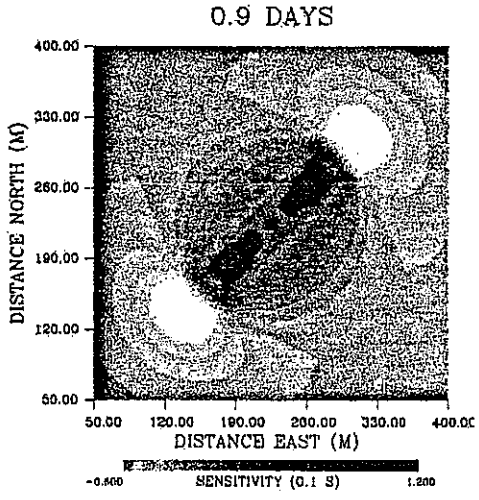

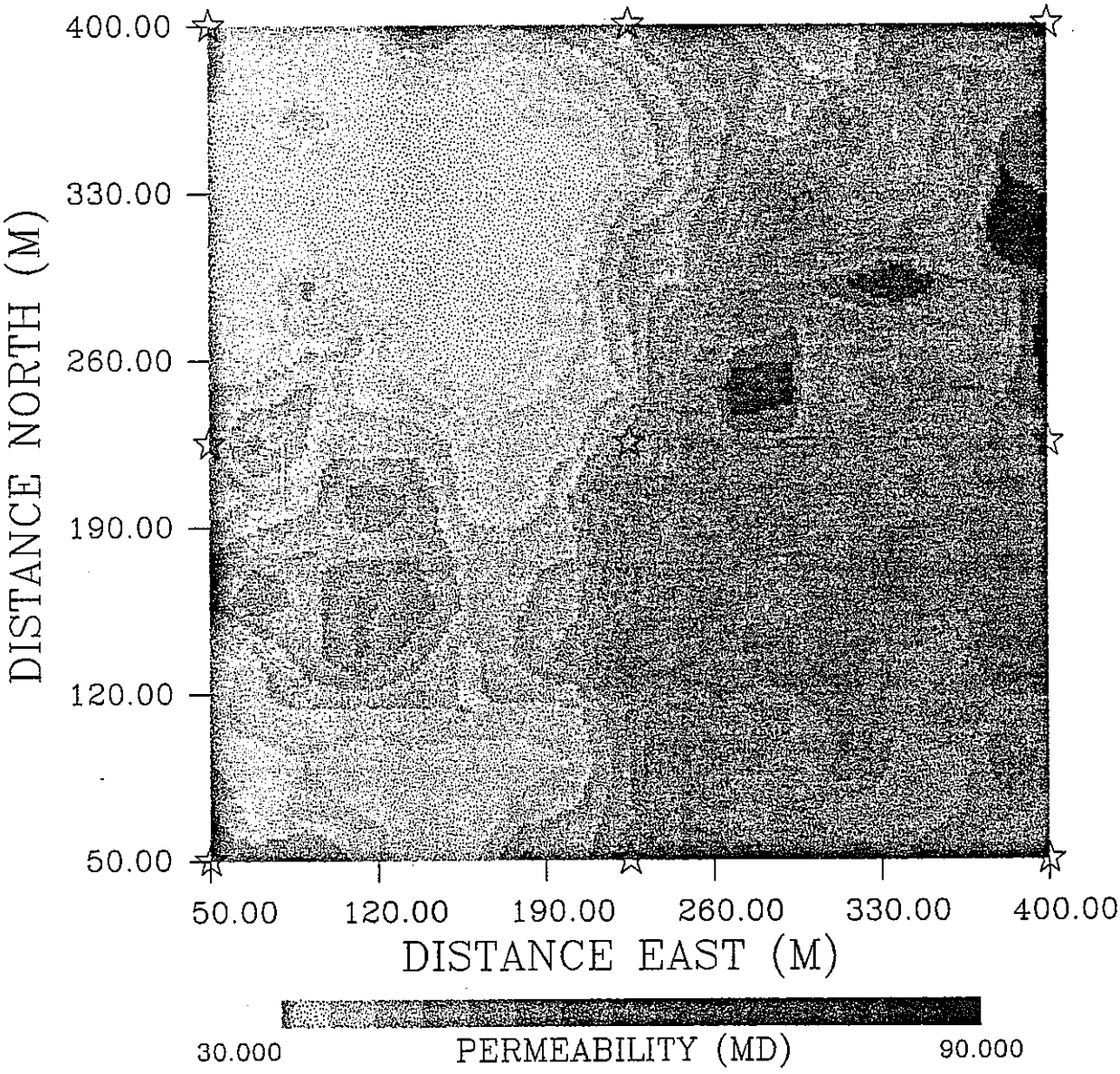
400.00
330.00
260.00
190.00
120.00
50.00
DISTANCE NORTH (M)
50.00
120.00
190.00
260.00
330.00
400.00
DISTANCE EAST (M)
30.000
PERMEABILITY (MD)
90.000

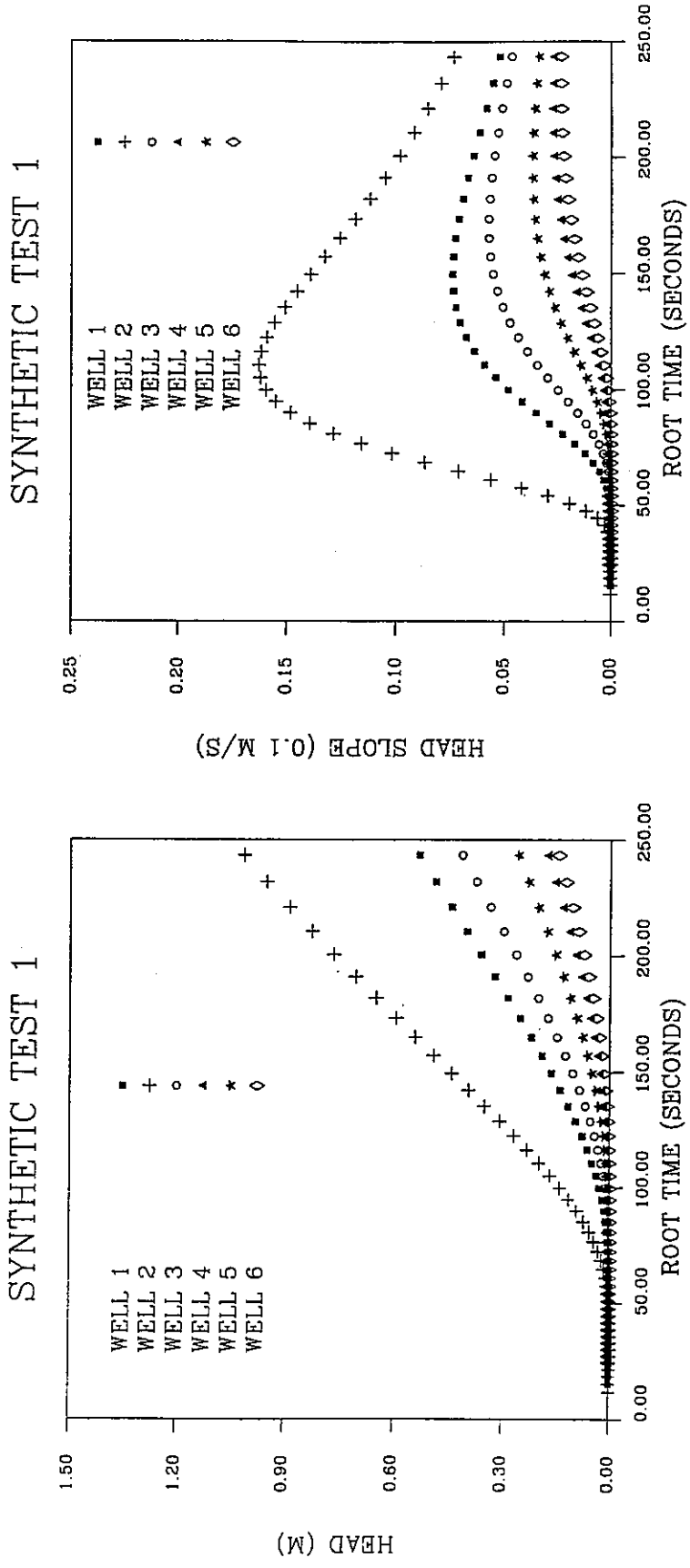
SYNTHETIC TEST 1
WELL 1
WELL 2
WELL 3
WELL 4
WELL 5
WELL 6
HEAD (M)
ROOT TIME (SECONDS)
0.00
0.30
0.60
0.90
1.20
1.50
0.00
50.00
100.00
150.00
200.00
250.00
SYNTHETIC TEST 1
WELL 1
WELL 2
WELL 3
WELL 4
WELL 5
WELL 6
HEAD SLOPE (0.1 M/S)
ROOT TIME (SECONDS)
0.00
0.05
0.10
0.15
0.20
0.25
0.00
50.00
100.00
150.00
200.00
250.00

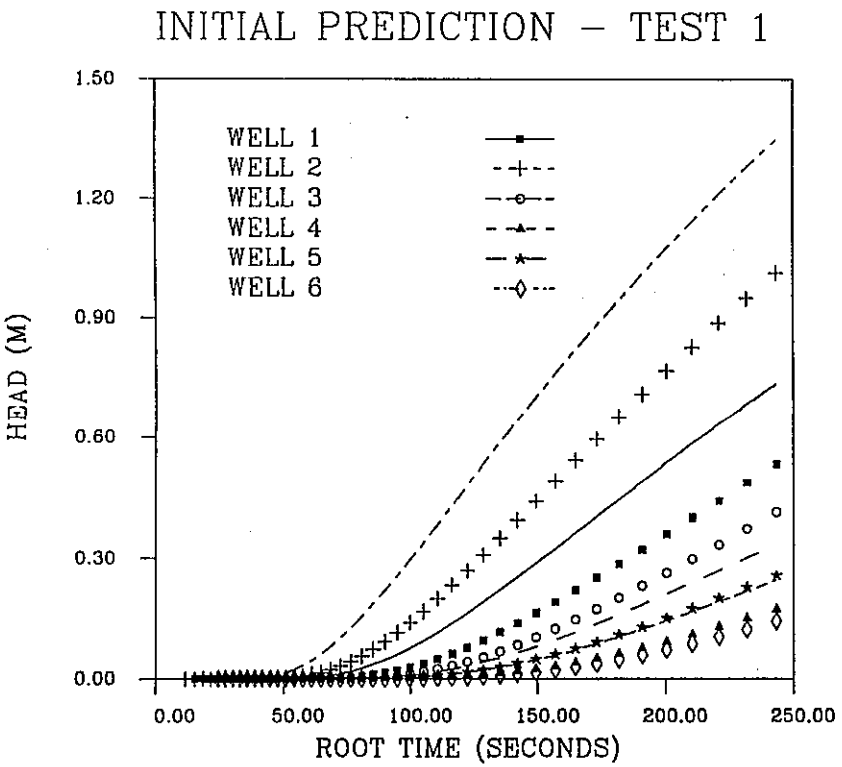
INITIAL PREDICTION － TEST 1
HEAD (M)
1.50
1.20
0.90
0.60
0.30
0.00
WELL 1
WELL 2
WELL 3
WELL 4
WELL 5
WELL 6
0.00
50.00
100.00
150.00
200.00
250.00
ROOT TIME (SECONDS)

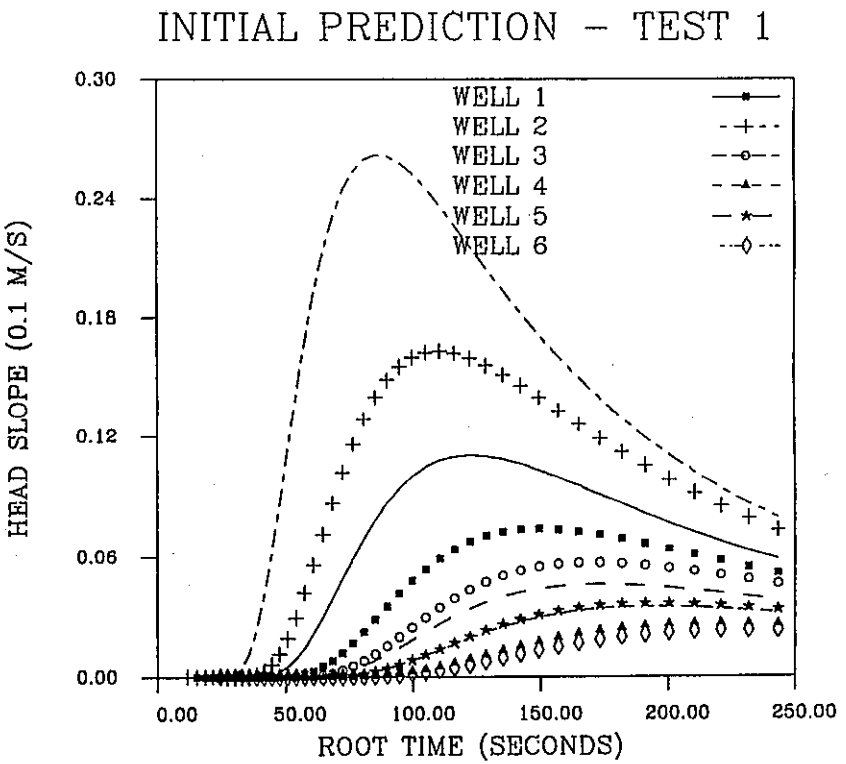
INITIAL PREDICTION － TEST 1
HEAD SLOPE (0.1 M/S)
0.30
0.24
0.18
0.12
0.06
0.00
WELL 1
WELL 2
WELL 3
WELL 4
WELL 5
WELL 6
0.00
50.00
100.00
150.00
200.00
250.00
ROOT TIME (SECONDS)

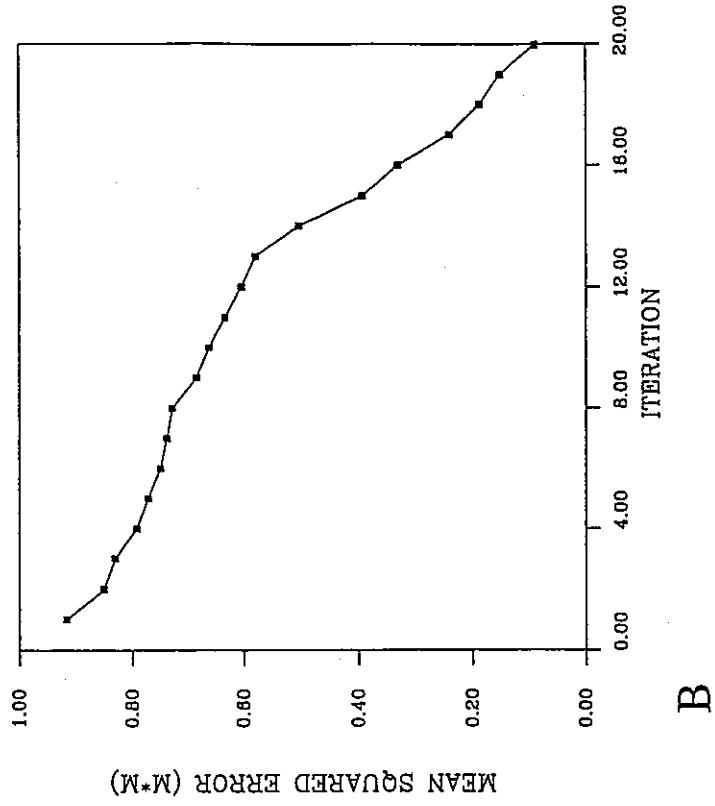
MEAN SQUARED ERROR (M*M)
1.00
0.80
0.60
0.40
0.20
0.00
0.00
4.00
8.00
12.00
16.00
20.00
ITERATION
B

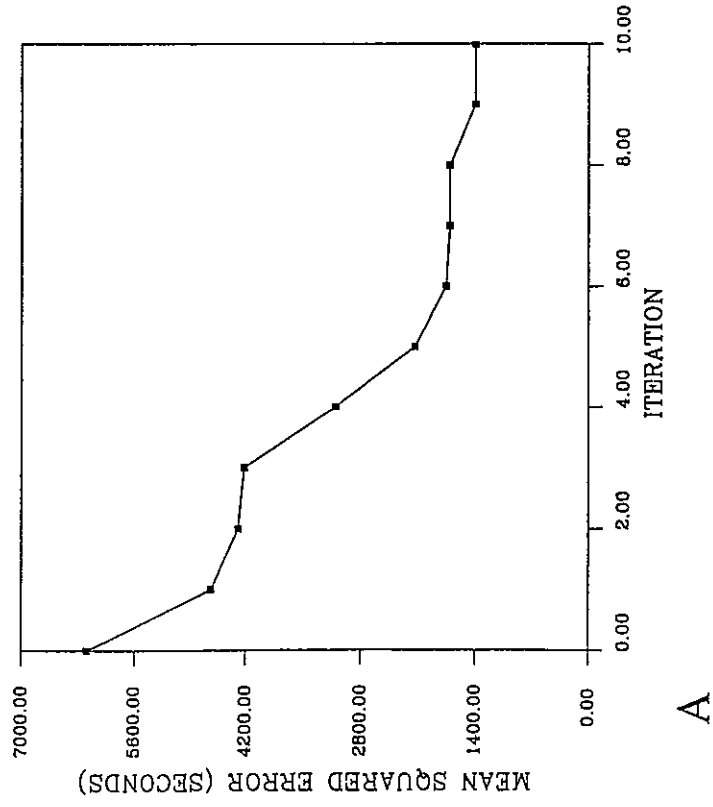
MEAN SQUARED ERROR (SECONDS)
7000.00
5600.00
4200.00
2800.00
1400.00
0.00
0.00
2.00
4.00
6.00
8.00
10.00
ITERATION
A

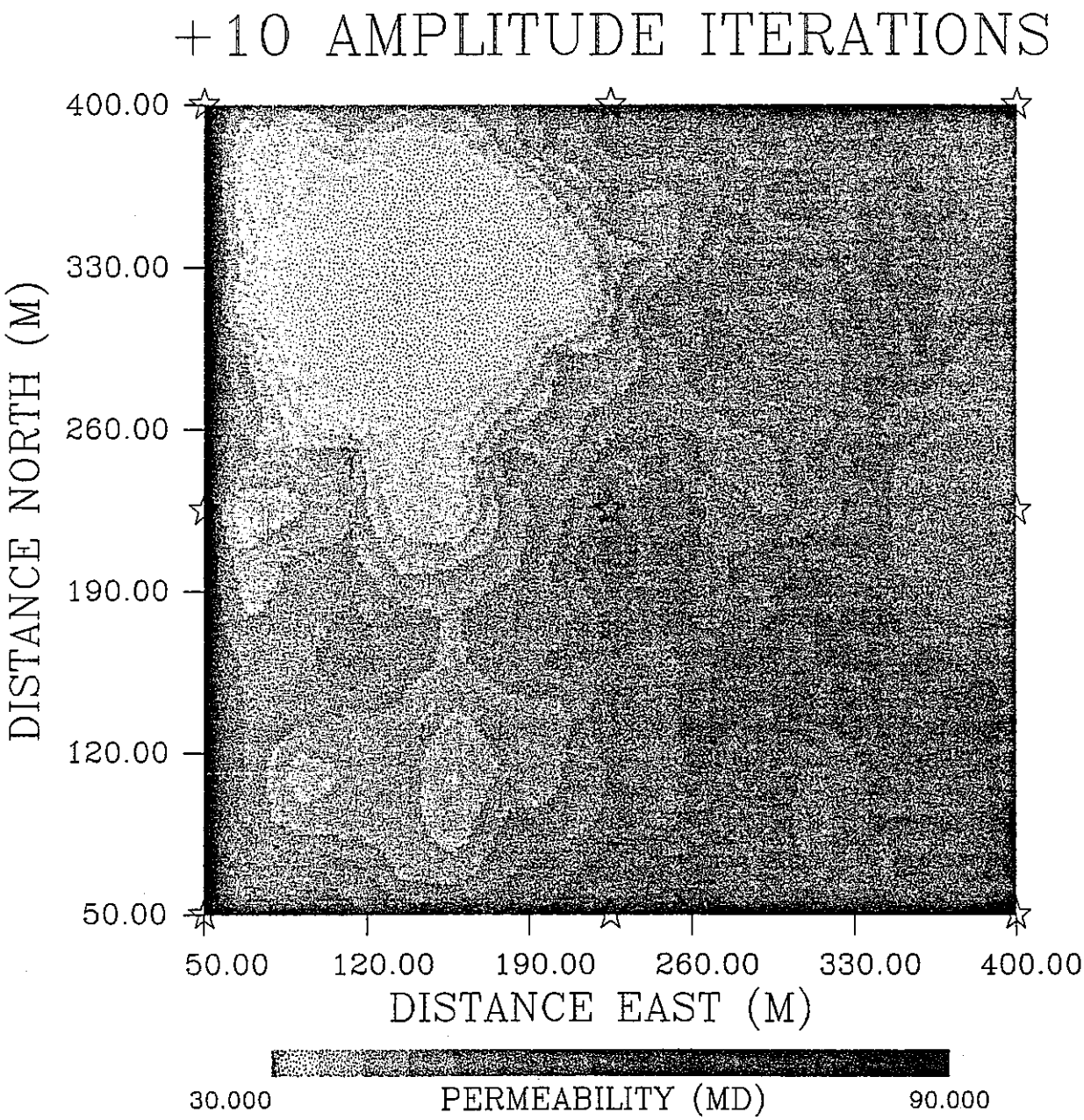
+10 AMPLITUDE ITERATIONS
400.00
330.00
260.00
190.00
120.00
50.00
DISTANCE NORTH (M)
50.00
120.00
190.00
260.00
330.00
400.00
DISTANCE EAST (M)
30.000
PERMEABILITY (MD)
90.000

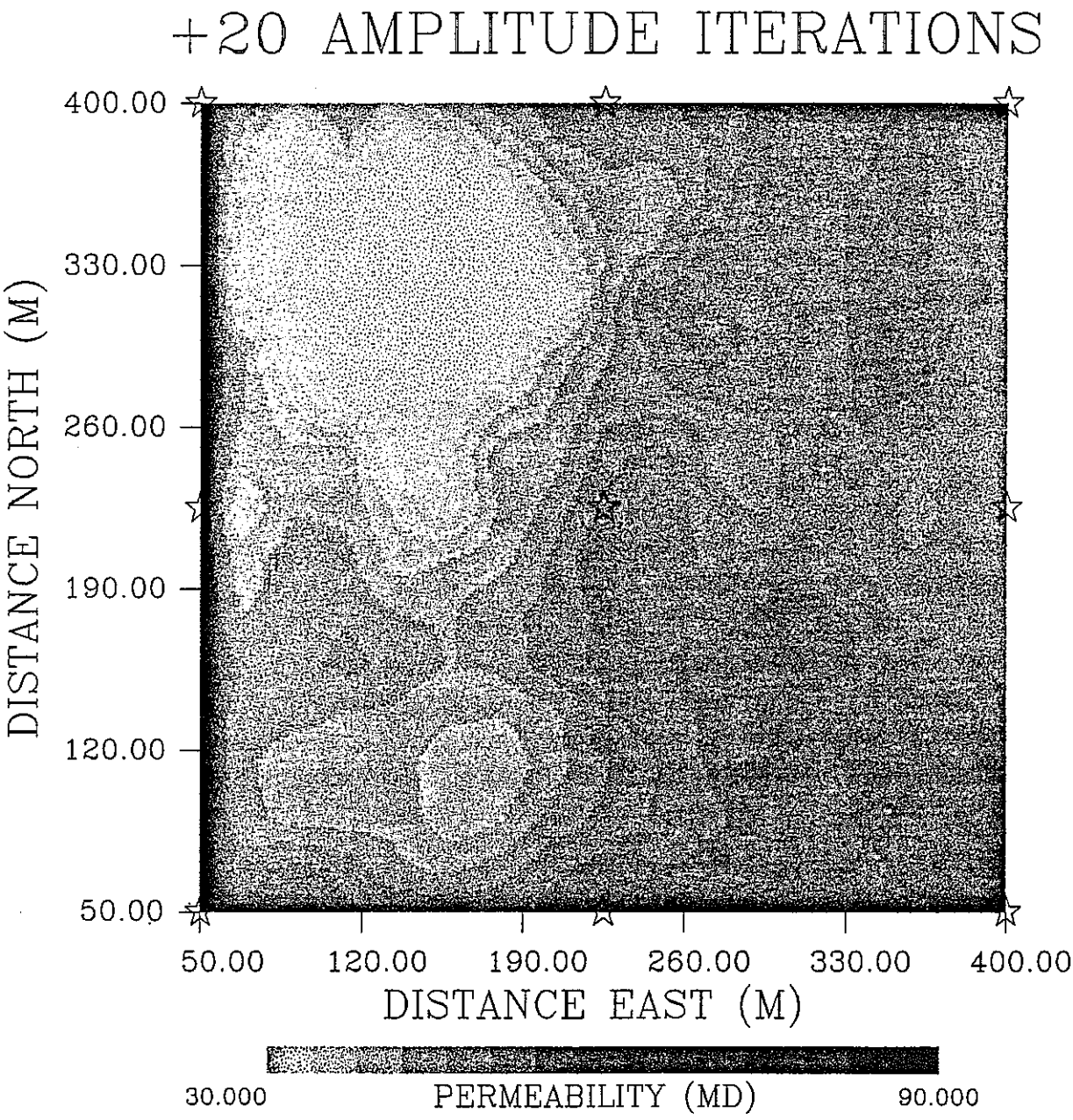
+20 AMPLITUDE ITERATIONS
400.00
330.00
260.00
190.00
120.00
50.00
DISTANCE NORTH (M)
50.00
120.00
190.00
260.00
330.00
400.00
DISTANCE EAST (M)
30.000
PERMEABILITY (MD)
90.000

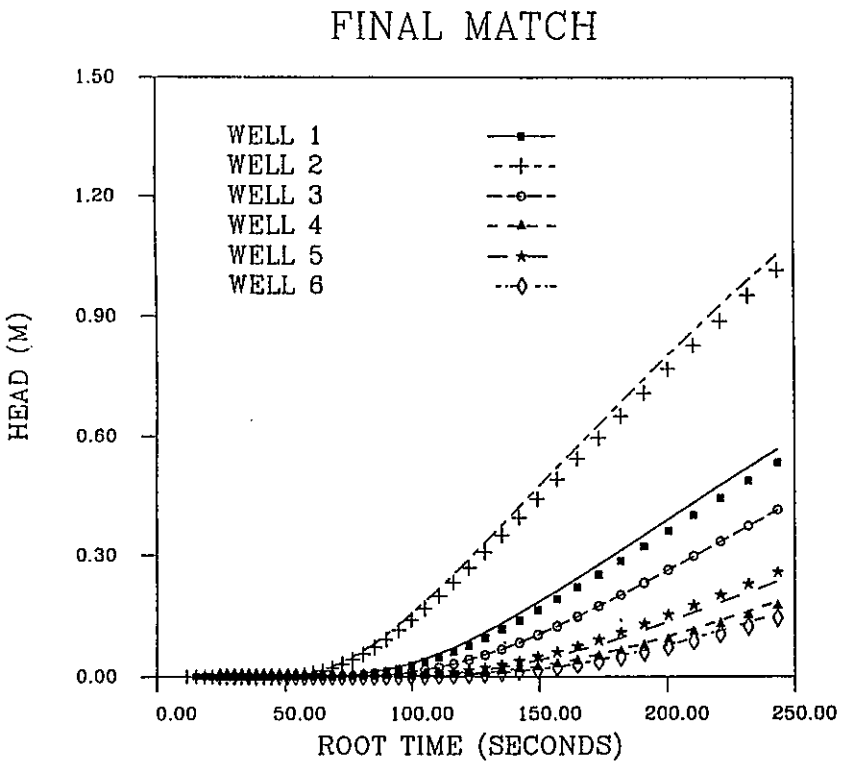
FINAL MATCH
HEAD (M)
1.50
1.20
0.90
0.60
0.30
0.00
WELL 1
WELL 2
WELL 3
WELL 4
WELL 5
WELL 6
0.00
50.00
100.00
150.00
200.00
250.00
ROOT TIME (SECONDS)

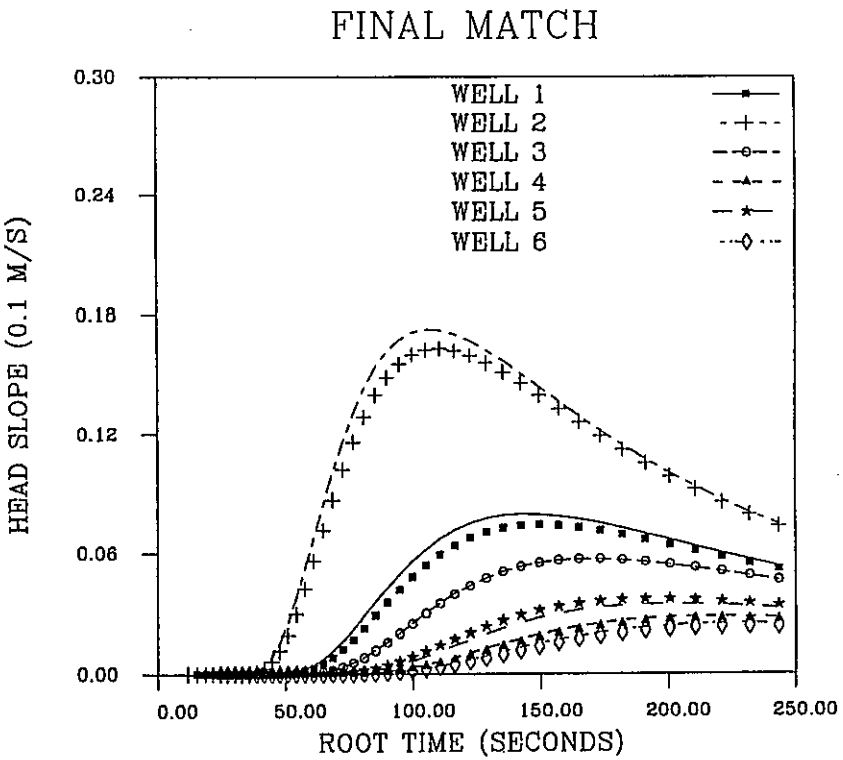
FINAL MATCH
HEAD SLOPE (0.1 M/S)
0.30
0.24
0.18
0.12
0.06
0.00
WELL 1
WELL 2
WELL 3
WELL 4
WELL 5
WELL 6
0.00
50.00
100.00
150.00
200.00
250.00
ROOT TIME (SECONDS)

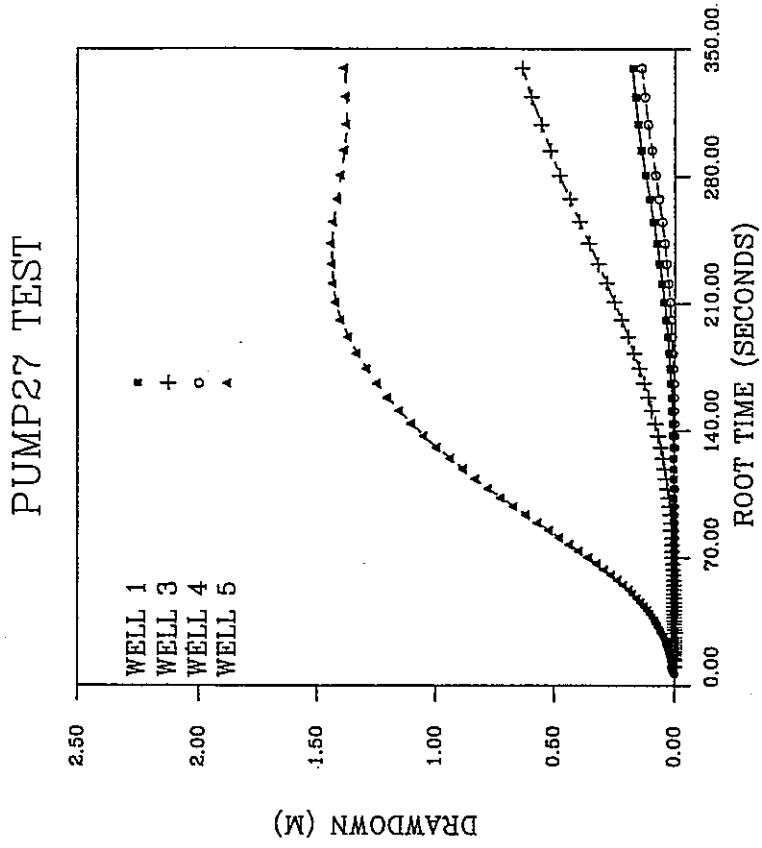
PUMP27 TEST
WELL 1
WELL 3
WELL 4
WELL 5
DRAWDOWN (M)
ROOT TIME (SECONDS)
0.00
0.50
1.00
1.50
2.00
2.50
0.00
70.00
140.00
210.00
280.00
350.00

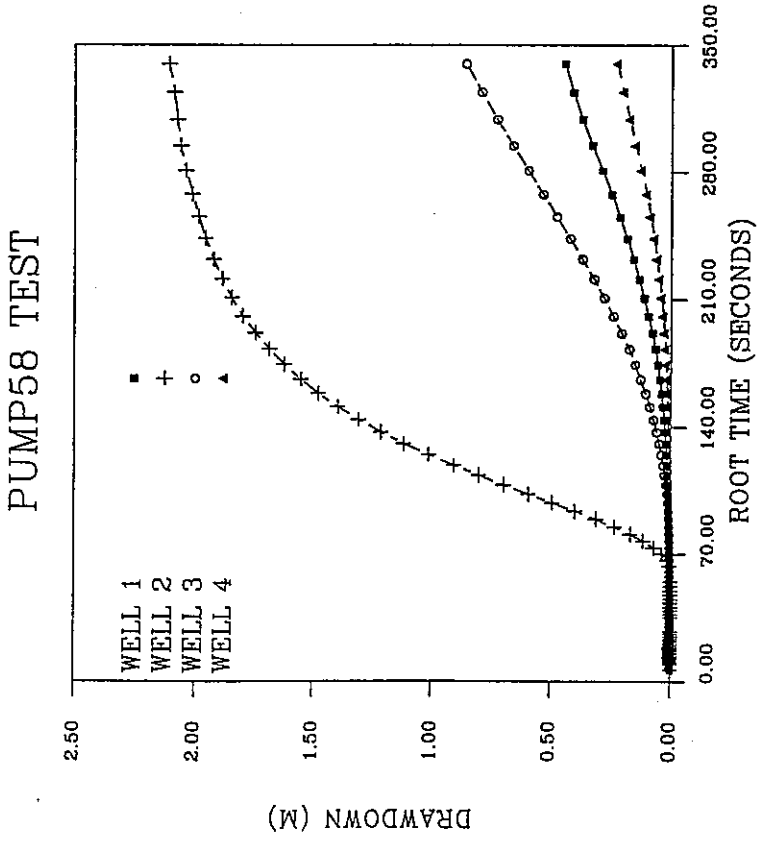
PUMP58 TEST
WELL 1
WELL 2
WELL 3
WELL 4
DRAWDOWN (M)
ROOT TIME (SECONDS)
0.00
0.50
1.00
1.50
2.00
2.50
0.00
70.00
140.00
210.00
280.00
350.00

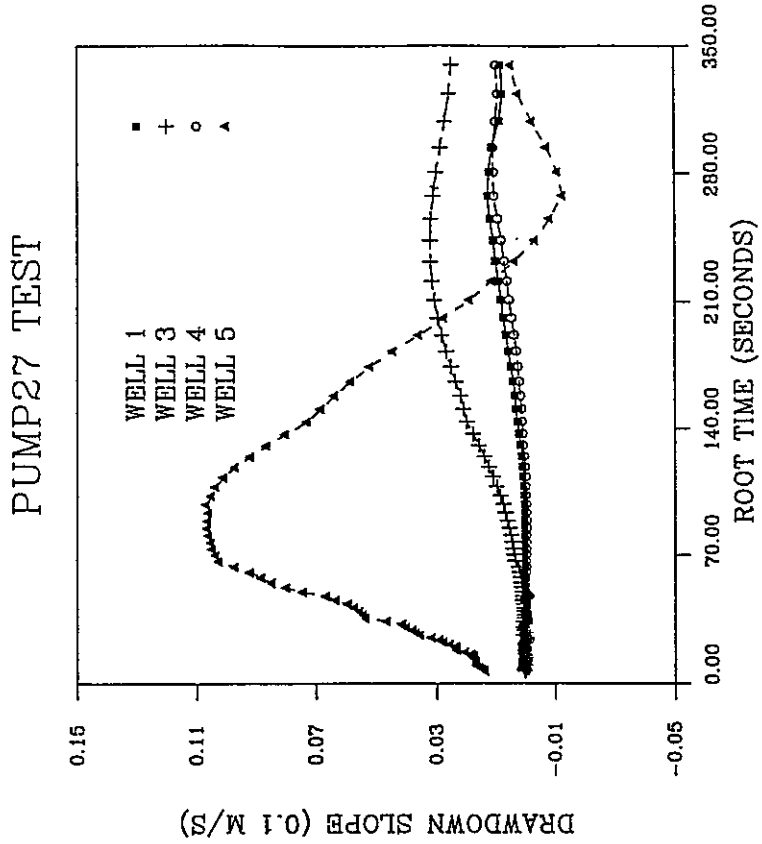
PUMP27 TEST
WELL 1
WELL 3
WELL 4
WELL 5
0.15
0.11
0.07
0.03
-0.01
-0.05
DRAWDOWN SLOPE (0.1 M/S)
0.00
70.00
140.00
210.00
280.00
350.00
ROOT TIME (SECONDS)

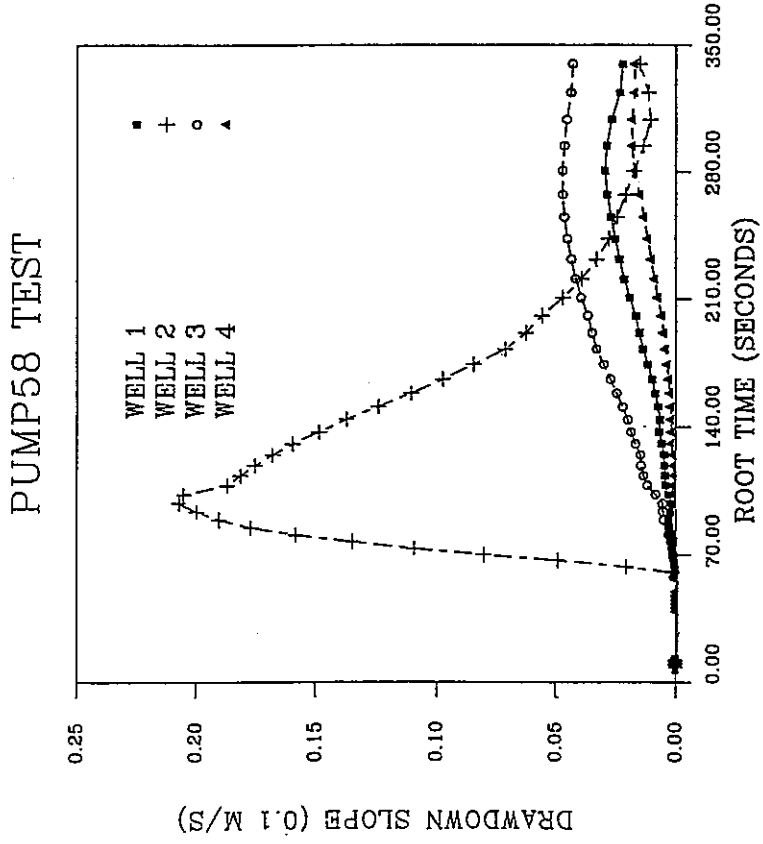
PUMP58 TEST
WELL 1
WELL 2
WELL 3
WELL 4
0.25
0.20
0.15
0.10
0.05
0.00
DRAWDOWN SLOPE (0.1 M/S)
0.00
70.00
140.00
210.00
280.00
350.00
ROOT TIME (SECONDS)

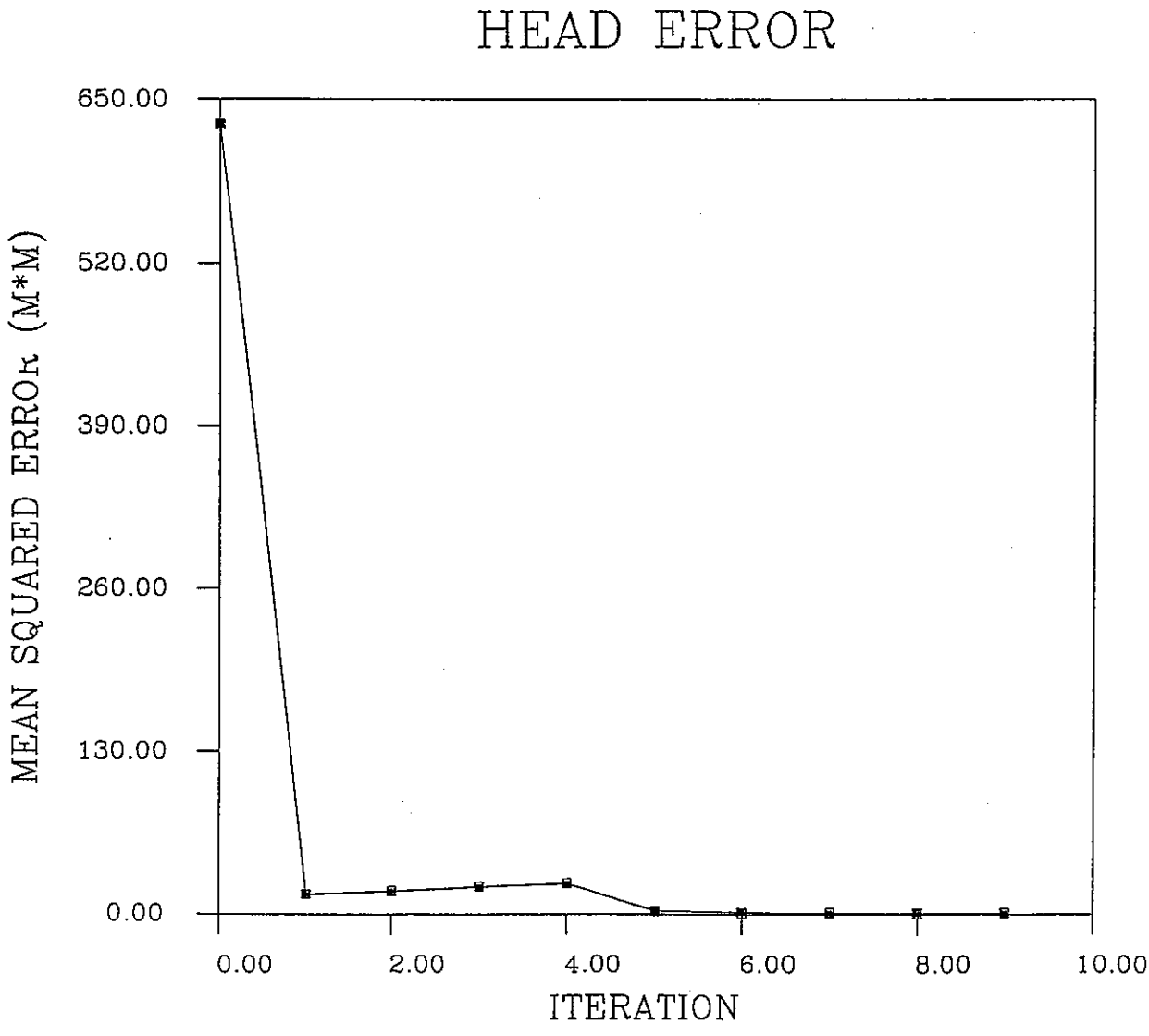
HEAD ERROR
650.00
520.00
390.00
260.00
130.00
0.00
MEAN SQUARED ERROR (M*M)
0.00
2.00
4.00
6.00
8.00
10.00
ITERATION

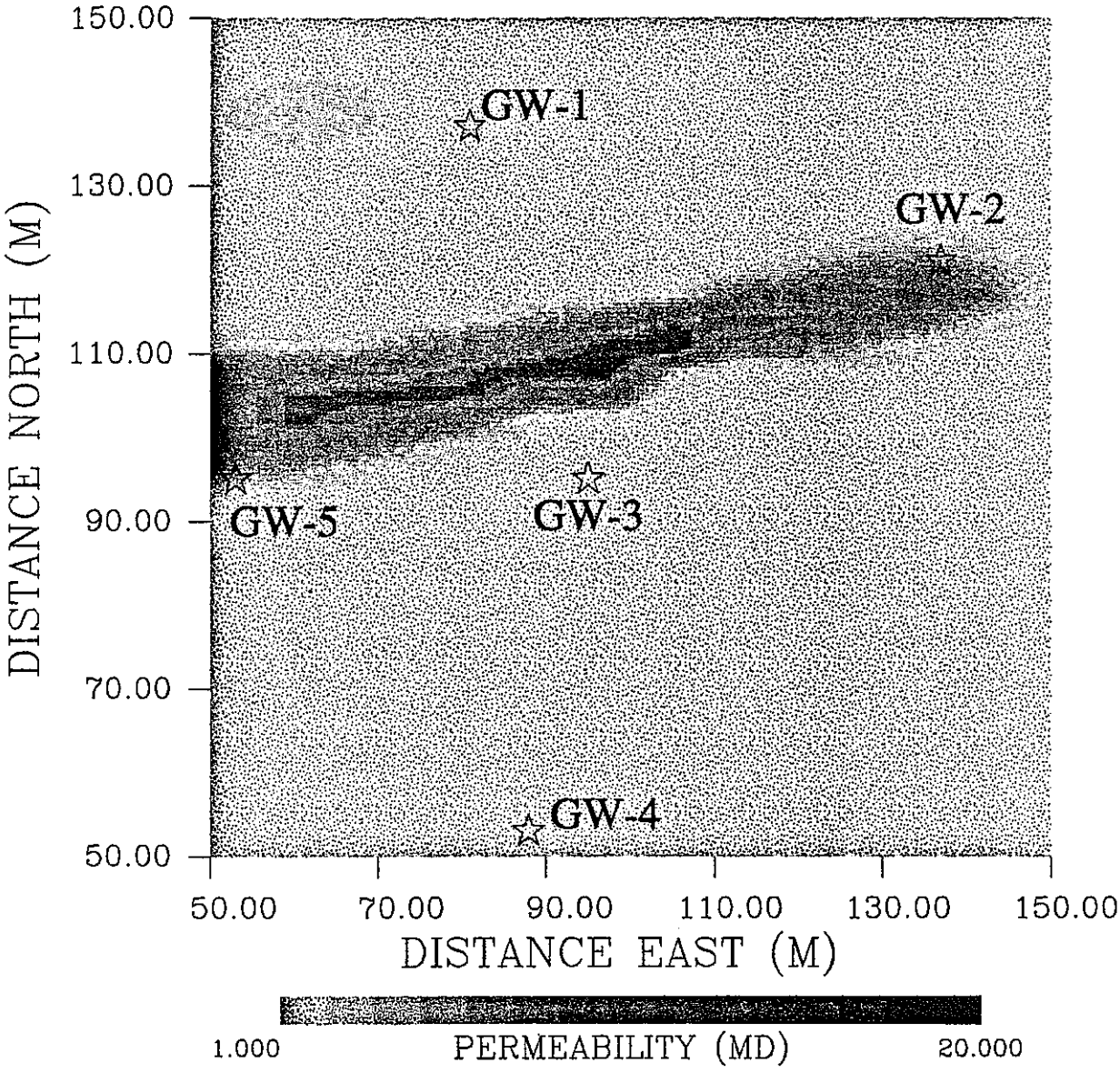
150.00
130.00
110.00
90.00
70.00
50.00
DISTANCE NORTH (M)
GW-1
GW-2
GW-3
GW-4
GW-5
50.00
70.00
90.00
110.00
130.00
150.00
DISTANCE EAST (M)
1.000
PERMEABILITY (MD)
20.000

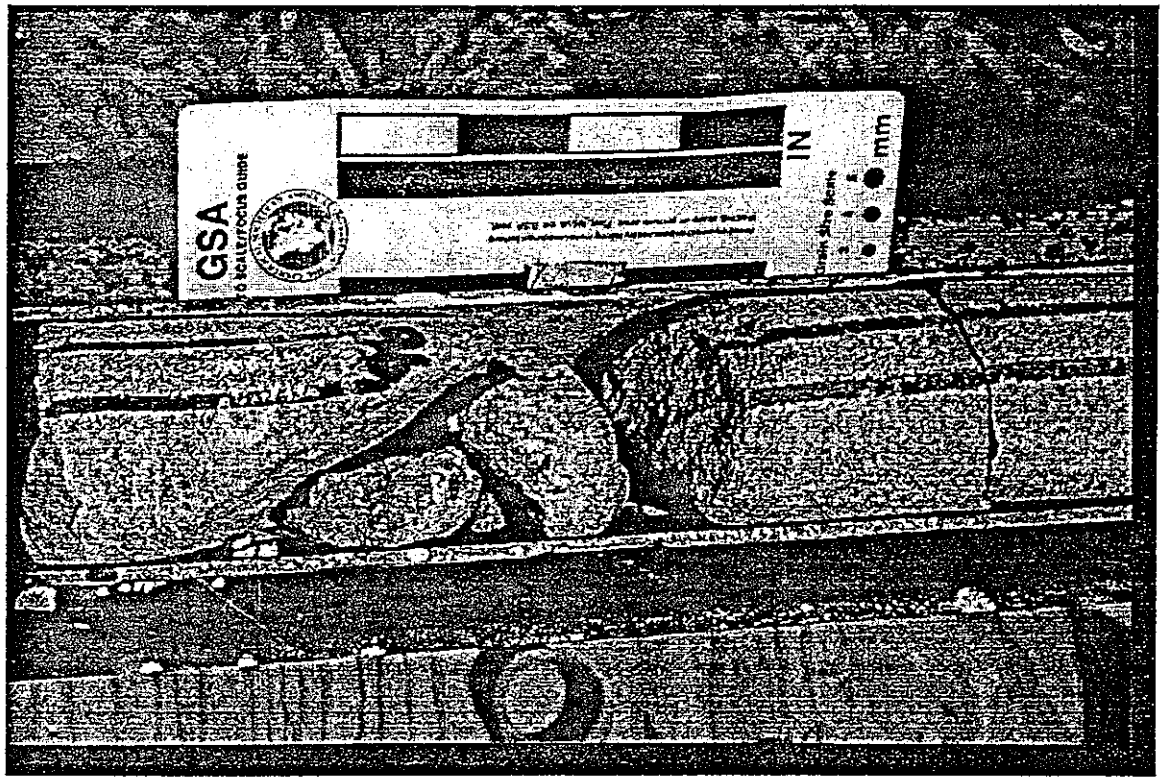
GSA
IN
mm

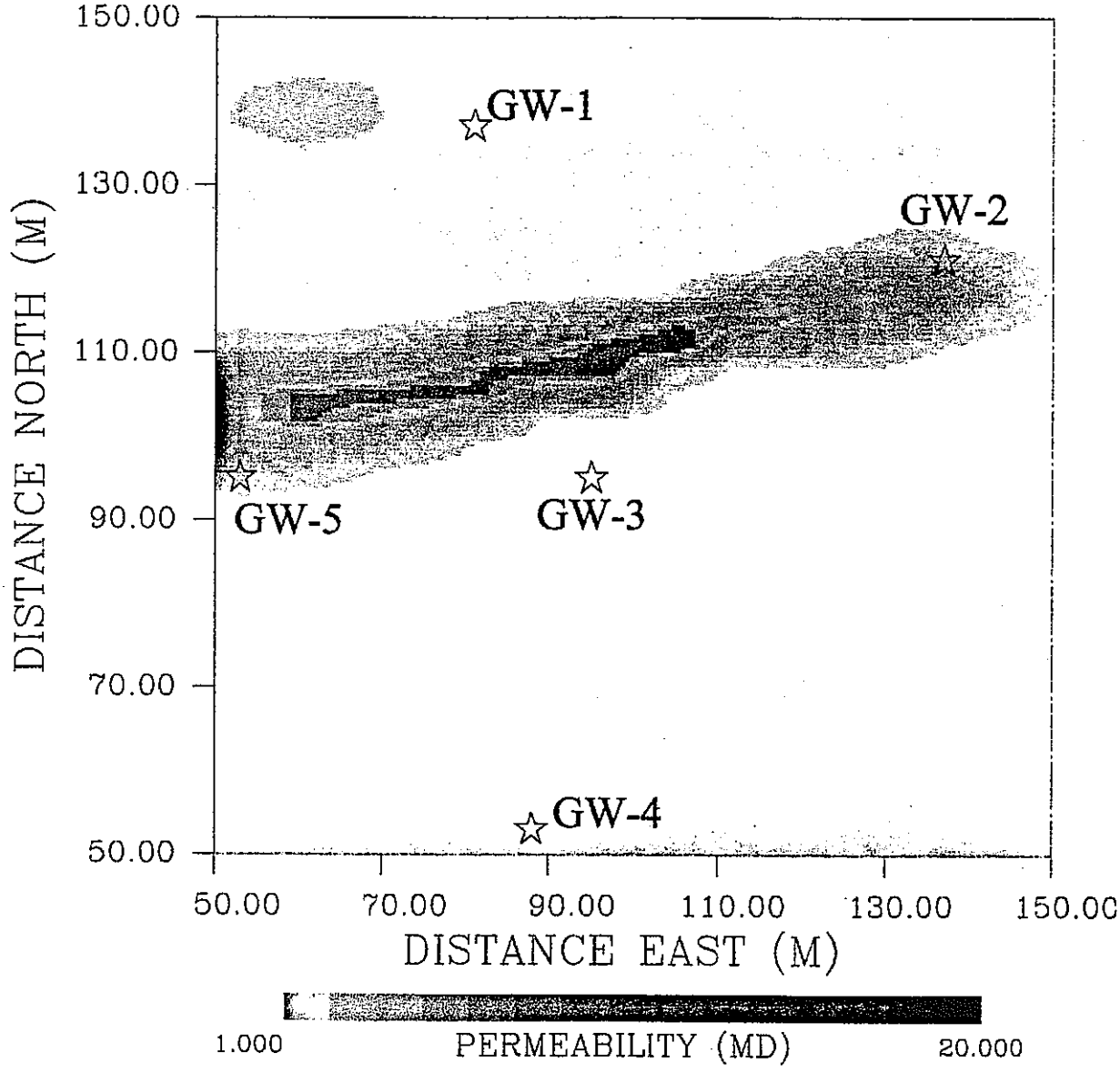
150.00
130.00
110.00
90.00
70.00
50.00
DISTANCE NORTH (M)
GW-1
GW-2
GW-3
GW-4
GW-5
50.00
70.00
90.00
110.00
130.00
150.00
DISTANCE EAST (M)
1.000
PERMEABILITY (MD)
20.000

# Multi-Continua Description of Flow in Composite Heterogeneous Media

Mark Shvidler and Kenzi Karasaki

Earth Science Division
Lawrence Berkeley National Laboratory
Berkeley, California 94720

## Abstract

Adequacy of the description and the qualitative prediction of flow and transport processes in subsurface systems essentially depends on how well a model represents the heterogeneity that is intrinsic in real field. One of the simplest models to describe the heterogeneity structure is a so-called composite system. In this model it is assumed that the whole media is composed of homogeneous components that are distributed in space randomly or in a particular periodic manner. Flow and transport simulation in composite systems can usually be reduced to solving partial differential equations with variable discontinuous coefficients and averaging the solutions, which can be accomplished by numerical simulations using the Monte-Carlo approach. A different approach, related to averaging the differential equations of flow and leads to new equations that link averaged fields in composite media. This description is designated as mono-continuum or global description. If the homogeneous components of a composite system, so-called phases, have essentially different hydrodynamic and/or geometric parameters, it is natural to study averaging of the fields on the individual phases of the composite along with the global averaging. This approach reduces to a more detailed description of processes in multi-continua. It takes into consideration the mean fields in the individual continuum phase as well as the cross-flows and cross-forces between continua. However, this description is usually non-closed because the number of equations is less that number of unknown functions (mean fields and exchange terms). To overcome this difficulty, the phenomenological theory of unsteady motion in heterogeneous media (dual-porosity media, fractured porous media) postulates a special interaction mechanism for closing the equations. This paper presents the exact equations of mass-balance and moment-balance for each phase of the composite. The exact physical sense of exchange terms in the multi-continua models is explained. We then demonstrate that joint

consideration of the mono-continual and the multi-continual systems of equations in the case of two-phase random composite leads to a closed description, and from that, we can find the exchange terms. For periodic composite system the same approach leads to a closed description for any number of phases. We successively study the composite systems with a random and periodical structure. The terms describing the interactions between continua (such as the exchange of fluids and momentum between phases) are calculated. Finally, we examine the hypothesis customarily made in the phenomenological models that the cross-flow is proportional to the mean pressure difference. We find the hypothesis as generally unsatisfactory considering its region of applicability (micro and macro isotropic composite medium).

## 1. INTRODUCTION

The problem of rationally describing flow and transport in real, macroscopically essentially inhomogeneous media is of considerable interest in the theory and its technical applications.

Stochastic approach for flow and transport in heterogeneous random systems (including random composite media) involves the probabilistic treatment of percolation parameters and flow and transport equations, the determination of the functional from the statistical solution or the analysis of equations relating the unknown and given functionals [e.g., *Shvidler,* 1985; *Dagan,* 1989; *Gelhar,*1993 ]

Inhomogeneous systems having periodic structure are a convenient model for studying processes in heterogeneous media. The theory of averaging the processes in periodic (as distinct from stochastic) structures is well established, and constructive methods for analyzing many processes in periodic media have been developed [e.g., *Bensoussan et al*, 1978; *Bakhvalov and Panasenko*, 1989; *Jikov at al.*, 1993]

The description in terms of averaged fields represented by the theory of homogenization leads to equations that relate these fields to the effective characteristics of the inhomogeneous medium. Under certain conditions, the averaged equations can be treated as conservation laws, and their system as a mono-continuum model of the process. Obviously, this description must contain and utilize sufficient information on the fields in the individual phases of the periodic or random composite system and the inter-phase transfer processes.

A more detailed description involves the determination of the mean fields in each phase, i.e. the conditionally averaged fields and the equations relating these fields. If it is possible to construct such equations and treat them as the equations of certain process in a phase of the composite

system, such a description would be a multi-continua one in accordance with the number of phases.

Irrespective of the method of realizing the multi-continuum description, it is necessary to solve the central problem of closing the systems of equations associated with terms responsible for inter-continuum transfers of mass, momentum, energy, etc.

The phenomenological theory of the unsteady motion of a homogeneous fluid in heterogeneous composite systems (media with dual porosity, fractured porous media), which postulates the special interaction mechanism, is well studied. In this approach, the flow in each phase of the composite is characterized by its own mean pressure or head and mean flow-velocity fields, the relation between which takes the form of Darcy's law. The rate of fluid transfer among the phases is assumed to be proportional to the difference of the mean head of each phase.

We examine the problem of conditional averaging of a system of flow equations for a weakly compressible fluid in a random and periodic composite medium. The equations of the multi-continua model were developed, and the parameters regulating the interactions between the phase continuum were calculated.

For those cases in which, for one and the same process, a mono-continuum description can be realized and the conservation laws of the multi-continua model can be obtained, it has been shown that the splitting of the globally averaged fields is possible, that the closing transfer terms for the binary random system can be expressed in terms of the characteristic of the mono-continuum and the mean fields in the phase continua , and that their interactions can be calculated. The information thus obtained for some random and periodical systems makes it possible to evaluate and refine the phenomenological closing hypothesis. As an example, we show that when a heterogeneous system is locally isotropic and macro-isotropic, the hypothesis

of the proportionality of the cross-flow between the phases to the difference of phase pressures or head can be regarded in some cases as an approximate rule. On the other hand, this relation is generally inadequate in the cases of overall anisotropy.

The article is consisted of 5 sections, with this introduction being section 1. In section 2 we examine the flow in random composite systems. Here, we consider the exact conditional averaged equations of fluid transport and averaged equations of momentum for each phase of the composite random media. These equations make up a non-closed system that is interpreted as a multi-continua model of the process. For a binary composite system, the inclusion of the equations of mono-continua (global) model in this non-closed system of the equations for the same process in the same composite system enables the closed multi-continua description, which makes it possible to directly compute the parameters a multi-continuum models that respond for interaction between continua. We examine a partial but important case of "meso-equilibrium" system and obtain the simple relations for cross-flows between phases, cross-forces, etc.

In section 3 we examine some examples of random composite systems and present the analysis results.

In section 4 the above analysis approach is applied to periodical composite media. Here we also examine the multi-continua model and present conditional averaged equations. In contrast to the stochastic approach, the system that joins the equations of mono-continuum and multi-continua models together with explicit expansion of the local fields with respect to fast and slowly changing variables makes a closed description possible for the composite system with any number of phases.

In section 5 we present some examples of periodic composite systems, for which we can obtain exact expressions for phase heads and their differences. Also examined in detail is the two-phase

layered system for which pressure difference and cross-flows are obtained quantitatively. Here we discuss the same method of closing the equations of phenomenological models.

The approach that is presented in this article for random and periodic composite media was briefly published by *Shvidler* [1986a,b; 1988] and *Shvidler and Karasaki* [1994,1999]. In this paper we set forth the problem in more detail and present new theoretical results and some applications.

## 2. RANDOM COMPOSITE MEDIA

### 2.1.Mono-continuum (global) description of flow in random medium

Let us consider the unsteady flow of a homogenous, compressible fluid in a heterogeneous, in particular, composite deformable random medium in a three-dimensional domain $\Omega$ with boundary $\partial\Omega$. The problem is mathematically described by the equations:

$$div\, v(x,t)+\alpha(x)\frac{\partial u(x,t)}{\partial t}=f(x,t), \tag{2.1}$$

$$\sigma^{-1}(x)\, v(x,t)+\nabla u(x,t)=0, \tag{2.2}$$

$$u(x,0)=u_0(x), \quad u|_{\partial\Omega}=\varphi\,(x,t), \tag{2.3}$$

Here $u(x,t)$ is the head, $v(x,t)$ is the Darcy`s velocity vector, $\sigma(x)$ is the symmetric and positive definite conductivity tensor, whose components are a random functions of $x$ , and scalar $\alpha(x)$ is the specific storage of the porous media-fluid system, which is also a positive random function. We assume that both random fields $\alpha(x)$ and $\sigma(x)$ are stochastically homogeneous, that is, all probability density of these random functions are invariant to translation in unbounded space. The source density $f(x,t)$ is a square integrable function. In the

present paper we only consider non-random initial and boundary conditions (2.3) for $u(x,t)$. It should be noted that non-random flux condition lead to random boundary condition for $u(x,t)$ , and requires special analysis.

We introduce the fields $U(x,t)$ and $V(x,t)$, unconditionally averaged over the ensemble of realizations of the random fields $\sigma(x)$ and $\alpha(x)$:

$$U(x,t) = \langle u(x,t) \rangle , \; V(x,t) = \langle v(x,t) \rangle \tag{2.4}$$

If we assume that $\delta$ - so-called micro-scale of the stochastically homogeneous fields $\sigma(x)$ and $\alpha(x)$ - satisfies the condition $\delta << l_\Omega$ , where $l_\Omega$ is the macro-scale in region $\Omega$, then averaging over the probability measure in (2.4) can be replaced by averaging over the volume of the region $\omega_\Delta$ , whose meso-scale $\Delta$ satisfies the inequalities:

$$\delta \; << \; \Delta \; << \; l_\Omega \tag{2.5}$$

It is known [e.g., *Bakhvalov and Panasenko*,1989 ] that unconditional averaging of the system (2.1),(2.2) and (2.3) can be obtained by expanding the fields $u(x,t)$ and $v(x,t)$ in powers of the small parameter $\mu = \delta / l_\Omega$ that is a dimensionless length scale of heterogeneity for the random fields $\alpha(x)$ and $\sigma(x)$. Thus the averaged equations (2.1) and (2.2) can be represented in the form:

$$\mathrm{div} V(x,t) \; + \; \alpha^* \frac{\partial U(x,t)}{\partial \; t} \; + \mu \frac{\partial}{\partial \; t} \lambda \left[ DU(x,t) \right] = f(x,t) \tag{2.6}$$

$$\left( \sigma^* \right)^{-1} V(x,t) \; + \; \nabla U(x,t) = \mu \; \left( \sigma^* \right)^{-1} \gamma \left[ DU(x,t) \right] \tag{2.7}$$

Here the scalar $\alpha^* = \langle \alpha(x) \rangle$ is constant and the tensor $\sigma^* = const$ is so-called the effective conductivity tensor. It should be noted that the non-random constants scalar $\alpha^*$ and tensor $\sigma^*$ fully define the connection between the vector-field $V(x,t)$ and scalar field $U(x,t)$ in the limiting case of $\mu \to 0$ only. The expressions – the scalar-correlation $\mu\lambda[DU(x,t)] = \langle [\alpha(x) - \langle \alpha(x) \rangle][u(x,t) - U(x,t)] \rangle$ and the vector-correlation $\mu\gamma[DU(x,t)] = \langle [\sigma^* - \langle \sigma(x) \rangle][\nabla u(x,t) - \nabla U(x,t)] \rangle$ are asymptotic series in power of the parameter $\mu$, whose coefficients are linear combinations of the derivatives of the field $U(x,t)$ with respect to $x$ and $t$. Because both series are infinite and contain the derivatives of any order, the equations (2.6) and (2.7) are non-local.

Obviously, we must add the non-random conditions (2.3) to the equations (2.6) and (2.7) and refer the (2.3) to the function $U(x,t)$, that is: $U(x,t_0) = u_0(x)$, $U(x,t)|_{\partial\Omega} = \varphi(x,t)$. Thus, in terms of $U(x,t)$ and $V(x,t)$ there exists a closed description of the process of non-stationary flow in heterogeneous porous media. The chief difficulties in realizing this description are (a) determining the tensor $\sigma^*$ and (b) constructing the series $\lambda[DU(x,t)]$ and $\gamma[DU(x,t)]$.

The unconditional averaged system: the equation of mass balance (2.6) and the equation of momentum balance (2.7), describes the mono-continuum model of flow in the medium, in particular, in composite medium, which is a closed description in terms of the mean fields $U(x,t)$ and $V(x,t)$.

## 2.2. Multi-continua description of flow in random composite medium

For a more detailed description for composite medium we go over to conditional averaging of the fields $u(x,t)$ and $v(x,t)$ over the composite phases and introduce the random indicator function

$$z_i(x) = \{1\ ,\ if\ \ x \in \Omega_i\ ,\ and\ \ 0\ ,\ if\ \ x \notin \Omega_i\} \tag{2.8}$$

where $\Omega_i$ is the portion of the domain $\Omega$ occupied by the i –th phase, i =1,…,m.

For any $x$ the indicator functions satisfy the relations:

$$\sum_i^m z_i(x) = 1\ ,\ \langle z_i(x)\rangle = \theta_i, \tag{2.9}$$

where $\theta_i$ is the volume fraction of the i-th phase in the composite, and for stochastically homogeneous medium $\theta_i = const$. Then from (2.9) we have

$$\sum_i^m \theta_i = 1 \tag{2.10}$$

If the phases are homogeneous ,we can write $\alpha(x) = \sum_i^m \alpha_i z_i(x)$ and $\sigma(x) = \sum_i^m \sigma_i z_i(x)$ ,where for each i-th phase $\alpha_i = const$ and $\sigma_i = const$ , and they are non-random scalars and tensors respectively. If the fields $\alpha(x)$ and $\sigma(x)$ are stochastically homogeneous , after averaging these equations we have $\langle\alpha(x)\rangle = \sum_i^m \alpha_i\theta_i$ and $\langle\sigma(x)\rangle = \sum_i^m \sigma_i\theta_i$ .

For describing the conditional averaging of the any random field $y(x)$ we use the following relation:

$$\langle y(x)\rangle_i = \langle y(x)\rangle,\quad if\ x \in \Omega_i \tag{2.11}$$

and for any random field we can write

$$\langle y(x,t)\rangle_i = \langle z_i(x)\ y(x,t)\rangle \ / \ \theta_i \tag{2.12}$$

Thus, for the conditional averaging of $y(x,t)$, it is sufficient to unconditionally average $z_i(x)\ y(x,t)$ and renormalize the result by dividing by $\theta_i$. (It should be noted that here in (2.12) and elsewhere we do not assume summation on repeating indices!)

Taking (2.12) into consideration , we introduce the phase parameter – conditionally averaged head in the i-th phase:

$$U_i(x,t) = \langle\ u(x,t)\ \rangle_i \tag{2.13}$$

It is obvious that unconditionally and conditionally averaged heads are bound by the relation :

$$U(x,t) = \sum_i^m \theta_i U_i(x,t) \tag{2.14}$$

For conditionally averaged flow velocity in the i-th phase:

$$V_i(x,t) = \langle\ v(x,t)\ \rangle_i \tag{2.15}$$

and we have

$$V(x,t) = \sum_i^m \theta_i V_i(x,t) \tag{2.16}$$

We introduce the continuum i-th phase flow velocity which is analogous to Darcy`s velocity, that is the mean velocity of liquid in pores distributed (spread) in all space.

$$V_i^*(x,t) = \theta_i V_i(x,t) \tag{2.17}$$

And from equation (2.16) we have

$$V(x,t) = \sum_{i}^{m} V_i^*(x,t) \tag{2.18}$$

It is easy to see that

$$\left\langle z_i(x)\, divv(x,t)\right\rangle = divV_i^*(x,t) + Q_i(x,t) \tag{2.19}$$

$$Q_i(x,t) = -\left\langle v(x,t)\nabla z_i(x)\right\rangle \tag{2.20}$$

Then

$$\left\langle z_i(x)\ \ \nabla u(x,t)\right\rangle = \nabla\left[\theta_i U_i(x,t)\right] + \mathrm{P}_i(x,t) \tag{2.21}$$

$$\mathrm{P}_i(x,t) = -\left\langle u(x,t)\nabla z_i(x)\right\rangle \tag{2.22}$$

According to the definition (2.8) the vector $\nabla z_i(x)$ is non-zero only on the boundary $\partial\Omega_i$ that separates the i-th phase from the different phases. To study the behavior of the vector $\nabla z_i(x)$ on the almost everywhere smooth surface $\partial\Omega_i$ we introduce at an arbitrary point $A_i \in \partial\Omega_i$ a local orthogonal coordinate system where the axis $\varsigma_A$ is orthogonal to $\partial\Omega_i$ at point $A_i$ and directed inside $\Omega_i$, and the axes $\eta_A$ and $\zeta_A$ are tangential to $\partial\Omega_i$ .

If the equation $\varsigma_A = f_i(\eta_A,\zeta_A)$ describes the face $\partial\Omega_i$, we can write $z_i = H\left[\varsigma_A - f_i(\eta_A,\zeta_A)\right]$, where H[ ] is Heaviside`s step-function. In vicinity of origin we have expansion $f_i(\eta_A,\zeta_A) = \left[\partial f(0,0)/\partial\eta_A\right]\eta_A + \left[\partial f_i(0,0)/\partial\zeta_A\right]\zeta_A$ . Because the axes $\eta_A$ and $\zeta_A$ are tangential, the above derivatives are zero and near point $A_i$ the indicator-function $z_i(\varsigma_A,\eta_A,\zeta_A) = H(\varsigma_A)$ .Therefore $\nabla z_i\big|_{A_i} = \delta(\varsigma_A)\vec{e}_{\varsigma_A}$ where $\delta(\varsigma_A)$ is the Dirac`s $\delta$-function, and $\vec{e}_{\varsigma_A}$ is a unit-vector on the axis $\varsigma_A$ .

The scalar correlation $Q_i(x,t)$ and vector correlation $\mathrm{P}_i(x,t)$ have a clear physical

significance. Let $\omega$ be an arbitrary subdomain of the domain $\Omega$. For each realization inside the subdomain $\omega$ the surface $S_i^\omega$ separates i-th phase from other phases that are distributed in $\omega$ and ,generally speaking, $S_i^\omega$ is multiply connected. We consider the expression $Q_i^\omega = |\omega|^{-1} \int_\omega Q_i(x,t)\,d\omega = -|\omega|^{-1} \int_\omega \langle v(x,t)\nabla z_i(x)\rangle\, d\omega = -|\omega|^{-1} \left\langle \int_\omega v(x,t)\nabla z_i(x)\,d\omega \right\rangle$ and after taking into account that $\nabla z_i(x)$ is zero everywhere excepting the points of surface $S_i^\omega$ , we can write $Q_i^\omega = -|\omega|^{-1} \left\langle \int_{S_i^\omega} v_n(x,t)\big|_{S_i^\omega}\, dS_i^\omega \right\rangle$. Here $v_n(x,t)\big|_{S_i^\omega}$ is the continuos projection of the vector $v(x,t)\big|_{S_i^\omega}$ on the normal $n_i(x)$ to surface $S_i^\omega$ ,that is directed inside $\Omega_i$.

Thus, the covariance $Q_i(x,t)$ is the specific mean cross-flow of fluid from the i-th continuum phase to the rest. Because the vector $\nabla z_i(x)$ in point $x \in S_i^\omega$ is perpendicular to $S_i^\omega$ and directed inside $\Omega_i$, the positive cross-flow $Q_i(x,t)$ denotes that mean flow from $\Omega_i$ is more than the flow into $\Omega_i$.

Similarly we consider the expression $\mathrm{P}_i^\omega = |\omega|^{-1} \int_\omega \mathrm{P}_i(x,t)\,d\omega = -|\omega|^{-1} \int_\omega \langle u(x,t)\nabla z_i(x)\rangle d\omega$

$= |\omega|^{-1} \left\langle \int_\omega u(x,t)\nabla z_i(x)\,d\omega \right\rangle$ and again taking into account the characteristics of the vector $\nabla z_i(x)$ , we can write $\mathrm{P}_i^\omega = -|\omega|^{-1} \left\langle \int_{S_i^\omega} u(x,t)\big|_{S_i^\omega} n_i(x)\,dS_i^\omega \right\rangle$ .

Thus the vector $\mathrm{P}_i(x,t)$ is the mean specific cross-force from the i-th phase acting on the surface that separates the other phases from the i-th phase.

And obviously, because $\sum_i z_i(x) = 1$ we have from (2.20) and (2.22) the conditions of compatibility:

$$\sum_i^m Q_i(x,t) = 0\ ,\ \sum_i^m \mathrm{P}_i(x,t) = 0 \qquad (2.23)$$

Now, multiply the equations (2.1) and (2.2) by $z_i(x)$ and taking into account the relations (2.13), (2.15), (2.17), (2.19), (2.20), (2.21) and (2.22), after averaging we have for the i-th phase

$$div V_i^*(x,t) + \alpha_i\theta_i \frac{\partial U_i(x,t)}{\partial t} + Q_i(x,t) = \theta_i f(x,t) \tag{2.24}$$

$$\sigma_i^{-1} V_i^*(x,t) + \nabla\left[\theta_i U_i(x,t)\right] + \mathrm{P}_i(x,t) = 0 \tag{2.25}$$

Although the conservative system of equations (2.24) and (2.25) is non- closed (because the cross-flows $Q_i(x,t)$ and cross-forces $\mathrm{P}_i(x,t)$ have not been evaluated in terms of $U_i(x,t)$ and $V_i(x,t)$ ), this system can be treated as the exact flow equations in the i-th continuum-phase. For this case in the mass balance condition (2.24) the term $Q_i(x,t)$ determines the rate of mass transfer between the i-th continuum-phase and the other continuum-phases. Equation (2.25) is the modified Darcy's law in the form of momentum balance and the vector $\mathrm{P}_i(x,t)$ is the specific cross-force from the i-th continuum-phase to the other continuum phases.

Such interpretation of the system of equations (2.24) and (2.25) for all composite phases together with (2.23) – the conditions of compatibility for cross-flows and cross-forces-provides a possibility of a statement about the multi-continua description for transport of flow in the composite media. In this description the conditions of mass and momentum balances in each continuum-phase are realized, and moreover, the continua exchange the fluid and momentum between them.

The system of equations (2.23), (2.24) and (2.25) looks like the phenomenological equations presented earlier by *Rubinstein* [1948] (who studied the heat transport in heterogeneous media) and *Barenblatt at al.* [1960]. But there exist significant differences. For example, the exact equation of balance of momentum (2.25) contains the vector-functions $\Psi_i$ that represent the

force interaction between the i-th phase and the other phases that were ignored by these authors. Moreover, contrary to the phenomenological models, the coefficients of the averaged equations are defined exactly through the parameters of the composite media.

For a physical interpretation of the mono and multi-continua models it is possible to use the averaged equations as the balance conditions for any volume when the volumes are sufficiently small. In examination of one representative realization the averaging is derived on surfaces or volumes. For statistical regularity of the results a different kind of averaging is necessary that applies some conditions.

One of these conditions with respect to scales of hierarchy is presented in the inequality (2.5). This condition is sufficient for the mono-continuum description, but for multi-continuum description some conditions that guarantee the stability of conditional averaging should be added. For example, let the composite system be the matrix with randomly or regularly distributed inclusions (so- called granular media) (Fig.1). It is obvious that a control volume $\omega_\Delta$ must contain a sufficient number of inclusions, and that the surface of control volume $\partial\omega_\Delta$ must dissect some part of inclusions and the fraction of the dissecting surface must be similar to volume fraction of the inclusions. Only under these conditions for volume or surface the averaging is stable and identical to the ensemble averaging. Similar condition must be met for the control volume and surface in a layered system (Fig.2).

### 2.3.Alternative multi-continua model

Along with the multi-continua model that represent non-closed system of equations (2.23), (2.24) and (2.25), it is possible to construct an alternative and equivalent multi-continua model.

In this case we introduce a scalar function

$$q_i(x,t) = \langle z_i(x)\, divv(x,t) \rangle \tag{2.26}$$

and vector-function $G_i(x,t)$

$$G_i(x,t) = \langle z_i(x)\, \nabla u(x,t) \rangle \tag{2.27}$$

From equations (2.19) and (2.21) we find that

$$q_i(x,t) = divV_i^*(x,t) + Q_i(x,t) \tag{2.28}$$

$$G_i(x,t) = \nabla[\theta_i U_i(x,t)] + \mathrm{P}_i(x,t) \tag{2.29}$$

Obviously, the cross-flow $Q_i(x,t)$ and flow $q_i(x,t)$ have different physical meanings. Whereas the $q_i(x,t)$ define the total flow from the i-th phase to the rest, the $Q_i(x,t)$ describes the flow transfer between i-th phase and different phases.

Using the functions $q_i(x,t)$ and $G_i(x,t)$ we can rewrite the system of equations (2.23), (2.24) and (2.25) in the different form

$$\alpha_i \theta_i \frac{\partial U_i(x,t)}{\partial t} + q_i(x,t) = \theta_i f(x,t) \tag{2.30}$$

$$\sigma_i^{-1} V_i^*(x,t) + G_i(x,t) = 0 \tag{2.31}$$

$$\sum_i^m q_i(x,t) = \sum_i^m divV_i^*(x,t) \tag{2.32}$$

$$\sum_i^m G_i(x,t) = \nabla U(x,t) \tag{2.33}$$

The equation (2.30) is the flow balance and the equation (2.31) is the momentum balance for the i-th phase. The equations (2.32) and (2.33) are the conditions of the compatibility for flows

$q_i(x,t)$ and forces $G_i(x,t)$. We conclude that the multi-continua description (2.23), (2.24) and (2.25) are preferable because it is more convenient for understanding the process and will be used in the subsequent analyses. In some cases we use the above relations in addition to computing the flow $q_i(x,t)$ and $G_i(x,t)$.

### 2.4. Closure problem

In order to close the conditionally averaged system and to determine the fields $U_i(x,t)$ , $V_i(x,t)$, the cross-flows $Q_i(x,t)$ and the cross-forces $\mathrm{P}_i(x,t)$, it is natural to employ the results of unconditional averaging of the system of equations (2.1),(2.2) and (2.3) (i.e. , the global averaged system of equations (2.6) and (2.7) and compare the number of dependent variables and equations for them.

It should be noted that after changing variables $U(x,t)$ and $V(x,t)$ in the global averaged closed system (2.6) and (2.7) according to equations (2.14) and (2.16) the new system is non- closed with respect to the variables $U_i(x,t)$ and $V_i(x,t)$ .

In addition we should note that although the global averaged system of equations (2.6) and (2.7) and conditional averaged system (2.23),(2.24) and (2.25) are joint the mono-continuum and multi-continua models of the same composite media and non-steady flow , both systems are independent in the sense that the equations of global averaged system in the form (2.6) and (2.7) are not derivable from the system (2.23),(2.24) and (2.25) .

Let us consider the three-dimensional flow process in a composite medium with m-phases. In this case to describe flow in one phase of multiphase media we use two scalar functions $U_i(x,t)$ and $Q_i(x,t)$ and two vector functions $V_i(x,t)$ and $\mathrm{P}_i(x,t)$. That results in a total of 8

(1+1+3+3=8) dependent variables for each phase, and 8m unknown functions for the m-phase composite. On the other hand, for the description of the process in each phase we can use one scalar equation of conservation of mass and one vector equation of conservation of momentum, that is 1+3=4 equations and for m-phase system –4 x m equations. Furthermore, for the m-phase case we have one scalar equation of the compatibility of the cross-flows and one vector equation of the compatibility of cross-forces, that is altogether 4m+4 equations.

The globally averaged system contains one scalar function $U(x,t)$ and one vector function $V(x,t)$, i.e. 4 unknown functions and two equations: one scalar equation (2.6) for conservation of mass and for the composite system as a whole we require the averaged vector equation (2.7) - the condition of conservation of momentum. This globally averaged system is closed and can be solved separately with respect to mean head $U(x,t)$ and mean velocity $V(x,t)$.

So far we have 4m + 4 + 4 = 4m+8 equations. We can add some more equations: the scalar condition (2.14) –the relation between $U(x,t)$ and $U_i(x,t)$ and the vector condition (2.16) – the relation between $V(x,t)$ and $V_i(x,t)$.

Thus, for unsteady flow we finally have 8m + 4 unknown functions for 4m+12 independent equations. It is obvious that for binary composite media, that is for m=2, we have 20 independent equations with 20 unknown functions. The system is closed and, after solving it, we can express all the unknown functions in terms of $U(x,t)$.

By summing the equations (2.24) over all i, we obtain the mass balance equation for the entire composite system of the multi-continua model:

$$div\ V(x,t) + \sum_i \alpha_i \theta_i \frac{\partial U_i(x,t)}{\partial t} = f(x,t) \qquad (2.34)$$

which contains the conditionally and unconditionally averaged fields $U_i(x,t)$ and $V(x,t)$.

Similarly, we can obtain the equation of momentum balance for the whole composite system in terms of $U(x,t)$ and $V_i^*(x,t)$ as

$$\sum_i \sigma_i^{-1} V_i^*(x,t) + \nabla U(x,t) = 0 \tag{2.35}$$

Then after comparing the equations (2.6) and (2.34), we can write one equation for $U_i(x,t)$:

$$\sum_i^m \alpha_i \theta_i \frac{\partial U_i(x,t)}{\partial t} = \alpha^* \frac{\partial U(x,t)}{\partial t} + \mu \frac{\partial}{\partial t} \lambda(DU(x,t)) \tag{2.36}$$

And after differentiating the equation (2.14) we have

$$\sum_i^m \theta_i \frac{\partial U_i(x,t)}{\partial t} = \frac{\partial U(x,t)}{\partial t} \tag{2.37}$$

For two phases i and j and $\alpha_i \neq \alpha_j$ the system of equations (2.36) and (2.37) have unique solutions of $\partial U_i(x,t)/\partial t$ and $\partial U_j(x,t)/\partial t$. Integrating them with respect to time and using the initial conditions $U_i(x,t_0)=u_0(x)$ and $\lambda[DU(x,t_0)]=0$, we obtain

$$U_i(x,t) = U(x,t) + \mu\theta_i^{-1}(\alpha_i - \alpha_j)^{-1} \lambda(DU(x,t)), \tag{2.38}$$

$$U_j(x,t) = U(x,t) + \mu\theta_j(\alpha_j - \alpha_i)^{-1} \lambda(DU(x,t))$$

Combining the globally averaged equation (2.7) with equation (2.23) and the second equation from (2.23) and taking into account the solution (2.38), we find the vectors: $\mathrm{P}_i(x,t)$ and $\mathrm{P}_j(x,t)$

$$\mathrm{P}_i(x,t) = (\sigma_j - \sigma_i)^{-1}\left[(\langle\sigma\rangle - \sigma^*)\nabla U(x,t) + \mu\gamma(DU(x,t))\right] + \mu(\alpha_i - \alpha_j)^{-1} \nabla\lambda(DU(x,t)) \tag{2.39}$$

$$\mathrm{P}_j(x,t) = (\sigma_i - \sigma_j)^{-1}\left[(\langle\sigma\rangle - \sigma^*)\nabla U(x,t) + \mu\gamma(DU(x,t))\right] + \mu(\alpha_j - \alpha_i)^{-1} \nabla\lambda(DU(x,t)) \tag{2.40}$$

We can derive the relations (2.38),(2.39) and (2.40) somewhat differently after computing $\mu\lambda\left[DU(x,t)\right]=\left\langle\alpha'(x)u'(x,t)\right\rangle$,where $u'(x,t)=u(x,t)-U(x,t)$ and $\alpha'(x)=\alpha(x)-\left\langle\alpha(x)\right\rangle$. For a two-phase composite, we have $\alpha(x)=\alpha_i z_i(x)+\alpha_j z_j(x)$ and after computing $\left\langle\alpha'(x)u'(x,t)\right\rangle$, we find $\mu\lambda(DU(x,t))=\theta_i\theta_j(\alpha_i-\alpha_j)\left[U_i(x,t)-U_j(x,t)\right]$ and the relation (2.38). It is appropriate to note that for each component of tensor $\sigma^{lm}(x)$ of two-phase composite medium the correlation moment between $\sigma^{ml}(x)$ and fluctuation of head $u'(x,t)$ can be written as $\left\langle\sigma^{ml}(x)u'(x,t)\right\rangle=\theta_i\theta_j\left(\sigma_i^{ml}-\sigma_j^{ml}\right)\left[U_i(x,t)-U_j(x,t)\right]$ and it is proportional to $\left\langle\alpha'(x)u'(x,t)\right\rangle$.This results from the fact that for two-phase composite the coefficient of correlation between any component $\sigma^{lm}(x)$ and $\alpha(x)$ is +1 if $K^{lm}=\left(\sigma_i^{lm}-\sigma_j^{lm}\right)\left(\alpha_i-\alpha_j\right)$is positive, and –1 if $K^{lm}$ is negative. Similarly we find $\left\langle\sigma'(x)\ \nabla u'(x,t)\right\rangle=\left(\sigma_i-\sigma_j\right)\left\{\theta_i\theta_j\ \left[\nabla U_i(x,t)-\nabla U_j(x,t)\right]+\mathrm{P}_i(x,t)\right\}$. Using the relationship $\left\langle\sigma'(x)\nabla u'(x,t)\right\rangle=\left(\sigma^*-\left\langle\sigma\right\rangle\right)\nabla U(x,t)-\mu\gamma(DU)$ which derived from (2.7), we can directly obtain the relations (2.39) and (2.40) .

The mean phase velocities are

$$V_i^*(x,t)=-\ \sigma_i\ G_i(x,t)\ ,\ V_i^*(x,t)=-\sigma_j G_i(x,t), \tag{2.41}$$

where the mean phase forces are

$$G_i(x,t)=\left(\sigma_j-\sigma_i\right)^{-1}\left[\left(\sigma_j-\sigma^*\right)\nabla U(x,t)+\mu\gamma(DU(x,t))\right]+2\mu\left(\alpha_i-\alpha_j\right)^{-1}\nabla\lambda(DU(x,t))$$

(2.42)

$$G_j(x,t)=(\sigma_i-\sigma_j)^{-1}\left[(\sigma_i-\sigma^*)\nabla U(x,t)+\mu\gamma(DU(x,t))\right]+2\mu(\alpha_j-\alpha_i)^{-1}\nabla\lambda(DU(x,t))$$

Substituting (2.38) in (2.24), it is possible to determine the cross-flows $Q_i(x,t)$ as

$$Q_i(x,t)=\theta_i\left\{f(x,t)-divV_i(x,t)-\alpha_i\left[\frac{\partial U(x,t)}{\partial t}+\frac{\mu}{\theta_i(\alpha_i-\alpha_j)}\frac{\partial\lambda(DU(x,t))}{\partial t}\right]\right\} \tag{2.43}$$

So, let the mono-continua description of flow in a random composite system is realized, e.g. are known the tensor of effective conductivity for all system $\sigma^*$, the expressions : the scalar $\mu\lambda[DU(x,t)]$ and vector $\mu\gamma[DU(x,t)]$.

We have shown here that in this case for two-phase $i$ and $j$ composite random medium we can Find these fields: the phase mean heads $U_i(x,t)$ and $U_j(x,t)$, the phase mean Darcy`s velocity $V_i^*(x,t)$ and $V_j^*(x,t)$, the cross-flows $Q_i(x,t)$ and $Q_j(x,t)$, cross-forces $\mathrm{P}_i(x,t)$ and $\mathrm{P}_j(x,t)$, phase flows $q_i(x,t)$ and $q_j(x,t)$, phase forces $G_i(x,t)$ and $G_j(x,t)$.

## 2.5. Steady-state flow

Let the source density $f(x,t)$ and boundary function $\varphi(x,t)$ for large $t>>t_0$ weakly depends on $t$. In this case the flow tend to steady-state and we can use for steady-state stage the above results . All one has to do is to set all derivatives with respect to time $t$ to zero in equations (2.6) and (2.24) and in the expansions $\lambda[DU(x,t)]$ and $\gamma[DU(x,t)]$.

It is significant to note, that because the correlations $\langle\alpha'(x)u'(x,t)\rangle$ and $\langle\sigma^{lm}(x)u'(x,t)\rangle$ are proportional, these correlations for $t\to\infty$ have finite limits. Generally speaking, these correlatons are different from zero at these points $x$, where the conductivity components $\sigma^{lm}(x)$

are correlated with field $u(x) = \lim_{t\to\infty} u(x,t)$ . It is obvious that at these points $x$ the mean heads $U_i(x) \neq U_j(x)$ .

## 2.6. Meso-equilibrium approximation

It is a common knowledge that for basic processes in a natural heterogeneous system flow velocities are typically small. When a some perturbation is applied into the flow, the relatively short transition stage in the system creates a slowly changing process in time. Naturally, this stage of the process has been the main interest for application.

Bearing in mind that by applying sufficiently small $\mu$ on the meso-scale the system tends fast to a local equilibrium of mean phase heads. This state can be called as meso-equilibrium state. However, for a finite $\mu$ this is not to say that the mean phase heads are locally equal or are constant in space and time. As we shoved above, even when the flow is in steady-state, for finite $\mu$ in some cases the mean phase heads can be different. And only for $\mu \to 0$ the mean head difference tends to zero.

In this limiting case in all presented equations all terms containing small parameter $\mu$ and its positive powers can be neglected. Under these conditions, when a very strong heterogeneity exists, the terms to be neglected can contain large parameters and possibly impose some restriction on the small parameter $\mu$, such that accuracy of the averaged equations is sufficient at least outside the temporal border layer [ e.g.,*Bakhvalov and Panasenko,* 1989 ].

Let us consider the process of flow in a heterogeneous medium in which the scale of heterogeneity $\mu$ is so small that in the averaged equations (2.6) and (2.7) it is possible to retain only the dominant terms, i.e. $\mu \to 0$. Then, from (2.38) it follows that

$$U_i(x,t) = U_j(x,t) = U(x,t) \tag{2.44}$$

and from (2.39) and (2.40) the cross-force vectors $\mathrm{P}_i(x,t)$ and $\mathrm{P}_j(x,t)$ take the forms

$$\mathrm{P}_i(x,t) = \left(\sigma_j - \sigma_i\right)^{-1}\left(\langle\sigma\rangle - \sigma^*\right)\nabla U(x,t) \ , \ \mathrm{P}_j(x,t) = \left(\sigma_i - \sigma_j\right)^{-1}\left(\langle\sigma\rangle - \sigma^*\right)\nabla U(x,t) \quad (2.45)$$

It follows from (2.45) that in a medium with heterogeneous conductivity, the cross-force $\mathrm{P}_i(x,t)$ is zero only in a layered system, provided that $\nabla U(x,t)$ is directed along the layers.

For the mean phase velocities $V_i(x,t)$ we have

$$V_i(x,t) = -\sigma_i^* \nabla U(x,t) \quad (2.46)$$

where the tensor $\sigma_i^*$ is

$$\sigma_i^* = \theta_i^{-1}\sigma_i\left(\sigma_j - \sigma_i\right)^{-1}\left(\sigma_j - \sigma^*\right) \quad (2.47)$$

which can be called the phase conductivity. It satisfies the relations

$$\sum_i \theta_i \sigma_i^{-1}\sigma_i^* = I \quad , \quad \sum_i \theta_i \sigma_i^* = \sigma^* \quad (2.48)$$

For the cross-flows in the meso-equilibrium approximation we have from (2.43)

$$Q_i(x,t) = \theta_i\left\{f(x,t) + div\left[\sigma_i^* \nabla U(x,t)\right] - \alpha_i \frac{\partial U(x,t)}{\partial t}\right\} \quad (2.49)$$

or after replacing the $\partial U(x,t)/\partial t$ from global averaged system (2.6) and (2.7) by setting $\mu = 0$ and substituting into (2.49) we have the cross-flow in another form

$$Q_i(x,t) = \frac{\theta_i}{\langle\alpha\rangle}\left\{\left(\langle\alpha\rangle - \alpha_i\right) f(x,t) + div\left[\left(\langle\alpha\rangle\sigma_i^* - \alpha_i\sigma^*\right)\nabla U(x,t)\right]\right. \quad (2.50)$$

If for large time the flow is steady-state, the dependence of the cross-flows $Q_i(x)$ in (2.50) on the parameters $\alpha_i$ is only by appearance because in this case $div\left(\sigma^* \ \nabla U(x)\right) + f(x) = 0$ then we have from (2.50):

$$Q_i(x) = \theta_i \left[ f(x) + div \left( \sigma_i^* \nabla U(x) \right) \right] \tag{2.51}$$

For meso-equilibrium stage, the general equation of phase flow $q_i(x,t)$ is

$$q_i(x,t) = \frac{\theta_i}{\langle \alpha \rangle} \left[ \left( \langle \alpha \rangle - \alpha_i \right) f(x,t) - \alpha_i \, div \left( \sigma^* \nabla U(x,t) \right) \right] \tag{2.52}$$

If the composite system is micro and macro isotropic, and the tensors $\sigma_i$ and $\sigma^*$ are isotropic, then for $f(x,t) = 0$ we have

$$Q_i(x,t) = \theta_i \frac{\langle \alpha \rangle \sigma_i^* - \alpha_i \sigma^*}{\langle \alpha \rangle} \nabla^2 U(x,t) \tag{2.53}$$

$$q_i(x,t) = -\theta_i \frac{\alpha_i \sigma^*}{\langle \alpha \rangle} \nabla^2 U(x,t) \tag{2.54}$$

or, in another form,

$$Q_i(x,t) = \theta_i \frac{\langle \alpha \rangle \sigma_i^* - \alpha_i \sigma^*}{\sigma^*} \frac{\partial U(x,t)}{\partial t} \tag{2.55}$$

$$q_i(x,t) = -\theta_i \alpha_i \frac{\partial U(x,t)}{\partial t} \tag{2.56}$$

It is obvious that in a fully isotropic medium the phase cross-flows $Q_i(x) = 0$ and phase flows $q_i(x) = 0$ when the flow is steady-state.

We can rewrite equation (2.55) as

$$Q_i(x,t) = \theta_i \alpha_i \frac{\kappa_i^* - \kappa^*}{\kappa^*} \frac{\partial U(x,t)}{\partial t} \tag{2.57}$$

where $\kappa^* = \sigma^* / \langle \alpha \rangle$ is effective diffusivity for all system, and $\kappa_i^* = \sigma_i^* / \alpha_i$ is the effective phase diffusivity, which is obviously different from $\kappa_i = \sigma_i / \alpha_i$, the phase local diffusivity.

As can be seen from equation (2.57) the sign of cross-flow $Q_i(x,t)$ is defined by the relation between parameters $\kappa_i^*$ , $\kappa^*$ that are dependent on the quantities $\sigma_i$ $/\sigma_j$ *and* $\alpha_i$ / $\alpha_j$ as well as on the geometry of heterogeneity.

Let the conductivity of the composite system be homogeneous, that is $\sigma_i = \sigma_j = \sigma$. For any $f(x,t)$ we have from (2.55)

$$Q_i(x,t) = \theta_i\, \theta_j \left(\alpha_j - \alpha_i\right) \frac{\partial U(x,t)}{\partial t} \tag{2.58}$$

If $\alpha_i < \alpha_j$ the cross-flow $Q_i(x,t)$ has the same sign as $\partial U(x,t)/\partial t$, that is when the mean pressure increases in time, the i-th phase deliver flow to the j-th phase. Conversely, when the mean pressure falls, the i-th phase obtain flow from the j-th phase. If $\alpha_i > \alpha_j$ the signs are opposite and , when the mean pressure increases, the i-th phase obtains flow, and when mean pressure falls , the i-th phase delivers flow to the j-th phase. In the case where $\alpha_i \to a$, $\alpha_j \to \alpha$, but $\sigma_i \neq \sigma_j$, we have

$$Q_i = \theta_i \alpha \frac{\sigma_i^* - \sigma^*}{\sigma^*} \frac{\partial U(x,t)}{\partial t} \tag{2.59}$$

It is easy to show that $\sigma_i^* < \sigma^*$ when $\sigma_i < \sigma_j$ and for $\sigma_i > \sigma_j$ the inequality is $\sigma_i^* > \sigma^*$. So, when $\sigma_i < \sigma_j$ the signs of the cross-flow $Q_i(x,t)$ and the derivative $\partial U(x,t)/\partial t$ are opposite and for $\sigma_i > \sigma_j$ the signs are identical. It is interesting to examine the case $\sigma_i << \sigma_j$ and $\theta_i >> \theta_j$ that in some sense can be related to the i-th porosity system with the j-th fracture system. Neglecting some terms in general system of equations we obtain

$$\alpha_i\theta_i \frac{\partial U(x,t)}{\partial t} + Q_i(x,t) = \theta_i f(x,t) \quad , \quad \theta_j \, div \, V_j(x,t) - Q_i(x,t) = \theta_j f(x,t) \tag{2.60}$$

$$V_i(x,t) \approx 0 \qquad , \qquad V_j(x,t) = -\theta_j^{-1} \, \sigma^* \, \nabla U(x,t) \tag{2.61}$$

The system of equation (2.60) and (2.61) bears similarities to the phenomenological equations of flow in fissured porous media derived by *Barenblatt at al.* [1960]. The difference lies in the fact that the system of (2.60) and (2.61) is closed, and all it parameters are completely defined.

Eliminating the phase cross-flow $Q_i(x,t)$ leads to the global averaged equation of pressure $U(x,t)$

$$\alpha_i \, \theta_i \frac{\partial U(x,t)}{\partial t} = \sigma^* \nabla^2 U(x,t) + f(x,t) \tag{2.62}$$

After determining $U(x,t)$ from (2.62) under appropriate initial and boundary conditions we can determine the i-th phase cross-flow

$$Q_i(x,t) = \theta_i \left[ f(x,t) - \alpha_i \frac{\partial U(x,t)}{\partial t} \right] \tag{2.63}$$

and from (2.61)-the j-th phase flow velocity $V_j(x,t)$, the phase flows $q_i(x,t) = Q_i(x,t)$, $q_j \approx 0$.

We now examine the steady-state flow when $f(x) = 0$ in an binary composite system that is anisotropic for mean phase flow. There can be three variants in this case.

1. Either one or both of the tensors $\sigma_i$ and $\sigma_j$ are anisotropic, and the tensor $\sigma^*$ is anisotropic.

2. Either one or both of the tensors $\sigma_i$ and $\sigma_j$ are anisotropic, but the tensor $\sigma^*$ is isotropic.

3. Tensors $\sigma_i$ and $\sigma_j$ are isotropic but the tensor $\sigma^*$ is anisotropic.

In all of three cases the tensors $\sigma_i^*$ and $\sigma_j^*$ are anisotropic and the globally averaged equation is $div\ \left(\sigma^*\ \nabla U(x)\right) = 0$, where the tensor $\sigma^*$ as noted in case 2 can be isotropic. Analysis of the expression for $Q_i(x)$ in (2.51) shows that for steady-state flow with $f(x) = 0$,

$$Q_i(x) = \theta_i div\left(\sigma_i^* \nabla U(x)\right) \tag{2.64}$$

Because in the case of phase flow anisotropy the tensors $\sigma_i^*$ and $\sigma^*$ are non-similar (i.e., the components of these tensors are non-proportional ) and if $\nabla\ U(x) \neq const$, the phase cross-flow $Q_i(x)$ is non-zero.

This result is paradoxical at first sight, but besides the demonstrated calculation, the detailed qualitative analysis explains this effect.

Let the composite medium be a granular medium, that matrix conductivity be $\sigma_j$, and the conductivity of the inclusions be $\sigma_i$ (Fig.1). It is obvious that for steady-state flow, the cross-flow from each i-th phase inclusions in the j-th phase matrix is zero. On the other hand, here we argue that the mean cross-flow from the i-th continuum into the j-th continuum is finite and differ from zero under these conditions.

This contradiction stems from the expanded incorrect transfer of the mechanism of cross-flow from individual inclusion to the aggregate of many inclusions that are contained in the representative control volume. As indicated above, for those inclusions the basic part is completely confined in the control volume and the cross-flow from these inclusions into the matrix is zero when flow is steady-state. But there exists the cross-flow inside the control volume at the surface of those inclusions that are dissected by the control volume surface. If the

composite medium is anisotropic for mean phase flow and $\nabla\ U(x) \neq const$, the cross-flows on the cut are not compensated for meso-scale control volume.

We now study a more clear example of layered system that contains homogeneous layers with conductivity $\sigma_i$ and $\sigma_j$ (Fig.2). Such a system is micro or macro anisotropic. Each layer intersects the border of control volume at least twice and since it is assumed that the gradient of the mean pressure is not constant, the flow from layer outside the border of the control volume is statistically non-compensated. This means that the cross-flow from i-th layers to j-th layers is statistically non-compensated.

The discussions above show that the multi-continuum description has non-trivial exceptions. For example, the mean cross-flow in granular composite system with isolated inclusions under some conditions is non-zero, whereas for each inclusions the cross-flow is zero, is a peculiar kind of "payment" for continual description of flow in inclusions that do not compose a connected space.

## 3. EXAMPLES

Let us now study some cases where the meso-equilibrium globally averaged systems can be easily constructed, thus the computation of simple closing relations for the phase cross-flows $Q_i(x,t)$ and the phase cross-forces $\mathrm{P}_i(x,t)$ are possible.

### 3.1Case1

Let a two-dimensional infinite random heterogeneous system be composed of two subdomains with isotropic conductivities $\sigma_i$ and $\sigma_j$ that are statistically equivalently distributed in the plane ( for example, like an unbounded chess board with randomly distributed "white" and "black" squares). In this case the mean concentration of the phases are equal and $\theta_i = \theta_j = 1/2$.

It is well known (e.g., *Shvidler, 1985*) the effective conductivity for such a systems is isotropic and $\sigma^* = \sqrt{\sigma_i\,\sigma_j}$ , then from (2.46) and (2.47) :

$$\sigma_i^* = \frac{2\sigma_i\sqrt{\sigma_j}}{\sqrt{\sigma_i}+\sqrt{\sigma_j}} \quad , \quad \sigma_j^* = \frac{2\sigma_j\sqrt{\sigma_i}}{\sqrt{\sigma_i}+\sqrt{\sigma_j}} \tag{3.1}$$

$$V_i(x,t) = -\frac{2\sigma_i\sqrt{\sigma_j}}{\sqrt{\sigma_i}+\sqrt{\sigma_j}}\nabla U(x,t)\ ,\ V_j(x,t) = -\frac{2\sigma_j\sqrt{\sigma_i}}{\sqrt{\sigma_i}+\sqrt{\sigma_j}}\nabla U(x,t) \tag{3.2}$$

$$\mathrm{P}_i(x,t) = \frac{1}{2}\frac{\sqrt{\sigma_j}-\sqrt{\sigma_i}}{\sqrt{\sigma_i}+\sqrt{\sigma_j}}\nabla U(x,t)\ ,\ \mathrm{P}_j(x,t) = -\mathrm{P}_i(x,t) \tag{3.3}$$

Further, by setting $f(x,t) = 0$ ,

$$Q_i(x,t) = \frac{\sqrt{\sigma_i\sigma_j}\left(\alpha_j\sqrt{\sigma_i}-\alpha_i\sqrt{\sigma_j}\right)}{2\langle\alpha\rangle\left(\sqrt{\sigma_i}+\sqrt{\sigma_j}\right)}\nabla^2 U(x,t) \quad , \quad Q_j(x,t) = -Q_i(x,t) \tag{3.4}$$

$$q_i(x,t) = -\frac{\alpha_i\sqrt{\sigma_i\,\sigma_j}}{\alpha_i+\alpha_j}\nabla^2 U(x,t) \quad , \quad q_j(x,t) = -\frac{\alpha_j\sqrt{\sigma_i\sigma_j}}{\alpha_i+\alpha_j}\nabla^2 U(x,t) \tag{3.5}$$

It is easy to see that when $\sigma_i/\sigma_j = \alpha_i^2/\alpha_j^2$ the mean cross-flow $Q_i(x,t) = 0$ at any time $t$ when flow is transient. The mean cross-force $\mathrm{P}_i(x,t) = 0$ only if $\sigma_i = \sigma_j$. Because the system is micro and macro- isotropic, the phase mean cross-flow $Q_i(x) = 0$ for steady-state flow.

### 3.2.Case2

The second case is different from the previous one only in the sense that conductivity of subdomains are anisotropic

$$\sigma_i = \begin{pmatrix} a & 0 \\ 0 & b \end{pmatrix},\ \sigma_j = \begin{pmatrix} b & 0 \\ 0 & a \end{pmatrix} \tag{3.6}$$

This system is globally isotropic and $\sigma^* = \sqrt{ab}$ (Shvidler 1985). After simple manipulation we obtain

$$\sigma_i^* = \frac{2}{\sqrt{a}+\sqrt{b}}\begin{pmatrix}\sqrt{b} & 0\\ 0 & \sqrt{a}\end{pmatrix}, \quad \sigma_j^* = \frac{2}{\sqrt{a}+\sqrt{b}}\begin{pmatrix}\sqrt{a} & 0\\ 0 & \sqrt{b}\end{pmatrix} \tag{3.7}$$

$$V_i(x,t) = -\frac{2\sqrt{ab}}{\sqrt{a}+\sqrt{b}}\begin{pmatrix}\sqrt{a} & 0\\ 0 & \sqrt{b}\end{pmatrix}\nabla U(x,t)\ ,\ V_j(x,t) = -\frac{2\sqrt{ab}}{\sqrt{a}+\sqrt{b}}\begin{pmatrix}\sqrt{b} & 0\\ 0 & \sqrt{a}\end{pmatrix}\nabla U(x,t) \tag{3.8}$$

$$\mathrm{P}_i(x,t) = \frac{\sqrt{b}-\sqrt{a}}{2\left(\sqrt{a}+\sqrt{b}\right)}\begin{pmatrix}1 & 0\\ 0 & -1\end{pmatrix}\nabla U(x,t) \tag{3.9}$$

$$Q_i(x,t) = \frac{1}{2}\left\{ f(x,t) + \frac{2\sqrt{ab}}{\sqrt{a}+\sqrt{b}}\nabla\left[\begin{pmatrix}\sqrt{a} & 0\\ 0 & \sqrt{b}\end{pmatrix}\nabla U(x,t)\right] - \alpha_i\frac{\partial U(x,t)}{\partial t}\right\} \tag{3.10}$$

$$q_i(x,t) = \frac{1}{2}\left[ f(x,t) - \alpha_i\frac{\partial U(x,t)}{\partial t}\right] \tag{3.11}$$

It is obvious that when $f(x) = 0$ and under steady-state flow the globally averaged equation is $\nabla^2 U(x) = 0$ and the phase cross-flow $Q_i(x) = 0$ only if $a = b$ or $\nabla U(x) = const$. The phase cross-force $\mathrm{P}_i(x) = 0$ only when $a = b$.

### 3.3.Case 3

The next example involves three-dimensional, two-phase layered medium composed of homogeneous anisotropic layers. Let the layers be directed perpendicular to the $x_3$-axis, and the phases conductivity be such that

$$\sigma_i = \begin{pmatrix} a_i & 0 & 0 \\ 0 & b_i & 0 \\ 0 & 0 & c_i \end{pmatrix} \quad , \quad \sigma_j = \begin{pmatrix} a_j & 0 & 0 \\ 0 & b_j & 0 \\ 0 & 0 & c_j \end{pmatrix} \tag{3.12}$$

Then

$$\sigma^* = \begin{pmatrix} \langle a \rangle & 0 & 0 \\ 0 & \langle b \rangle & 0 \\ 0 & 0 & \langle c^{-1} \rangle^{-1} \end{pmatrix}, \sigma_i^* = \begin{pmatrix} a_i & 0 & 0 \\ 0 & b_i & 0 \\ 0 & 0 & \langle c^{-1} \rangle^{-1} \end{pmatrix} \tag{3.13}$$

Where

$$\langle a \rangle = a_i \theta_i + a_j \theta_j \quad , \quad \langle b \rangle = b_i \theta_i + b_j \theta_j \quad , \quad \langle c^{-1} \rangle^{-1} = c_i c_j \left( c_i \theta_j + c_j \theta_i \right)^{-1} \tag{3.14}$$

and the global averaged flow equation is

$$\langle \alpha \rangle \frac{\partial U(x,t)}{\partial t} = \langle a \rangle \frac{\partial^2 U(x,t)}{\partial x_1^2} + \langle b \rangle \frac{\partial^2 U(x,t)}{\partial x_2^2} + \langle c^{-1} \rangle^{-1} \frac{\partial^2 U(x,t)}{\partial^2 x_3^2} + f(x,t) \tag{3.15}$$

Then, from (2.46) and (2.45), we compute the components of the i-th phase flow velocity and cross-force as

$$V_{i1}(x,t) = - a_i \frac{\partial U(x,t)}{\partial x_1} \quad , \quad V_{i2}(x,t) = - b_i \frac{\partial U(x,t)}{\partial x_2} \quad , \quad V_{i3}(x,t) = - \langle c^{-1} \rangle^{-1} \frac{\partial U(x,t)}{\partial x_3} \tag{3.16}$$

$$\mathrm{P}_{i1}(x,t) = 0 \ , \ \mathrm{P}_{i2}(x,t) = 0 \ , \ \mathrm{P}_{i3}(x,t) = \theta_i^{-1} \frac{\langle c \rangle - \langle c^{-1} \rangle^{-1}}{c_j - c_i} \frac{\partial U(x,t)}{\partial x_3} \tag{3.17}$$

Notice that the longitudinal components of the phase cross-force are zero. This is partly because in our example the longitudinal main axes of the tensors $\sigma_i$ and $\sigma_j$ are aligned with the layers.

For the mean phase cross-flow and phase flow we can write

$$Q_i(x,t) = \theta_i \left[ f(x,t) + a_i \frac{\partial^2 U(x,t)}{\partial x_1^2} + b_i \frac{\partial^2 U(x,t)}{\partial x_2^2} + \langle c^{-1} \rangle^{-1} \frac{\partial^2 U(x,t)}{\partial x_3^2} - \alpha_i \frac{\partial U(x,t)}{\partial t} \right] \tag{3.18}$$

$$q_i(x,t) = -\alpha_i\,\theta_i \frac{\partial U(x,t)}{\partial t} \tag{3.19}$$

If the averaged flow is one-dimensional and perpendicular to the layers, the cross-flow is

$$Q_i(x,t) = \theta_i\left(\langle\alpha\rangle - \alpha_i\right)\frac{\partial U(x,t)}{\partial t} \tag{3.20}$$

and is proportional to $q_i(x,t)$.

Let the averaged three-dimensional flow be a steady-state. Then the averaged equation is

$$\langle a\rangle \frac{\partial^2 U(x)}{\partial x_1^2} + \langle b\rangle \frac{\partial^2 U(x)}{\partial x_2^2} + \left\langle c^{-1}\right\rangle^{-1} \frac{\partial^2 U(x)}{\partial x_3^2} + f(x) = 0 \tag{3.21}$$

and for the cross-flow $Q_i(x)$ we have

$$Q_i(x) = \theta_i\left[f(x) + a_i \frac{\partial^2 U(x)}{\partial x_1^2} + b_i \frac{\partial^2 U(x)}{\partial x_2^2} + \left\langle c^{-1}\right\rangle^{-1} \frac{\partial^2 U(x)}{\partial x_3^2}\right] \tag{3.22}$$

It is obvious that for $f(x) = 0$, if the longitudinal components of tensors $\sigma_i$ ,$\sigma_j$ are not equal and when $\nabla U(x,t) \neq const$, the phase cross-flow $Q_i(x) \neq 0$.

### 3.4.Case 4

We consider a model that imitates some porous space with system of fractures. Let an unbounded porous media – a matrix with isotropic conductivity $\sigma_m$ and diffusivity $\alpha_m$ be randomly and statistically uniformly dissected by three infinite and mutually orthogonal systems of plates with parameters $\sigma_f$ and $\alpha_f$ that simulate the infinite fractures along each Cartesian axis. In this case the Cartesian axis are principal axis for the global effective conductivity tensor.

We assume that the matrix conductivity $\sigma_m$ is significantly smaller than the fracture conductivity $\sigma_f$ and the concentration of each parallel system of the fractures $c_k$ (orthogonal to the k-Cartesian axis ) is significantly less than unity.

Under these assumptions the $\sigma_k^*$ - mean component of the effective conductivity tensor that are associated with k-axis is defined mainly by the matrix and the fractures that are parallel to k-axis. The contribution in the k-component of effective conductivity from the fractures that are orthogonal to k-axis is significantly less if the $\sigma_m << \sigma_f$, and if the fracture concentration $c = c_1 + c_2 + c_3 << 1$.

Thus effective conductivity tensor $\sigma^*$ is approximated by

$$\sigma^* = \langle\sigma\rangle I - \sigma_f C \tag{3.23}$$

where $\langle\sigma\rangle = \sigma_m(1-c) + \sigma_f c$, and the tensor $C$ is

$$C = \begin{pmatrix} c_1 & 0 & 0 \\ 0 & c_2 & 0 \\ 0 & 0 & c_3 \end{pmatrix} \tag{3.24}$$

Then the global averaged flow equation in a fractured medium with porous parallelepiped blocks has the form

$$\nabla\left[\sigma^* \nabla U(x,t)\right] + f(x,t) = \langle\alpha\rangle \frac{\partial U(x,t)}{\partial t} \tag{3.25}$$

After using for $\sigma^*$ the expression (3.23) we have

$$\sigma_m^* = \sigma_m\left[I + \frac{\sigma_f}{(1-c)(\sigma_f - \sigma_m)} C\right],\ \sigma_f^* = \sigma_f\left[I - \frac{\sigma_f}{c(\sigma_f - \sigma_m)} C\right] \tag{3.26}$$

$$V_m(x,t) = -\sigma_m\left[I + \frac{\sigma_f}{(1-c)\ (\sigma_f - \sigma_m)}C\right]\nabla U(x,t)\ ,\ V_f(x,t) = -\sigma_f\left[I - \frac{\sigma_f}{c\ (\sigma_f - \sigma_m)}C\right]\nabla U(x,t)$$

The mean m-th and f-th phase cross-forces are

$$\mathrm{P}_m(x,t) = \frac{\sigma_f}{\sigma_f - \sigma_m}C\nabla U(x,t)\ ,\ \mathrm{P}_f(x,t) = \frac{\sigma_f}{\sigma_m - \sigma_f}C\nabla U(x,t) \tag{3.27}$$

Then for mean phase cross-flow

$$Q_m(x,t) = (1-c)\,f(x,t) + \sigma_m(1-c)\nabla\left\{\left[I + \frac{\sigma_f}{(1-c)(\sigma_f - \sigma_m)}C\right]\nabla U(x,t)\right\} - \alpha_m(1-c)\frac{\partial U(x,t)}{\partial t} \tag{3.28}$$

It is obvious that if the effective conductivity tensor is non-isotropic (for this it is sufficient that not all concentrations $c_k$ are equal), the source density $f(x)$ is zero under steady-state flow, and if $\nabla U(x) \neq const$, then the mean phase cross-flow $Q_m(x) \neq 0$.

If the porous medium with fractures is macro-isotropic ( $c_1 = c_2 = c_3 = c/3$ ), we have

$$\sigma^* = \left[\sigma_m(1-c) + \sigma_f(2c/3)\right]I \tag{3.30}$$

$$\sigma_m^* = \sigma_m\left[1 + \frac{\sigma_f\, c}{3(1-c)(\sigma_f - \sigma_m)}\right]I \quad , \quad \sigma_f^* = \sigma_f\left[1 - \frac{\sigma_f}{3(\sigma_f - \sigma_m)}\right]I \tag{3.31}$$

$$V_m(x,t) = -\sigma_m\left[1 + \frac{\sigma_f c}{3(1-c)(\sigma_f - \sigma_m)}\right]\nabla U(x,t)\ ,\ V_f(x,t) = -\sigma_f\left[1 - \frac{\sigma_f}{3\ (\sigma_f - \sigma_m)}\right]\nabla U(x,t) \tag{3.32}$$

$$\mathrm{P}_m(x,t) = \frac{c\ \ \sigma_f}{3\ (\sigma_f - \sigma_m)}\nabla U(x,t) \tag{3.33}$$

$$Q_m(x,t) = (1-c)\left\{ f(x,t) + \sigma_m \left[ 1 + \frac{c\sigma_f}{3(1-c)(\sigma_f - \sigma_m)} \right] \nabla U(x,t) - \alpha_m \frac{\partial U(x,t)}{\partial t} \right\} \qquad (3.34)$$

In this case $Q_m(x) = Q_f(x) = 0$ when $f(x) = 0$ and the flow is steady-state.

We have now completed the analysis of the mesoscale equilibrium approximation for multi-continuum models in stochastic media. It should be noted again that the more exact description that takes into account the deviation from the mesoscale equilibrium resulted in a better representation of global averaging.

## 4. PERIODIC COMPOSITE SYSTEMS

### 4.1. Problem formulation. Mono-continuum description

Let us now introduce a positive length-dimension parameter $\varepsilon$ and determine the functions $\sigma^\varepsilon(x) = \sigma(x/\varepsilon)$ and $\alpha^\varepsilon(x) = \alpha(x/\varepsilon)$, for which $Y$-periodic functions $\sigma(y)$ *and* $\alpha(y)$ are $\varepsilon Y$ - periodic in the variable $x$. As $\varepsilon \to 0$ the edges of the period of these functions tend to zero and, consequently, $\sigma^\varepsilon(x)$ and $\alpha^\varepsilon(x)$ are a model of the system with small-scale periodic heterogeneity.

Following *Bakhvalov and Panasenko* [1989 ], we use the standard method of solving the equations (2.1), (2.2 ) and (2.3) in which $\alpha(x)$ and $\sigma(x)$ are periodic functions. The solution is found in the form of two-scale expansion in the fast $y = x/\varepsilon$ and slow $x$ variables asymptotic with respect to the parameter $\varepsilon$

$$u^\varepsilon(x,t) = \sum_{n=0}^{\infty} \varepsilon^n u_n(x,y,t) \quad , \quad v^\varepsilon(x,t) = \sum_{n=0}^{\infty} \varepsilon^n v_n(x,y,t) \qquad (4.1)$$

where the functions $u_n(x,y,t)$ and $v_n(x,y,t)$ are Y-periodic in the fast variable $y$.

Substituting (4.1) in the system (2.1), (2.2) and (2.3) that describes the flow in periodic media also, if $\alpha(x)$ and $\sigma(x)$ are periodic functions, and expanding the operators in the powers of $\varepsilon$, we can obtain a set of equations for $u_n(x,y,t)$, $v_n(x,y,t)$ whose solutions satisfy the expansion (4.1). Averaging these equations over the representative volume of the region $\omega_\Delta$ (whose meso-scale $\Delta$ satisfies the inequalities $\varepsilon << \Delta << l_\Omega$ ) is equivalent to averaging over the domainY-cell period by means of the operator $\langle f(x,y,t)\rangle = |Y|^{-1}\int_Y f(x,y,t)\,dy$, where $|Y|$ is volume of domain $Y$.

The averaged system for the mean functions $U(x,t)=\langle u^\varepsilon(x,t)\rangle$, $V(x,t)=\langle v^\varepsilon(x,t)\rangle$ is

$$divV + \alpha^* \frac{\partial U}{\partial t} + \varepsilon \frac{\partial \bar{\lambda}(x,t)}{\partial t}(x,t) = f \ , \ \bar{\lambda}(x,t) = \langle \alpha(y)(u_1 + \varepsilon u_2 + ...)\rangle \qquad (4.2)$$

$$(\sigma^*)^{-1} V(x,t) + \nabla U(x,t) = \varepsilon \bar{\gamma}(x,t) \ , \ \bar{\gamma}(x,t) = -\sigma(y)(\nabla_x u_1 + \nabla_y u_2 + \varepsilon \nabla_x u_2 + ....) \ \rangle \qquad (4.3)$$

The effective storage capacity $\alpha^* = const$ and conductivity tensor $\sigma^* = const$ can be written in the form:

$$\alpha^* = \langle \alpha(y)\rangle \ , \ \sigma_{ij}^* = \langle \sigma_{ij}(y)\rangle + \left\langle \sum_k \sigma_{ik}(y) \frac{\partial W^j}{\partial y_k} \right\rangle \qquad (4.4)$$

where $W^l(y)$ is the Y-periodic generalized solution of the problem

$$\sum_{i,j} \frac{\partial}{\partial y_i}\left[\sigma_{ij}(y)\frac{\partial W^l}{\partial y_j}\right] = -\sum_i \frac{\partial}{\partial y_i}\sigma_{ij}(y) \ , \ \langle W^l(y)\rangle = 0 \qquad (4.5)$$

The expansion (4.1) for $u^\varepsilon(x,y,t)$ can be written in the form:

$$u^\varepsilon(x,t) = u_0(x,t) + \varepsilon u_1(x,y,t) + \varepsilon^2 u_2(x,y,t) + ... \qquad (4.6)$$

where

$$u_0(x,t) = U(x,t) \quad , \quad u_1(x,y,t) \quad = \quad \sum_s W^s(y)\frac{\partial U(x,t)}{\partial x_s} \tag{4.7}$$

$$u_2(x,y,t) \quad = \quad W(y)\frac{\partial U(x,t)}{\partial t} + \sum_{r,p} W^{rp}(y)\frac{\partial^2 U(x,t)}{\partial x_r \partial x_p} \tag{4.8}$$

Here $W(y)$ and $W^{rp}(y)$ are the Y-periodic solutions of the following equations

$$\sum_{k,j}\frac{\partial}{\partial y_k}\left[\sigma_{kj}(y)\frac{\partial W(y)}{\partial y_j}\right] \quad = \quad \alpha(y) - \langle\alpha(y)\rangle \tag{4.9}$$

$$\sum_{k,j}\frac{\partial}{\partial y_k}\left[\sigma_{kj}(y)\frac{\partial W^{rp}(y)}{\partial y_j}\right] = \sigma^*_{rp} - \sigma_{rp}(y) - \sum_k \frac{\partial}{\partial y_k}\left[\sigma_{kr}(y)W^p(y)\right] - \sigma_{rj}(y)\frac{\partial W^p(y)}{\partial y_j} \tag{4.10}$$

that satisfy the conditions

$$\langle W(y)\rangle = 0 \, , \langle W^{rp}(y)\rangle = 0 \tag{4.11}$$

Then for $v^\varepsilon(x,t)$ we have

$$v^\varepsilon(x,t) = -\sigma(y)\left\{\nabla_x u_0(x,t) + \nabla_y u_1(x,y,t) + \varepsilon\left[\nabla_x u_1(x,y,t) + \nabla_y u_2(x,y,t)\right] + \varepsilon^2 \nabla_x u_2(x,y,t) + \ldots\right\} \tag{4.12}$$

The averaged system in equations (4.2) and (4.3) has the same form as the globally averaged stochastic system of equation (2.6) and (2.7). The difference is that, in the periodic case, an explicit procedure for calculating the tensor $\sigma^*$ and the parameters of the averaged equations scalar $\bar{\lambda}(x,t)$ and vector $\bar{\gamma}(x,t)$ are shown. Furthermore it is especially significant that the explicit expansions (4.6) and (4.12) for fields $u^\varepsilon(x,t)$ and $v^\varepsilon(x,t)$ are shown here. As demonstrated by Sanchez-Palencia (1980), the $U(x,t)$ and $V(x,t)$ fields, the means over a small representative volume $\omega_\Delta$ in the space of the slow variable $x$ containing sufficiently number of cell-periods, are macroscopic fields. The usual integral conservation conditions for

arbitrary macroscopic domains can be written in terms of $U(x,t)$ and $V(x,t)$. The identity of the volume and surface averaging of the velocity field is ensured by satisfying the condition $div_y\ v_0(x,y,t)=0$, which follows from equations (2.1), (2.2), (4.7) and (4.12)

Thus the closed system of equations (4.2) and (4.3) together with the equations from (4.4) to (4.12) describes the mono-continual model of flow in a periodical composite medium in terms of mean head $U(x,t)$ and mean flow velocity $V(x,t)$.

## 4.2.Multi-continua description

In order to analyze the fields in the phases of a composite system, we introduce the indicator function $z_i(y)$ of the fast variable $y$ defined as

$$z_i(y)=\{1\ \ if\ \ y\in Y_i\ and\ 0\ \ if\ y\in Y\setminus Y_i\ \} \tag{4.13}$$

and the mean value of the function $\varphi(x,y,t)$ of the $i$- phase, that is local in the space of slow variable $x$ and time $t$

$$\varphi_i(x,t)=\langle\varphi(x,y,t)\rangle_i=\langle\varphi(x,y,t)\ z_i(y)\rangle\theta_i^{-1},\quad \theta_i=|Y_i|/|Y| \tag{4,14}$$

where $\theta_i=$ const, which is the volume fraction of the $i$-th phase in the cell-period.

Now for periodic case we discuss the conditional averaging of the initial system (2.1), (2.2) and (2.3) over the representative volume $\omega_\Delta$, taking into account the fact that the conditional averaging operation commutes with differentiation with respect to time and the slow variable $x$, we obtain the following system of equations for each i-th phase from m-phase composite medium:

$$divV_i^*(x,t)+\alpha_i\theta_i\frac{\partial U_i(x,t)}{\partial\ t}+Q_i(x,t)=\theta_i\ f(x,t) \tag{4.15}$$

$$\sigma_i^{-1} V_i^* (x,t) + \theta_i \nabla U_i (x,t) + \mathrm{P}_i (x,t) = 0 \tag{4.16}$$

Here

$$U_i (x,t) = \left\langle u^\varepsilon (x,t) \right\rangle \quad , \quad V_i^* (x,t) = -\sigma_i \theta_i \left\langle \nabla u^\varepsilon (x,t) \right\rangle \tag{4.17}$$

$$Q_i (x,t) = -\left\langle v^\varepsilon (x,t) \nabla z_i (y) \right\rangle , \mathrm{P}_i (x,t) = -\left\langle \left[ u^\varepsilon (x,t) - U(x,t) \right] \nabla z_i (y) \right\rangle \tag{4.18}$$

Since $\sum_{i=1}^{m} z_i (x) = 1$ , we have

$$\sum_{i=1}^{m} Q_i (x,t) = 0 , \sum_{i=1}^{m} \Psi_i (x,t) = 0 \tag{4.19}$$

At this point we need to take into account that any representative volume $\omega_\Delta$ consists of two parts - $\omega_\Delta^1$ and $\omega_\Delta^2$ . The first part $\omega_\Delta^1$ includes all whole internal cells and the second part $\omega_\Delta^2$ includes non-integer cells inside the representative volume $\omega_\Delta$ and adjoining to the border $\partial\omega_\Delta$ . In some of the non-integer cells, the border $\partial\omega_\Delta$ intersects only one phase, in the rest of the cells the border intersects at least two phases. As indicated earlier, in the stochastic case, the cross-flow from dissected inclusions under some conditions (e.g. in steady-state flow) is significantl.

It is easy to see that the conditionally averaged system (4.15), (4.16) and (4.19) is completely identical to the conditionally averaged system (2.23), (2.24) and (2.25), that corresponds to the stochastic composite media. This formal expression is nonrandom because the media with periodical structure are a special case of all the realization of the stochastic field formed by random shift of one periodical structure. In the stochastic problem the treatment of the equation in (2.1) as continuum conservation laws is based on the obvious fact of the multiple and fairly arbitrary dissection by the surface of the representative control volume of various subdomains in the heterogeneous random system . In contrast, in the periodic system, the identity of the conditional means over the macroscopic volume and surface requires the satisfaction of certain

additional conditions. It can be shown that for phase flow the equality of the means over the volume and the surface of the cell-period is satisfied by the condition $div_y v_0(x,y,t) = 0$ in the absence of sources of the field $z_i(y)v_0(x,y,t)$, which is equivalent to the orthogonality of the velocity $v_o(x,y,t)$ to the phase surface. This is also equivalent to (a) the condition $\sigma_i = 0$, or (b) when $\sigma_i \neq 0$, the system is layered and the flow occurs in the directions of the layers. These conditions considerably limit the class of media in question, which again emphasizes the point that, in the multi-continuum approach the requirement that surface and volume means over each cell be equal is physically unjustified. It should be replaced by the natural condition of equality of the surface and volume means in macroscopic domain containing not only many whole cells but also fractions of cells dissected by the surface of the control volume, which, therefore cannot be arbitrary.

The scalar function $Q_i(x,t)$ and the vector function $\mathrm{P}_i(x,t)$ have a clear physical significance. The $Q_i(x,t)$ is the specific mean cross-flow of fluid from the i-th continuum-phase to the different phases and $\mathrm{P}_i(x,t)$ is the mean specific force from the other phases acting on the surface bounding the i-th phase.

The system (4.15), (4.16) and (4.19) is closed since after substitution of the expressions (4.6) and (4.12) into equations (4.17 and (4.18) the functions $Q_i(x,t)$ and $\mathrm{P}_i(x,t)$ have been evaluated in terms $U_i(x,t)$ . The system can be treated as the exact flow equations in the i -th continuum. Equation (4.15) is the mass balance for the continuum-phase and equation (4.16) is the modified Darcy's law – the impulse balance for the phase.

Considering the system (4.15), (4.16) and (4.19) together with the system (4.2), (4.3) in the multiphase case results in a closed set of equations, that link the conditional mean fields

$U_i(x,t)$ , $V_i(x,t)$ , $Q_i(x,t)$ , $\mathrm{P}_i(x,t)$ and $G_i(x,t)=\theta_i\langle\nabla u(x,t)\rangle_i$ with the conditional phase flow $q_i(x,t)$ by the relation

$$q_i(x,t) = Q_i(x,t) + \ div\ V_i^*(x,t) \tag{4.20}$$

in terms of the averaged field $U(x,t)$ that can be found from global system (4.2) and (4.3).Combining the systems (4.2),(4.3) and (4.15),(4.16) and (4.19) we can write the two-phase composite meso-scale approximation of the phase fields and the interaction parameters as

$$U_i(x,t)=U(x,t)\ ,\ V_i^*(x,t)=-\ \theta_i\sigma_i^*\nabla U(x,t)\ ,\quad \sigma_i^*=\theta_i^{-1}\sigma_i(\sigma_j-\sigma_i)^{-1}(\sigma_j-\sigma^*) \tag{4.21}$$

$$Q_i(x,t)=\theta_i\left[f(x,t)\ +\ div\left(\sigma_i^*\nabla U\right)-\alpha_i\frac{\partial U(x,t)}{\partial t}\right] \tag{4.22}$$

$$\mathrm{P}_i(x,t)=\left(\sigma_j-\sigma_i\right)^{-1}\left(\langle\sigma\rangle-\sigma^*\right)\nabla U(x,t)\ ,\ G_i(x,t)=\theta_i\sigma_i^{-1}\sigma_i^*\nabla U(x,t) \tag{4.23}$$

$$q_i(x,t)=\theta_i f(x,t)-\alpha_i\theta_i\frac{\partial U(x,t)}{\partial t}\ \ or\ \ q_i(x,t)=\theta_i f(x,t)-\frac{\alpha_i}{\langle\alpha\rangle}\theta_i div\left(\sigma^*\nabla U(x,t)\right) \tag{4.24}$$

The identity of the globally and conditionally averaged equations for periodic and stochastic media leads to the complete formal coincidence of the characteristics presented in section 2 of this paper. The result concerning the finiteness of the cross-flow $Q_i(x,t)$ in systems with anisotropy for steady-state process remains valid. Note if $\sigma^*/\langle\alpha\rangle=\sigma_i^*/\alpha_i$, that is $\kappa^*=\sigma^*/\langle\alpha\rangle$ - the effective diffusivity for composite is equal to i-th phase effective diffusivity $\kappa_i^*=\sigma_i^*/\alpha_i$ , the cross-flow $Q_i(x,t)=0$ for any non-steady-state flow.

## 5.APPLICATION EXAMPLES

As already mentioned above, for closure purposes of the phenomenological theories , the hypothesis concerning the structure of the transfer terms between the phase continua are used . In

particular, *Rubinstein* [1948],*Barenblatt, Zheltov and Kochina* [1960], *Khoroshun and Soltanov* [1984] assumed a proportional relationship between the cross flow and the phase pressure difference (the phase temperature difference in similar heat transport problems ). In the case of periodic systems this hypothesis can be tested by direct calculation.

Applying the conditional averaging operator $\langle\ \rangle_i$ to the expressions (4.6), (4.7) and (4.8) we obtain the following quadratic (in $\varepsilon$) expression for the mean i-th phase pressure :

$$U_i(x,t) = U(x,t) + \varepsilon \sum_s \beta_i^s \frac{\partial U(x,t)}{\partial x_s} + \varepsilon^2 \left[ \beta_i \frac{\partial U(x,t)}{\partial t} + \sum_{r,p} \beta_i^{rp} \frac{\partial^2 U(x,t)}{\partial x_r \partial x_p} \right] \tag{5.1}$$

$$\beta_i^s = \left\langle W^s(y) \right\rangle_i \ , \quad \beta_i = \left\langle W\ (y) \right\rangle_i \ , \quad \beta_i^{rp} = \left\langle W^{rp}(y) \right\rangle_i \tag{5.2}$$

As can be seen from the system of equations (4.5),(4.9) and (4.10), the signs and the modules of the vector components $\beta_i^s$ and the tensor-components $\beta_i^{rp}$ depend on the conductivity field $\sigma(x)$ only , but the scalar $\beta_i$ depends on both $\sigma(x)$ and $\alpha(x)$ fields.

If the cell-period $Y$ contains two phases i and j , we have

$$\theta_i\ \beta_i^s + \theta_j\ \beta_j^s = 0 \ , \quad \theta_i\ \beta_i + \theta_j \beta_j = 0 \quad , \quad \theta_i\ \beta_i^{rp} + \theta_j\ \beta_j^{rp} = 0 \tag{5.3}$$

and the phase head difference $\Delta_{ij}(x,t) = U_i(x,t) - U_j(x,t)$ has the form

$$\Delta_{ij}(x,t) = \theta_j^{-1} \left\{ \varepsilon \sum_s \beta_i^s \frac{\partial U(x,t)}{\partial x_s} + \varepsilon^2 \left[ \beta_i \frac{\partial U(x,t)}{\partial t} + \sum_{r,p} \beta_i^{rp} \frac{\partial^2 U(x,t)}{\partial x_r \partial x_p} \right] \right\} \tag{5.4}$$

and in general $\Delta_{ij}(x,t)$ is **the first order** in small parameter $\varepsilon$.

As shown by *Bakhvalov and Panasenko* [1989], if in the cell-period Y the tensor $\sigma(y)$ has certain symmetry properties, then the functions $W^s(y)$ will possess corresponding symmetry. In

particular, if the plane $y_h = 0$ is a plane of symmetry of the tensor $\sigma(y)$, then the function $W^h(y)$ will be odd with respect to the variable $y_h$, and consequently $\beta_i^h = 0$.

We will consider the case in which the tensor $\sigma(y)$ is symmetric about all the coordinate planes, for example, there is a spherical inclusion at the center of the space cell. If $\sigma(y)$ is an isotropic tensor, then this periodic system will be micro-isotropic and macro-isotropic and the effective conductivity tensor is spherical ($\sigma_{rp}^* = \sigma_o^* \delta_{rp}$). Because of symmetry $\beta_i^s = 0$ , $\beta_i^{rp} = \beta_i^* \delta_{rp}$ and the parameter $\eta_{ij}(x,t) = \Delta_{ij}(x,t)/\varepsilon^2$ is obtained from (5.4) as

$$\eta_{ij}(x,t) = \theta_j^{-1}\left(\beta_i \frac{\partial U(x,t)}{\partial t} + \beta_i^* \nabla^2 U(x,t)\right) \tag{5.5}$$

The general conclusion that the vector $\beta_i^s = 0$ and the tensor $\beta_i^{rp}$ is proportional to the unit-tensor $\delta_{rp}$ is implied from the fact that the completely isotropic field $\sigma(x)$ determines a unique zero –vector and a unit-tensor.

Comparing the expression (5.5) with the globally averaged system (4.2) and (4.3), and eliminating $\nabla^2 U(x,t)$ from (5.5), we obtain with the same accuracy :

$$\eta_{ij}(x,t) = \theta_j^{-1}\left(\beta_i + \beta_i^* \frac{\langle\alpha\rangle}{\sigma_0^*}\right)\frac{\partial U(x,t)}{\partial t} \tag{5.6}$$

It is easy to show that the when $f(x,t)$ same approximation for microscopic and macroscopic isotropic systems in (4.22) and (4.24) leads to relations

$$Q_i(x,t) = \theta_i (\sigma_0^*)^{-1}\left[\langle\alpha\rangle\sigma_i^* - \alpha_i\sigma_0^*\right]\frac{\partial U(x,t)}{\partial t}\ ,\ q_i(x,t) = -\theta_i\alpha_i \frac{\partial U(x,t)}{\partial t} \tag{5.7}$$

Thus, $\eta_{ij}(x,t)$ with the same accuracy is approximately proportional to $Q_i(x,t)$ or $q_i(x,t)$ and

$$Q_i(x,t)=\frac{\theta_i\theta_j\left[\langle\alpha\rangle\sigma_i^*-\alpha_i\sigma_0^*\right]}{\varepsilon^2\left[\beta_i\sigma_0^*+\beta_i^*\langle\alpha\rangle\right]}\left(U_i(x,t)-U_j(x,t)\right), \tag{5.8}$$

$$q_i(x,t)=-\frac{\theta_i\theta_j\alpha_i\sigma_0^*}{\varepsilon^2\left[\beta_i\sigma_0^*+\beta_i^*\langle\alpha\rangle\right]}\left(U_i(x,t)-U_j(x,t)\right),\ Q_i(x,t)=\left[1-\frac{\langle\alpha\rangle\sigma_i^*}{\alpha_i\sigma_0^*}\right]q_i(x,t) \tag{5.9}$$

If the symmetry conditions are not satisfied for the tensor $\sigma(y)$, then, in order to estimate the order of the pressure difference with respect to the parameter $\varepsilon$, it is necessary to solve a fairly complex problem for the cell-period.

### 5.1.Case 1

As an example we consider the problem of two-dimensional cell depicted in Fig.3 and let (a) $\sigma(y)=\sigma\varpi$ *if* $y_1<y_2$ *and* $(b)$ $\sigma(y)=\sigma$ *if* $y_1>y_2$ where the arbitrary parameter $\varpi>>1$. After solving the cell-problem asymptotically with respect to the large parameter $\varpi$ (see Bakhvalov and Panasenko, 1989 ) we determine that the head difference can be written as

$$\Delta_{21}(x,t)=U_2(x,t)-U_1(x,t)=0.0386470\,\varepsilon\left(\frac{\partial U(x,t)}{\partial x_1}-\frac{\partial U(x,t)}{\partial x_2}\right) \tag{5.10}$$

Obviously, the quantity $\Delta_{21}(x,t)$ is positive if the vector $\nabla U(x,t)$ is directed from the domain of high conductivity $D_2$ into the domain $D_1$; otherwise it is negative. If the vector $\nabla U(x,t)$ is directed along the phase interface in the cell $(y_1=y_2)$, then the head difference will be zero. We note that for the global averaged steady and spatially homogeneous flow, the expression for $U_2(x)-U_1(x)$ being linear in $\varepsilon$ is exact, and the cross-flow $Q_1(x)=Q_2(x)=0$.

### 5.2.Case 2

We will consider a problem that can be solved exactly as above. Let, the cell-period have the form depicted in Fig.4. Solving asymptotically the corresponding problem for the cell, we obtain the head difference:

$$\Delta_{21}(x,t) = U_2(x,t) - U_1(x,t) = 0.0338216\,\varepsilon\,\frac{\partial U(x,t)}{\partial x_1}, \tag{5.11}$$

which is positive for a vector $\nabla U(x,t)$ directed into the right-hand half plane ; otherwise it is negative.

It is obvious that creating the finite quantity with dimension like cross-flow from the head difference is possible after dividing the head difference by $\varepsilon^2$. In our case this operation leads to an unlimited amount of cross-flow when $\varepsilon \to 0$ and therefore, the linear proportional dependence between cross flow and head difference does not exist.

### 5.3. Case 3

We will now consider the case of an inhomogeneous layered system for which all the computations can be performed in by quadratic approximation in small parameter $\varepsilon$. In the cell-period $(|y_3| \le 1/2)$ let the parameters be as follows: the capacity $\alpha(y) = \alpha_1$ *if* $y_3 > y_0$ *and* $\alpha(y) = \alpha_2$ *if* $y_3 < y_0$ and the tensor of conductivity $\sigma(y) = \sigma_1$ *if* $y_3 > y_0$ *and* $\sigma(y) = \sigma_2$ *if* $y_3 < y_0$.

For example, let $y_0 = 0$, i.e., $\theta_1 = \theta_2 = 1/2$. Solution of the equation (4.5), (4.9), (4.10) and (4.11) leads to the determination of $W^s(y)$, $W(y)$, $W^{\pi}(y)$. Because of symmetry $\beta^s = 0$ the expressions $\eta_{12}(x,t) = (U_1(x,t) - U_2(x,t))/\varepsilon^2$, $Q_1(x,t)$, $q_1(x,t)$ take the form

$$\eta_{12}(x,t)=\frac{1}{6\sigma_{33}^{*}}\left[\left(\frac{\alpha_2-\alpha_1}{\alpha_1+\alpha_2}-\frac{\sigma^2 11-\sigma_{11}^{1}}{\sigma_{11}^{1}+\sigma_{11}^{2}}\right)\sigma_{11}^{*}\frac{\partial^2U(x,t)}{\partial x_1^2}+\left(\frac{\alpha_2-\alpha_1}{\alpha_1+\alpha_2}-\frac{\sigma_{22}^{2}-\sigma_{22}^{1}}{\sigma_{22}^{1}+\sigma_{22}^{2}}\right)\sigma_{22}^{*}\frac{\partial^2U(x,t)}{\partial x_2^2}+\right.$$

$$\left.+\left(\frac{\alpha_2-\alpha_1}{\alpha_1+\alpha_2}+\frac{\sigma_{33}^{2}-\sigma_{33}^{1}}{\sigma_{33}^{1}+\sigma_{33}^{2}}\right)\sigma_{33}^{*}\frac{\partial^2U(x,t)}{\partial x_3^2}\right] \tag{5.12}$$

$$Q_1(x,t)=\frac{1}{2\langle\alpha\rangle}\left[\left(\sigma_{11}^{1}\langle\alpha\rangle-\alpha_1\sigma_{11}^{*}\right)\frac{\partial^2U}{\partial x_1^2}+\left(\sigma_{22}^{1}\langle\alpha\rangle-\alpha_2\sigma_{22}^{*}\right)\frac{\partial^2U}{\partial x_2^2}+\left(\langle\alpha\rangle-\alpha_1\right)\sigma_{33}^{*}\frac{\partial^2U}{\partial x_3^2}\right] \tag{5.13}$$

$$q_1(x,t)=-\frac{\alpha_1}{2\langle\alpha\rangle}\left(\sigma_{11}^{*}\frac{\partial^2U(x,t)}{\partial x_1^2}+\sigma_{22}^{*}\frac{\partial^2U(x,t)}{\partial x_2^2}+\sigma_{33}^{*}\frac{\partial^2U(x,t)}{\partial x_3^2}\right) \tag{5.14}$$

We note that in these expressions the derivative with respect to time has been eliminated with the aid of the globally averaged equation

$$\langle\alpha\rangle\frac{\partial U(x,t)}{\partial t}=\sum_i\sigma_{ii}^{*}\frac{\partial^2U(x,t)}{\partial x_i^2}\ ,\ \sigma_{11}^{*}=\langle\sigma_{11}\rangle\ ,\ \sigma_{22}^{*}=\langle\sigma_{22}\rangle\ ,\ \sigma_{33}^{*}=\left\langle(\sigma_{33})^{-1}\right\rangle^{-1} \tag{5.15}$$

It is easy to see from (5.12) and (5.13) that in the general case of unsteady three-dimensional flow for arbitrary layered systems, the head difference $U_1(x,t)-U_2(x,t)$ is not proportional to $Q_1(x,t)$ or $q_1(x,t)$.

However, under certain conditions proportionality may be observed. In concluding the present study we make the following observations.

**1.** If the transverse component of conductivity of the layers are equal $\left(\sigma_{33}^{1}=\sigma_{33}^{2}=\sigma_{33}\right)$, then for three-dimensional non-steady flow

$$Q_1(x,t)=3\ \sigma_{33}\,\varepsilon^{-2}\left(U_1(x,t)-U_2(x,t)\right) \tag{5.16}$$

**2.** If the layers are isotropic but inhomogeneous and the globally averaged flow has a transverse component, then the cross flow $Q_i(x,t)$ and the head difference are not proportional.

3. If the global flow is purely longitudinal $(\partial U(x,t)/\partial x_3 = 0)$, the cross flow and the head difference are related trough the expression

$$Q_1(x,t) = \frac{6\sigma_1\sigma_2\,\varepsilon^{-2}}{\sigma_1+\sigma_2}(U_1(x,t) - U_2(x,t)) \tag{5.17}$$

4. For purely one-dimensional unsteady transverse flow$\left(\partial U(x,,t)/\partial x_1 = \partial U(x,t)/\partial x_2 = 0\right)$, the relationship between $Q_1(x,t)$ and $(U_1 - U_2)$ is given by

$$Q_1(x,t) = \frac{3\sigma_2(\alpha_0 - 1)}{\alpha_0\sigma_0 - 1}\varepsilon^{-2}\left(U_1(x,t) - U_2(x,t)\right) \tag{5.18}$$

where $\alpha_0 = \alpha_2/\alpha_1$ , $\sigma_0 = \sigma_2/\sigma_1$ .

In Fig.5, the first quadrant of the plane $(\alpha_0, \sigma_0)$ is divided by the straight line $\alpha_0 = 1$, along which the cross-flow is zero and the hyperbola $\alpha_0\sigma_0 = 1$, along which the head difference is zero, into four regions, within which the sign of the proportionality factor is constant. Obviously, in region II and IV the sign of cross flow $Q_1(x,t)$ and that of head difference are opposite, which implies that cross flow occurs from the phase with the reduced head into the phase in which the head is higher than mean. We note that in phenomenological constructions using the proportionality hypothesis it is routinely assumed that the signs are identical. It seems likely that an analogous situation exist for fully isotropic systems. Because the denominator as well as the numerator in (5.8) can be positive or negative, the coefficient in front of the head difference may be negative by some combination of the $\sigma$ and $\alpha$ fields.

5. If in a layered system with isotropic layers the flow is in a steady-state limit, the cross-flow and the head difference are proportional and have the same sign

$$Q_1(x)=\frac{3\sigma_1\sigma_2}{\sigma_1+\sigma_2}\varepsilon^{-2}\left(U_1(x)-U_2(x)\right) \tag{5.19}$$

6. In all the cases involving the same layered system, when any of the derivatives entering into the globally averaged equation (5.15) vanishes, the cross flow and the head difference will be proportional. However, in accordance with (5.17), (5.18) and (5.19) the proportionality factor will depend to a considerable extent on the process considered. In the case of a purely transverse flow the proportionality factor may change sign depending on the relation between the conductivity and the capacities of the layer. Thus, the proportionality factor depends not only on the geometric and physical parameters of the layered system, but also on the process realized, or more precisely, on the macroscopic boundary conditions.

Comparing the following examples we can see how sensitive this dependence is to the process. Let us compare purely longitudinal flow in quasi-steady period with purely steady-state and quasi-longitudinal flow (expression (5.17) and (5.19)). Obviously, the proportionality factors differ by a factor of two. A similar comparison between purely transverse flow in the quasi-steady period and steady-state, quasi-transverse flow leads to a comparison of expression (5.18) and (5.19). In this case it is possible to observe not only a quantitative but also a qualitative difference in the proportionality factors. We note that in accordance with (5.12),(5.13) and (5.14) the proportionality factor is a ratio of linear combinations of the derivatives entering into the global averaged equation. Obviously, in the neighborhood of zero values of all derivatives the behavior of this ratio will depend on the rate at which each derivative tends to zero and, in principle, may be arbitrary. In other words, the proportionality factor essentially depends on the process presented in the composite system. Similar conclusions follow from an examination of layered systems composed of anisotropic layers. Consequently, we can state that fairly generally

the cumulants function of flow-velocity random process. In general the exactly averaged equation is non-local. In some exceptional cases the averaged equation is a differential or integro-differential equation of finite order.

We presented and analyzed in detail two one-dimensional cases (for Gaussian and telegraph random flow-velocity with the identical exponential correlation function) where the exactly averaged equations are second order parabolic and hyperbolic types , respectively . We studied the behavior of different initial plumes, the evolutions and convergence of them for large time . We illustrated the process how the mean concentration distribution for both flow-velocity cases approaches a unique asymptotic limit.

**Acknowledgements**

Authors would like to thank Dmitry Silin of Lawrence Berkeley National Laboratory for his critical review. This work was partially supported by JNC (Japan Nuclear Cycle Development Institute). The work was conducted under the U.S. Department of Energy Contract No.DE-AC03-76SF00098.

## REFERENCES

Bakhvalov, N.S. and G.P. Panasenko, Homogenization : Averaging Processes in Periodic Media; Mathematical problems in the Mechanics of Composite Material , Kluwer Academic, Higham.Mass.,1989.

Barenblatt, G.I., Yu.P. Zheltov and I.N. Kochina , Fundamentals of the theory of single-phase flow in fissured rocks , *Prik.Mat. Mech.*,24 ,852, 1960.

Bensoussan, A., J.L.Lions and G.C.Papanicolaou , *Asymptotic Analysis for Periodic Structure.* North-Holland , Amsterdam ,1978

Dagan, G., *Flow and Transport in Porous Formation*, Springer-Verlag , N.Y.,1989

Gelhar, L.W.,*Stochastic Subsurface Hydrology* , Prentice-Hall,Englwood Cliffs ,N.Y.,1993

Khoroshun, L.P., and N.S. Soltanov ,*Thermoelastic of Two-Component Mixtures* (in Russian) , Naukova Dumka , Kiev (1984)

Rubinstein, L.I., Heat Propagation in Heterogeneous Media , (in Russian) *Izv.Akad . Nauk SSSR , Ser.Geogr.,Geofiz.*,12 , 27 (1948)

Sanches-Palencia , E., Non-Homogeneous Media and Vibration Theory, Lecture Notes in Physics , Vol.127,Springer, Berlin (1980)

Shvidler, M.I., *Statistical Hydrodynamics of Porous Media*,(in Russian) , Nedra , Moscow, (1985)

Shvidler,M.I.,Conditional Averaging of Percolation Fields in Heterogeneous Media , *Dokl.Akad.Nauk SSSR* , 288 ,1074 – 1078,(1986a) ,

Shvidler, M.,I., Conditional Averaging of Unsteady Percolation Fields in Random Composite Porous Media , *Fluid Dynamics* , 21,5,735-740 , (1986b) ,

Shvidler, M., I., Multicontinuum Description of Percolating Flow through Periodic Inhomogeneous Porous Media , *Fluid Dynamics* , 23 , 6, 894-901(1988)

Shvidler, M. and K.Karasaki , Multi-Continuum Models of Flow and Transport in Heterogeneous Porous Media (abstract) , *Eos . Trans. AGU, Fall Meeting suppl.*, 270, 1994

Shvidler, M. and K. Karasaki , Multi-continuum Description of Flow and Transport in the Composite Heterogeneous Media , *Proc. Intern. Symp.on Dynamics of Fluids In Fractured Rocks, Concept and Recent Advances,* 363, Berkeley,1999

Jikov, V.V, S.M.Kozlov and Oleinik, O.A., *Homogenization of Differential Operators and Integral Functionals,* Springer-Verlag, Berlin,1994

## List of Figures

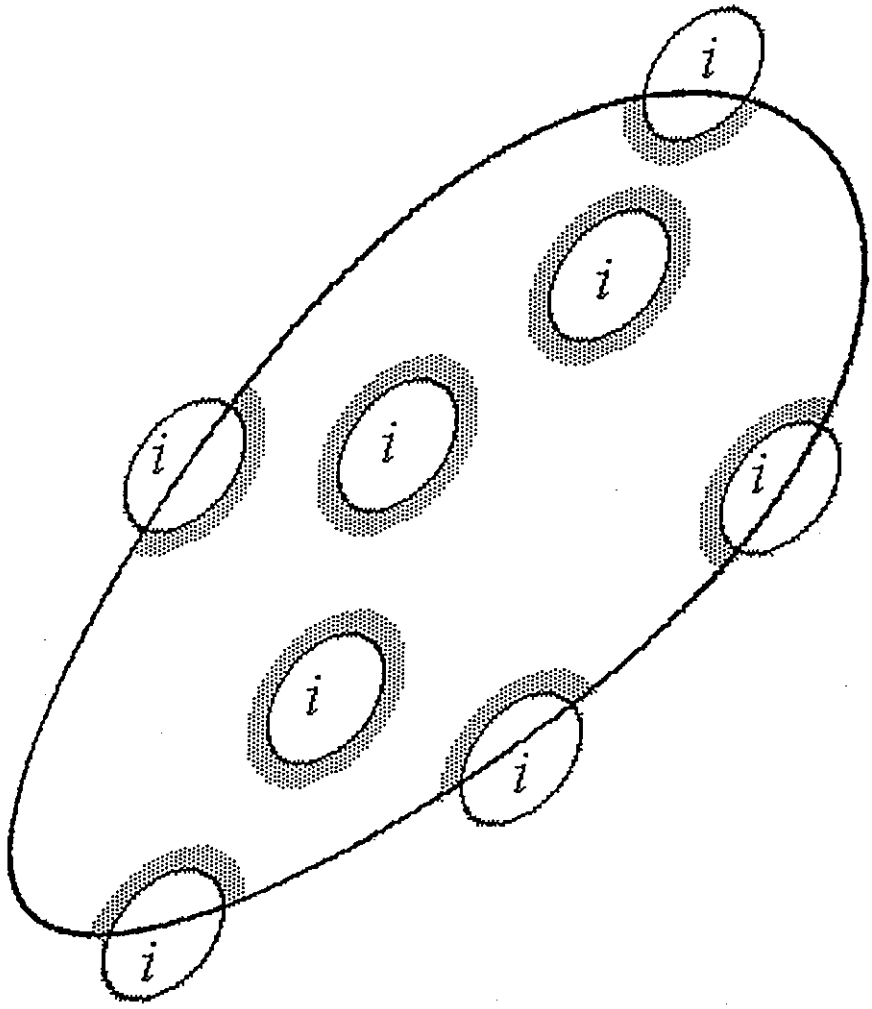


Internal inclusions

Inclusions dissected by the boundary

Figure 1

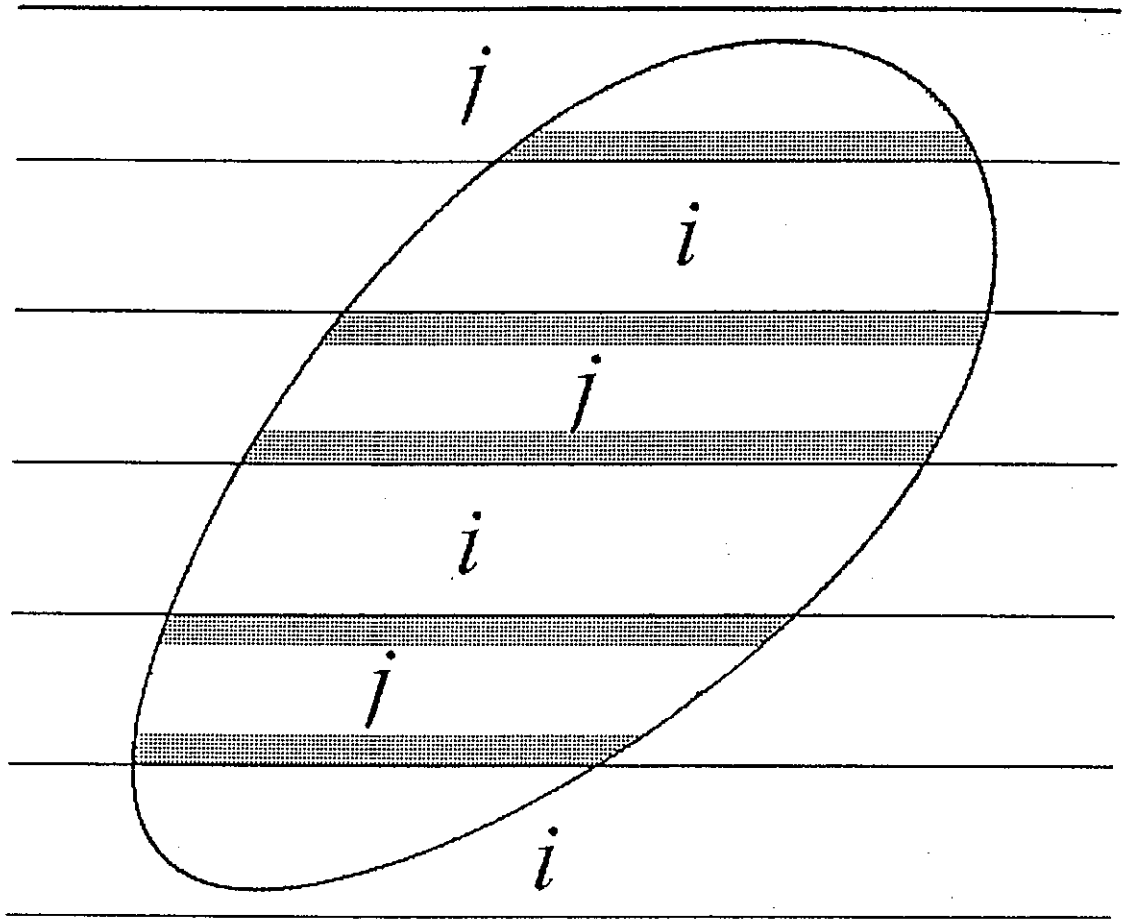


Figure 2

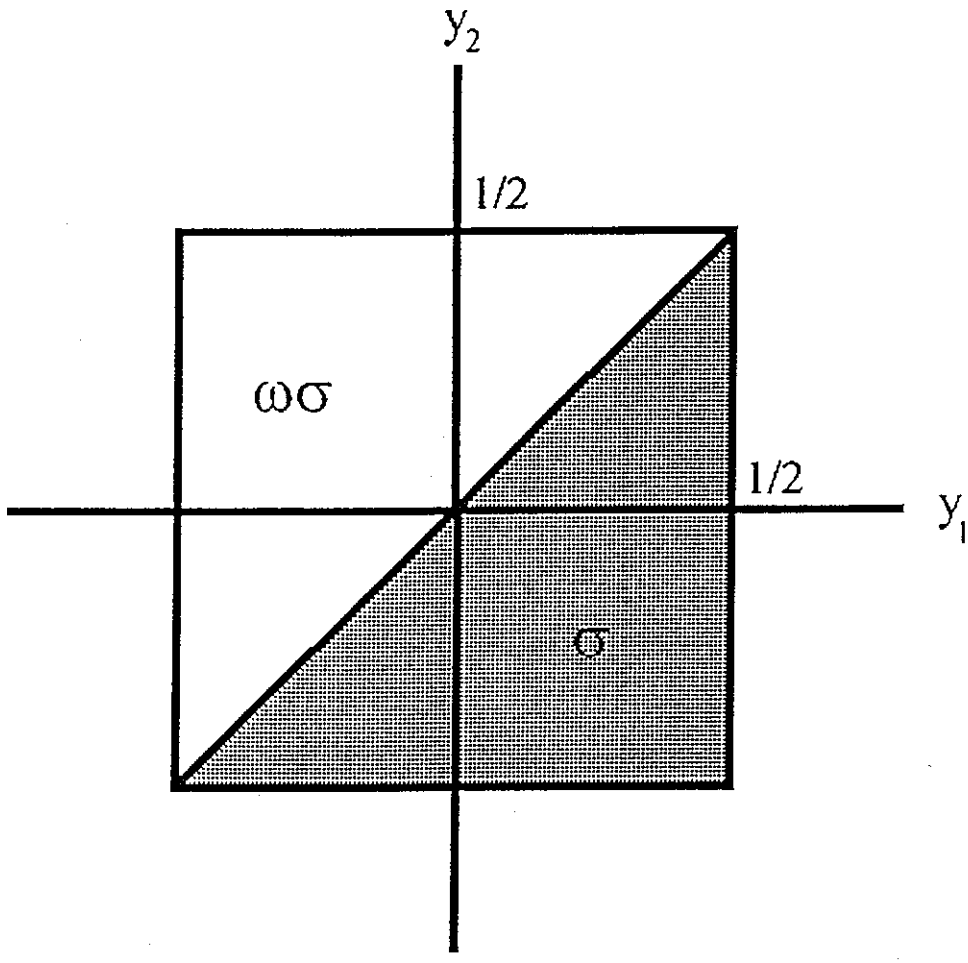


Figure 3

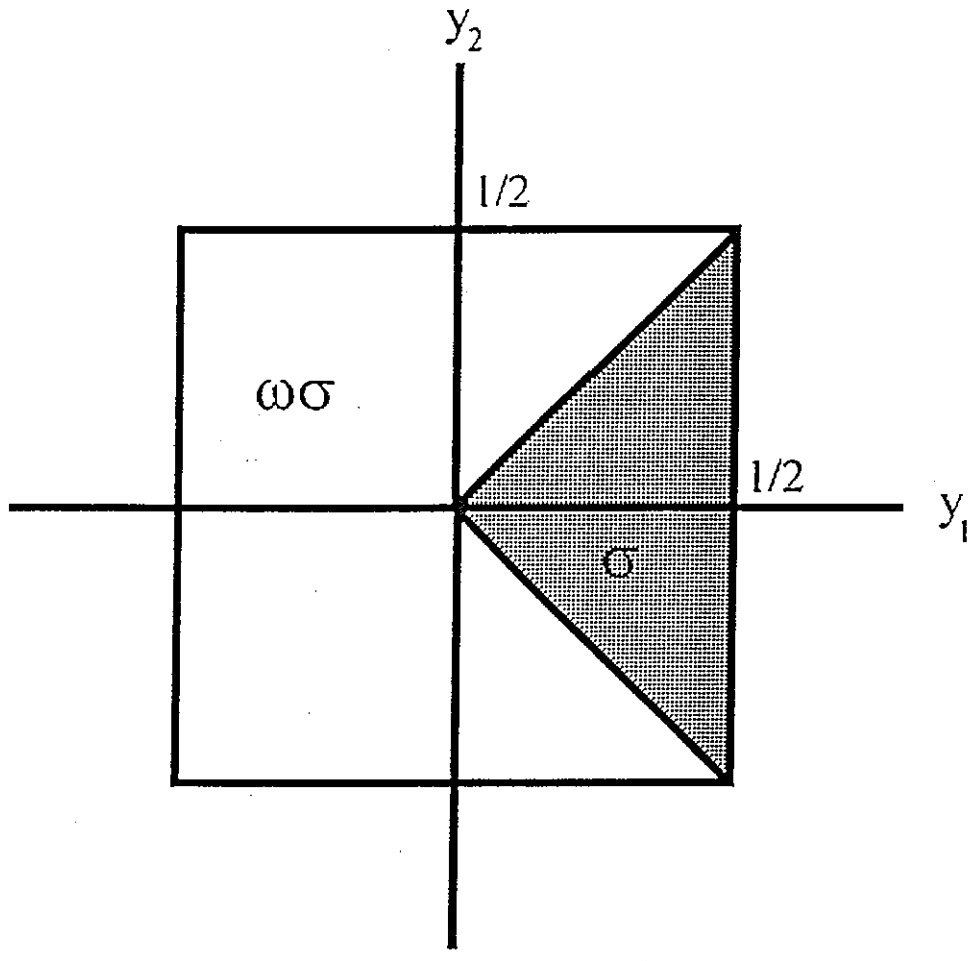


Figure 4

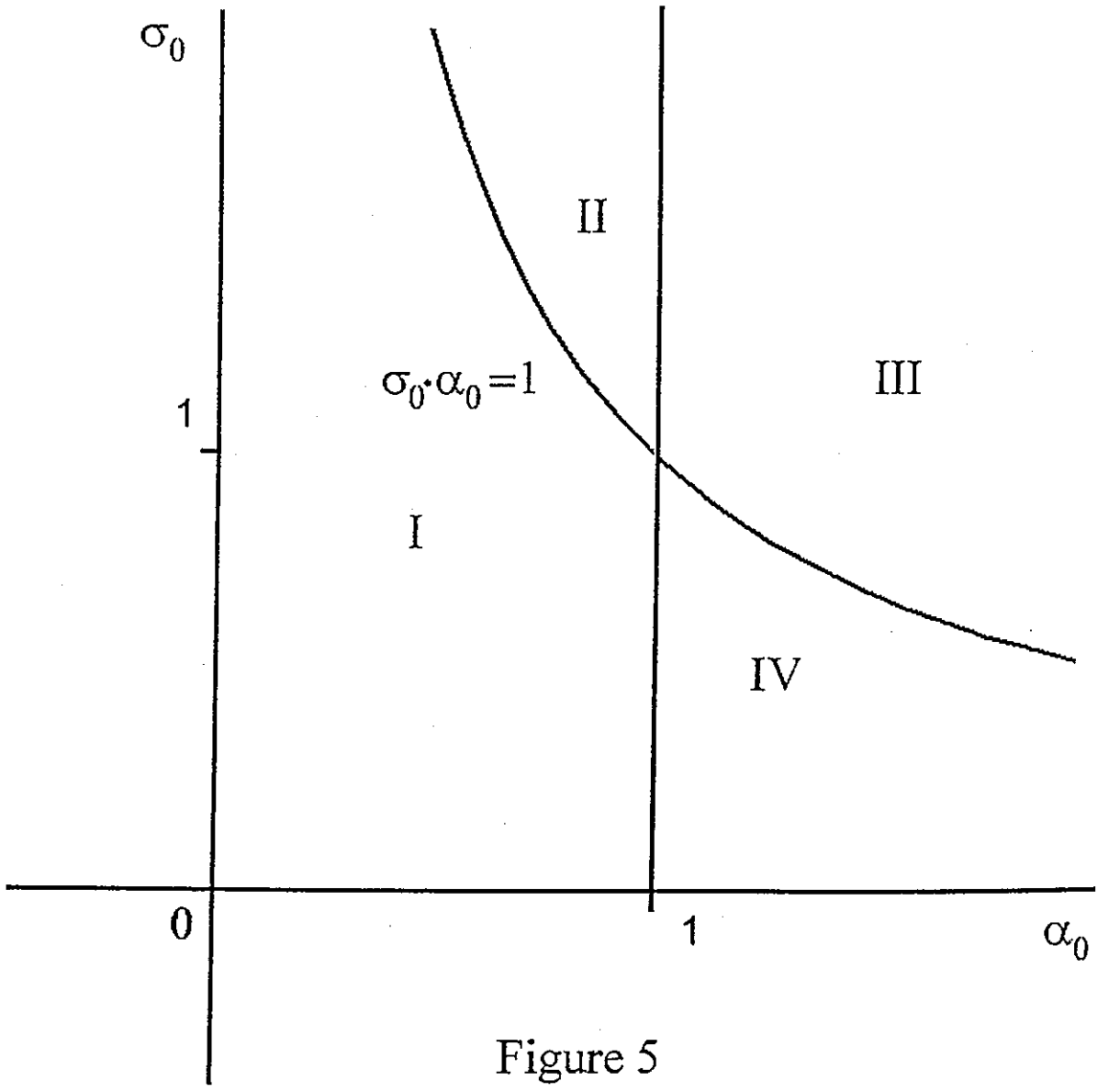


Figure 5

# Progress Report:

# Calculation of Flow Wetted Surface Area in Single Fracture System

Guomin Li and Chin-Fu Tsang

**Earth Sciences Division**
**E.O. Lawrence Berkeley National Laboratory**
**Berkeley, Ca 94720**

May 2000

## Introduction

Potential radionuclide migration into fractured rocks has inspired many studies and much research dealing with the different aspects of fluid flow and tracer transport in individual fracture planes. The earliest conceptual models of fluid flow and tracer transport idealized a fracture as a pair of smooth and parallel plates separated by a constant distance representing the aperture of the fracture. The models lead to the well-known cubic law to describe the hydraulic behavior of the fracture (Witherspoon et al. 1980). Dispersion is incorporated in terms of both the transverse velocity profile across the fracture (Taylor dispersion) and a small-scale surface roughness that locally perturbs the mean flow. Some field experiments involving solute transport in single fractures showed that flow is strongly nonuniform and that such a model may not be representative of the in situ conditions. Tsang and Tsang (1987) proposed the variable-aperture channel model for transport through fractured medium to explain strongly heterogeneous flow with channels characterized by an aperture density distribution and a spatial correction length.

In recent years, numerical methods have become powerful tools used in many studies to understand the behavior of tracer movement in fractured rocks. Using these tools, tracer transport in fractured rocks can be described by the advection-dispersion equations as in a porous medium. By seeking a solution to the equations, we can simulate fluid flow and tracer transport. The stochastic approach to flow and transport analysis seeks approximate

solutions of the stochastic partial differential equations for flow and transport in randomly heterogeneous porous media. It does this by assuming that the hydrogeologic parameters are random functions of space, i.e., random fields. Computational experiments are done on a hypothetical flow field with given statistical properties for the hydrogeological parameters. Many researchers found that dispersion in porous media results predominantly from the irregularity from microscopic flow paths and to the macroscopic variations in microscopic velocities and the dispersivity increases with the distance between the source and the scale-dependent observation point. A Lagrangian type of simulation technique, which takes into account such effects, is a way to model solute transport in heterogeneous porous media.

The particle-tracking method is one such approach. In this approach, a solute plume is presented with a large number of particles that carry the tracer and move in the flow field according to spatially variable local velocities. In our calculations, we focus on the single fracture that was represented as a two-dimensional, strongly heterogeneous, permeable medium to study the so-called flow wetted area where flow is studied to transport tracer. This area provides for fracture-matrix intersection such as matrix diffusion and sorption. This is recognized as an important quantity effect of flow and tracer transport in fractured rock.

## Definition of Wetted Surface Area

In this study, flow wetted surface area is defined as the area of those elements where one or more particles have passed through. Thus it describes the particle distribution moving through the flow domain. A fully heterogeneous model generated by the SISIM module of GSLIB (*Geostatistical Software Library and User's Guide*, by Deutsch and Journel, 1998) with a mean permeability of $0.71\times10^{-12}$ $m^2$ was used to perform the calculations of flow and particle-tracking. All particles are placed at the left-hand high-piezometric head boundary. The initial distribution of the particles in a cell on the inflow boundary is weighted by flowrate into that cell. In this base case, the standard deviation of the log permeability around the mean is 0.8748, and the correlation length is one cell size for both directions.

## Flow Model and Boundary Condition

The domain is 2.5 m in length and 1.0 m wide. The groundwater flow through this domain is calculated for constant piezometric-head boundaries: the left-hand boundary is assumed at a head of 0.0025 m and right-hand boundary at 0 m, with no-flow conditions imposed on the upper and lower boundaries.

A finite-element grid comprised of 40 × 100 elements and 41 × 101 nodes. The 2-D steady flow simulations are performed for the full heterogeneous permeability field with geometric mean of $0.71 \times 10^{-12}\,m^2$.

## Particle Tracking Results

In the particle-tracking method, a solute plume is presented with a large number of particles that carry the solute and move in the flow field according to spatially variable local velocities.

From the above flow-potential-distributions results, the velocities of the fluid can be calculated at every node or center of element. All particles are let in at the left-hand high-piezometric head boundary and collected at the right-hand low-piezometric head boundary.

At the left-hand boundary, we assumed a constant concentration. Then, 1,000 particles were released into the flow domain, the particles moving mainly along preferred paths while large parts of the flow field are not affected. It looks like transport has the channeling characteristic, and many of the particles move slower than that in the homogeneous model with the same mean permeability field as in the heterogeneous model.

A simple formula is used to scale the heterogeneous field:

$$\kappa' = f \times (\kappa - \underline{\kappa}) + \underline{\kappa} \qquad (1)$$

where $\kappa$ is the $\log_{10}$ permeability in the base case, $\kappa'$ is the new scaled permeability in ($\log_{10}$), $\underline{\kappa}$ is the $\log_{10}$ mean permeability, and f is the scaling factor. In Equation (1), we can get a different permeability field by choosing a different value for the factor f :

f = 0, then $\kappa' = \underline{\kappa}$, homogeneous field;

f = 1, then $\kappa' = \kappa$, reference (base-case) heterogeneous field;

f > 1, higher heterogeneous field;

and f < 1, lower heterogeneous field.

We assumed that $\sigma$ is the standard deviation of the $\log_{10}$ mean permeability in the base case and $\sigma'$ is the standard deviation in the scaled case. Then we get the following relationship between $\sigma$ and $\sigma'$:

$$\sigma' = f \times \sigma \qquad (2)$$

Figure 1 shows the wetted area distributed through the system at $5 \times 10^{15}$ seconds in the base case. Figure 2 shows the wetted area distributed through the system at $5 \times 10^{15}$ seconds in the heterogeneous field, with the scaled factor 2.0. Flowrate weighting is used to distribute the initial location of the particles. In the two figures, the upper one shows the wetted area distribution with one or more particles moving through its domain, and the bottom one shows the wetted area distribution with more than 10 particles moving through the element. It is clear that particles primarily move along preferred paths, through the high-permeability connected elements in the flow system, while large parts of the field are not significantly affected. In Figures 1, the percentages of the wetted area are 91.7 and 70.5 from top to bottom. In Figure 2, the percentages are 67.5 and 51.2, respectively.

Figures 3 shows the distance traveled by the fastest particle over the total transport distance as a function of time in both homogeneous and heterogeneous fields. Figure 4 gives the percentage of the wetted area versus time in both a heterogeneous and homogeneous field. The wetted area in the heterogeneous field was defined as one or more particles moving through an element. The curves show the percentages tend toward some limiting numbers after a certain time. The entire domain is wetted in the

homogeneous field but only in some places in the heterogeneous field. Figure 4 shows that in the higher heterogeneous field, we have a lower percentage of wetted area. On the other hand, as shown in Figure 3, the stronger heterogeneous field, the faster the first particle flowed out the right boundary.

## Summary

The purpose of this preliminary work is to apply particle-tracking to potential radionuclide migration in simple fracture systems. Simulations of particle tracking can be used as a tool to understand potential radionuclide movement in a heterogeneous field. Detailed simulations are underway to study the effect on flow wetted area resulting from the degree of heterogeneity and the range of spatial correlation. Matrix diffusion and sorption will be introduced to study the effect of flow wetted area on tracer transport and its retardation by these process.

## Reference

Deutsch, C.V., A.G. Journal, GSLIB – Geostatistical Software Library and User's Guide, Oxford Univ. Press, New York.

Tsang, Y.W., C.F. Tsang, Channel model of flow through fractured medium, Water Resour. Res., 23, 467-479, 1987.

Witherspoon, P. A., J. S. Y. Wang, K. Iwai, and J. E. Gale, Validity of cubic law for fluid flow in a deformable rock, Water Resour. Res., 16, 1016-1024, 1980.

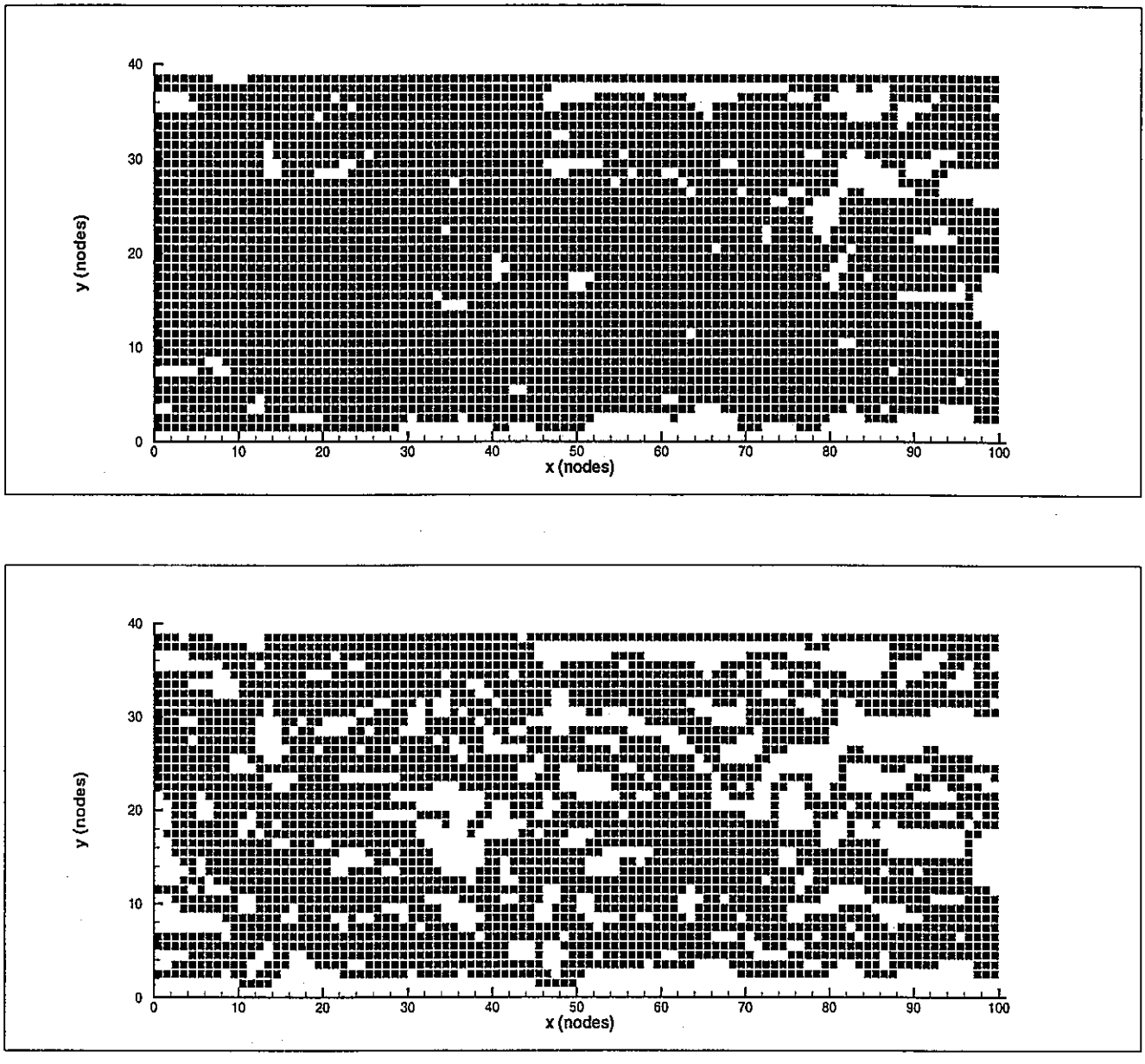


**Figure 1.** The wetted area distributed through the flow domain at $5 \times 10^{14}$ seconds with the scaled factor f of 1.0 (the base case). In the top part of the figure, the wetted area is defined as one or more particles moving through an element. In the bottom part, the wetted area is defined as more than 10 particles moving through an element. Total number of particle tracks is 1,000.

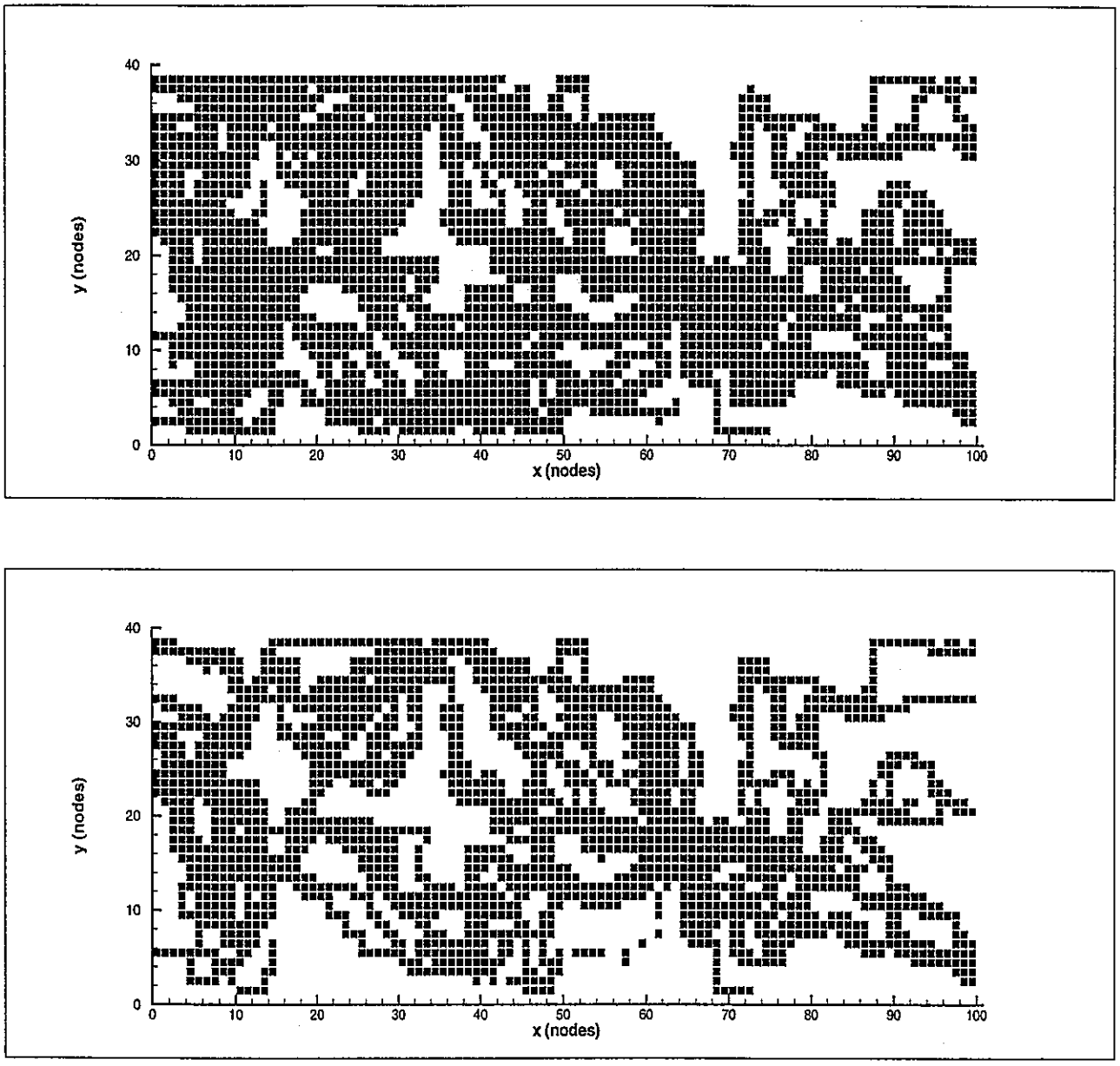


**Figure 2.** The wetted area distributed through the flow domain at $5 \times 10^{14}$ seconds with the scaled factor f of 2.0. In the top part of the figure, the wetted area is defined as one or more particles moving through an element. In the bottom part, the wetted area is defined as more than 10 particles moving through an element. Total number of particle tracks is 1,000.

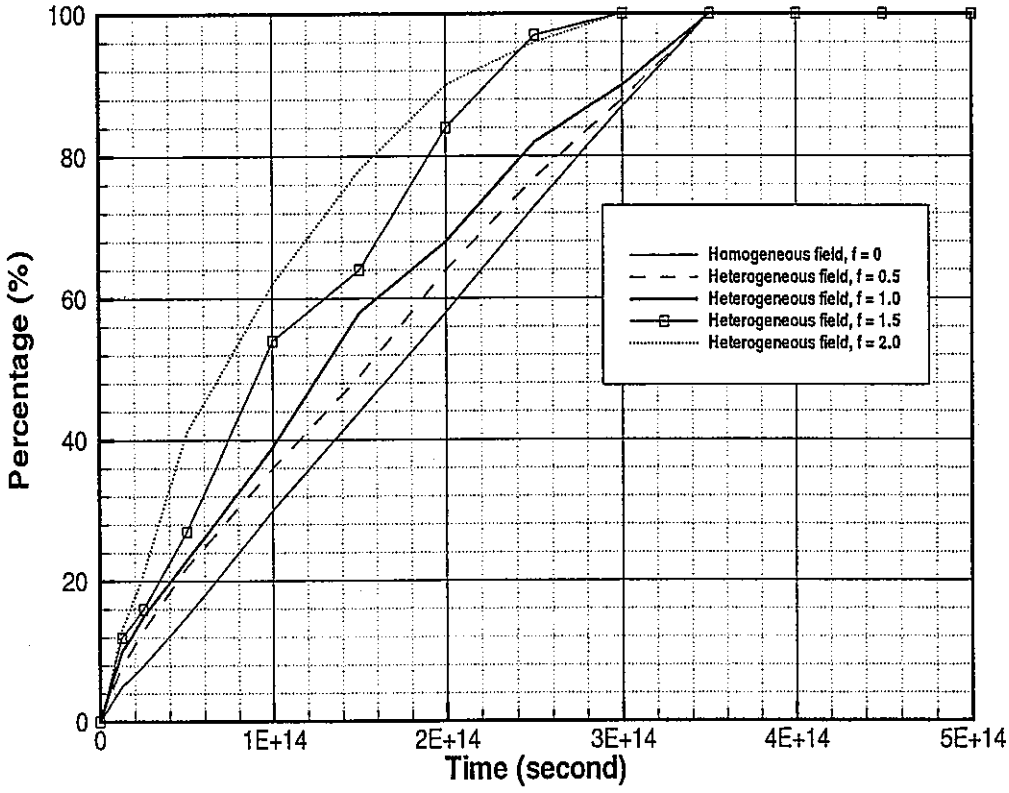


**Figure 3.** Distance traveled by the fastest particle over total transport distance as a function of time in both homogeneous and heterogeneous fields.

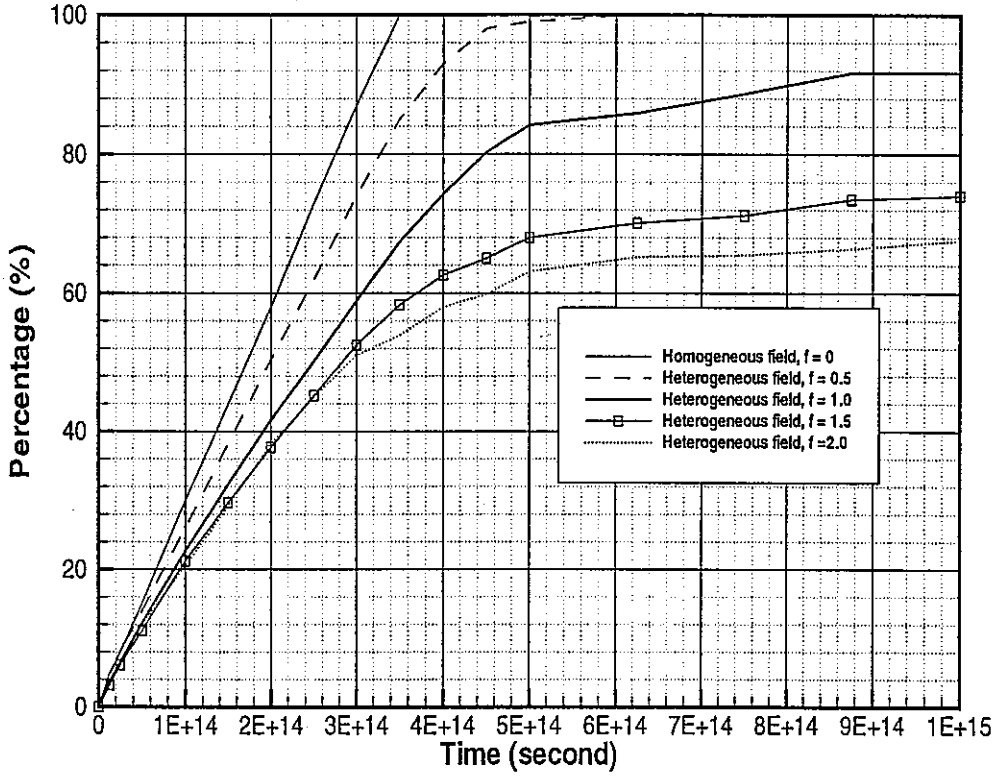


**Figure 4.** Percentages of the wetted area as a function of time in both homogeneous and heterogeneous fields. The wetted area in heterogeneous fields is defined as one or more particles moving through an element.

# Progress Report:

## Tracer Mixing at Fracture Intersections

*Guomin Li and Chin-Fu Tsang*

**Earth Sciences Division**
**E.O. Lawrence Berkeley National Laboratory**
**Berkeley, CA 94706**

**May 2000**

## 1. Introduction

This is a progress report on our study of the mixing behavior of tracers at fracture intersections calculated by the particle-tracking method, presenting the progress of work from the start of the study until now.

There are basically two types of fracture junction (fracture intersection): continuous junction and discontinuous junction. A continuous junction is characterized by each inflow branch being connected by a corresponding outflow branch. At a discontinuous junction, the sequence of inflow branches is interrupted by one or more outflow branches (an example is a T-junction). Wilson and Witherspoon (1976) and Robinson and Gale (1990) describe experimental studies of flow through a continuous junction, while Hull and Koslow (1986) report a laboratory experiment for a discontinuous junction. In their studies, the streamline routing was proposed to determine the advective mass transfer in the intersection (Wilson and Witherspoon 1976; Robinson and Gale 1990; Hull and Koslow 1986). Berkowitz et al. (1994) applied a random-walk particle-tracking method to study mixing behavior at an idealized fracture junction. Philip (1988) has solved the boundary-value problem that describes the microscale flow pattern at an intersection of two equal-aperture orthogonal fractures. Philip (1988) characterizes the mixing process at a fracture intersection in terms of a local Peclet number, expressing the interplay between

advective and diffusive mass transfer. Li (1995) applied a numerical lattice-gas automata (LGA) model to study the relationship between mixing behavior and the junction Peclet number.

## 2. Methodology

A two-dimensional inviscid and irrotational steady flow is assumed in this study (Figure 1). The pressure H in the domain is described by the differential equation

$$\nabla^2 H = 0 \qquad (1)$$

subject to boundary conditions.

The fluid velocity can be defined for a chosen volumetric flow through the fracture junction under chosen boundary conditions, for different permeability values of the inflow and outflow branches. Then, the advective transfer of tracer spreading (resulting from streamlines taking a two-dimensional configuration with differing path lengths controlled under the distribution of velocities) can be estimated.

To compare different numerical results, we introduced the Peclet number $P_e$ to represent the flow conditions. The local Peclet number can be defined as

$$P_e = 1.414\, b\, v / D \qquad (2)$$

where v is the average velocity within the "cross-section" area, b is the width of the fractures (where two intersecting fractures are assumed to have the same width), and D is the molecular diffusion coefficient of the tracer. The Peclet number expresses the relative importance between advection and diffusion within the intersection area. As the fluid velocity increases, the Peclet number increases, and the influence of diffusion decreases. On the other hand, as the fluid velocity decreases, the Peclet number decreases, and diffusion tends to play a relatively more important role in the transport process.

Diffusive processes within the individual fracture will depend upon the boundary condition, the permeability distributions, the residence time of mass in the system, and the magnitude of the fluid diffusion coefficient. Clearly if the residence time in the fracture is sufficiently long, diffusion spreads mass across streamlines and results in a transverse concentration profile.

The general nonreactive mass-transport problem for a dissolved, neutrally buoyant specis involves the solution of the mass balance equation

$$\partial c / \partial t + \nabla ( c \bullet v ) - \nabla ( D_f \bullet \nabla c ) = 0 \qquad (3)$$

for the concentration c over a period of time, subject to a set of initial and boundary conditions for c. $D_f$ represents the diffusion coefficient.

In the calculations that fellow, a random-walk, particle-tracking model has been applied to simulate tracer transport in fracture junctions by moving particles through space using individual advective and diffusive steps. This method is based upon analogies between mass transport equations and certain stochastic differential equations. A particle is displaced according to the following simple relationship (Thomson and Gelhar 1990):

$$X^n = X^{n-1} + A (X^{n-1}) \Delta t + B(X^{n-1}) \cdot Z \sqrt{\Delta t} \qquad (4)$$

where $X^n$ is its position at time level $n\Delta t$, A is a deterministic forcing vector, B is a deterministic scaling matrix, and Z is a vector of random numbers with mean zero and variance one. The motion of one particle will thus be statistically independent from that of another. If a large number of identical particles associated with a particular component are moved simultaneously, then their number density f (x, t) will approximately satisfy the Ito-Fokker-Planck equation (Kinzelbach 1988):

$$\partial f/\partial t + \nabla ( A \bullet f ) - \nabla\nabla:(1/2\, B \bullet B^T \bullet f) = 0. \quad (5)$$

Equation (3) represents the balance of mass for a conservative aqueous constituent. The particle-tracking method succeeds if the particle number density f in Equation (5) is proportional to c in Equation (3), subject to A and B by

$$A \equiv v + \nabla \bullet D_f \quad (6)$$

and

$$B \bullet B^T \equiv 2D_f \quad (7)$$

Thompson and Gelhar (1990) discussed some of the issues concerning the computational approximations required in applying a random-walk particle model, Equation (4).

## 3. Structure and Boundary Condition

Figure 1 shows the fracture intersection model and its boundary conditions. The groundwater flow through this domain is also calculated for constant piezometric head boundaries: the left-hand boundary and the bottom boundary are assumed to be at 1 μm head, and the right-hand boundary and the top boundary are assumed to be at 0 μm head.

The 2-D flow domain is a finite-difference grid comprised of 70 × 70 nodes, with each grid block 1 × 1 μm. The domain is divided into two intersecting fractures of 10 μm width and a high permeability of 1.0 $\mu m^2$, surrounded by a very low permeability background of $1.0 \times 10^{-30}$ $\mu m^2$ representing impermeable rock matrix.

Let particles be applied at the left-hand high head boundary. The random walk method is based on particle transport under the influence of both rock spatial fluid velocities and diffusion, and is possible for some particles to go backward out of the left-hand inflow boundary or to jump out of the upper and lower boundaries from one time step to the next one. We assume that the particle will disappear once it goes out the left-hand boundary,

and will be bounced back (perfect reflection) into the modeling domain if it goes out of the flow domain into the low-permeability background region.

## 4. Simulation Results

### *4.1 Effects of Diffusive Process*

We consider only the diffusion effect on tracer transport. Thus the dispersion term D is

$$D = D_f \tag{8}$$

in which $D_f$ means the diffusion coefficient.

The permeability field in the model (Figure 1) is made up of a central high permeability (1.0 $\mu m^2$) embedded in a very low permeability ($1.0 \times 10^{-30}$ $\mu m^2$) background. The permeability is the uniform value in the flow field. It means that the flow-rate in the left fracture is same as that in the lower fracture (plug flow 50/50).

From the above flow model, the velocities can be calculated at any position in the domain. All particles are let in at 5 μm from the left-hand high-piezometric head boundary and collected at the right-hand low-piezometric head boundary. A plot of the number of particles collected at the right-hand boundary and top boundary at different arrival times constitutes the breakthrough curves. In these calculations, 20 particles were used to show the solute flow lines and 5,000 particles to plot the breakthrough curves.

Figures 2 and 3 show the 20 particle traces with different Peclet number for the intersection model.

Figure 2 shows that all the particles move from the left-hand boundary to the top boundary, for the very high Peclet number of 118,000. It means the diffusion term is too small to affect the particle movement in the flow field, so that particles follow the

streamlines. Figure 3 shows that under the condition of the Peclet number with a small value, some of the input particles jump into nearby streamlines. Some of these particles then move out of the right-hand boundary.

What percentage of particles can go through the right-hand boundary? It is clear that more particles will go through the right-hand boundary if there is a very small Peclet number. In these calculations, around 5,000 particles were used to investigate the percentage of particles that moved through the right-hand boundary. Figure 4 shows the percentage of particle distribution in the outflow branches versus the Peclet number.

Figure 5 shows the comparisons of tracer-mixing characteristics (the percentage of the particles throughout the right-hand fracture branch) at the junction with other two numerical results. The results compare well with the LGA calculation and the behavior that there are numerical inaccuracies in Birkowitz et al. (1994). The comparison will be further investigated.

*4.2 Effects on initial position of the particles*

To investigate the relationship between the initial position of the particles relative to the left-hand boundary and the resulting character of tracer transport, the particles are let in at 5, 10 and 20 μm from the left-hand high-piezometric head boundary. A plot of the number of particles collected at for the three cases the right-hand boundary at different arrival times constitutes the breakthrough curves. In these calculations, 5,000 particles were used to track the tracer transport and to plot the breakthrough curves. The flow-rate in the left-hand fracture branch is assumed to be same as that in the lower fracture branch (plug flow 50/50).

Figure 6 shows the comparisons of the tracer mixing characteristics at the junction for the different distances that the particles were initially placed from the east fracture. For the three models, no significant difference is found.

*4.3 Effects of the flow-rate ratio*

In the above model, the permeability is the same in all fracture branches. In other words, the flowrate in the left fracture branch is the same as that in the lower fracture branch (plug flow 50/50). This model is considered to be the base model.

Let us adjust the permeability distribution to get different ratios of the flowrate in the right-hand fracture branch and the upper fracture branch. Two models, Model A and Model B, were chosen to study the tracer mixing in the fracture intersection. In Model A, we assume that the permeability in upper and lower fracture branches is two times that in left and right fracture branches, including the junction area. The ratio of the flowrate in left fracture to that in lower fracture is about 35/65. In Model B, it is assumed that the permeability in left and right fracture branches is ten times the other two fracture branches, including the junction area. The ratio of the flowrate in the left-hand fracture branch to that in the lower fracture branch is around 35/65.

In Models A and B, all particles are let in at 5 μm from the left-hand high-piezometric head boundary and collected at the right-hand low-piezometric head boundary. In these calculations, 20 particles were used to show the solute flow lines and 5,000 particles to plot the breakthrough curves.

Figures 7 and 8 show the 20 particle traces with different Peclet number for Model A. Figure 7 shows that all the particles move from the left-hand boundary and to the top boundary for the very high Peclet number of 118,000. The 20 particle tracers follow the streamlines that occupy nearly half of the flowrate in the upper fracture branch. Figure 8 shows that under the condition of the Peclet number with a small value, some of the input particles jump into nearby streamlines. Then some of these particles have the chance to move out of the right-hand boundary.

Figure 9 shows the percentage of particle distribution in the outflow branches versus the Peclet-numbers.

Figures 10 and 11 show the 20 particle traces with different Peclet number for Model B. Figure 10 shows that particles move from the left-hand boundary to the top boundary (upper fracture branch) for the very high Peclet number of 118,000. Some of the particles incoming streamlines occupy the whole upper fracture and the rest of the particles from the left-hand fracture branch flow into the right-hand fracture branch. Figure 11 shows the tracer-mixing behavior in the fracture junction under the condition of the Peclet number with a small value.

Figure 12 shows the percentage of particle distribution in the outflow branches versus the Peclet numbers, and figure 13 shows the comparison of tracer mixing characteristics at the junction in Model A and B, and the numerical results in base model.

## 5. Summary and Conclusion

The purpose of this preliminary work is to apply random-walk methods to potential radionuclide migration in fracture intersections. A random-walk model can be used to understand the diffusion process through fracture intersection and to investigate the transport of particles to different outflow fractures, depending on the mixing behavior.

The above results show that the Peclet number is the key parameter controlling tracer mixing at a fracture intersection. When the Peclet number is very small, the streamlines are no longer important for particle migration calculations, so that the percentage of particles moving across the right-hand boundary is near 50%, as would be expected.

Now that the method is shown to be looking properly, we are planning to perform further studies of transport at fracture intersections under more complex conditions.

## 5. Reference

Birkowitz, B., C. Naumann, L. Smith, Mass transfer at fracture intersections: An evaluation of mixing models, Water Resour. Res., 30, 1765-1773, 1994.

Hull, L. C., K. Koslow, Streamline routing through fracture junctions, Water Resour. Res., 22, 1390-1400, 1984.

Kinzelbach, W., The random walk method in pollutant transport simulation, in Groundwater Flow and Quality Modeling, edited by E. Custodio, A. Gurgui, and J. P. Lobo Ferreira, pp. 227-245, D. Reidel, Norwell, Mass., 1988.

Li, C.H., Low peclet number mixing behavior at fracture junctions, Ph.D Thesis, New Mexico Institute of Mining and Technology, 1995.

Philip, J., The fluid mechanics of fracture and other junctions. Water Resour. Res., 24, 239-246, 1988.

Robinson, J.W., J.E. Gale, A laboratory and numerical investigation of solute transport in discontinuous fracture systems, Ground Water, 28(1), 25-36, 1990.

Tompson, A. F. B., L. W. Gelhar, Numerical simulation of solute transport in three-dimensional, randomly heterogeneous parous media, Water Resour. Res., 26, 2541-2562, 1990

Tsang, Y.W., C.F. Tsang, Flow channeling in a singer fracture as a two-dimensional strongly heterogeneous porous medium, Water Resour. Res., 25, 2076-2080, 1989.

Wilson, C. R., P. A. Witherspoon, Flow interference effects at fracture intersections, Water Resour., Res., 12, 102-104, 1976.

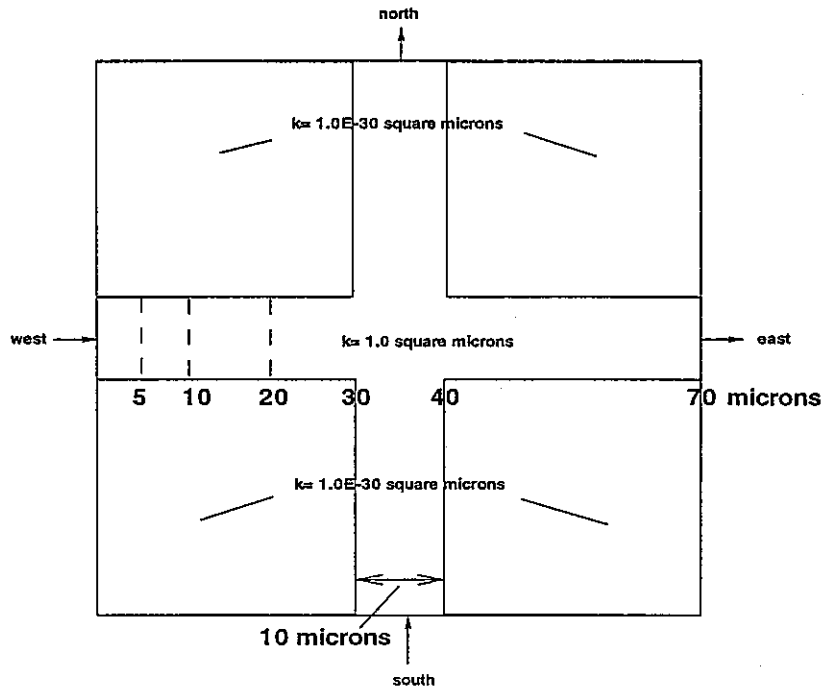


**Figure 1.** Cross-fracture model and boundary condition. Pressure gradient from left to right and from down to up is $1.43 \times 10^{-4}$.

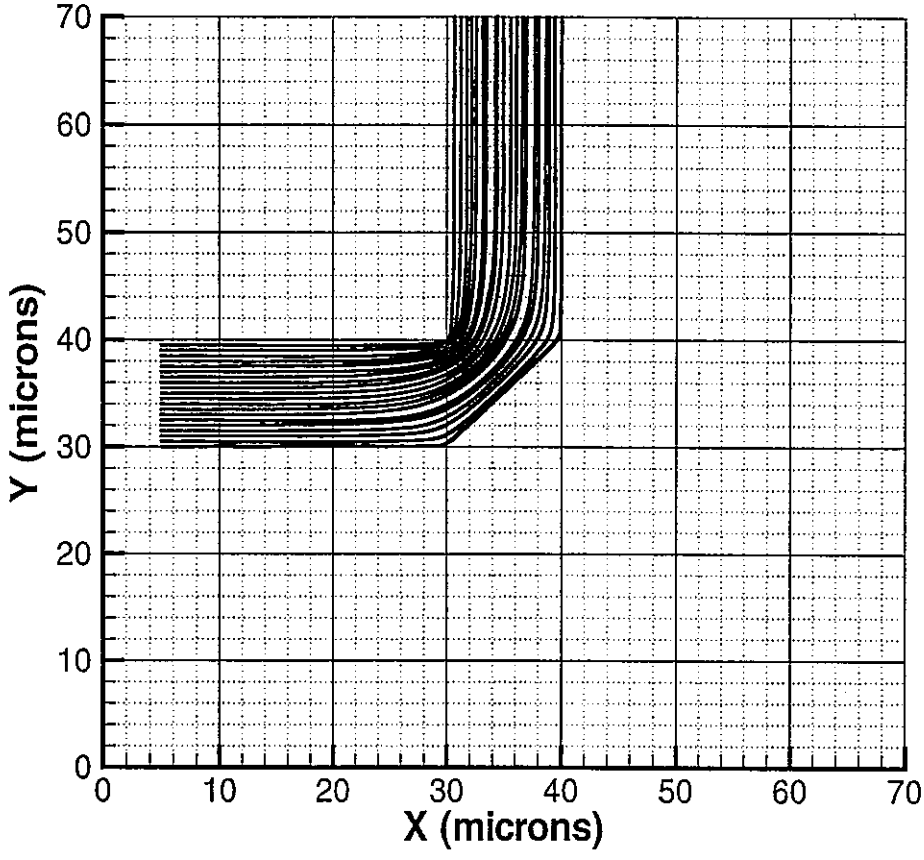


**Figure 2.** Spatial particle trace in base model with plug flow 50/50 for Peclet number of 118,000.

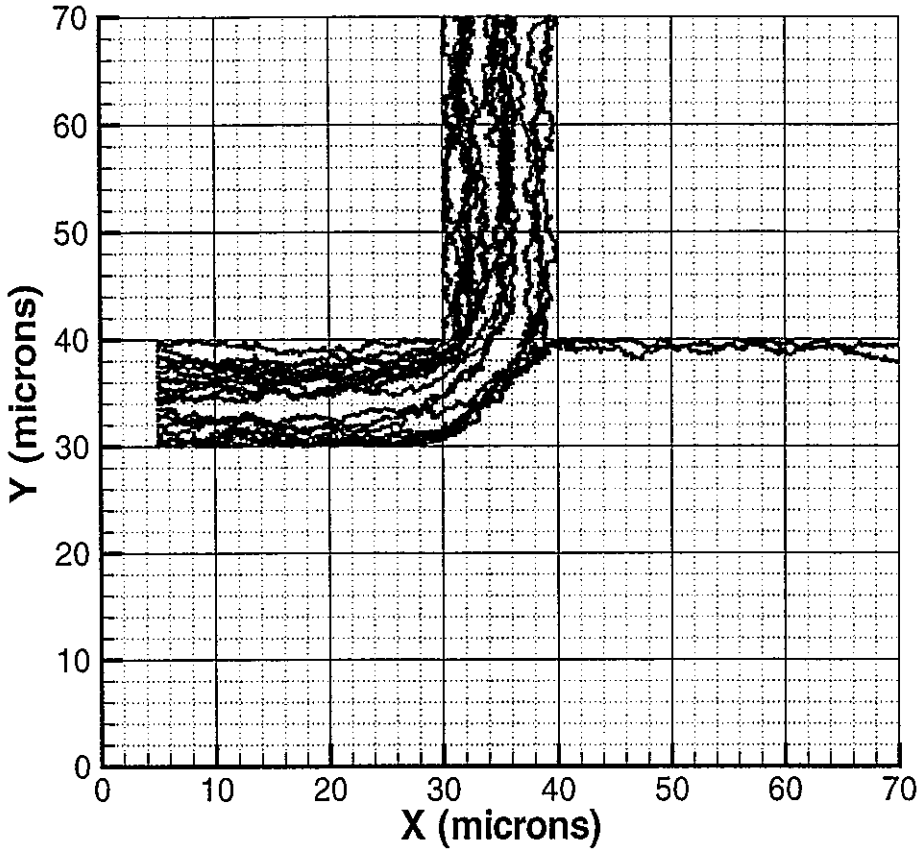


**Figure 3.** Spatial particle trace in base model with plug flow 50/50 for Peclet number of 118.

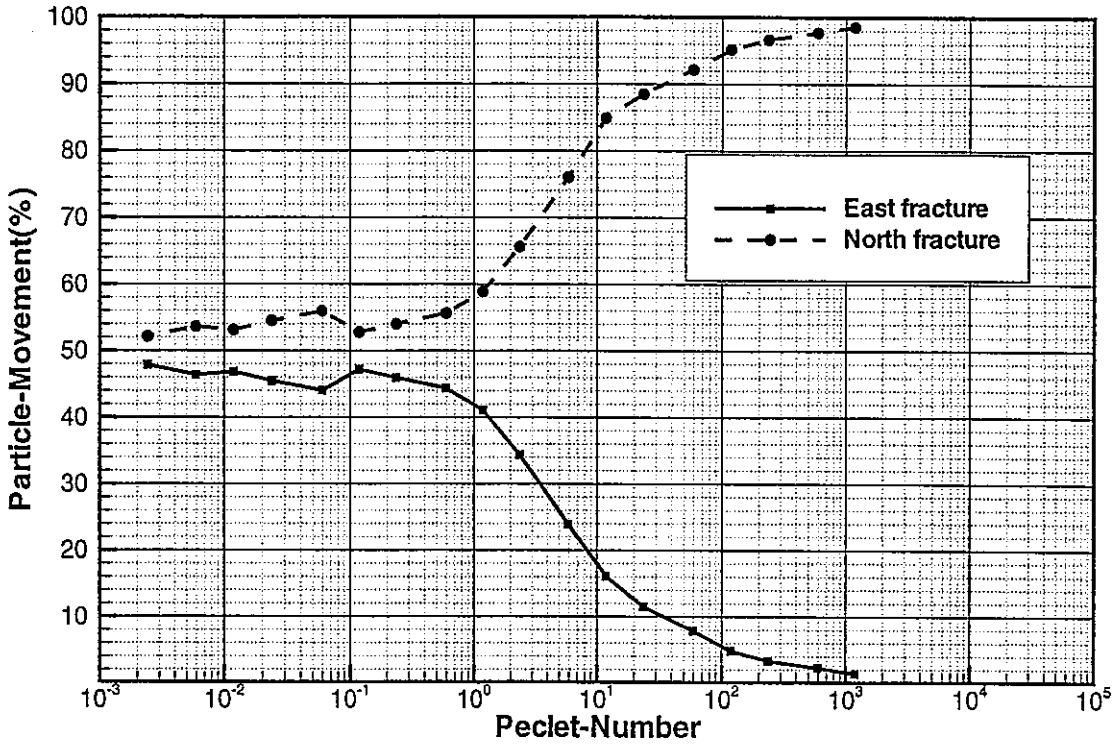


**Figure 4.** The percentage of the particles passing through the boundaries over the total particles is a function of the Peclet number. The low curve is the percentage of the particles passing through the right-hand boundary. Particles are placed in west fracture at 5 μm to the left boundary.

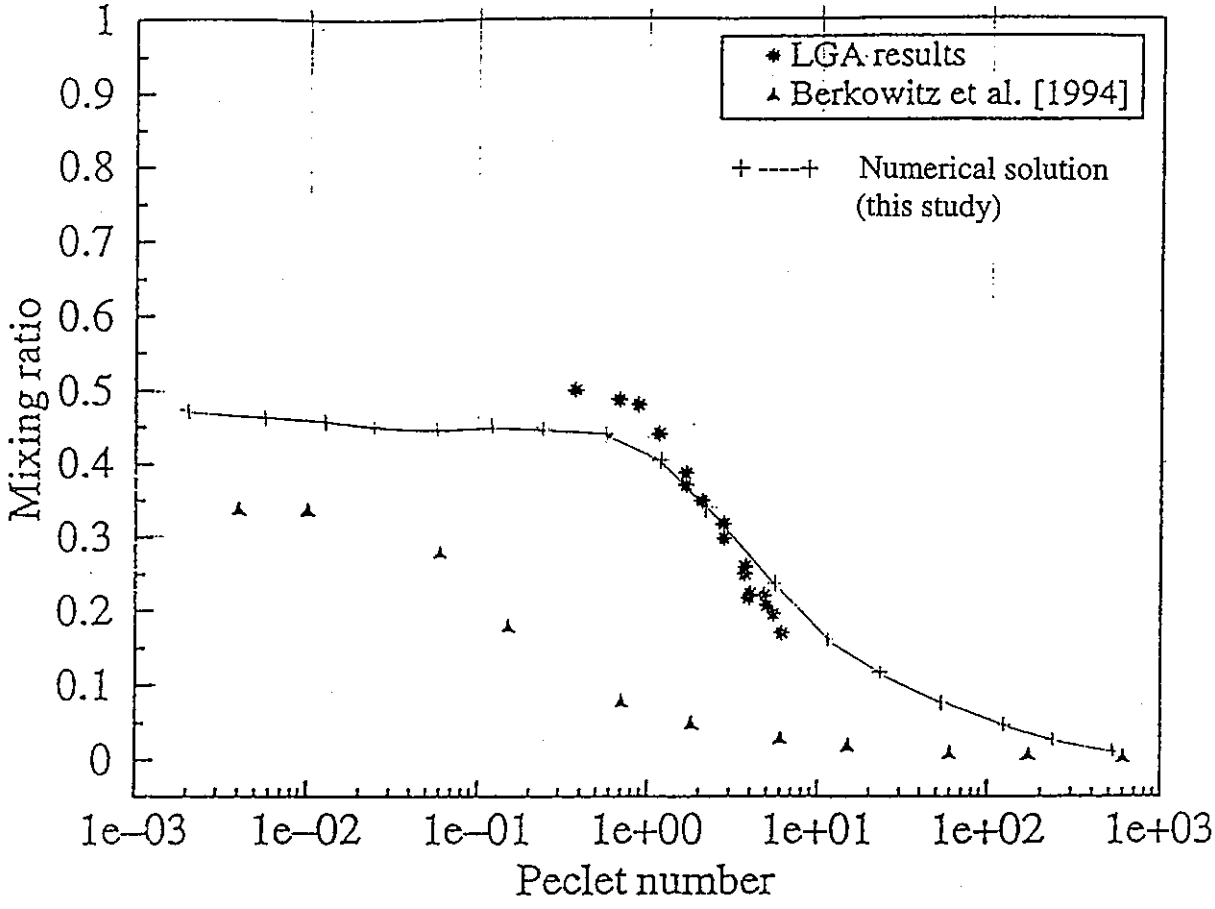


**Figure 5.** Comparisons of mixing characteristics (the percentage of the particles throughout the right-hand boundary) at junction with other two numerical results.

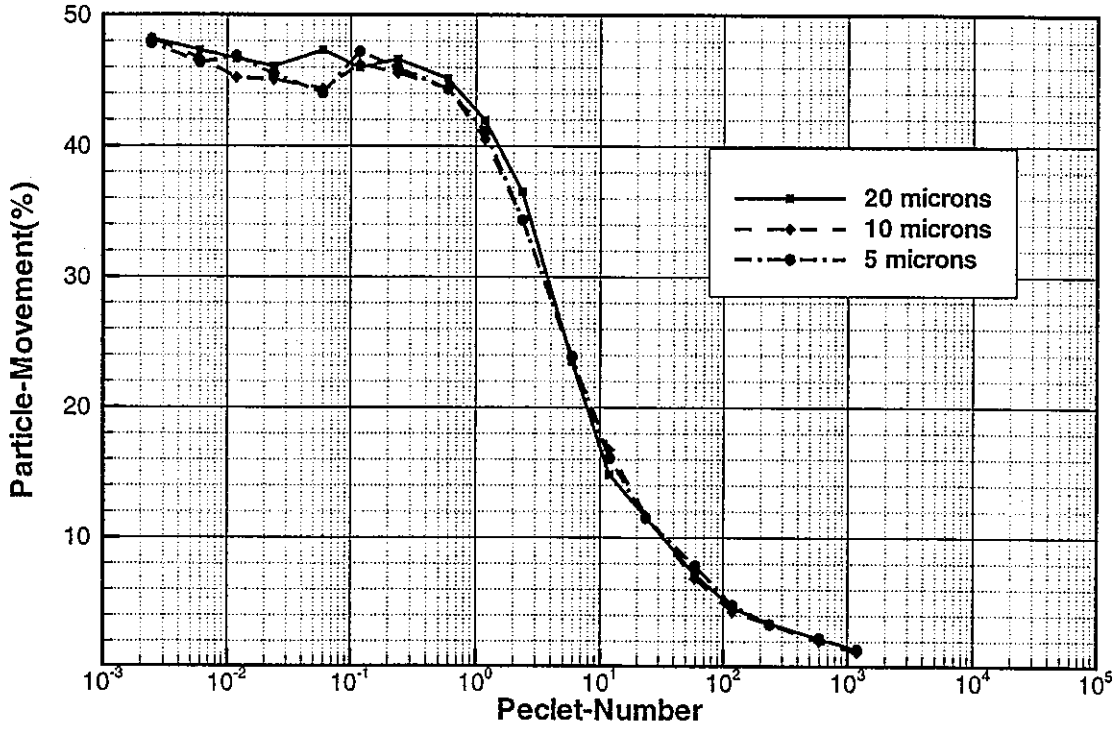


**Figure 6.** Comparisons of mixing characteristics at junction in terms of the resulting percentage of the particles from the left boundary exist the right boundary. The different curves are for the different distances at which the particles were placed relative to the left boundary (see Figure 1).

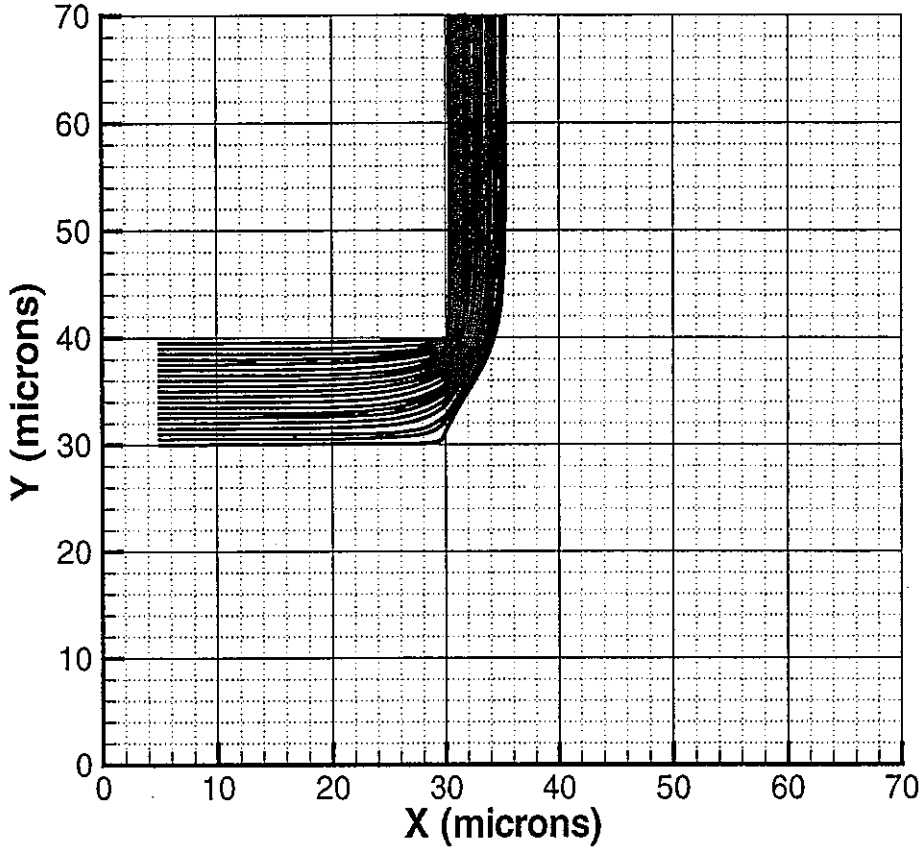


**Figure 7.** Spatial particle trace in Model A with plug flow 35/65 for Peclet number of 118,000.

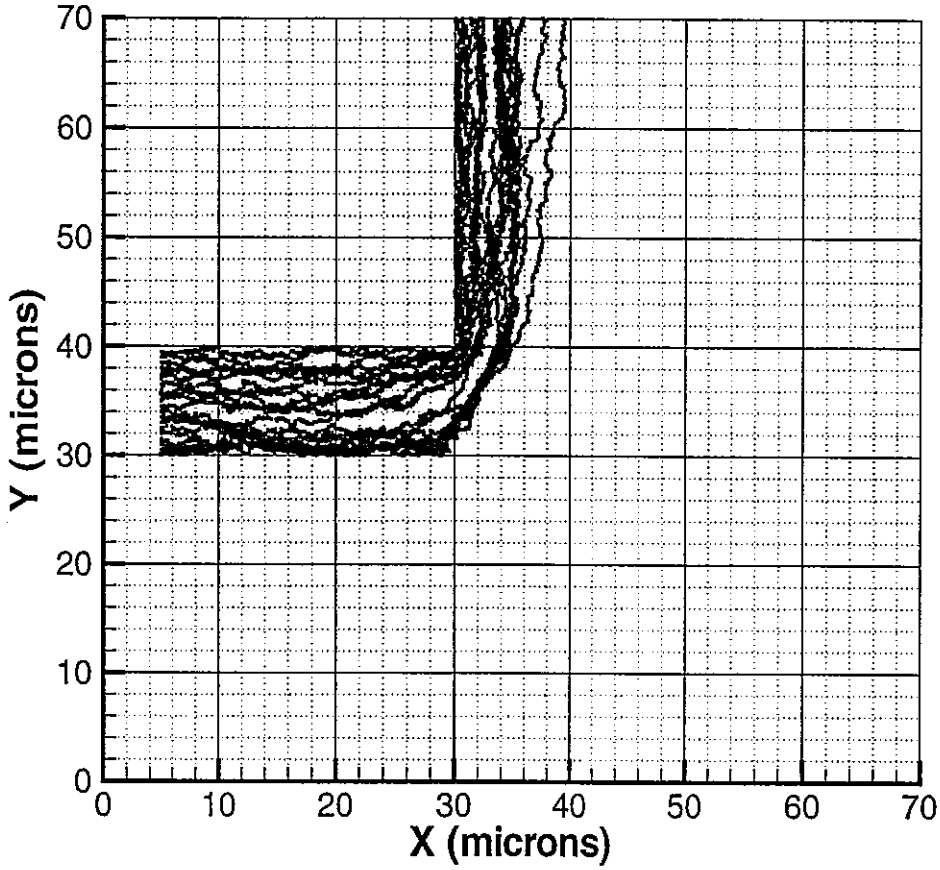


**Figure 8.** Spatial particle trace in Model A with plug flow 35/65 for Peclet number of 118.

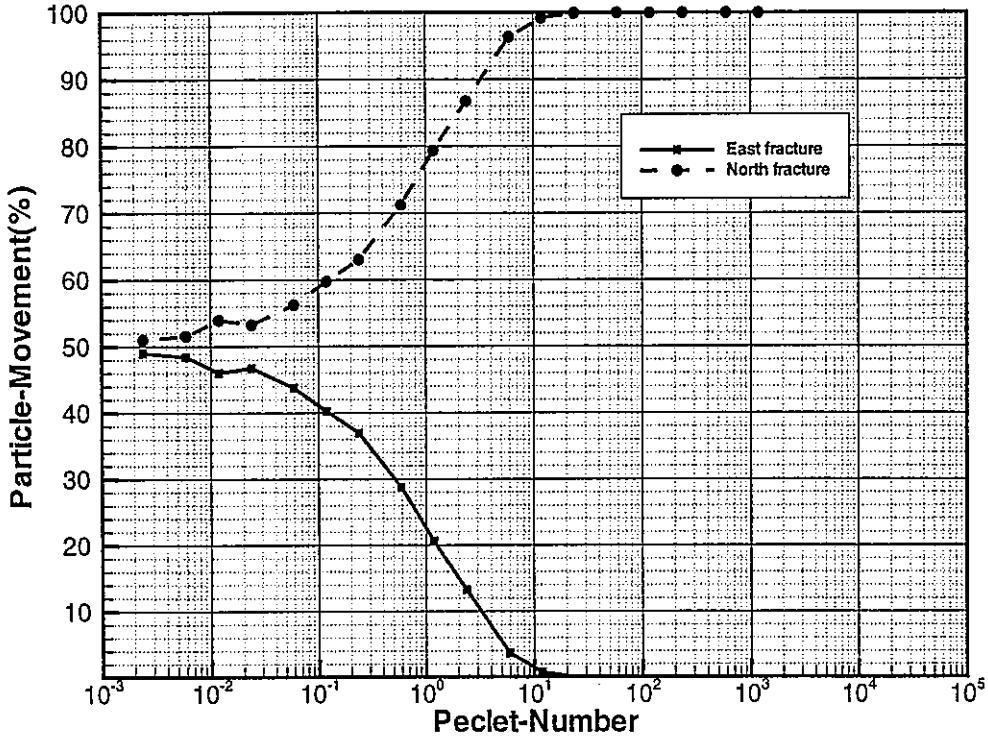


**Figure 9**. The percentage of the particles passing through the boundaries over the total particles is a function of the Peclet number for Model A. The low curve is the percentage of the particles Passing through the right boundary. Particles were placed in west fracture at 5 μm to the left boundary.

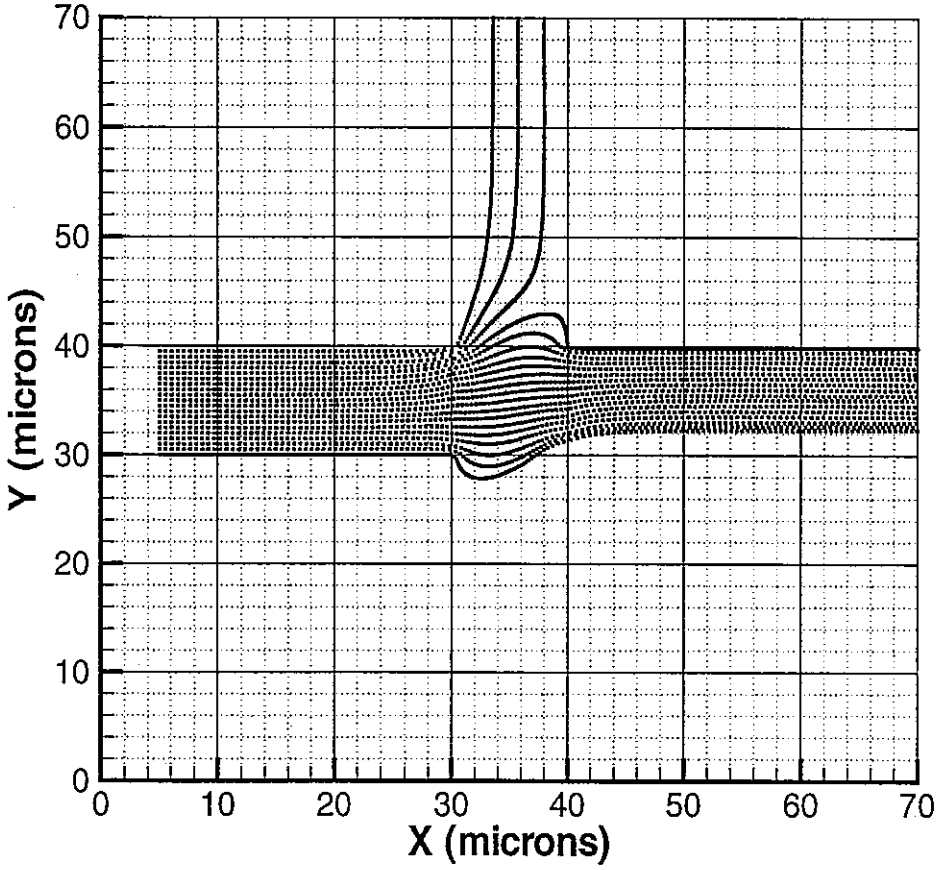


**Figure 10.** Spatial particle trace in Model B with plug flow 65/35 for Peclet number of 118,000.

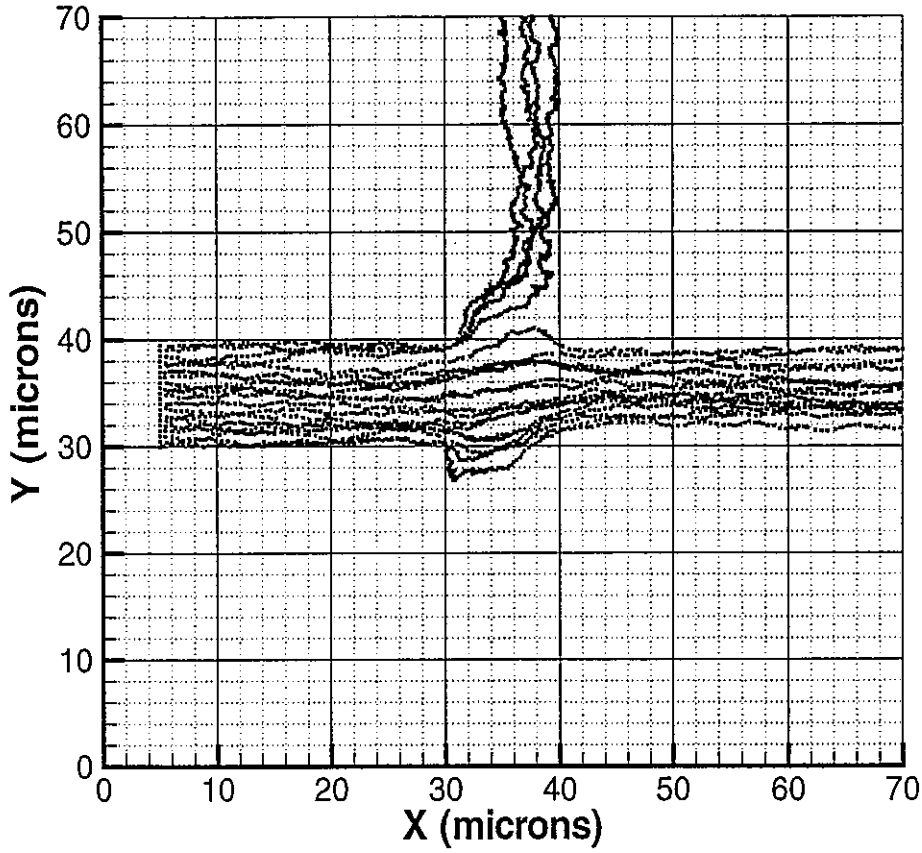


**Figure 11**. Spatial particle trace in Model B with plug flow 65/35 for Peclet number of 118.

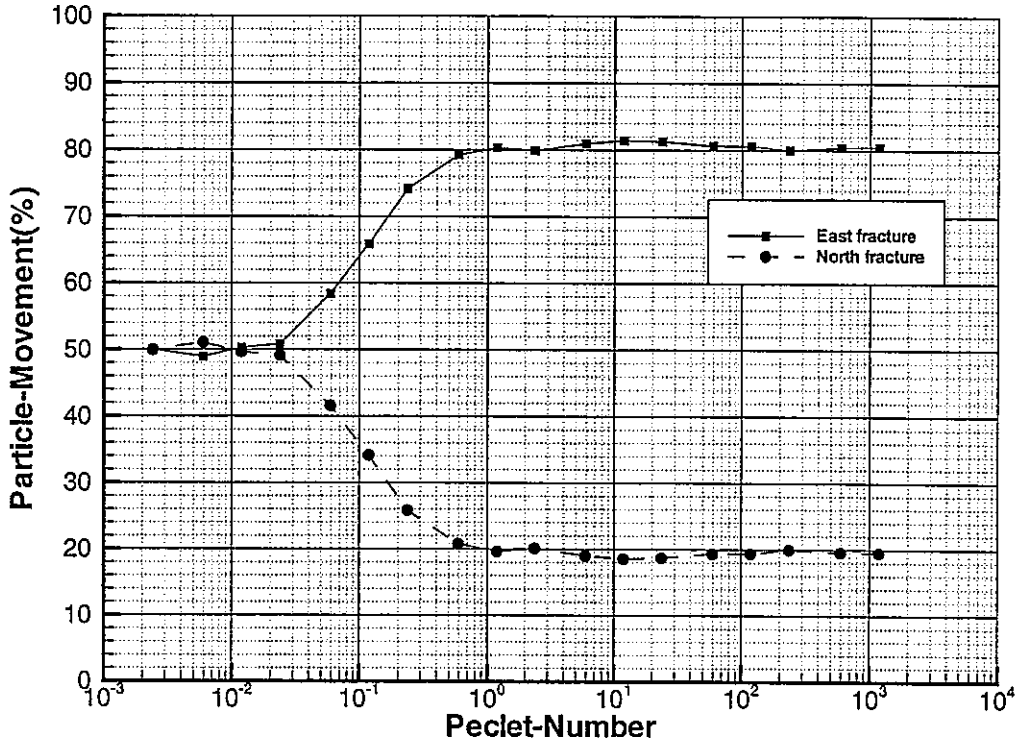


**Figure 12.** The percentage of the particles passing through the boundaries over the total particles is a function of the Peclet number for Model B. The low curve is the percentage of the particles passing through the right boundary. Particles were placed in the west fracture at 5 μm to the left boundary.

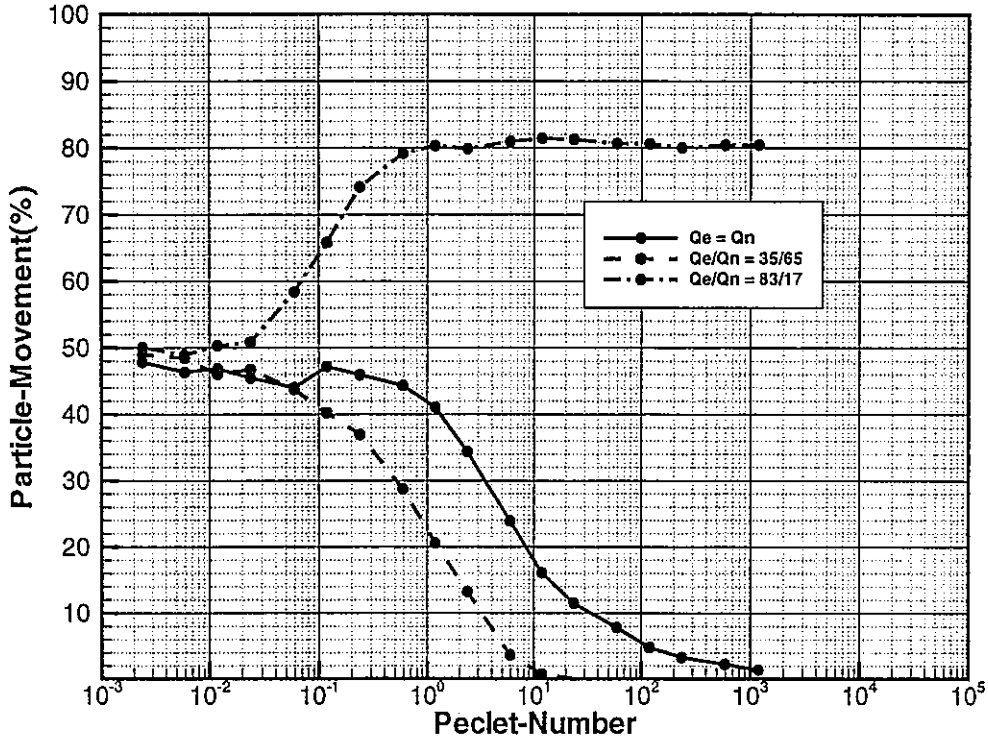


**Figure 13.** Comparisons of mixing characteristics (in terms of the resulting percentage of the particles from the left boundary exist the right boundary) at junction in Model A and Model B with the base model.

# A Summary and Review of the TILA-99 Approach to Performance Assessment

Chin-Fu Tsang

Earth Science Division
Ernest Orlando Lawrence Berkeley National Laboratory
Berkeley, California 94720, USA

## Introduction

This Summary and Review of the TILA-99 Report* is prepared at the request of the Japan Nuclear Cycle Development Institute (JNC). The summary 's focus is on the approach and methodology for geosphere flow and transport predictions in performance assessment, as discussed in the TILA-99 report, and on lessons learned.

The TILA-99 project is a postclosure safety assessment for a potential nuclear waste repository by the responsible Finnish organization POSIVA OY. Its focus is on the normal evolution of the repository at candidate sites in Finland and on the potential release and transport of radionuclides from the repository into the geosphere and biosphere.

The TILA-99 report is organized as follows. After an introduction in Chapter 1, Chapters 2–4 present a description of the spent fuel to be disposed, the disposal concept,

* TILA-99, Safety Assessment of Spent Fuel Disposal in Hästholmen, Kivetty, Olkiluoto and Romuvaara, by Timo Vieno and Henrik Norman, Report POSIVA 99-07, POSIVA OY, Helsinki, Finland; March 1999.

and the general safety regulation being proposed by the Finnish regulatory agency STUK. Then the selection and characterization of four candidate sites and a summary of their characteristics are presented in Chapter 5. Chapter 6 discusses the expected normal evolution of the repository, Chapter 7 introduces their regional-to-site scale analyses of flow and transport. Then the performance of engineering barriers are discussed in Chapter 8. Chapters 9 and 10 describe the approach of scenarios for release and transport analyses of radionuclides and the dose conversion factors used to convert release rates to indicative dose rates.

Site-specific analyses of release and transport of radionuclides from (1) a single initially defective copper-iron canister and from (2) a canister assumed to disappear after 10,000 years are presented in Chapter 11. Chapter 12 evaluates a large number of sensitivity and "what if" analyses, together with a discussion of the completeness of calculated cases and other methodological ambiquities. Consequences of multiple canister failures are given in Chapter 13. The concluding Chapter 14 contains a discussion of the results in the context of the proposed regulatory criteria and their implications for site selection and further research needed.

The current summary and review will follow the following outline. A list of overall general comments will be given in the next section, which we hope will guide the readers as we get into details in the following sections. Then the history of the Finnish nuclear waste management program is briefly described so that we may understand the context of the TILA-99 report and why four sites are being considered in this report. For each of the four sites, the key factor is the presence of fracture zones. The method for their identification and classification is described in the next section, with a discussion of how a repository will be located within the site. The section following will present what TICA-99 project calls the normal evolution scenario. Following this, the models used,

scenarios and cases selected, and analyses made will be described, discussed, and commented upon. A few general remarks will conclude this review.

## Overall General Comments

The TILA-99 approach follows closely the KBS-3 of the Swedish nuclear waste management program. The spent fuel assemblies are to be emplaced in copper-iron canisters, which will be disposed in a repository excavated at a depth of about 500 meters in crystalline bedrock. Because of the similarity in the basic disposal concept, the TILA-99 report is able to make use of much information and data from the Swedish Nuclear Waste Management Company (SKB) and the Swedish Nuclear Power Inspectorate (SKI).

On the other hand, the TILA-99 project has not followed the postclosure performance assessment framework used by SKB in its SR-97 report or the one used by SKI in its SITE 94 report. Instead, in TILA-99, simplified analysis using conservative conditions and parameter values are emphasized. This is the reason that the TILA-99 methodology does not appear to be as detailed or sophisticated as those found in, for example, the SR-97 and the SITE94 reports, or the NIREX95 report of NIREX, who is in charge of the United Kingdom nuclear waste management. (The latter two reports were summarized and reviewed in the last two years under the same JNC-DOE cooperative program as the current report.) For example, the SR-97 report uses a detailed system of so-called "THMC diagrams" for canister, buffer, near-field and far-field regions, while the SITE-94 report contains gives good discussions on consistency among different types of data and on comparison among alternative structural and conceptual models. The NIREX-95 report has a structure-based definition of different types of fractures and uses a formal expert elicitation method to obtain some of their characterizing parameter values. In contrast, while these methods and their issues are clearly in the TILA-99 authors' thinking, they have not gone into them in detail. To supplement their simplified analyses,

TILA-99 has performed a most interesting series of sensitivity and what-if analyses. Furthermore, for some uncertain cases, TILA-99 has been able to "design away" some significant problems. In other words by adjusting the repository design, some important problems can be alleviated.

One problem with simplified analyses is that it is very difficult to validate the applicability of these simplifications. What appear to be conservative assumptions may turn out to be not so conservative if a full and detailed analysis is made under some particular conditions. This can be a serious issue and needs to be evaluated carefully.

The TILA-99 report aims for a report that is "robust, transparent, traceable and reproducible." I believe that the authors have succeeded to a significant extent. It is a well-organized and relatively easy-to-read report.

## A Brief History of the Finnish Waste Management Program

Very briefly, the history of the Finnish waste management program proceeds along the following steps. During the period 1983–1985, site identification surveys were made, and then from 1986 to 1992, preliminary site investigations were conducted. During 1993–2000, detailed site investigations of four sites were carried out. Two of the sites are inland, Romuvaara and Kivetty, and the other two are coastal, Olkiluoto and Hästholmen. The choice of these four sites are based on the relatively fewer uncertainties on these sites and that conditions for conducting exploratory investigation of these sites are more favorable than others. Note that the characteristics of the site related to the performance or safety of a repository to be located there play a relatively minor role in the selection process.

The plan is that in 2000 one of the four sites will be selected for confirmatory investigation, including the construction of an underground rock characterization facility.

If all goes well, construction of the repository will start in 2010 and the emplacement of spent fuel canisters in 2020.

The TILA-99 report is dated 1999, before the selection of a single site for confirmatory investigations. Thus this report covers the four sites, using at each the same methodology for flow and transport calculations and allowing for the different site conditions.

## Site Characterization

The site characterization activities so far on the four sites selected for evaluation are preliminary. Its emphasis is on fracture zones at the site. This characterization is based mainly on surface geological and geophysical surveys as well as downhole tests in about 30 wells at each site. The kinds of downhole well tests employed are double-packer pressure transient testing with packer intervals of 2 m or larger; injection tests, flow meter tests and long term pressure transient tests. General correlation exists between permeablility measured in a wellbore section and the presence of "open" fractures. However, they also found several exceptional cases where large permeability is measured without significant "open" fractures. How to understand these cases and how to use this information in modeling flow and transport and evaluating uncertainty are not emphasized in this report.

From these surface and downhole surveys, fracture zones are identified. These are defined as locations with a high density of fractures. The rest are defined as "intact rock." In the context of this report, "intact rock" can contain fractures up to a density of 1–3 fractures per meter. In subsequent analyses described in the TILA-99 report, except for the near field the flow and transport are assumed to be along the fracture zones, and the role of "intact rock" is neglected. Whether this is an acceptable simplification or

conservative condition needs careful consideration. In any case, this simplification needs to be kept in mind when evaluating the final performance assessments.

TILA-99 groups the observed fracture zones in three ways. The first is "fracture zone classes, " which is defined according to the confidence in the identification of these features. The classes are: directly observed, probable, or possible. The second way is according to fracture zone types based on the degree of fracturing. The types are: crush zone, major fracture zones, fracture zones, and "open or more abundant fracturing." The third way of grouping is according to the dip angle of the fracture zones, defined as steep, with dip angles greater than 60°, between 30°–60°, and smaller that 30°. As an example, the categorization of the fracture zones observed at one of the four sites, in Kivetty bedrock, is shown in Table 1 (TILA-99-99 Report: Table 5-1). At this site, the total number of identified fracture zones is 29.

## Locating Repository within a Site

To conduct performance assessment of a repository for a given site, one would need to specify the location of the repository, since that defines the distribution of potential sources for radionuclide leakage and migration. TILA-99 presents a few general but very useful principles in locating the repository. First, with the identification and categorization of major fracture zones at the site, we need to ensure that the repository avoids the major fracture zones.

Second, the hydrogeologic and geochemical environment at the site needs to be considered. For example, high salinity areas and depths should be avoided, since high salinity would require expensive materials for some of the construction elements and would also adversely affect the performance of engineering barriers. Third, constructability is also an issue in repository siting. Questions such as lithology, bedrock fracturing and engineering properties, and magnitude and orientation of regional in-situ

stress field need to be taken into account. Fourth, we need to be ready to allow "real-time" adjustments of repository siting, thus avoiding large-conducting features discovered during excavation of repository tunnels and deposition holes.

These are all factors that should be borne in mind. For this reason, the repository at a site could well have two or three parts. Figure 1 (TILA-99 Report Figure 5–7) shows what a repository might look like at the Romuvaara site, showing a three-part repository, and how it could avoid major fracture zones.

## Normal Evolution and Major Physiochemical Processes

TILA-99 considers the normal evolution of a repository in a series of time scales:

0 – 100 years

100 – 10,000 years

10,000 – 100,000 years

100,000 – 1 M years

Beyond 1 M years

Most of the important processes occur during the first 100 years. Major processes include:

- Temperature change about +2 to 3°
- Rainfall increase about +10 to 20%
- Sea level about the same
- Initial period: water drained from repository tunnels changing water chemistry
- Canister corrosion (copper canisters assumed to be initially intact)
- Fracture movements due to excavation

- Engineering buffer, bentonite, saturates in about 10 years
- Bentonite swelling pressure
- Surface temperature of canister to attain 100°C
- Thermal expansion
- Gas production at canister or engineering materials
- Resaturation of excavation disturbed zone (EDZ) tunnels, in a few years.

All the above factors and processes need to be considered in models for performance assessment. For the longer time periods, additional factors will need to be considered. For example, over the 100–10,000 year range, one would need to consider the next glaciation which has a cycle of about 20,000 years.

The step of identifying the important factors and processes to be included in performance assessment is an important one. Various organizations, such as SKB and SKI, have used a formal process and framework. TILA-99 does not appear to do so, but instead it takes advantage of these efforts, as well as efforts on this by the Nuclear Energy Agency (NEA), to build up its list of factors and processes.

## Models for Flow and Transport

In the simplified analyses that TILA-99 is using, two models are defined for the calculation of flow and transport corresponding to scales. These are respectively models from regional to site scale and then from site to canister scale. This is illustrated in Figure 2 (TILA-99 Report Figure 7-1).

The regional-to-site scale model corresponds to the scaling from the repository scale of about 10 km to the site scale of 2–3 km. At this level of detail, about 30 hydraulically significant fracture zones (from interpretation of hydraulic testing and surface surveys)

are identified. The repository itself is assumed to be a high conductivity feature. Thus there is a possibility that it may connect with fracture zones that are not connected prior to repository construction. We may remark here that even if the tunnels are well sealed by engineering buffer materials, the presence of higher-conductivity EDZ around the repository still makes it a higher conductivity feature.

At this large scale, the computational model used is the equivalent single porous medium model. Based on this, the overall flow pattern and evolution of the distribution of groundwater salinity are calculated. Thus one is able to trace the flow paths from different points of the repository to the biosphere. For one of the four sites under study in TILA-99, 50 flow paths are traced, and for each of the other three, 150–200 such paths are calculated. A few of the flow paths from a repository layout at Romuvaara are shown as examples in Figure 3 (TILA Report: Figure 7-2). The analysis showed that the impact on flow as a result of heat generation from the waste canisters is much less than that due to topographical gradients, salinity variations or land uplift.

Because of its smaller scale, a fracture network model is used for the site-to-canister model. Several conceptual models can be applied to build up the fracture network, ranging from infinite fractures and a resistor network to stochastic fractures. The boundary conditions and driving forces applied to the site-to-canister model are abstracted from the results of the larger regional-to-site model. Based on this, flow through "intact" rock, EDZ, and fracture zones in the near field of the repository is calculated. The analysis shows that the key quantity is WL/Q along the flow paths, in the fracture network, where

W = width of the flow path

L = length of the flow path

Q = flow rate along the flow path

This analysis is illustrated in Figure 4 (TILA Report: Figure 7-5).

## Scenarios and Analysis Approach

The calculated cases for the repository performance assessment are built up from a list of relevant features, events, and processes (FEPs). Here the TILA project reviews the FEP databases from SKB, SKI, and NEA. Out of such reviews, they identified 1261 project-specific FEP's. These were classified into (1) related to scenarios, (2) related to model, (3) primary data, (4) discussed or (5) excluded because of low probability. It is commented here that such a classification decision at an early stage, based on one's intuition without detailed analysis, could be lead to significant errors. We should bear the classes of FEP's in mind as we progress through performance assessment and evaluate the uncertainty of our predictions. TILA-99 appears to recognize this by its statement that "completeness and robustness of a performance assessment can be assessed only by considering the analyzed scenario assumptions, models, and data together."

The approach to analyses for repository assessment used in TILA-99 follows the outline below. It is a good outline, though it can still be improved (see the Concluding Remarks section below).

- Base case: copper canister initially intact
- Reference cases:
  - Single initially defective canister with one hole - 5 $mm^2$ or 1 $cm^2$
  - Copper canister disappears after 10,000 years
- Sensitivity studies
- "What if" analyses
- Discussion of completeness of analyses

- Evaluation of multiple-canister failure

The base case assumes no initially defective copper canisters. Apparently, this is not an unreasonable assumption provided that there is careful quality control in the manufacturing and checking process. In other words, if there are 1,400 canisters in the repository, the probability of a defective canister is significantly less than one. The reference case of a hole in the canister is illustrated in Figure 5 (TILA-99 Report: Figure 11-4). In this case, a hole is arbitrarily assumed from which fuel-element leakage out of the canister interior can occur, and radionuclides can then migrate through the bentonite buffer into the fractured rock. The disappearing canister case assumes that after 10,000 years, leakage from the fuel elements can occur all around the canister. To illustrate what are the information involved in these calculations, the compartment data for the "hole-in-canister" and "disappearing canister" cases are given in Table 2 and 3 respectively (TILA-99 Report: Tables 11-8 and 11-7).

## Near-field Flow and Transport

For the near field, potential radionuclide migration starts at the canister. Here, three escape routes are identified. These are illustrated in Figure 6 (TILA-99 Report: Figure 11-3):

$Q_F$ - from bentonite buffer around the canister to rock fissures intersecting the deposition hole

$Q_{DZ}$ - from backfill at the top of the deposition hole to EDZ below the tunnel floor

$Q_{TDZN}$ - from tunnel to the rock and EDZ

Beyond the deposition hole, there are also the migration routes from the tunnel to nearby tunnels ($Q_{TTI}$), and to the tunnel and EDZs in the $N^{th}$ tunnel in general ($Q_{TDZN}$).

To proceed with the calculations, TILA-99 utilizes the permeability data from borehole measurements in packer tests at 2 m intervals and builds up 6 m sections to represent the deposition holes. The data statistics on the hydraulic conductivity measurements of 2 m sections in wells at the four sites under study are shown in Table 4 (TILA-99 Report: Table 11-11). When these 2 m sections are randomly combined to form 6 m sections representing the deposition holes, permeability of the deposition holes are calculated. Table 5 (TILA-Report: Table 11-12) shows a comparison of the percentages of "dry" rock sections with $K < 10^{-10}$ m/s when we consider: (1) 2 m sections directly from data, (2) random combinations of two 2 m sections to form 4 m cases, and (3) random combination of three 2 m sections to represent the 6 m deposition holes. Those particular 6 m deposition holes with very high permeabilities built up in this way are rejected. In practice, they will be sealed and not used for waste-canister disposal. From this exercise, we have multiple realizations of the permeability and fracture distribution of the deposition hole. Then the flow rates around the deposition holes are calculated using estimated maximum local hydraulic gradients.

To calculate the flow rate around the deposition hole, we must have the local hydraulic gradients as well as the permeability or hydraulic conductivity. Values of these gradients are obtained from results of the regional-to-site scale flow simulation. A range of values are used, with the maximum gradient representing the gradient between the repository (represented by a high-isotropic permeability feature) and the nearest fracture zone in the bedrock. This is probably a conservative estimate for the gradient near a canister within the repository. The total flow rates $Q_{deephole}$ around a depository hole are then calculated. These are illustrated in Table 6 (TILA-99 Report: Table 11-15).

A simple analysis is then developed in the TILA-99 report to calculate the flow from bentonite into rock ($Q_F$ in Figure 6), using not only $Q_{deephole}$, flow velocity u, and aperture

$b_v$ within the nearby fracture, but also two other transfer coefficients. The first is $Q_{cf}$, which is the equivalent flow rate from the surface of the canister to the mouth of the rock fissure. It is dependent on diffusion coefficient within the bentonite buffer. The second is $Q_{bf}$, which is equivalent flow considering boundary layer (film) resistance between the stagnant water in the bentonite and the water flowing in the rock fissure. This is dependent on molecular diffusion in water and water velocity in the fissure.

Putting all these together, $Q_F$ is calculated for various conditions at the four sites. These are shown in Table 7 (TILA-99 Report: Table 11-16) as $Q_{Fcal}$. To be conservative, they have chosen slightly larger round-off numbers, $Q_F$ in the Table, for further calculations.

Note that TILA-99 found that the main transport resistance is the boundary layer resistance, represented by $Q_{bl}$, between the stagnant water in the bentonite buffer and the water flowing in the rock fissures.

Similar type of analyses are applied to calculate $Q_{DZ}$, $Q_{TDZ}$, etc. These flow transfer processes depend on a number of factors, each with significant uncertainties:

- Absolute and relative permeabilities of rock, disturbed zone, and backfill materials
- Orientation of tunnels relative to the local hydraulic gradient
- Effects of fracture zones intersecting the tunnels
- Hydraulic properties of backfill as a function of salinity (higher salinity at coastal sites and lower at inland sites)
- Long-term properties of backfill and seals.

Estimates of $Q_{DZ}$ and $Q_{TDZ1}$ for the Finnish sites and shown in Table 8 (TILA-99 Report Table 11-17).

In general, TILA-99 simulations are performed in the statistical sense using ranges of factors (such as hydraulic conductivity and gradients) from different simulations and thus obtain flow ranges. This is in contract to simulations of cases one by one, in which each case is internally deterministic and specifically defined. The former, according to TILA-99, represents a simplified and conservative approach. It is interesting to consider carefully the strengths and weaknesses of these two approaches in relationship to the goals of repository performance assessment.

## Far-field Flow and Transport

For the far-field flow simulations of flow and transport, once the migration pathways have been calculated on the region-to-site model, the key process is matrix diffusion and absorption. In TILA-99, a finite diffusion depth is assumed, ~10 cm. Then the key parameter is WL/Q, which is called the transport resistance, and WL is the flow-wetted surface. For conservatism, no dispersion along the routes, no fracture filling and no stagnant pools next to the flow paths are assumed. It is believed that all these factors would increase the transport times of radionuclide migration.

The anion-exclusion effect reduces matrix diffusion and thus enhances anion transport in the far field. However, for the near field this effect impedes anion transport through the bentonite buffer. The effect of cation surface diffusion, on the other hand, decreases the far-field transport while promoting diffusion through the bentonite buffer in the near field. In these cases, conservative alternatives are chosen in the simulations. For example, estimates of cation surface diffusion are included in the near-field calculations, but not included in the far field.

Again, estimates of WL/Q are made in the statistical sense. The range of flows Q is obtained either from fracture network model simulations or from calculations based on the range of hydraulic conductivities in 6 m borehole sections representing deposition

holes. The flow wetted areas WL are calculated from a fracture network model, using unit Q value. The product of the two ranges gives estimates of the range of WL/Q for the four sites under different scenarios. An example of the results is shown in Table 9 (TILA-99 Report: Table 11-18).

Thermal effects are not considered in the simulations of the far field flow and transport, since thy are shown not to affect the flow pattern significantly. Note that this conclusion may not be valid in general and should be evaluated carefully.

Finally the flow and transport data calculated for the reference scenarios are shown in Table 10 (TILA-99 Report: Table 11-19).

## Sensitivity and "What if" Analyses

One of the main strengths of the TILA-99 report is its careful consideration and clear presentation of sensitivity and "what if" analyses. Under sensitivity analysis, the following cases are considered:

- Alternative canister failure times (canister disappearing at 0, $10^3$, $10^5$, and $10^6$ years)
- Alternative source term models
- Case of very high solubilities in reducing conditions
- Case of oxidizing conditions in the near field
- Case of transport along 10 tunnel sections each with a leaking canister
- Alternative penetration depths of matrix diffusion (1 and 4 cm)
- Alternative dispersion (Pe number = 2) along flow paths in the far field
- Alternative dose conversion factor (increased by a factor of 10)

- Use of realistic retardation data in the near field and far field respectively

The "what if" scenarios include:

- Case of combination of very high groundwater flow and high saline groundwater chemistry
- Case of very poor performance of the bentonite buffer
- Case of gas production in a canister with its displacement of contaminant water out of the canister
- Effect of glacial melt water involving very high flow and oxidizing conditions in the geosphere, buffer, and backfill
- Effect of post-glacial faulting at 30,000 years, breaking canister, displacing bentonite, enhancing flow and transport and bringing about oxidizing conditions in the whole near field and geosphere.

As can be seen, some of these sensitivity and "what if" scenarios represent rather drastic conditions. For each, the impact and probability of occurrence are evaluated. TILA-99's conclusions indicate a consistent picture of performance for the modeled transport system – the system is robust and can tolerate even much more conservative assumptions without drastic impact on potential releases to the biosphere. Further, except for certain very unlikely events, such as post-glacial faulting which cuts through several barriers at the same time, the results are still orders of magnitude below the regulatory limits. The only negative case is the combination of very high flow rate and high saline groundwater chemistry conditions.

Beyond the sensitivity and "what if" analyses, TILA-99 also generally discussed additional issues, ranging from microbe and colloidal transport, effect of concrete in the

repository and high pH plume, gas bubbles and human intrusions. There is also a discussion of completeness and risk estimation.

## Concluding Remarks

TILA-99 is an interesting report. As noted above, it attempts to do performance assessment of a potential nuclear waste repository using simplified, conservative conditions. This is not easy, and care should be taken to ensure that simplifications used are indeed conservative. Such simplifications should also be recorded, tracked, and borne in mind all the way through analysis to predictions and conclusions, to ensure that they are indeed conservative.

It is also interesting that TILA-99 does not perform multiple-case analysis, in which each case is deterministic and specifically defined. Then ranges of predictions are built from many such case calculations. Rather, in TILA-99, ranges of parameters and conditions are used from data and submodel calculations, and these are then combined to give ranges of predictions. It is not clear which is a better approach for the purpose of performance assessment. It is still an open scientific question. It is noted that the TILA-99 approach needs to be done with great care to ensure that there is no internal inconsistency.

One weakness in the analysis approach described in TILA-99 is the lack of evaluation of alternative structural and conceptual models of the sites, as well as evaluation of consistencies among different types of characterizing data. Such evaluations were done very carefully by, for example, the SKI in their SITE94 report.

On the other hand, one strength of the TILA-99 report is its careful analysis and clear presentation of sensitivity and "what if" analyses. I believe it is a good pattern that should be followed by other performance assessment efforts.

## Table Captions

Table 1 (TILA-99-99 Report: Table 5-1) Number of fracture zones in each class, type and dip category in Kivetty's bedrock model. The total number of fracture zones is 29.

Table 2 (TILA-99 Report: Table 11-8) Compartment data of the near-field transport model in the "hole in canister" case.

Table 3 (TILA-99 Report: Table 11-7) Compartment data of the near-field transport model in the "disappearing canister" case.

Table 4 (TILA-99 Report: Table 11-11) Statistics of hydraulic conductivity measurements (2 m sections) in intact rock below the depth of 200 meters (Poteri & Laitinen 1999).

Table 5 (TILA-Report: Table 11-12) Percentage of "dry" rock sections where the hydraulic conductivity is below the measurement limit ($K<10^{-10}$ m/s). The proportions of the "dry" intervals have been calculated by combining randomly all measurements over 2 m sections, and alternatively on the basis of data sets where the highest conductivities have been cut off (Poteri & Laitinen 1999).

Table 6 (TILA-99 Report: Table 11-15) Total flow rates in the rock around deposition hole: values selected for TILA-99.

Table 7 (TILA-99 Report: Table 11-16) Transfer coefficient ($Q_F$) from the bentonite into the rock. The cases and the primary input parameters and the $Q_F$ values selected for use in the near-field transport analyses are indicated by **bold**. Other entries are sensitivity analyses and calculated intermediate results.

Table 8 (TILA-99 Report Table 11-17) Transfer coefficients (flow rates) from the top of deposition hole and from the tunnel section above the deposition hole into the geosphere and the corresponding water turn-over times.

Table 9 (TILA-99 Report: Table 11-18) Estimated transport resistances (WL/Q) of migration paths (Poteri & Laitinen 1999).

Table 10 (TILA-99 Report: Table 11-19) Summary of flow and transport data for the reference scenarios.

## Figure Captions

Figure 1 (TILA-99 Report Figure 5–7) An example of locating deposition tunnels for 2,200 canisters containing 4,000 tU of spent fuel at the depth of 500 meters at Romuvaara (Äikäs et al. 1999d).

Figure 2 (TILA-99 Report Figure 7-1) Analyses of groundwater flow and solute transport in the regional-to-site and site-to-canister scales (Poteri & Laitinen 1999).

Figure 3 (TILA Report: Figure 7-2) Example of flowpaths from a repository layout at Romuvaara. The upper and lower figures present the same situation. The fracture zone R8 has been removed from the upper figure to show the flowpaths behind (Kattilakoski & Koshinen 1999).

Figure 4 (TILA Report: Figure 7-5) Estimation of the ratio of the flow wetted surface and flow rate along a flowpath in the fracture network (Poteri & Laitinen 1999).

Figure 5 (TILA-99 Report: Figure 11-4) Near-field transport model in the "hole in canister" case.

Figure 6 (TILA-99 Report: Figure 11-3) Near-field transport model in the "disappearing canister" case.

*Table 5-1. Number of fracture zones in each class, type and dip category in Kivetty's bedrock model. The total number of fracture zones is 29.*

| Fracture zone class | Fracture zone type | General dip |
|---|---|---|
| Directly observed: 17<br>Probable: 9<br>Possible: 3 | Crush zone: -<br>Major fracture zone: 9<br>Fracture zone: 16<br>Open or more abundant fracturing: 4 | Steep (>60°): 23<br>Moderate (30°-60°): 6<br>Shallow (<30°): - |

Table 1

*Table 11-8. Compartment data of the near-field transport model in the "hole in canister" case.*

Canister interior
- fuel: Loviisa: 1.44 tU, Olkiluoto: 2.14 tU
- water volume: Loviisa 425 litres, Olkiluoto: 700 litres
- number of compartments: 1

Hole in the canister
- length: 5 cm
- area: 5 $mm^2$ ("small") or 1 $cm^2$ ("large")
- filling: water; bentonite for cations in non-saline water (because $D_e = 5 \cdot 10^{-9}$ $m^2/s > D_w = 2 \cdot 10^{-9}$ $m^2/s$)
- transfer coefficients through the hole are calculated from the above data (the model contains thus no compartments in the hole)

Bentonite between the hole and rock
- hemisphere having a radius of 0.35 m
- number of compartments (hemisphere shells): 48
- transfer into the geosphere from the outermost compartment: $Q_F$

Table 2

*Table 11-7. Compartment data of the near-field transport model in the "disappearing canister" case.*

---

Canister interior
- fuel: Loviisa: 1.44 tU, Olkiluoto: 2.14 tU
- water volume: Loviisa 425 litres, Olkiluoto: 700 litres
- number of compartments: 1

Bentonite around the canister
- height: Loviisa: 3.6 m, Olkiluoto: 4.8 m
- inner radius: 0.53 m
- outer radius: 0.88 m
- number of compartments (in the radial direction): 22
- transfer into the geosphere from the outermost compartment: $Q_F$

Bentonite above the canister
- height: 1.5 m
- area: 2.4 $m^2$ (horizontal cross-section)
- number of compartments (in the vertical direction): 20

Backfill in the top of the deposition hole
- height: 1.0 m
- area: 2.4 $m^2$ (horizontal cross-section)
- number of compartments: 1
- transfer into the geosphere: $Q_{DZ}$

Backfill in the tunnel
- number of tunnel sections modelled: N = 1
- volume: 100 $m^3$
- number of compartments: 1
- no diffusion resistance in the tunnel, i.e. the diffusion distance between the backfill compartments in the deposition hole and tunnel is 0.5 m, and the diffusion area is 2.4 $m^2$
- transfer into the geosphere: $Q_{TDZ1}$
- transfer into the next tunnel section: $Q_{TT1} = 0$

---

Table 3

*Table 11-11. Statistics of hydraulic conductivity measurements (2 m sections) in intact rock below the depth of 200 metres (Poteri & Laitinen 1999).*

| | | Over measurement limit ($K > 10^{-10}$ m/s) | | |
|---|---|---|---|---|
| | Total number of measurements | Total | Upper cut-off $K < 10^{-7}$ m/s | Upper cut-off $K < 10^{-8}$ m/s |
| Hästholmen | 1400 | 381 / 27% | 332 / 24% | 227 / 16% |
| Kivetty | 1370 | 197 / 14% | 170 / 12% | 119 / 9% |
| Olkiluoto | 1719 | 175 / 10% | 153 / 9% | 126 / 7% |
| Romuvaara | 771 | 74 / 10% | 73 / 9% | 61 / 8% |

Table 4

*Table 11-12. Percentage of "dry" rock sections where the hydraulic conductivity is below the measurement limit ($K < 10^{-10}$ m/s). The proportions of the "dry" intervals have been calculated by combining randomly all measurements over 2 m sections, and alternatively on the basis of data sets where the highest conductivities have been cut off. (Poteri & Laitinen 1999).*

| | All measurem. | | | Upper cut-off $K_{2m} < 10^{-7}$ m/s | | | Upper cut-off $K_{2m} < 10^{-8}$ m/s | | |
|---|---|---|---|---|---|---|---|---|---|
| Number of combined 2 m sections | 1 | 2 | 3 | 1 | 2 | 3 | 1 | 2 | 3 |
| Hästholmen | 73 | 53 | 39 | 76 | 58 | 44 | 84 | 70 | 59 |
| Kivetty | 86 | 73 | 63 | 88 | 77 | 67 | 91 | 83 | 76 |
| Olkiluoto | 90 | 82 | 74 | 91 | 82 | 74 | 93 | 85 | 78 |
| Romuvaara | 90 | 81 | 72 | 91 | 83 | 76 | 92 | 86 | 80 |

Table 5

*Table 11-15. Total flow rates in the rock around deposition hole: values selected for TILA-99.*

| Case | $Q_{dephole}$ (l/yr) |
|---|---|
| Non-saline groundwater | |
| All sites: "median" | 0.5 |
| Romuvaara and future Olkiluoto: "95th percentile" | 10 |
| Kivetty and future Hästholmen: "95th percentile" | 50 |
| A "very wet" location | 200 |
| Saline groundwater | |
| Present-day Hästholmen and Olkiluoto: "median" | 0.5 |
| Present-day Olkiluoto: "95th percentile" | 5 |
| Present-day Hästholmen: "95th percentile" | 25 |
| A "very wet" location | 100 |

Table 6

*Table 11-16. Transfer coefficient ($Q_F$) from the bentonite into the rock. The cases and the primary input parameters and the $Q_F$ values selected for use in the near-field transport analyses are indicated by bold. Other entries are sensitivity analyses and calculated intermediate results.*

| | $Q_{dephole}$ (l/yr) | $2b_V$ (μm) | u (m/yr) | $Q_{cf}$ (l/yr) | $Q_{bl}$ (l/yr) | $Q_{Fcal}$ (l/yr) | $Q_F$ (l/yr) |
|---|---|---|---|---|---|---|---|
| Sensitivity analysis | 400 | 680 | 330 | 5.4 | 12 | 3.7 | |
| **Non-saline sites, very wet** | **200** | 540 | 210 | 5.3 | 7.4 | 3.1 | **5** |
| **Saline sites, very wet** | **100** | 430 | 130 | 5.1 | 4.7 | 2.4 | **3** |
| **KI, 95%<br>HH-f, 95%** | **50** | 340 | 84 | 5.0 | 2.9 | 1.9 | **2** |
| **HH-pd, 95%** | **25** | 270 | 53 | 4.9 | 1.9 | 1.3 | **1.5** |
| SA: $2b_V$ = 300 μm | 10 | 300 | 19 | 4.9 | 1.2 | 0.98 | |
| **RO, 95%<br>OL-f, 95%** | **10** | 200 | 29 | 4.7 | 1.0 | 0.83 | **1** |
| SA: $2b_V$ = 100 μm | 10 | 100 | 57 | 4.4 | 0.71 | 0.61 | |
| OL-pd, 95% | 5 | 160 | 18 | 4.6 | 0.63 | 0.56 | **0.6** |
| Sensitivity analysis | 1 | 93 | 6.2 | 4.3 | 0.22 | 0.21 | |
| **All sites, median** | **0.5** | 74 | 3.9 | 4.2 | 0.14 | 0.13 | **0.2** |
| Sensitivity analysis | 0.1 | 43 | 1.3 | 4.0 | 0.047 | 0.046 | |

HH = Hästholmen, KI = Kivetty, OL = Olkiluoto, RO = Romuvaara
pd = present-day, f = future, SA = sensitivity analysis

Table 7

*Table 11-17. Transfer coefficients (flow rates). from the top of deposition hole and from the tunnel section above the deposition hole into the geosphere and the corresponding water turn-over times.*

| | Top of deposition hole | | Tunnel | |
|---|---|---|---|---|
| | $Q_{DZ}$ (l/yr) | Water turn-over time (years) | $Q_{TDZ1}$ (l/yr) | Water turn-over time (years) |
| All sites, "median" | 2 | 240 | 100 | 200 |
| All sites, "95th percentile" | 10 | 48 | 500 | 40 |
| Saline sites, "very wet" | 30 | 16 | 1500 | 13 |
| Non-saline sites, "very wet" | 50 | 9.6 | 2000 | 10 |

Table 8

*Table 11-18. Estimated transport resistances (WL/Q) of migration paths (Poteri & Laitinen 1999).*

| | Range of WL/Q based on intact rock flow rates based on hydr. measurements (yr/m) | Range of WL/Q based on intact rock flow rates from fracture network simulations (yr/m) |
|---|---|---|
| Hästholmen - present-day | $8.0 \cdot 10^5$ - $4.0 \cdot 10^6$ | $9.1 \cdot 10^5$ - $1.6 \cdot 10^6$ |
| - not including 50 m of EDZ | $5.6 \cdot 10^2$ - $3.4 \cdot 10^6$ | $5.6 \cdot 10^2$ - $9.9 \cdot 10^5$ |
| Hästholmen - future | $1.8 \cdot 10^5$ - $7.1 \cdot 10^5$ | $1.2 \cdot 10^5$ - $4.2 \cdot 10^5$ |
| - not including 50 m of EDZ | $8.9 \cdot 10^4$ - $4.4 \cdot 10^5$ | $3.0 \cdot 10^4$ - $1.5 \cdot 10^5$ |
| Kivetty | $1.3 \cdot 10^5$ - $8.6 \cdot 10^5$ | $2.7 \cdot 10^5$ - $2.5 \cdot 10^6$ |
| - not including 50 m of EDZ | $5.6 \cdot 10^4$ - $6.0 \cdot 10^5$ | $2.0 \cdot 10^5$ - $2.2 \cdot 10^6$ |
| Olkiluoto - present-day | $5.8 \cdot 10^5$ - $1.1 \cdot 10^6$ | $1.4 \cdot 10^6$ - $4.5 \cdot 10^6$ |
| - not including 50 m of EDZ | $2.0 \cdot 10^5$ - $8.0 \cdot 10^5$ | $1.0 \cdot 10^6$ - $4.2 \cdot 10^6$ |
| Olkiluoto - future | $5.1 \cdot 10^5$ - $2.3 \cdot 10^6$ | $1.4 \cdot 10^6$ - $1.1 \cdot 10^7$ |
| - not including 50 m of EDZ | $2.0 \cdot 10^5$ - $2.0 \cdot 10^6$ | $1.1 \cdot 10^6$ - $1.1 \cdot 10^7$ |
| Romuvaara | $3.6 \cdot 10^4$ - $5.6 \cdot 10^5$ | $3.6 \cdot 10^4$ - $3.5 \cdot 10^6$ |
| - not including 50 m of EDZ | $2.2 \cdot 10^2$ - $5.2 \cdot 10^5$ | $2.2 \cdot 10^2$ - $3.5 \cdot 10^6$ |

Table 9

*Table 11-19. Summary of flow and transport data for the reference scenarios.*

| Case | Chemistry | Near-field transfer coefficients $Q_F$ (l/yr) | $Q_{DZ}$ (l/yr) | $Q_{TDZ1}$ (l/yr) | Transport resistance WL/Q (yr/m) | Canister |
|---|---|---|---|---|---|---|
| **ns50** | **non-saline** | **0.2** | **2** | **100** | $5{\cdot}10^4$ | **Olkiluoto** |
| **sal50** | **saline** | **0.2** | **2** | **100** | $5{\cdot}10^4$ | **Olkiluoto** |
| K95=Hf95 | non-saline | 2.0 | 10 | 500 | $2{\cdot}10^4$ | Olkiluoto |
| Hpd95 | saline | 1.5 | 10 | 500 | $2{\cdot}10^4$ | Olkiluoto |
| R95=Of95 | non-saline | 1.0 | 10 | 500 | $2{\cdot}10^4$ | Olkiluoto |
| Opd95 | saline | 0.6 | 10 | 500 | $2{\cdot}10^4$ | Olkiluoto |
| vhflowns | non-saline | 5.0 | 50 | 2000 | $5{\cdot}10^3$ | Olkiluoto |
| vhflowsal | saline | 3.0 | 30 | 1500 | $1{\cdot}10^4$ | Olkiluoto |
| ns50Lo | non-saline | 0.2 | 2 | 100 | $5{\cdot}10^4$ | Loviisa |
| sal50Lo | saline | 0.2 | 2 | 100 | $5{\cdot}10^4$ | Loviisa |

H = Hästholmen, K = Kivetty, O = Olkiluoto, R = Romuvaara
pd = present-day, f = future, ns = non-saline, sal = saline, Lo = Loviisa canister
50 = median, 95 = 95th percentile, vhflow = very high flow

Table 10

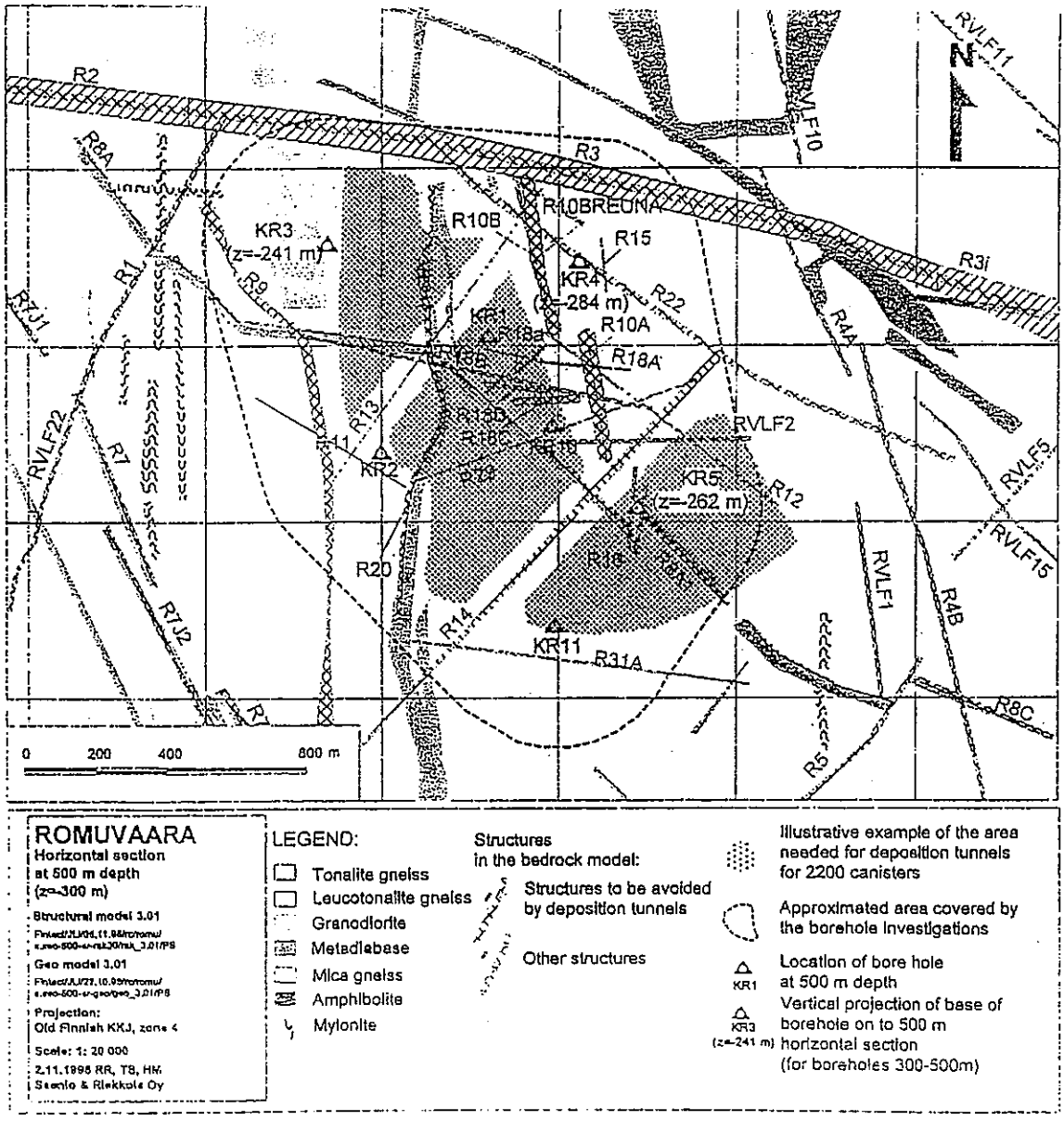


*Figure 5-7. An example of locating deposition tunnels for 2 200 canisters containing 4 000 tU of spent fuel at the depth of 500 metres at Romuvaara (Äikäs et al. 1999d).*

Figure 1

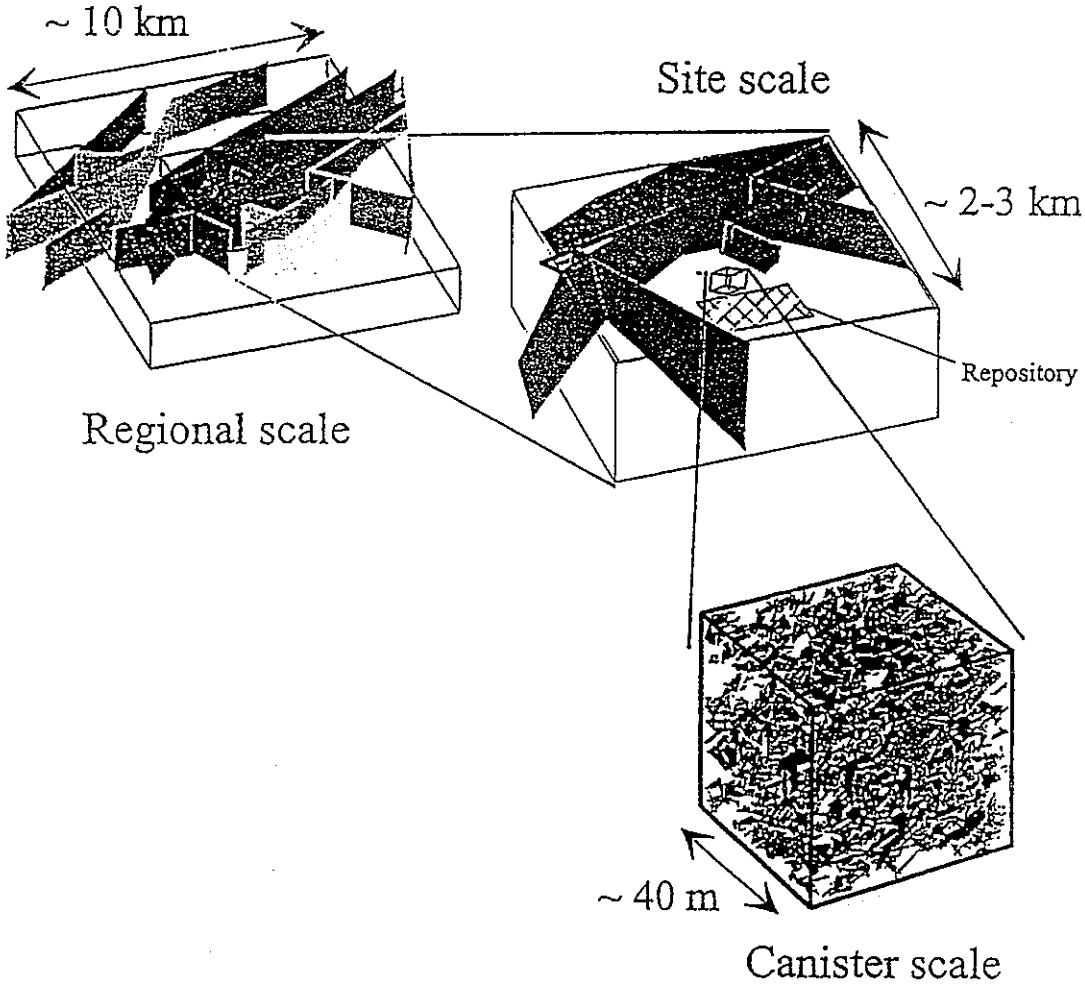


*Figure 7-1. Analyses of groundwater flow and solute transport in the regional-to-site and site-to-canister scales (Poteri & Laitinen 1999).*

Figure 2

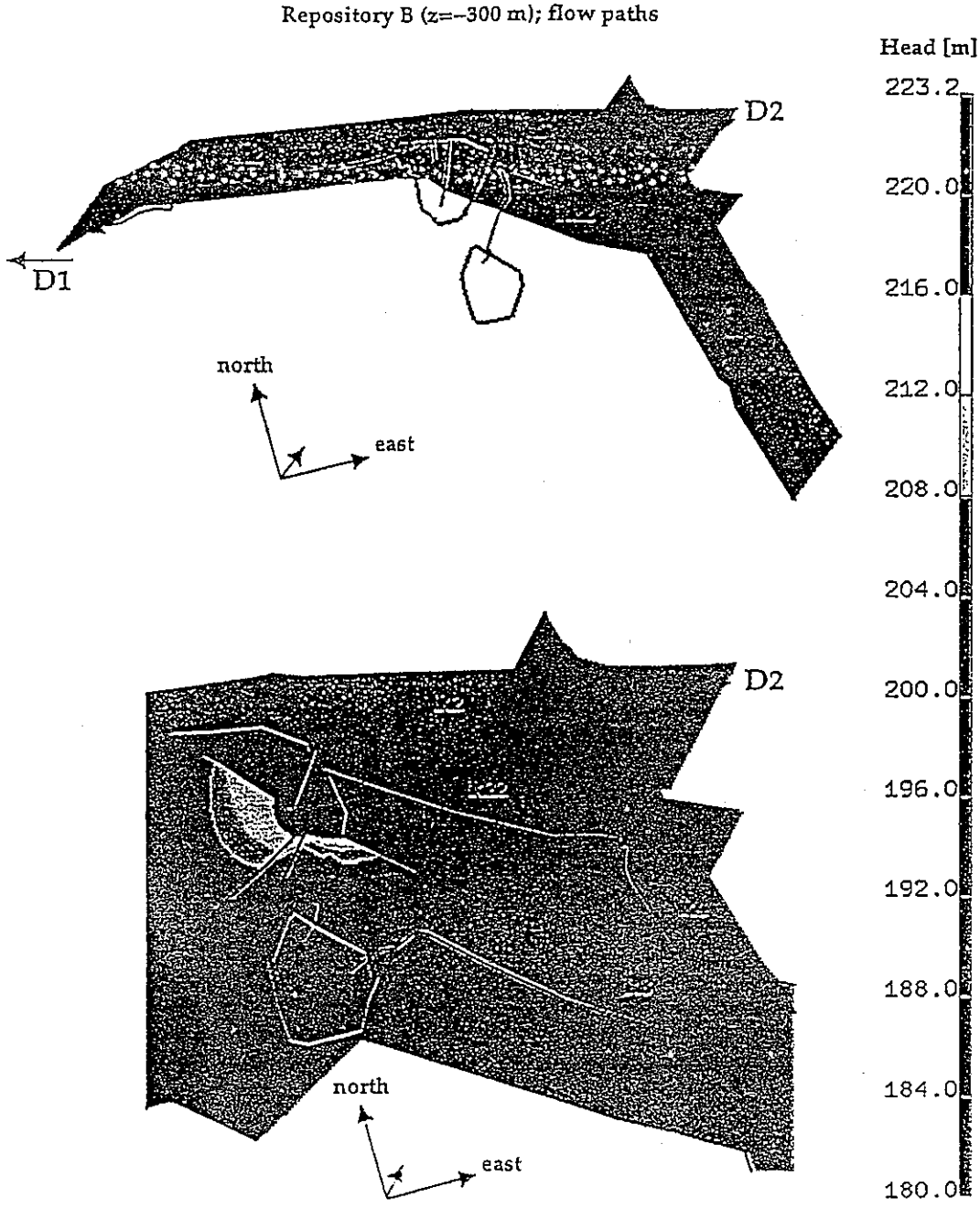


*Figure 7-2. Example of flowpaths from a repository layout at Romuvaara. The upper and lower figures present the same situation. The fracture zone R8 has been removed from the upper figure to show the flowpaths behind (Kattilakoski & Koskinen 1999).*

Figure 3

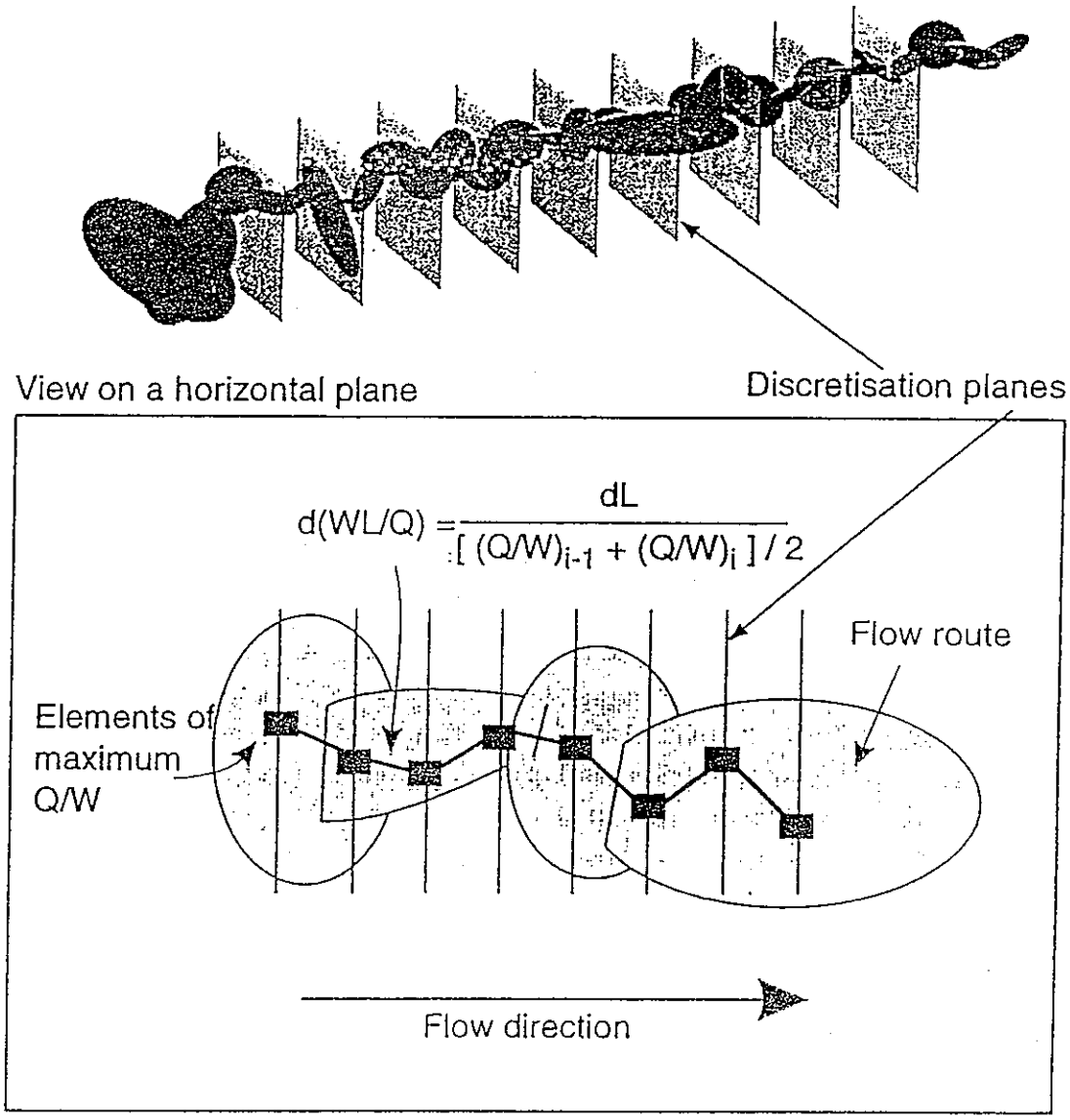


*Figure 7-5. Estimation of the ratio of the flow wetted surface and flow rate along a flowpath in the fracture network (Poteri & Laitinen 1999).*

Figure 4

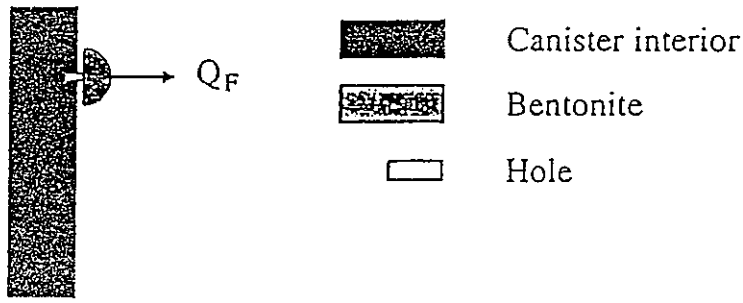


*Figure 11-4. Near-field transport model in the "hole in canister" case.*

Figure 5

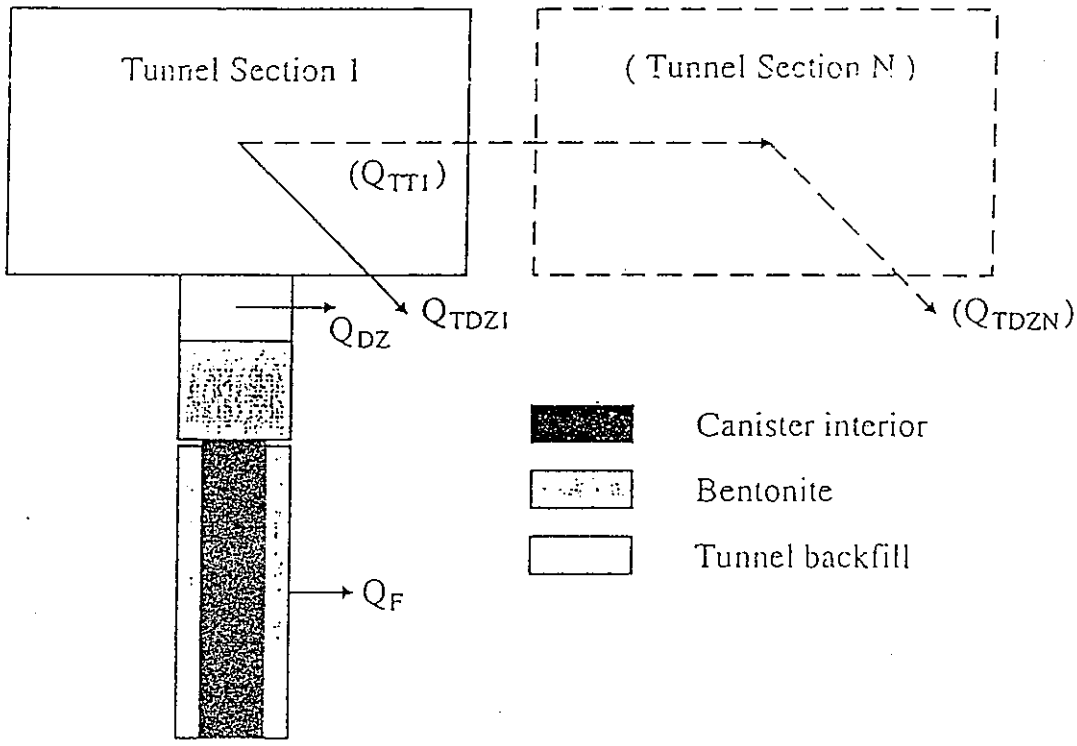


*Figure 11-3. Near-field transport model in the "disappearing canister" case.*

Figure 6

# Modeling Groundwater Flow and Mass Transport in Heterogeneous Media—Issues and Challenges

Chin-Fu Tsang

*Earth Sciences Division,*
*Ernest Orlando Lawrence Berkeley National Laboratory,*
*Berkeley, California 94720, USA*

## ABSTRACT

The need for predictions of groundwater flow and contaminant transport in the subsurface—over large distances and long time periods—has imposed extraordinary demands on the field of hydrogeology. Such a need arises in assessing the safety of a geologic nuclear waste repository and in evaluating groundwater contamination and remediation designs. One of the main difficulties in modeling groundwater flow and mass transport is the heterogeneity of the flow system, both in terms of its characterization through *in situ* measurements and its conceptualization and simulation. This paper reviews some important issues and challenges in modeling flow and transport in heterogeneous media, and discusses approaches to address certain aspects of the problem. Topics discussed include dynamic flow channeling, tracer breakthrough curves, multiple scales for flow in fractured rocks, different scales in measurement, modeling, prediction and heterogeneity, and system characterization and analysis for predictive modeling.

# 1. INTRODUCTION

The need for predictions of groundwater flow and contaminant transport in the subsurface over large distances and long time periods arises in the safety assessment of a geologic nuclear waste repository or in the evaluation of groundwater contamination and remediation designs. These problems are of great concern in many countries. They require calculations of flow and transport in geologic systems over distances of tens to hundreds of kilometers and time periods of 10,000–100,000 years. This need imposes extraordinary demands on the field of hydrogeology. One of the main difficulties in modeling groundwater flow and mass transport is the heterogeneity of the flow system, both in terms of the system's characterization through *in situ* measurements and its conceptualization and simulation. This is also an important basic science problem in hydrogeology. This paper reviews a number of scientific issues and challenges in flow and transport in heterogeneous media and indicates possible approaches to certain aspects of the problem.

Heterogeneity of groundwater flow systems may be considered in terms of large, intermediate, and small features. The large features include major fault zones, layering structures, or regional compartmentation of areas with different hydraulic conductivity or permeability. The small features include permeability variations on a scale much smaller than the scale of measurement. Intermediate features are those of the same order as the measurement scale. It is quite apparent that large features would have a significant impact on flow and transport. They can be detected and characterized through a careful program of surface geologic and geophysical surveys, downhole logging at a number of locations, and short-term and long-term hydraulic tests. Once these large features are identified and

characterized, flow and transport calculations may be made using numerical methods such as the finite-difference or finite-element methods. Continued progress in methodologies and techniques is being made to perform this kind of work, such as geophysical tomography and joint inversion of hydrologic and geophysical data (e.g., Alumbaugh and Neuman, 1997; Smith et al., 1999; Wilt et al., 1995; Nekut, 1994; Tichelaar et al., 1997; Walsh, 1993; Vasco et al., 1997, 1998; Lee, 1995; Hyndman et al., 1994; Rector, 1995; Rubin et al., 1992; Karasaki et al., 2000).

For small-scale features whose dimensions are much smaller than the measurement scale, some kind of averaging can usually be done. One well-known example is the dispersion coefficient that can be used to describe solute-concentration spreading that results from flow velocity variations (caused in turn by small-scale heterogeneity). A number of authors have developed expressions for dispersivity in terms of permeability variance and correlation length (see Gelhar and Axness, 1983; Gelhar, 1986, Dagan, 1984, 1986, 1990; Neuman et al., 1987, Neuman and Zhang, 1990; Rubin, 1990). However, for intermediate-scale features (typically 0.1 to 0.5 times the flow distance), the situation is not so simple.

We note that in principle we know how to handle the large and small features. With the former, we can use *in situ* surveys and borehole measurements, followed by deterministic modeling; with the latter, we can employ some kind of averaging and representation. Intermediate-scale heterogeneity is the main scientific challenge. A number of issues related to this challenge are discussed below.

## 2. DYNAMIC FLOW CHANNELING

Conventional approaches to flow and transport in heterogeneous media, even for intermediate-scale heterogeneity, assume the applicability of the well-known advective-dispersion equation (e.g., Javandel, et al., 1984), which may be written as

$$\frac{\partial}{\partial x_i}\left(D_{ij}\frac{\partial C}{\partial x_j}\right) - v_i\frac{\partial C}{\partial X_i} = \frac{\partial C}{\partial t}$$

where

$$v_i = -\frac{\bar{k}}{n}\frac{\partial h}{\partial x_i}$$

and

$$\frac{\partial^2 h}{\partial x_i^2} = 0$$

In these equations, C is the solute concentration, $v_i$ is the average pore velocity in the direction $x_i$, $D_{ij}$ is the dispersion coefficient tensor, n is the effective porosity, h is the hydraulic pressure head, $\bar{k}$ is the mean hydraulic conductivity and $x_i$ are the Cartesian coordinates.

For two-dimensional cases, if the flow is in the x direction with velocity v, and $D_{ij}$ can be defined as $D_L$ along the main direction of flow x and $D_T$ transverse to it, one gets the well-known solution for the spread of a tracer plume, which at t = 0 is a line concentration $C_o$ with length 2a normal to the flow direction (Javandel, et al., 1984, p. 19):

$$C(x,y,\tau) = \frac{C_o}{4(\pi D_L)^{1/2}} \exp\left[\frac{vx}{2D_L}\right] \cdot$$

$$\cdot \int_o^t \exp\left\{-\frac{v^2\tau^2 - x^2}{4D_L}\tau^{-5/2} \cdot \left[\operatorname{erf}\left(\frac{a-y}{2(D_T\tau)^{1/2}}\right) + \operatorname{erf}\left(\frac{a+y}{2(D_T\tau)^{1/2}}\right)\right]\right\} d\tau$$

This indicates a simple-body plume of tracers moving along the x direction with concentration smearing in the x and y direction, depending on the parameters $D_L$ and $D_T$, respectively.

However, in a system with intermediate-scale heterogeneity under a pressure gradient, flow will seek out separate paths of least resistance. The resulting tracer plume will not be a simple-body volume, but will follow a number of specific paths through the heterogeneous medium. These are paths of least total resistance, and such behavior is the *flow channel phenomenon* (Tsang and Tsang, 1987; 1989; Moreno and Tsang, 1994; Birkholzer and Tsang, 1997). Since the main flow paths are dependent not only on the heterogeneity field, but also on the orientation of the pressure gradient, we may call it *dynamic channeling* (Tsang et al., 2000).

To illustrate this phenomenon and its dependence on heterogeneity, let us consider a heterogeneous field that may be generated by using a geostatistical method (the Geostatistical Library GSLIB, Deutsch and Journel, 1992). The hydraulic conductivity k can be given by a lognormal distribution:

$$n(k)dk = \frac{1}{\sqrt{2\pi}\,\sigma \ln 10} \exp\left[-\frac{(\log k - \log \bar{k})^2}{2\sigma^2}\right]\frac{dk}{k}$$

where k is the value at each spatial location and $\sigma$ is its standard deviation in log k, around a mean $\bar{k}$. The spatial variational structure may be described by an exponential covariance function given by

$$E[\log k(r_1) - \log \bar{k}][\log k(r_2) - \log \bar{k}] = \sigma^2 \exp\left[-\frac{2|r_2 - r_1|}{\lambda}\right]$$

where E is the expectation value, $r_1$ and $r_2$ are two spatial points, and $\lambda$ is the spatial correlation length. For the exponential variogram, the effective spatial correlation range is three times the correlation length (see deMarsily, 1986). Let us define the ratio of the effective spatial correlation range to the total line flow distance as $\lambda' = 3\lambda/L$. Thus we can characterize the heterogeneous system by three parameters, $\bar{k}$, $\sigma$, and $\lambda'$.

Having generated the heterogeneous field, let us impose a pressure difference between the upper and lower boundaries, with side boundaries closed to flow. This can be solved straightforwardly by a finite difference or finite element method.

In Figures 1a–c, we show typical results for the 2-D case. The flow domain is discretized into 200 × 200 grid cells, and $\lambda'$ is 0.15. The lines show the tracks of the fastest 90% of the particles. For a small standard deviation of natural log permeability, $\sigma = 0.5$, flow is essentially vertical. The travel-time contrast is small among all the flow paths. However, as $\sigma$ increases, this contrast greatly increases, and flow becomes channelized (Figures 1b and 1c), with exit flow at the lower boundary concentrated at fewer and fewer locations.

Flow channeling also depends on the spatial correlation range as a fraction $\lambda'$ of the flow distance. If $\lambda'$ is small, channeling does occur, but the channels are closely spaced; there are many of them over the flow domain, and their effect is "averaged out."

However, for $\lambda'$ larger than ~0.1, it is found that flow channeling is important and is not very sensitive to the exact $\lambda'$ value. Some typical results are shown in Figures 2a–c for the same $\sigma$ value of 2.0, but $\lambda'$ values of 0.015, 0.15, 0.3, respectively.

According to these results, intermediate-scale heterogeneity gives rise to flow channeling, so that solute transport along these fast paths is much larger than the mean. Furthermore, a strong spatial variation of solute concentration exists along the low-pressure outflow area of the flow domain. How to deal with such variations in solute transport is an open question.

Similar results are obtained in 3-D systems (Moreno and Tsang, 1994, and Tsang et al., 2000). Further, flow channeling also occurs in unsaturated systems. In that case, it is also a function of the degree of saturation in the flow domain (Birkholzer and Tsang, 1997).

## 3. TRACER BREAKTHROUGH CURVES

One characteristic feature of flow channeling is the highly asymmetric tracer breakthrough curves at the exit boundary of the flow domain. Let a pulse of solute be deposited at the upper inflow boundary (see Figure 1 or 2) at time $t = 0$, and let it be followed by particle or tracer tracking. The particles representing the solute are then collected as a function of time at the lower exit boundary, integrated over the lower boundary area. Summing the arrivals of the particles builds up the tracer breakthrough curves, which describe the arrival of the solute resulting from a unit release at the upper boundary.

Figures 3a and 3b show breakthrough curves for different standard deviations in the permeability distribution over a 3-D flow domain and for two different ratios of correlation range to travel distance. For the large correlation range ($\lambda' = 0.3$; Figure 3b), the breakthrough curves for small heterogeneity show a clear narrow peak at $t = 1$, which is the time of arrival for a porous medium with uniform geometric-mean permeability. When heterogeneity increases, the peak is wider and moves in the direction of shorter travel time, with a longer tail at large travel times. If the heterogeneity becomes extremely large ($\sigma = 4$ or 6), the curves again show a narrow peak, but at very short travel times and with a long tail. When a very short correlation length is used ($\lambda' = 0.075$ case, Figure 3a), a clear peak at $t = 1$ is obtained only for porous media with small heterogeneity. The solution of the conventional advective-dispersive equation accurately describes the situation shown in Figure 3a or 3b for very small $\sigma$ values up to approximately $\sigma = 1.0$ (see curves labeled $\sigma = 0.5$ and $\sigma = 1.0$). The velocities peak around the mean flow velocity (with arrival time $t = 1$) and are symmetric on either side of the mean flow velocity. The spread of velocities about the mean increases with $\sigma$. However, as $\sigma$ becomes much larger, with $\sigma > 1.0$, flow begins to be focused in a few channels, and the breakthrough curves show a much earlier peak, quite distinct from the $t = 1$ peak, and a long tail. The early peak arrives in as little as one-tenth the time of travel for a constant-permeability medium (see the $\sigma = 6.0$ case in Figure 3b). Such a phenomenon is believed to have been seen in a number of field experiments (see, for example, the review by Tsang and Neretnieks, 1998).

These results have important practical significance. First, because of flow channeling, the peak arrival of a contaminant plume could be as much as an order of

magnitude sooner than expected. This is an important concern for evaluating the potential migration of a contaminant plume, and its possibility needs to be accounted for in safety assessments. Second, because of the emergence of flow channeling at strong heterogeneity, the usefulness of the conventional advective-dispersive equation for analyzing this class of tracer breakthrough curves is very much in question.

## 4. MULTIPLE SCALES FOR FLOW AND TRANSPORT IN FRACTURED ROCKS

For a fractured rock in which flow occurs through a fracture network, multiple levels exist for the scale of heterogeneity. At the small scale, equal to or less than the dimension of a single fracture in the fracture network, there is the spatial range of fracture aperture variability. At that scale, flow and solute transport are affected by a spatial scale, $\lambda_a$, characterizing the aperture variations over the single fracture plane. The next scale is the mean spacing, s, between successive fractures in the fracture network. Beyond this is the variation of fracture density over space with a correlation range of d. This is illustrated by Figure 4, which shows schematically the dispersivity (assumed to reflect the heterogeneity scale) as a function of flow distance. When the flow distances are smaller than the single fracture dimension, the dispersivity of solute transport should be of the order of $\lambda_a$. When the flow distances are greater than the mean fracture spacing, the dispersivity will be of the order of s, meaning that solute may go through alternative nearby fractures at a distance of about s apart. When the flow distances are even larger, the dispersivity will reflect the spatial correlation range d of fracture density variation. Thus, the dispersivity as a function of transport distance should display a multiple-step structure and will level off at about d if no higher-scale heterogeneity exists. In practice,

these multiple steps may merge with each other if the different scales, rather than being represented by single values of $\lambda_a$, s or d, are ranges of values overlapping with each other.

This concept is demonstrated by Nordqvist et al. (1996). In a detailed calculation, they developed a fracture network model that includes the effect of fracture aperture variation on each fracture in the network. One example of their results is shown in Figure 5, where the tracer breakthrough curves are shown for a number of transport distances. Fracture spacing s ranges between 4 and 8 m. Note the different x-axis scales for the different curves in this figure. At very small transport distances, less than 6 m, the breakthrough curves show a sharp peak with a very narrow spread, corresponding to $\lambda_a$. As the transport distance becomes larger than s (8–12 m), we see a two-peak structure. The separation between the two peaks corresponds to the effect of two alternative paths in the network separated by s. In these calculations, there is no spatial variation of fracture density. Thus, as the transport distance becomes larger than s, the breakthrough curves display a smooth single-hump structure, with its spread corresponding to the fracture spacing. These alternative tracer breakthrough curves have been noticed in field experiments (see the review by Tsang and Neretnieks, 1998).

## 5. DIFFERENT SCALES IN MEASUREMENT, MODELING, PREDICTION, AND HETEROGENEITY

Predictive modeling of flow and transport in a heterogeneous medium involves a number of scales besides that of the heterogeneity itself—from the scale of measurements for obtaining medium parameters, to grid cell size of the calculational model, to the sampling size or the scale for predictive quantities. These are illustrated in Figure 6.

In this figure, the heterogeneity scale $S_H$ is the separation between the gray circular areas representing permeability heterogeneity. Measurements, with the measurement scale $S_M$, may then cover different regions of the system. If the measurement data are permeability data from cores, $S_M$ will be on the order of core size, which is very small. If the measurement data are from well testing, $S_M$ will be larger. If they are from long-term interference pressure tests, then $S_M$ will be much larger. As can be seen, measurements with different $S_M$ will sample very different permeability properties, depending on the relative value of $S_M$ and $S_H$.

In performing predictive modeling, we need to account for two additional scales. The first is the scale of the grid cell for numerical calculations, $S_G$; the second is the dimension of the area over which the predictive or observation quantity is to be calculated, $S_O$. It is by no means simple to extract parameter values from *in situ* measurements and then assign them to grid cells if $S_G$ is very different from $S_M$. Much work has been done (Dagan, 1993; Desbarats, 1992a,b; Desbarats, 1994; Dykaar and Kitanidis, 1993; Indelman, et al., 1996; Neuman, et al., 1992; Paleologos, et al., 1996; Rubin and Gomez-Hernandez, 1990; Pozdniakov and Tsang, 1999) on the so-called upscaling that relates the grid-cell property to data of much smaller scale (i.e., $S_G >> S_M$). However, there are cases where $S_G < S_M$, and perhaps in such cases further measurements should be made with $S_M$ smaller or of the same order as $S_G$. It is also an open question whether $S_M$ should be much larger than $S_H$. Much depends on the need of prediction, with its observational scale $S_O$.

The lesson to learn is that in modeling, we need to be aware of these different scales—$S_H$, $S_M$, $S_G$, and $S_O$. To conduct modeling calculations with input parameters

without understanding these four scales could be an important source of error, one that is very often overlooked. On the whole, how these four scales interplay and the proper way to deal with them in predictive models are yet to be determined.

One example to illustrate the importance of this issue is the use of dispersivity to calculate solute transport. Very roughly, dispersivity may be used to represent the effect of heterogeneity and corresponds to $S_H$. If we solve this problem with an advective-dispersive equation and use an observation scale $S_O$ much smaller than $S_H$, the answer can be very wrong, because the advective-dispersive equation smooths out solute concentration over the $S_H$ scale. In other words, solutions of the conventional advective-dispersive equation are only valid if $S_O \gtrsim S_H$. It is possible to find examples in the literature where the advective-dispersive equation has been incorrectly used (i.e., when this condition does not hold).

## 6. SYSTEM CHARACTERIZATION AND ANALYSIS FOR PREDICTIVE MODELING

Prediction of flow and solute transport in a groundwater system requires characterizing the system to identify relevant features and processes and to obtain parameter values for model inputs. The required types of *in situ* measurements and observations depend on the predictive quantities to be calculated. The relationship was discussed in Tsang et al. (1994). It is not a simple problem because we must ensure that all the important features and processes are included in the model. In recent years, a number of countries have tried to develop procedures and methodologies for ensuring adequate characterization of a given site. These efforts have been made to enable modeling that includes a proper uncertainty estimate. The goal is predictions on nuclear

waste repository safety over tens or hundreds of thousand years. Nuclear waste management organizations that have gone through such efforts include NIREX in UK (NIREX95, 1995), SKI and SKB in Sweden (Site94, 1996 and SR97, 1999), and Posiva in Finland (TILA 97, 1999).

The procedures developed by these organizations can be broadly divided into a number of key steps:

(1) Identification of features, events, and processes (FEPs) relevant to the site under consideration.

(2) Evaluation of the interplay and influence of FEPs with each other.

(3) Geologic surveying and evaluation of the site, especially identification of major faults and fractures.

(4) Use of multidisciplinary data and information, such as geologic, geophysical, hydrological, and geochemical input. Investigation of their consistency in developing site characteristics.

(5) Analysis of system evolution under different scenarios that may occur over the next 10,000 to 100,000 years (including changes in rainfall levels and possible glaciation over the site).

(6) Use of three kinds of models: (a) models used in data interpretation; (b) models used in observation of system behavior and estimation of effective parameters; and (c) regional flow models to be used for predictive calculations.

(7) Use of alternative models with different degrees of sophistication to analyze the system and compare results.

(8) Evaluation of uncertainties not only in parameter values, but also in FEPs that describe the system and in scenarios and external processes impact the system.

(9) Use of "expert opinions" and a structured expert elicitation process for parameters and information that are not available for the particular site under study.

(10) Use of stochastic and probabilistic modeling methods.

As we can see from this list, it is a complex procedure, made necessary by the demand for defensible predictive modeling of flow and transport in heterogeneous field sites. Overall, these are preliminary efforts using techniques that are still improving and evolving. Much progress is needed before we can be confident in our prediction of system behavior and its uncertainty range.

## 7. SUMMARY AND CONCLUDING REMARKS

In this paper, we have discussed key scientific issues in the modeling of flow and mass transport in heterogeneous media, of which fractured rock is a particular class. Permeability heterogeneity on a scale comparable with the scale of the flow domain presents challenges, ranging from dynamic flow channeling, multipeak tracer breakthrough curves, and multiscale dispersivity for fractured rocks; to issues related to the interrelationship between measurement scale, heterogeneity scale, numerical grid scale, and the scale for which predictive quantities are to be calculated. All these issues are unresolved and deserve further research.

Finally, note that for the safety assessment of a nuclear waste repository or remediation of a contaminated site, a system characterization and analysis is needed to make a defensible prediction of system behavior, with a proper estimate of uncertainties. Considerable work towards this end has been applied in different countries, and

continued work is expected in the coming years. This work affords us further opportunity to study the issues presented in this paper and to attempt to meet the need of society for long-term and large-scale predictions of flow and mass transport in realistic geologic systems.

## 8. ACKNOWLEDGMENT

We thank C. Doughty and T.N. Narasimhan for their careful review of the manuscript. This work was jointly supported by the Japan Nuclear Cycle Development Institute (JNC) under a binational JNC/DOE Collaborative Agreement Annex with the DOE Office of Environmental Management, Office of Science and Technology, and by the Director, Office of Science, Office of Basic Energy Sciences, of the U.S. Department of Energy (DOE) under Contract No. DE-AC03-76SF00098.

REFERENCES

Alumbaugh, D.L. and G.A. Newman 1997. Three-dimensional massively parallel electromagnetic inversion: II. Analysis of a crosswell experiment. *Geophys. J. Int.* 128:355–363.

Birkhölzer, J. and C.F. Tsang 1997. Solute channeling in unsaturated heterogeneous porous media. *Water Resour. Res.* 33(10):2221–2238

Dagan, C. 1993. Higher-order correction of effective conductivity of heterogeneous formations of lognormal conductivity distribution. *Transp. Porous Media* 12:279–290.

Dagan, G. 1984. Solute transport in heterogeneous porous formations. *J. Fluid Mech.* 145:141–177.

Dagan, G. 1986. Statistical theory of groundwater flow and transport: Pore to laboratory, laboratory to formation, and formation to regional scale. *Water Resourc. Res.* 22(9):120S–134S.

Dagan, G. 1990. Transport in heterogeneous porous formations: spatial moments, ergodicity, and effective dispersion. *Water Resour. Res.* 26(6):1281–1290.

Desbarats, A.J. 1992a. Spatial averaging of the transmissivity in heterogeneous fields with flow toward well. *Water Resour. Res.* 28(3):757–767.

Desbarats, A.J. 1992b. Spatial averaging of the hydraulic conductivity in three-dimension heterogeneous porous media. *Mathl. Geol.* 24(3): 249–267.

Desbarats, A.J. 1994. Geostatistical analysis of aquifer heterogeneity from the core scale to the basin scale: A case study. *Water Resour. Res.* 30(3):673–684.

Deutsch, C.V. and A.G. Journal 1992. GSLIB—Geostatistical Software Library and Users Guide, Oxford University Press, New York and Oxford.

Dykaar, B.B. and P.K. Kitanidis 1993. Transmissivity of heterogeneous formation. *Water Resour. Res.* 29(4):985–1001.

Gelhar, L.W. 1986. Stochastic subsurface hydrology from theory to applications. *Water Resour. Res.* 22(9):135S–145S.

Gelhar, L.W. and C.L. Axness 1983. Three-dimensional stochastic analysis of macrodispersion in aquifers. *Water Resour. Res.* 19(1):161–180.

Hyndman, D.W., J.M. Harris, and S.M. Gorelick 1994. Coupled seismic and tracer test inversion for aquifer property characterization. *Water Resour. Res.* 30(7), 1965–1977.

Indelman, P., A. Fiori, and G. Dagan 1996. Steady flow toward wells in heterogeneous formation: mean head and equivalent conductivity. *Water Resour. Res.* 32(7):1975–1983.

Javandel, I., C. Doughty, and C.F. Tsang 1984. Groundwater Transport, *Water Resources Monograph* 10, American Geophysical Union, Washington, D.C.

Karasaki, K., B. Freifeld, A. Cohen, K. Grossenbacher, P. Cook, and D. Vasco 2000. A multidisciplinary fractured rock characterization study at Raymond Field Site, Raymond, California. *Journal of Hydrology*, accepted for publication.

Lee, D.S., V.M. Stevenson, P.F. Johnston, and C.E. Mullen 1995. Time-lapse crosswell seismic tomography to characterize flow structure in the reservoir during the thermal stimulation. *Geophysics* 60(3):660–666.

deMarsily, G. 1986. Quantitative hydrogeology, Orlando, Florida: Academic Press.

Moreno, L. and C.-F. Tsang 1994. Flow channeling in strongly heterogeneous porous media: A numerical study. *Water Resour. Res.* 30(5):1421–1430.

Nekut, A.G., 1994. Electromagnetic ray-trace tomography. *Geophysics* 55:371–377.

Neuman, S.P., and Y-K. Zhang 1990. A quasi-linear theory of non-Fickian and Fickian subsurface dispersion. 1. Theoretical analysis with application to isotropic media. *Water Resour. Res.* 26(5):887–902.

Neuman, S.P., C.L. Winter, and C.M. Newman 1987. Stochastic theory of field-scale dispersion in anisotropic porous media. *Water Resour. Res.* 23(3):453–466.

Neuman, S.P., S. Orr, O. Levin, and E. Paleologos 1992. Theory and high-resolution finite element analysis of 2D and 3D effective permeability in strongly heterogeneous porous media. In T.F. Russell, et al. (eds.), *Mathematical Modeling in Water Resources*, Vol. 2. New York: Elsevier, pp. 118–136.

NIREX95 1995. A preliminary analysis of the groundwater pathways for a deep repository at Sellafield. Volume 1: Development of the Hydrogeological Conceptual Model. Volume II: Derivation of Effective Hydrogeological Parameter for Regional Model III: Calculations of Risk. United Kingdom NIREX Limited, Science Report 5/95/012.

Nordqvist, A.W., Y.W. Tsang, C.F. Tsang, B. Dverstorp, and J. Andersson 1996. Effects of high variance of fracture transmissivity on transport and sorption at different scales in a discrete model for fractured rocks. *J. of Contaminant Hydrology* 22(1–2):39–66.

Paleologos, E.K., S.P. Neuman, and D. Tartakovsky 1996. Effective hydraulic conductivity of bounded, strongly heterogeneous porous media. *Water Resour. Res.* 32(5):1333–1342.

Pozdniakov, S.P. and C:-F. Tsang 1999. A semianalytical approach to spatial averaging of hydraulic conductivity in heterogeneous aquifers. *Journal of Hydrology*, 216, 78–98.

Rector, J.W., III 1995. Crosswell methods. *Geophysics* 60:627–920.

Rubin, Y. 1990. Stochastic modeling of macrodispersion in heterogeneous porous media. *Water Resourc. Res.* 26(1):133–141.

Rubin, Y. and J.J. Gomez-Hernandez 1990. A stochastic approach to the problem of upscaling of conductivity in disordered media: Theory and unconductional numerical simulations, *Water Resour. Res.* 26(4):691–701.

Rubin, Y., G. Mavko, and J. Harris 1992. Mapping permeability in heterogeneous aquifers using hydrological and seismic data. *Water Resour. Res.* 28(7), 1809–1816.

Site94 1996. Deep repository performance assessment project. Volumes 1 and 2, Swedish Nuclear Power Inspectorate (SKI), Report 96:36.

SR97 1999. Post-closure safety. Deep Repository for Spent Nuclear Fuel. Volumes I and II. Swedish Nuclear Fuel and Waste Management Company (SKB).

Smith, T., M. Hoversten, E. Gasperikova, and F. Morrison 1999. Sharp Boundary inversion of 2D magnetotelluric data. *Geophysical Prospecting* 47:469–486.

TILA-97 1999. Safety assessment of spent fuel disposal in Hästholmen, Kivetty, Olkiluoto, and Romuvaara. Posiva OY, Finland.

Tichelaar, B.W. and P.J. Hatchell 1997. Inversion of 4-C borehole flexural waves to determine anisotropy in a fractured carbonate reservoir. *Geophysics* 62(5):1432–1441.

Tsang, C.F. and I. Neretnieks 1998. Flow channeling in heterogeneous fractured rocks. *Reviews of Geophysics* 36(2):275–298.

Tsang, C.F., L. Gelhar, G. de Marsily, and J. Andersson 1994. Solute transport in heterogeneous media: A discussion of technical issues, coupling site characterization, and predictive assessment. *Adv. in Water Res.* 17(4):259–264.

Tsang, C.F., L. Moreno, Y. Tsang, and J. Birkholzer 2000. Dynamic channeling of flow and transport in saturated and unsaturated heterogeneous media. Accepted for *Geophysical Monograph 42*, T. Nicholson (ed.).

Tsang, Y.W. and C.F. Tsang 1987. Channel model of flow through fractured media. *Water Resour. Res.* 23(3):467–479.

Tsang, Y.W. and C.F. Tsang 1989. Flow channeling in a single fracture as a two-dimensional strongly heterogeneous permeable medium. *Water Resourc. Res.* 25(9):2076–2080.

Vasco, D.W., J.E. Peterson, Jr., and K.H. Lee 1997. Ground-penetrating radar velocity tomography in heterogeneous and anisotropic media. *Geophysics* 62(6):1758–1773.

Vasco, D.W., K.K. Karasaki, and L. Myer 1998. Monitoring of fluid injection and soil consolidation using surface tilt measurements. *Journal of Geotechnical and Geoenvironmental Engineering*. 124(1):29–37.

Walsh, J.J. (Society of Exploration Geophysicists, 63rd Annual Meeting and International Exhibition, Washington, DC, United States) 1993. Fracture estimation from parametric inversion of SV waves in multicomponent offset VSP data. In: *Society of Exploration Geophysicists; Expanded Abstracts with Biographies; Technical Program; 63rd Annual Meeting and International Exhibition*, Tulsa, OK:63:140–142

Wilt, M.J.; D.L Alumbaugh, H.F. Morrison, A. Becker, K.H. Lee, M. Deszcz-Pan, 1995. Crosswell electromagnetic tomography; system design considerations and field result. *Geophysics* 60(3):871-885.

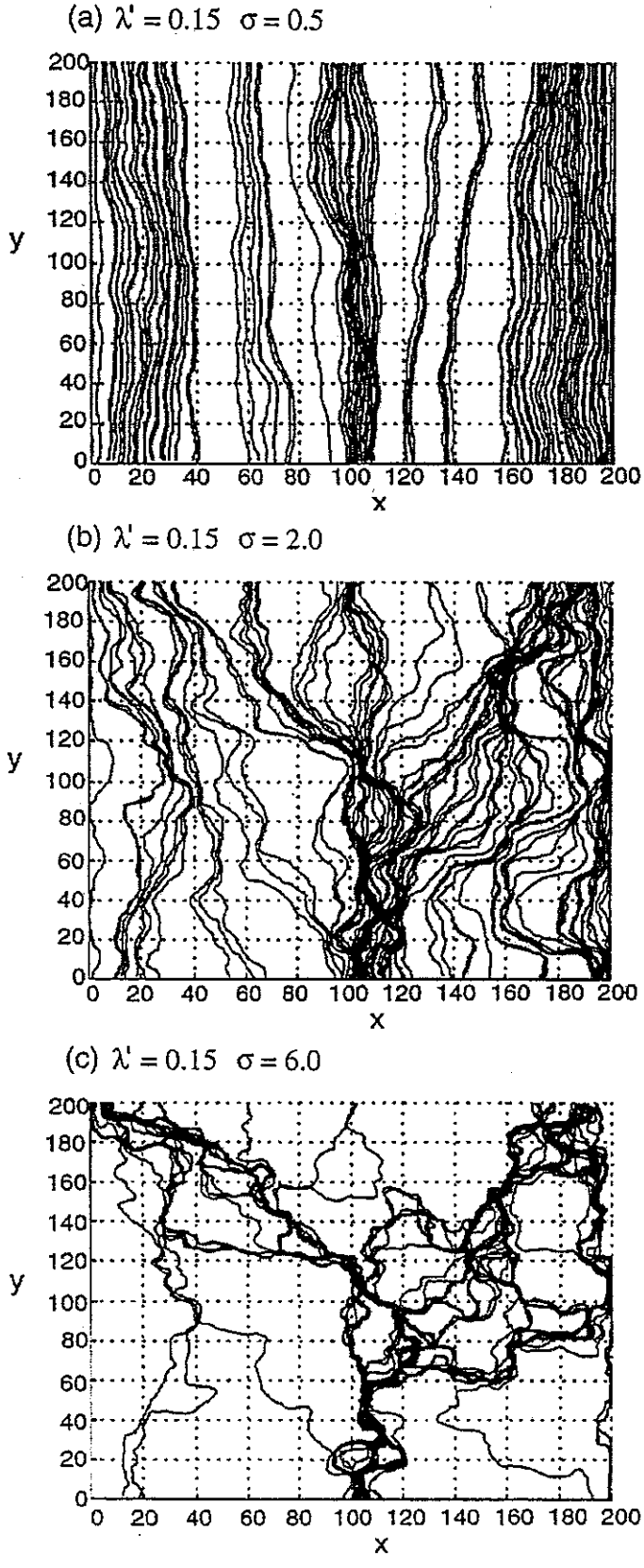


Figure 1a–c. Emergence of flow channeling, under a pressure step applied from the top to the bottom boundary, as a function of σ for a 2D heterogeneous medium. Tracer flow paths are shown for λ′ = 0.15 and σ = 0.5, 2.0, and 6.0 in a, b, and c respectively.

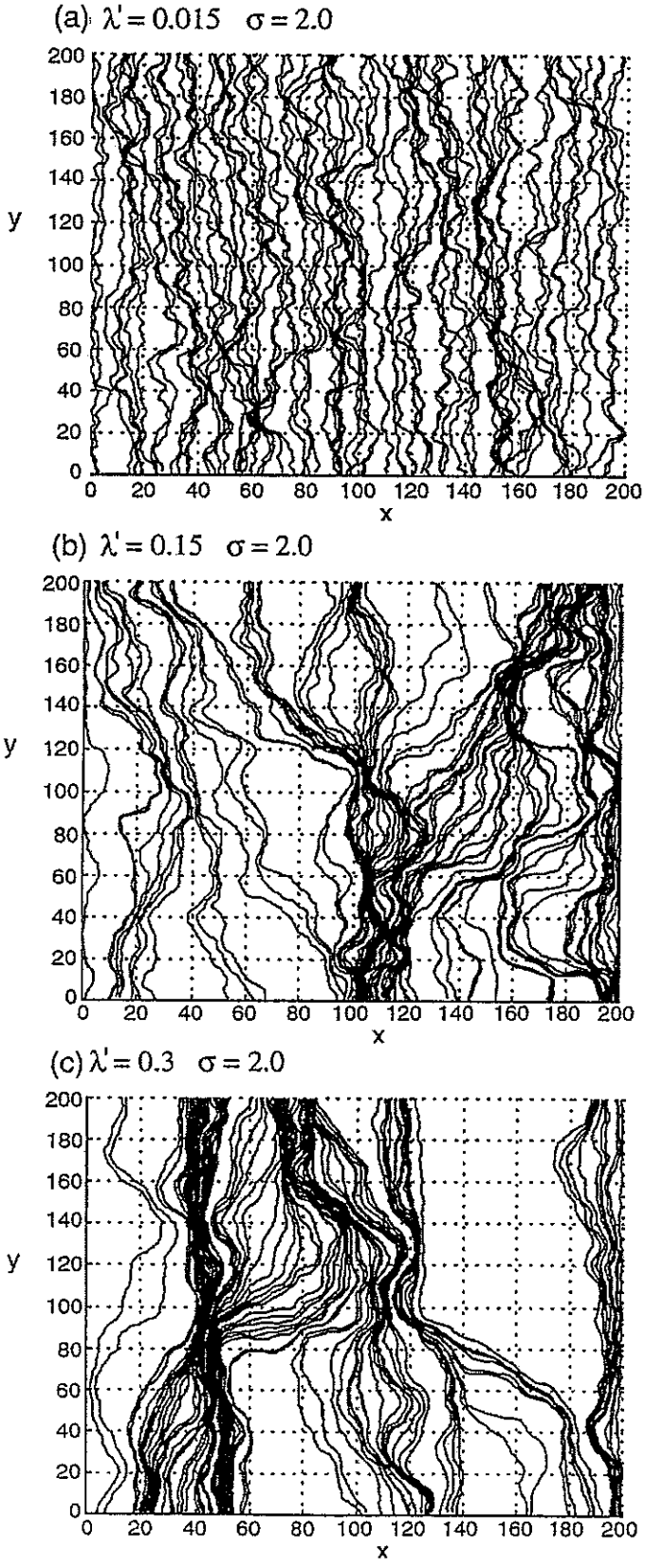


Figure 2a–c. Emergence of flow channeling, under a pressure step applied from the top to the bottom boundary, as a function of λ' for a 2D heterogeneous medium. Tracer flow paths are shown for σ = 6.0 and λ' = 0.015, 0.15, and 0.3 in a, b, and c respectively.

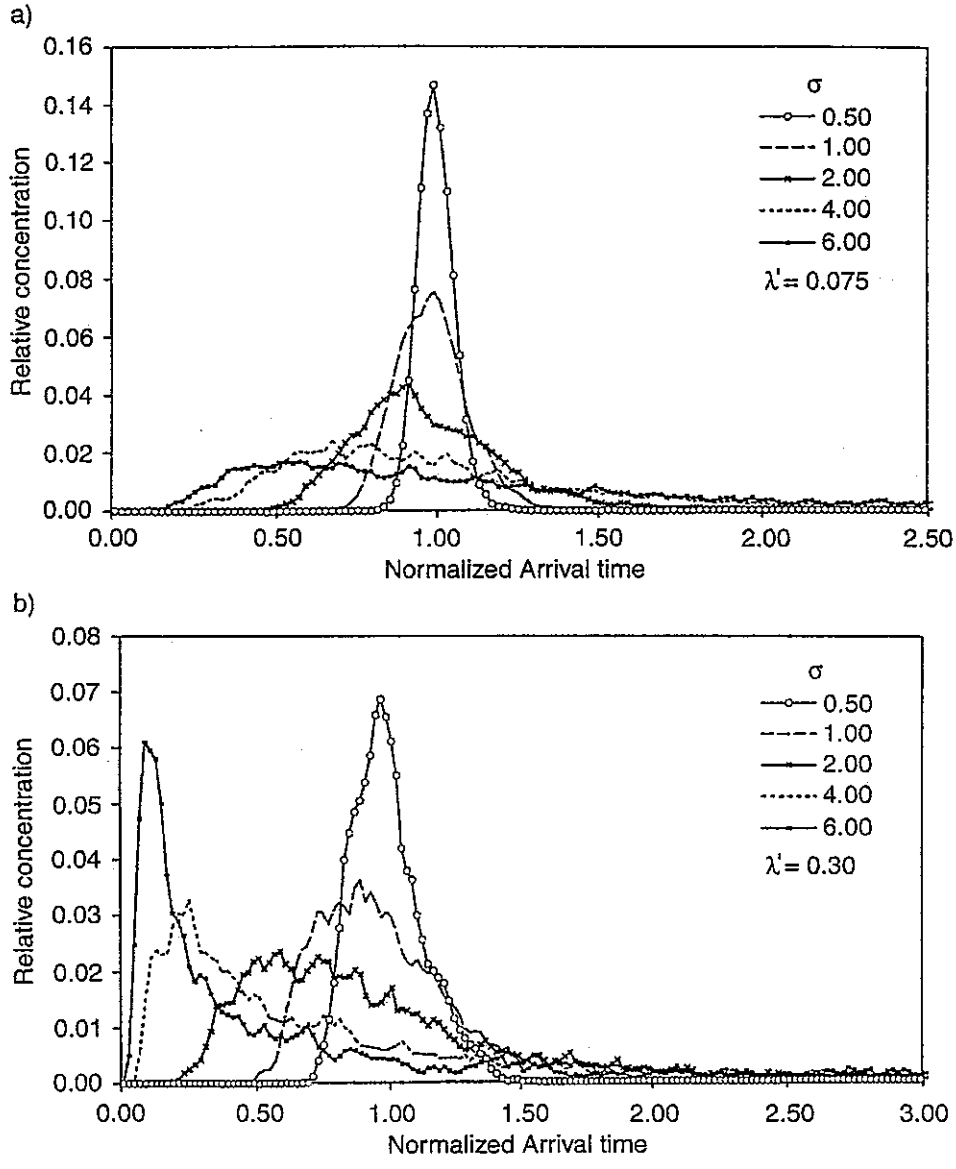


Figure 3a–b. Breakthrough curves for different standard deviation σ values and for a ratio of correlation length to travel length λ of .075 and 0.30 in figures a and b respectively. The x-axis gives the arrival time normalized to (i.e., in units of) the expected time if the medium were of constant permeability. The y-axis gives the concentration as a fraction of the input pulse concentration.

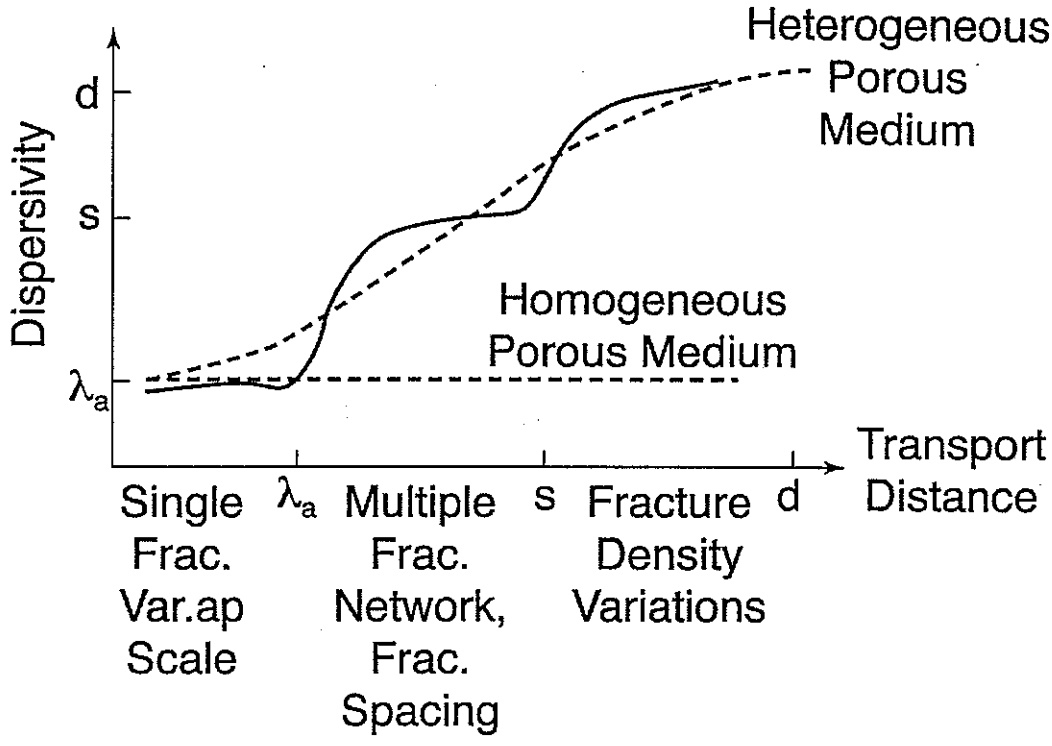


Figure 4. Schematic diagram of multiple-step dispersivity for flow and transport in fractured rocks.

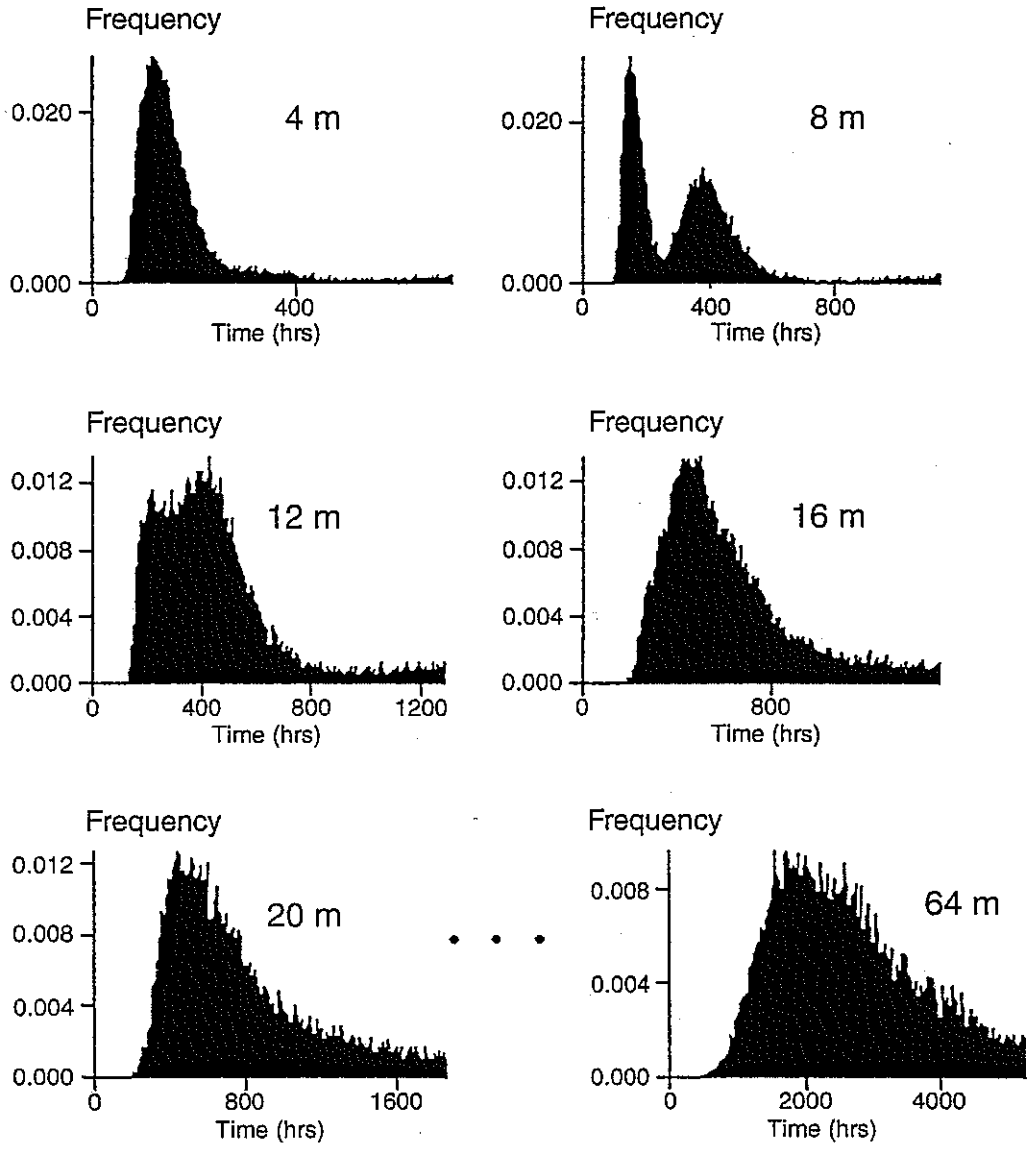


Figure 5. Tracer breakthrough curves for a fracture network, with variable apertures for each fracture. The fracture spacing ranges from 4 to 8 m. The transport distance is labeled on each plot.

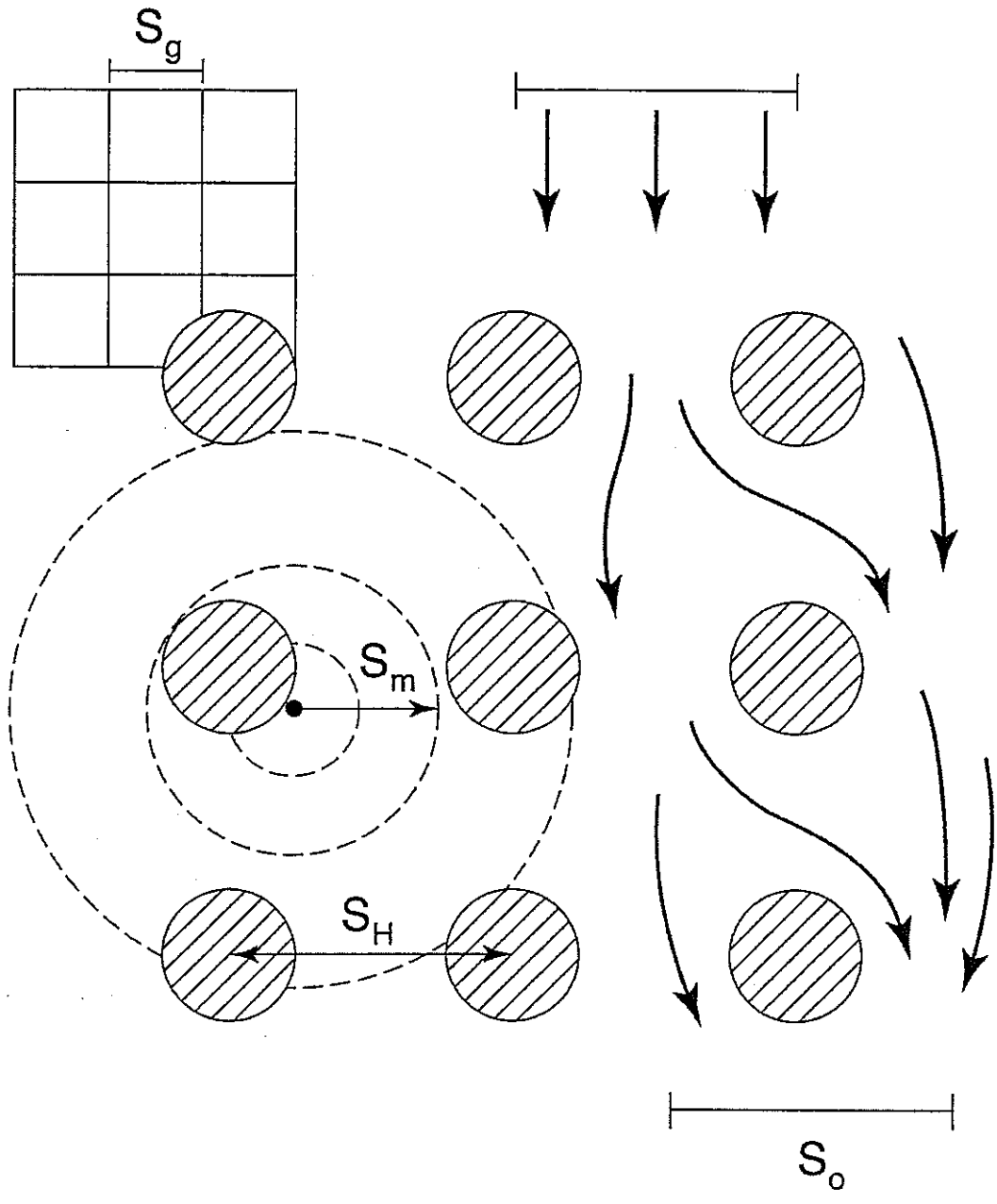


Figure 6. Schematic diagram of the different scales in predictive modeling: scale of heterogeneity $S_H$, scale of measurement $S_M$, scale of model grid $S_G$ and scale of observation or predictive quantity $S_O$.